



I. R. IRAN

ISSN: 2423-7167

e-ISSN: 1735-9244



International Journal of Engineering

Journal Homepage: www.ije.ir



TRANSACTIONS C: ASPECTS

Volume 37, Number 06, June 2024

Materials and Energy Research Center

INTERNATIONAL JOURNAL OF ENGINEERING

Transactions C: Aspects

DIRECTOR-IN-CHARGE

H. Omidvar

EDITOR IN CHIEF

G. D. Najafpour

ASSOCIATE EDITOR

A. Haerian

EDITORIAL BOARD

- | | | | |
|------|--|-------|--|
| S.B. | Adeloju, Charles Sturt University, Wagga, Australia | A. | Mahmoudi, Bu-Ali Sina University, Hamedan, Iran |
| K. | Badie, Iran Telecomm. Research Center, Tehran, Iran | O.P. | Malik, University of Calgary, Alberta, Canada |
| M. | Balaban, Massachusetts Ins. of Technology (MIT), USA | G.D. | Najafpour, Babol Noshirvani Univ. of Tech., Babol, Iran |
| M. | Bodaghi, Nottingham Trent University, Nottingham, UK | F. | Nateghi-A, Int. Ins. Earthquake Eng. Seis., Tehran, Iran |
| E. | Clausen, Univ. of Arkansas, North Carolina, USA | S. E. | Oh, Kangwon National University, Korea |
| W.R. | Daud, University Kebangsaan Malaysia, Selangor, Malaysia | M. | Osanloo, Amirkabir Univ. of Tech., Tehran, Iran |
| M. | Ehsan, Sharif University of Technology, Tehran, Iran | M. | Pazouki, MERC, Karaj, Iran |
| J. | Faiz, Univ. of Tehran, Tehran, Iran | J. | Rashed-Mohassel, Univ. of Tehran, Tehran, Iran |
| H. | Farrahi, Sharif University of Technology, Tehran, Iran | S. K. | Sadrnezhaad, Sharif Univ. of Tech, Tehran, Iran |
| K. | Firoozbakhsh, Sharif Univ. of Technology, Tehran, Iran | R. | Sahraeian, Shahed University, Tehran, Iran |
| A. | Haerian, Sajad Univ., Mashhad, Iran | A. | Shokuhfar, K. N. Toosi Univ. of Tech., Tehran, Iran |
| H. | Hassanpour, Shahrood Univ. of Tech., Shahrood, Iran | R. | Tavakkoli-Moghaddam, Univ. of Tehran, Tehran, Iran |
| W. | Hogland, Linnaeus Univ, Kalmar Sweden | T. | Teng, Univ. Sains Malaysia, Gelugor, Malaysia |
| A.F. | Ismail, Univ. Tech. Malaysia, Skudai, Malaysia | P. | Tiong, Nanyang Technological University, Singapore |
| M. | Jain, University of Nebraska Medical Center, Omaha, USA | X. | Wang, Deakin University, Geelong VIC 3217, Australia |
| M. | Keyanpour rad, Materials and Energy Research Center, Karaj, Iran | H. | Omidvar, Amirkabir Univ. of Tech., Tehran, Iran |

EDITORIAL ADVISORY BOARD

- | | | | |
|-------|--|-------|---|
| S. T. | Akhavan-Niaki, Sharif Univ. of Tech., Tehran, Iran | A. | Kheyroddin, Semnan Univ., Semnan, Iran |
| M. | Amidpour, K. N. Toosi Univ of Tech., Tehran, Iran | N. | Latifi, Mississippi State Univ., Mississippi State, USA |
| M. | Azadi, Semnan university, Semnan, Iran | H. | Oraee, Sharif Univ. of Tech., Tehran, Iran |
| M. | Azadi, Semnan University, Semnan, Iran | S. M. | Seyed-Hosseini, Iran Univ. of Sc. & Tech., Tehran, Iran |
| F. | Behnamfar, Isfahan University of Technology, Isfahan | M. T. | Shervani-Tabar, Tabriz Univ., Tabriz, Iran |
| R. | Dutta, Sharda University, India | E. | Shirani, Isfahan Univ. of Tech., Isfahan, Iran |
| M. | Eslami, Amirkabir Univ. of Technology, Tehran, Iran | A. | Siadat, Arts et Métiers, France |
| H. | Hamidi, K.N.Toosi Univ. of Technology, Tehran, Iran | C. | Triki, Hamad Bin Khalifa Univ., Doha, Qatar |
| S. | Jafarmadar, Urmia Univ., Urmia, Iran | | |

TECHNICAL STAFF

M. Khavarpour; M. Mohammadi; V. H. Bazzaz, R. Esfandiar; T. Ebadi

DISCLAIMER

The publication of papers in International Journal of Engineering does not imply that the editorial board, reviewers or publisher accept, approve or endorse the data and conclusions of authors.

CONTENTS

Transactions C: Aspects

J. Naseri, H. Hasanpour, A. Ghanbari Sorkhi	Accelerating Legislation Processes through Semantic Similarity Analysis with BERT-based Deep Learning	1050-1058
P. Padmaja, D. Vemana Chary, R. Erigela, G. Sirisha, S. K. ChayaDevi, M. C. Pedapudi, B. Balaji, S. Cheerala, V. Agarwal, Y. Gowthami	Improved Performance Analysis and Design of Dual Metal Gate FinFET for Low Power Digital Applications	1059-1066
M. Khodadadi, L. Riazi, S. Yazdani	A Novel Ensemble Deep Learning Model for Building Energy Consumption Forecast	1067-1075
M. Nouranbakhsh, K. Barkhordari, S. Ghasemi	Improvement of Sand Soil with Bio-micropiles and Bio-grout Injection in Reinforced Soils	1076-1084
H. Mohammadian KhalafAnsara, J. Keighobadi	Deep Reinforcement Learning with Immersion- and Invariance-based State Observer Control of Wave Energy Converters	1085-1097
A. I. Keksin, N. I. Sorokopud, N. N. Zakirov	Peculiarities of Abrasive Finishing of Surfaces of Parts Made of Aluminium Alloy of AMts Grade in Magnetic Field	1098-1105
S. M. Seyed Hosseini, K. Shahanaghi, S. Shasfand	Functional Model of Integrated Maintenance in Petrochemical Industries	1106-1117
F. Marchione	Stone Architecture in Abruzzo: Seismic Risk Analysis of Bell Tower of the Church of San Lorenzo in San Buono	1118-1126
M. Ansari, J. Jamali, M. H. Fatehi-Dindarlou, M. A. Rahgoshay, O. Mahdiyari	A Novel Sensor Integration Scheme for an Aided Inertial Navigation System Based on a Generalized PID Filter in the Presence of Observation Uncertainty	1127-1135
M. Ghamari, M. S. Karimi, P. B. Lourenço, H. S. Sousa	Flanges' Impact on Persian Historical Masonry Walls: Modeling Safety Factors	1136-1145
H. Rohbani, A. Moazemi Goudarzi, F. Morshedsolouk	Compressive Mechanical Properties and Water Absorption of Glass fiber-reinforced Plastics Pipes Aged in Caspian SeaWater	1146-1153
A. Anjomrouz	Improvement of Surface Evaporation by Reducing Heat Transfer to Fluid Bulk and Increasing Heat Absorption	1154-1163

M. Khanmohammadi, S. Razavi	Proposing New Artificial Intelligence Models to Estimate Shear Wave Velocity of Fine-grained Soils: A Case Study	1164-1174
G. R. Einy-Sarkalleh, R. Tavakkoli-Moghaddam, A. Hafezalkotob, S. E. Najafi	A Mathematical Model for Resource Sharing with Bilateral Contracts in a Supply Chain with Government Intervention under a Game Theory Approach	1175-1182
A. Imanifar, H. Yaghoobi	Using Reluctance Torque Theory in Spoke Type Permanent Magnet Vernier Motors to Increase Average Torque	1183-1193
X. Yang	Framework of Electric Vehicle Fault Diagnosis System Based on Diagnostic Communication	1194-1207



Accelerating Legislation Processes through Semantic Similarity Analysis with BERT-based Deep Learning

J. Naseri^a, H. Hasanpour^{*a}, A. Ghanbari Sorkhi^b

^a Faculty of Computer Engineering, Shahrood University of Technology, Shahrood, Iran

^b Faculty of Electrical and Computer Engineering, University of Science and Technology of Mazandaran, Behshahr, Iran

PAPER INFO

Paper history:

Received 22 November 2023

Received in revised form 06 January 2024

Accepted 20 January 2024

Keywords:

Text Mining

Neural Network

Semantic Search

Sentence Embedding in Vector Space

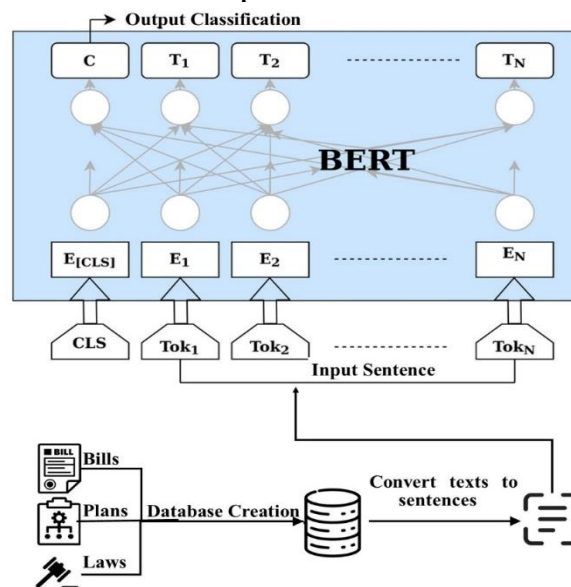
BERT Model

ABSTRACT

Countries are managed based on accurate and precise laws. Enacting appropriate and timely laws can cause national progress. Each law is a textual term that is added to the set of existing laws after passing a process with the approval of the assembly. In the review of each new law, the relevant laws are extracted and analyzed among the set of existing laws. This paper presents a new solution for extracting the relevant rules for a term from an existing set of rules using semantic similarity and deep learning techniques based on the BERT model. The proposed method encodes sentences or paragraphs of text in a fixed-length vector (dense vector space). Thereafter, the vectors are utilized to evaluate and score the semantic similarity of the sentences with the cosine distance measurement scale. In the proposed method, the machine can understand the meaning and concept of the sentences by using the BERT model coding method. The BERT model considers the position of the entities in the sentences. Then the semantic similarities of documents, calculating the degree of similarity between their documents with a subject, and detecting their semantic similarity are done. The results obtained from the test dataset indicated the precision and accuracy of the method in detecting semantic similarities of legal documents related to the Islamic Consultative Assembly of Iran, as well as the precision and accuracy of performance above 90%.

doi: 10.5829/ije.2024.37.06c.01

Graphical Abstract



*Corresponding Author Email: h.hasanpour@shahroodut.ac.ir (H. Hasanpour)

Please cite this article as: Naseri J, Hasanpour H, Ghanbari Sorkhi A. Accelerating Legislation Processes through Semantic Similarity Analysis with BERT-based Deep Learning. International Journal of Engineering, Transactions C: Aspects. 2024;37(06):1050-8.

1. INTRODUCTION

In a legal system, legislation plays a critical role in shaping the policies and regulations that guide a nation's development. Therefore, the process of enacting laws must be approached with a high degree of precision and deliberation to ensure that they are beneficial for the country's progress. To this end, a plan or bill sent to the assembly for approval is first evaluated and analyzed by experts from different aspects. However, human mistakes in data collection and evaluation of legal frameworks in the review of plans and bills can challenge this legislation. Artificial Intelligence (AI)-based software can play the role of an intelligent assistant in law and legislative affairs, and help representatives and experts prepare plans and bills, evaluate them, control documents regarding solecism, and identify and extract relevant laws. This capability accelerates the legislative process, decreases costs, and improves the quality of decrees (1, 2).

The legislative process is time-consuming, involving lengthy discussions and multiple levels of expertise (3). Hence, it is required to analyze a significant volume of textual data in a short timeframe, making it challenging to accurately assess the relationships between proposed bills and existing laws. The use of AI-powered software can significantly reduce the time and effort required for this analysis, allowing legislators to focus on critical decision-making and debate. Given the recent development in text processing, deep learning techniques based on BERT model (4) can be utilized for the semantic search of different parts of a plan and bill in the existing set of laws, and then they can be carefully evaluated by experts and legislators (5).

In this method, the text of a plan and bill, which is submitted to the assembly, is first pre-processed. Therefore, spelling errors are corrected, the text is converted into sentences, the word roots in the sentence are found, and the roles of words in the sentence are identified. Thereafter, the prepositions are removed and the text sentences are converted into numerical vectors (6). Further, the semantic similarities (7-9) of the text sentences with the relevant laws are extracted in such a way that the sentences or paragraphs of the texts are encoded in a vector space using BERT model based on deep learning. Then the scores of semantic similarities of the sentences are calculated using a similarity criterion. Additionally, the sentences with the same or close meanings are extracted. Therefore, the important semantic words are discovered from documents and the model identifies which sentences are semantically similar by considering the position of their constituents.

The comparison and evaluation of the proposed method with the existing methods for searching in the text indicated that this method can provide better results in the semantic search of documents due to recognizing

and understanding the relationships between words, and ultimately the meaning of the sentence.

The initial methods for text search, which perform the search only based on the matching of the query string, cannot work properly if the words are embedded in the sentence or the word is used in an expanded way in the sentence (6, 10).

In the second text search methods, which use Term Frequency - Inverse Document Frequency (TF-IDF) and BM25 techniques, the keywords are first extracted, and then the topics and meanings of the sentences are detected using these keywords. In this method, keywords are specified and weighed for the semantic analysis of sentences. Keywords represent the entire content of the text, and thus they are weighed based on the number of repetitions and their importance. However, this method cannot recognize synonyms and more complex search terms in a paragraph because TF-IDF and BM25 techniques work based on a "bag of words" simplifying principle. In other words, the text is classified into a set of words from which numerical vectors are generated, but the order and positions of the words in the text are not observed. Therefore, this method cannot accurately understand and extract semantic similarities of documents.

The third methods (such as the proposed method) are designed based on the neural network. In semantic search with the neural network, the neural model learns to encode a query as a vector to better understand the meaning or semantic value of a query and calculate the association between sentences by placing sentences in a vector space. This technique seeks to encode a sentence or paragraphs of short text into a fixed-length vector (dense vector space), and then use the vector to evaluate to some extent their similarities reflect human semantic judgments. In this method, the neural language model is designed based on the transformer architecture and it allows detecting the relationships between words easily, and then correctly extracting the semantic relationship of documents (11, 12).

The remainder of this paper is as follows. Section 2 presents a review of the literature on text processing and the use of artificial intelligence in legislation in recent years. Section 3 elaborates the proposed method and the different steps of this method, in addition to some basic concepts to identify the semantic similarities. Section 4 discusses the evaluation criteria, result analysis, and performance appraisal. Finally, the conclusion is presented in section 5.

2. LITERATURE REVIEW AND RESEARCH BACKGROUND

The Islamic Parliament Research Center of Iran has recognized the potential of AI in enhancing the policy-

making and planning processes, and has emphasized the need for skilled human resources in AI and law to effectively implement AI technology in the legislative process. This recognition highlights the importance of investing in AI-related training and education to support the effective use of AI in lawmaking (13).

The research conducted by Leskovec et al. (14) focused on the application of data mining techniques for analyzing textual data, specifically in terms of terminology extraction and document similarity assessment. The paper discussed various segmentation and distance measurement methods used in text analysis, including Euclidean, Jaccard, and cosine distances.

Researchers proposed a method that leverages semantic similarities in thesauri to identify key terms in textual data (15, 16). After pre-processing the text, significant words are initially identified using statistical techniques. Next, secondary key terms are generated by analyzing the embedded terms derived from the significant words and the thesaurus, with the TF-IDF weighting scheme. Finally, the ultimate key terms are selected based on the hierarchical and equivalent relations present in the thesaurus, utilizing clustering techniques (17).

Within the field of AI, textual databases continue to grow, encompassing an extensive range of documents such as new articles, books, and web pages. This rapid expansion highlights the pressing need for automated evaluation tools to assess text sources efficiently. One such solution is automatic text summarization, which utilizes text processing methods to extract precise summaries and employs scoring criteria and part-of-speech tagging to assign importance weights to words in a sentence (18).

Earlier research has utilized deep learning techniques to evaluate the semantic similarity of textual sentences by mapping them into a vector space. This approach involves embedding sentences and paragraphs of documents within a vector space and identifying the most similar embeddings from the collection, enabling the extraction of semantically similar documents that share a high degree of overlap (19).

Numerous researchers emphasized the potency of text mining in uncovering critical patterns within big data by analyzing unstructured text. The assessment of word or document similarities is a critical component of natural language processing and information retrieval, as these similarities can be identified through statistical calculations and word similarity measurements (20).

Jiang et al. (21) explored the extraction of semantic relationships between documents and text similarities, building a concept space for each term based on the Wikipedia knowledge base. This concept space is constructed by weighting various parts of the Wikipedia website, enabling the calculation of semantic similarities

between two terms. Moreover, two texts can be compared using the weighted concept space to evaluate their level of similarity.

Karaa (22) proposed a method for performing stemming, retrieving information, and locating documents relevant to users' information needs. Stemming is a pre-processing technique in text mining and a key requirement in natural language processing-related applications. Therefore, it plays a vital role in information retrieval systems, contributing to their accuracy and effectiveness.

Kamyar et al. (23) highlighted the significance of weighting words, a crucial step in language processing that influences the precision of text classification. They also presented a novel approach to weighting words, building upon the statistical TF-IDF weighting method. This method modifies the TF parameter, which measures word frequency in a text, by incorporating additional linguistic features that enhance its accuracy.

Reimers and Gurevych (24) evaluated the performance of BERT model and established that it displays exceptional performance in sentence classification and sentence pair regression. This model leverages the power of transformer networks and mutual encoding to encode two sentences as input, subsequently predicting a target value and mapping the text to a vector space, resulting in the extraction of semantic similarities between text sentences (25).

Before the advent of neural search, the initial approaches to text retrieval were restricted to basic string matching, which involved searching through databases or text files to identify instances of the query string. These methods were not sufficiently sophisticated to satisfy the demands of semantic search in large text corpora, resulting in limited accuracy and relevance of search results.

The second generation of text retrieval relied on algorithms such as TF-IDF and BM25 to identify crucial keywords in the text and extract semantic topics based on keyword weighting. Despite this advancement, these algorithms still faced challenges in identifying broader search queries within paragraphs and detecting synonyms, as they operated on the bag-of-words principle, converting text into numerical vectors without preserving the word order and position in the document.

The third generation of text retrieval, which encompasses the proposed method, has leveraged neural networks to enhance semantic search. This approach trains a model to encode queries as vectors, thereby enhancing the understanding and semantic value capture of the query. Moreover, it can establish relationships between sentences by placing them in a vector space, facilitating more sophisticated and accurate retrieval of relevant information.

3. THE PROPOSED METHOD

This section proposes a method for processing text and discovering semantic similarities in plans and bills. The overall structure of the proposed method is given in Figure 1.

The proposed method involves pre-processing textual data, including plans, bills, and laws, into a structured database (26). The BERT model, which has been pre-trained on large text datasets, is used to identify semantic similarities between sentences in the documents. The sequential neural network and transformer architecture enable the encoding of each text into a fixed-length vector, which is then used to score the semantic similarity of sentences based on cosine distance. This approach can effectively handle documents with multiple paragraphs, accurately extracting semantic similarities between sentences in plans, bills, and laws.

After the semantic similarity score is computed, the model extracts a semantic classification, identifying words with similar semantic values. Furthermore, it evaluates each target sentence in the text based on its context, considering the preceding and succeeding sentences, and measuring the score based on the position of the sentence. This classification of semantic similarities between plans and bills provides a valuable tool for legislative experts, enabling them to quickly identify relationships between laws and accurately detect semantic similarities between plans and bills (27).

The proposed method involves the following steps:

- **Pre-processing:** All plans, bills, and laws are entered into a structured database after text pre-processing.
- **Sentence extraction:** Sentences are extracted from the texts of plans, bills, and laws.
- **Semantic similarity analysis:** Deep learning and the BERT model are used to identify semantic similarities between sentences.
- **Score calculation:** The semantic similarity score of each document (plan or bill) is computed.
- **Semantic classification:** The semantic classification of documents is extracted based on the similarity score.

These sections are explained in detail as follows.

3.1. Pre-processing The first stage of the proposed method involves text pre-processing and preparation, including concept identification and extraction. Next, text enrichment is performed, which involves labeling the semantic roles of word components in the sentences, eliminating stop words such as "from" and "with," stemming the text words, and extracting and identifying keywords and nominal entities.

3.2. Using BERT Model To Identify Semantic Similarity

BERT is a deep learning algorithm

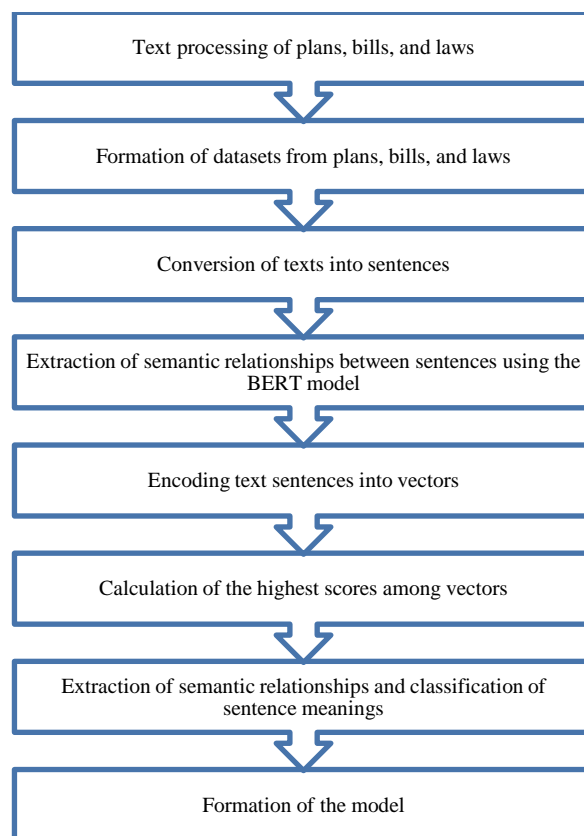


Figure 1. The overall structure of the proposed method

that focuses on natural language processing. It understands the meaning of the smallest units of spoken language, including the use of prepositions in text and expressions. By comprehending the structure and complexity of language, it grasps the relationships between words and their meanings. Additionally, unlike language models that can only read input text unidirectionally (from left to right or from right to left), BERT can process information bidirectionally simultaneously. This allows it to understand the meaning of words in context and within the text.

In the second stage of the semantic search, the semantic similarities between sentences are evaluated using the BERT model. Semantic search systems examine different criteria such as understanding the nature, meanings of words, and variety of words to find the concept of the search and use the meaning of words to provide more interactive results in a database and help the searcher to extract answers and results. Semantic search is performed by embedding words in the text and finding the closest embeddings to detect inputs with the same meanings as the query (27).

Using the BERT model, which is a pre-trained model on large texts, this paper seeks to identify semantic similarities between sentences. BERT model can perceive the meaning of sentences, using sequential

neural networks and a technical architecture called transformer. Sequential neural networks and a technical architecture, called transformer are famous and advanced neural network architecture for text processing and machine translation. Transformer utilizes self-attention layers to model dependencies between words in sentences. The transformer can pay attention to the connections between each word and other words of the sentence, using the self-attention operations on different words of the sentence.

3. 2. 1. Transformer Model Architecture A transformer model receives a sentence at the input and delivers its translation at the output.

As shown in Figure 2 this model is classified into groups, encoders and decoders, which are connected together.

In this structure, each encoder has two separate sub-layers, a self-attention layer, and a feedforward neural network. The encoder input first passes through a self-attention layer which helps the encoder focus on other words in the sentence during the word encoding process. The output of the self-attention layer enters a feedforward neural network layer.

Each decoder has two layers, self-attention and feedforward neural network, but in the decoders of the attention layer, there is another layer, called Encoder-Decoder Attention, which helps the decoder focus on relevant words. To the best of our knowledge, natural language processing first needs to convert the input words into vectors to be understandable for the machine, which is done by word embedding algorithms, and thus

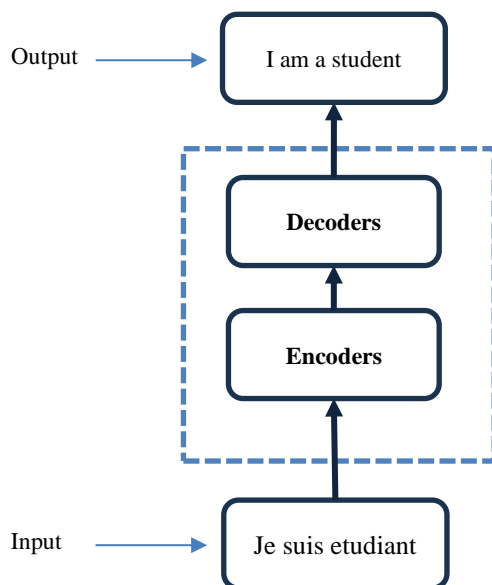


Figure 2. Transformer model architecture for text translation from French to English

they embed words in the transformer model only in the first encoder (lowest encoder). When each word is converted into a vector, each of the two sub-layers passes in the encoders. Therefore, these words enter the encoder in parallel, and another vector is added to each input embedding vector in the transformer model; thereby helping the model to recognize the position of each word or the space between different words in the input sequence.

The BERT model is beneficial for finding semantic similarities in documents since this model can collectively and simultaneously evaluate the semantic information of documents, analyze the connections between sentences and different stages of text processing, and thus easily identify the latent semantic similarities of the text (28-30).

Thereafter, the texts are converted into vectors and special features (the same features of an entity) are extracted. These special features are the criteria which are used to score the semantic similarities. Then, the semantic analysis of words is performed to find the semantic similarities between the text components. In the next stage, the feature selection is performed based on repetition and removal of irrelevant information, aiming to eliminate irrelevant and extra information from the text.

The most important feature is selected through the scores of words, and thus only important and relevant information with semantic similarities remains. Therefore, the semantic similarity score between the text components is calculated. This score is based on the sentence and criterion positions. At this stage, the semantic classification of documents is extracted after calculating the semantic similarity score (plan or bill). This classification helps legislative experts make decisions to find the relationships of laws and detect the rate of semantic similarity between plans and bills with laws (31, 32).

This manuscript utilized transformer-based models as the most advanced language models based on deep neural networks. These models are particularly effective for natural language processing problems (33). For example, assume the following sentence: "I like to read articles about artificial intelligence". To use the BERT model, first, we convert the sentence into numerical vectors. This stage is done as pre-processing, consisting of several stages. Tokenization is the first stage (at this stage, all punctuation marks are converted into a string of words by removing blank spaces and commas). Therefore, the sentence is divided into smaller tokens. For example, our sentence is tokenized as follows: "I, like, to, read, articles, about, artificial, intelligence". These tokens are displayed as a string of numeric numbers. In chipping, the second stage, the BERT model usually accepts only fixed-length inputs. Therefore, if the length of a sentence is longer than the limit of the model, we must decrease its

components or make it a fixed length. At this stage, only selecting some tokens and removing the rest is considered as a common technique.

The third stage comprises the conversion of vectors. As the tokens are ready, the BERT model utilizes its transformer layers to assign vectors to each token. These vectors are usually vectors with large dimensions. Thus the connections between words are modeled in the sentence. Model training is the fourth stage where the models are trained using large sets of labeled data to learn linguistic features and relations. This training consists of optimization and adjustment of the weights related to the model to have the best performance in different problems. To this end, sentences and words in the text can be converted into numerical vectors through the transformer and BERT model. Furthermore, these vectors can be used for a large number of language-processing tasks such as text classification, entity recognition, and translation. This technique encodes the sentence in a fixed-length vector (dense vector space) and embeds each word in the vector space into two vectors, lexical and semantic (see Figure 3).

The similarity between these vectors is calculated at this stage after mapping the words in the vector space using the Cosine distance criterion. Therefore, the coded terms have a set of corresponding vectors in this vector space. If the text has similar words, the vectors are placed close to each other in the vector space, and if they have opposite meanings, the vectors move away from each other or their directions are opposite. Therefore, the semantic similarity score is obtained by calculating the differences.

4. IMPLEMENTATION AND ANALYSIS OF RESULTS

4. 1. Database This manuscript analyzes data from 250 documents approved by the Islamic Consultative Assembly from 2006-2021, including 50

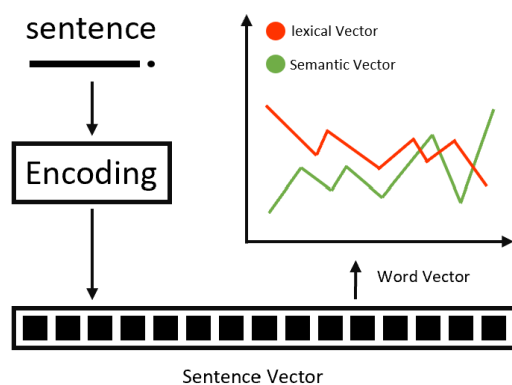


Figure 3. Comparing lexical vector and semantic vector of a sentence Using Bert Model

bills, 50 plans, and 150 laws. The documents analyzed include Law of Objectives, Duties, and Organizations of the Ministry of Science, Research, and Technology; the statute of the Islamic Republic of Iran Broadcasting (IRIB); the Law of the Iranian Tobacco Company; the Law of universities and higher education centers; and the plan for the conservation and management of rivers in Iran. Examples of bills analyzed include the annual budget bill and the bill to amend the statute of the cultural heritage organization (34).

4. 2. Data Analysis A total of 100 plans and bills, and 150 laws were considered to analyze the results. The semantic similarity scores were measured to extract the semantic similarity of the plans and bills with the laws, using the model, and then compared them with experts' opinions.

The present model aims to present a system as an assistant for legislation experts in such a way that the model can quickly discover and recognize the semantic similarities of documents. In this method, the plans and bills related to the laws are scored, and a scoring threshold is obtained for the performance and accuracy of the results. In other words, the plan or bill is compared with the law sentence by sentence, the semantic score is calculated, and the sentences and paragraphs of the texts are encoded in a fixed-length vector (dense vector space). Furthermore, the vectors are used for evaluation and scoring the sentences, using cosine distance. Additionally, this method compares experts' previously measured semantic similarity with the semantic similarity score discovered by the model.

This research aimed to design and implement an AI model based on deep learning as an assistant to experts in finding laws related to plans and bills that are proposed to the Islamic Consultative Assembly. The AI model developed in this research should work in such a way that it can have the minimum error in finding the relevant semantic items, and the model can extract the maximum relevant semantic items.

To evaluate the performance of the AI model, we compared its results with the opinions of experts in the Islamic Consultative Assembly. This comparison of the model settings and parameters revealed that the error rate in detecting semantic similarities decreased. After conducting multiple tests and gathering extensive feedback and information from the assembly, we determined that a semantic similarity score of 34% or higher indicates a correct extraction of relevant semantic items.

The Receiver Operating Characteristic (ROC) curve of this model is shown in Figure 4 to evaluate the efficiency of data classification parameters, called True Positives (TP), False Positives (FP), True Negatives (TN), and False negatives (FN). The TP class occurs when the expert and the AI model report the positive

semantic similarity between the two documents. The FP class happens when the expert reports a negative semantic similarity between the two documents, but the AI model reports a positive semantic similarity between the two documents. The TN class occurs when the expert and the AI model declare a negative semantic similarity between the two documents. Furthermore, the FN class happens when the expert declares a positive semantic similarity between the two documents, but the AI model declares a negative semantic similarity between the two documents. The ROC curve indicate the good performance and very high precision of the model in the evaluation. Implementation results of the proposed model on three sample plans and bills from the dataset are shown in Table 1.

Table 2 compares the results between experts and the AI model on the data provided in this research. The best result was found regarding the accuracy and precision of the model performance by considering a 34% threshold of the similarity score for documents. A precision of above 96% was obtained for the model on the evaluation data. Results provided in Table 2 indicate the accuracy

and precision of the AI model in detecting the semantic similarities of legal documents related to the Islamic Consultative Assembly. It also shows the achievement of accuracy and precision of performance above 90%.

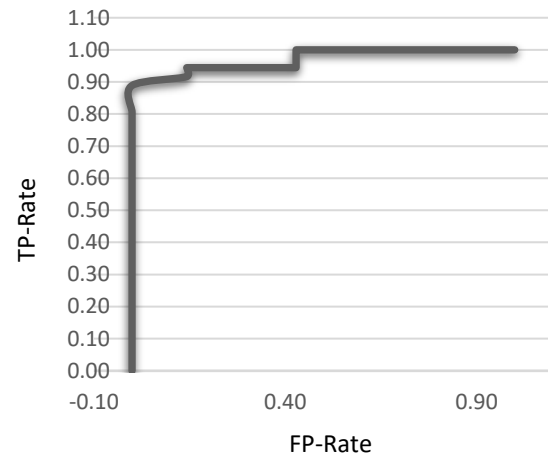


Figure 4. ROC curve of the method evaluation

TABLE 1. Dataset model, comparison of the results between experts and artificial intelligence model

Name of plan or bill	Name of relevant law	Semantic evaluation percentage of the expert	Semantic evaluation percentage of the model	Semantic similarity of the expert	Semantic similarity of the model	Confusion
1. The plan of regulating some financial, administrative, and support regulations of the Ministry of Education- 15/06/2010	The Law on the creation of education councils in provinces, counties, and districts- 18/05/2000	40	43	No	yes	FN
2. The plan of saving and revitalizing Iran's lakes and wetlands- 15/06/2010	The law on Iran's fifth development plan- 5/01/2011	40	27	No	No	TN
3. The plan of supporting handicraft masters and artists- 15/06/2010	The law on social insurance for carpet weavers, and handicraft workers with ID- 9/08/2009	20	29	No	No	TN

TABLE 2. Results of the proposed method evaluation with specific parameters for test dataset samples

The mean score of semantic similarities of sentences given by the expert	59
The mean score of semantic similarities of sentences (proposed method)	48
Performance statistics	TP=36, FP=3, FN=0, TN=4
Precision	0.92
Recall	1.0
Accuracy	0.93
Precision and recall outcome- F1-Score	0.96

5. CONCLUSION

The semantic searching method proposed in this paper was designed and implemented using a neural network, BERT model, and transformer architecture based on deep learning. This paper introduces a model that offers an efficient and useful solution for detecting laws related to plans and bills. The model can encode sentences or paragraphs into fixed-length vectors, using cosine distance to evaluate and score sentences. Furthermore, the proposed approach's consideration of text conceptual and semantic relationships suggests that it is well-suited for classifying complex texts and accurately extracting semantic relationships. The test dataset sample results

demonstrate the method's high precision and accuracy in identifying semantic similarities between relevant legal documents on real datasets.

6. REFERENCES

- National strategic plan for research and development of artificial intelligence and legislation in Iran. In: Center MR, editor.: Islamic Parliament Research Center of The Islamic Republic of IRAN; 2018.
- Research in artificial intelligence and legislation and review of civil law in the field of robotics of the European Union Parliament. In: Center MR, editor.: Islamic Parliament Research Center of The Islamic Republic of Iran; 2019.
- Burri T, Von Bothmer F. The new EU legislation on artificial intelligence: a primer. Available at SSRN 3831424. 2021. <https://doi.org/10.2139/ssrn.3831424>
- Farhoodi M, Toloie Eshlaghy A, Motadel M. A Proposed Model for Persian Stance Detection on Social Media. *International Journal of Engineering, Transactions C: Aspects*. 2023;36(6):1048-59. <https://doi.org/10.5829/IJE.2023.36.06C.03>
- Cath C. Governing artificial intelligence: ethical, legal and technical opportunities and challenges. *Philosophical Transactions of the Royal Society A: Mathematical, Physical and Engineering Sciences*. 2018;376(2133):20180080. <https://doi.org/10.1098/rsta.2018.0080>
- Kornilova A, Eidelman V. BillSum: A corpus for automatic summarization of US legislation. arXiv preprint arXiv:191000523. 2019. <https://doi.org/10.48550/arXiv.1910.00523>
- Saraswat N, Li C, Jiang M. Identifying the Question Similarity of Regulatory Documents in the Pharmaceutical Industry by Using the Recognizing Question Entailment System: Evaluation Study. *JMIR AI*. 2023;2(1):e43483. <https://doi.org/10.2196/43483>
- Amur ZH, Kwang Hooi Y, Bhanbhro H, Dahri K, Soomro GM. Short-Text Semantic Similarity (STSS): Techniques, Challenges and Future Perspectives. *Applied Sciences*. 2023;13(6):3911. <https://doi.org/10.3390/app13063911>
- Fradelos G, Perikos I, Hatzilygeroudis I, editors. Using Siamese BiLSTM Models for Identifying Text Semantic Similarity. *IFIP International Conference on Artificial Intelligence Applications and Innovations*; 2023: Springer.
- Devlin J, Chang M-W, Lee K, Toutanova K. Bert: Pre-training of deep bidirectional transformers for language understanding. arXiv preprint arXiv:181004805. 2018. <https://doi.org/10.48550/arXiv.1810.04805>
- Silic A, Saric F, Basic BD, Snajder J, editors. TMT: Object-oriented text classification library. 2007 29th International Conference on Information Technology Interfaces; 2007: IEEE.
- Reimers N, Gurevych I. Making monolingual sentence embeddings multilingual using knowledge distillation. arXiv preprint arXiv:200409813. 2020. <https://doi.org/10.48550/arXiv.2004.09813>
- Artificial Intelligence and Legislation. In: Center MR, editor.: Islamic Parliament Research Center of The Islamic Republic of Iran; 2018.
- Leskovec J, Rajaraman A, Ullman JD. Mining of massive data sets: Cambridge university press; 2020.
- Sadjadi S, Mashayekhi H, Hassanpour H. A two-level semi-supervised clustering technique for news articles. *International Journal of Engineering, Transactions C: Aspects*. 2021;34(12):2648-57. <https://doi.org/10.5829/IJE.2021.34.12C.10>
- Hassanpour H, AlyanNezhadi M, Mohammadi M. A signal processing method for text language identification. *International Journal of Engineering, Transactions C: Aspects*. 2021;34(6):1413-8. <https://doi.org/10.5829/IJE.2021.34.06C.04>
- Rao KS, Murthy D, Kancherla GR. Semantic similarity based automatic document summarization method. *International Journal of Engineering and Advanced Technology (IJEAT)* ISSN.2249-8958. <https://doi.org/10.35940/ijeat.F8566.088619>
- Hosseiniikhah T, Ahmadi A, Mohebi A. A new Persian text summarization approach based on natural language processing and graph similarity. *Iranian Journal of Information Processing and Management*. 2018;33(2):885-914. <https://doi.org/10.35050/JIPM010.2018.084>
- Wang B, Liu W, Lin Z, Hu X, Wei J, Liu C. Text clustering algorithm based on deep representation learning. *The Journal of Engineering*. 2018;2018(16):1407-14. <https://doi.org/10.1049/joe.2018.8282>
- Dang S, Ahmad PH. Text mining: Techniques and its application. *International Journal of Engineering & Technology Innovations*. 2014;1(4):22-5.
- Jiang Y, Zhang X, Tang Y, Nie R. Feature-based approaches to semantic similarity assessment of concepts using Wikipedia. *Information Processing & Management*. 2015;51(3):215-34. <https://doi.org/10.1016/j.ipm.2015.01.001>
- Karaa WBA. A new stemmer to improve information retrieval. *International Journal of Network Security & Its Applications*. 2013;5(4):143. <https://doi.org/10.5121/ijnsa.2013.5411>
- Kamyar H, Kahani M, Kamyar M, Poormasoomi A, editors. An automatic linguistics approach for persian document summarization. 2011 International Conference on Asian Language Processing; 2011: IEEE.
- Reimers N, Gurevych I. Sentence-bert: Sentence embeddings using siamese bert-networks. arXiv preprint arXiv:190810084. 2019. <https://doi.org/10.48550/arXiv.1908.10084>
- Le Q, Mikolov T, editors. Distributed representations of sentences and documents. *International conference on machine learning*; 2014: PMLR.
- Haveliwala TH, Gionis A, Klein D, Indyk P, editors. Evaluating strategies for similarity search on the web. *Proceedings of the 11th international conference on World Wide Web*; 2002.
- Pennington J, Socher R, Manning CD, editors. Glove: Global vectors for word representation. *Proceedings of the 2014 conference on empirical methods in natural language processing (EMNLP)*; 2014.
- Sutskever I, Vinyals O, Le QV. Sequence to sequence learning with neural networks. *Advances in neural information processing systems*. 2014;27. <https://doi.org/10.48550/arXiv.1409.3215>
- Mikolov T, Chen K, Corrado G, Dean J. Efficient estimation of word representations in vector space. arXiv preprint arXiv:13013781. 2013. <https://doi.org/10.48550/arXiv.1301.3781>
- Khosrovian K, Pfahl D, Garousi V, editors. Gensim 2.0: a customizable process simulation model for software process evaluation. *International conference on software process*; 2008: Springer.
- Hossain MZ, Akhtar MN, Ahmad RB, Rahman M. A dynamic K-means clustering for data mining. *Indonesian Journal of Electrical engineering and computer science*. 2019;13(2):521-6. <https://doi.org/10.11591/ijeecs.v13.i2.pp521-526>
- Yi J, Zhang Y, Zhao X, Wan J. A novel text clustering approach using deep-learning vocabulary network. *Mathematical Problems in Engineering*. 2017;2017. <https://doi.org/10.1155/2017/8310934>

33. Navigli R, Velardi P. Structural semantic interconnections: a knowledge-based approach to word sense disambiguation. *IEEE transactions on pattern analysis and machine intelligence*. 2005;27(7):1075-86. <https://doi.org/10.1109/TPAMI.2005.149>
34. Floridi L. The European Legislation on AI: A brief analysis of its philosophical approach. *Philosophy & Technology*. 2021;34(2):215-22. <https://doi.org/10.1007/s13347-021-00460-9>

COPYRIGHTS

©2024 The author(s). This is an open access article distributed under the terms of the Creative Commons Attribution (CC BY 4.0), which permits unrestricted use, distribution, and reproduction in any medium, as long as the original authors and source are cited. No permission is required from the authors or the publishers.



Persian Abstract

چکیده

مدیریت و اداره کشورها بر پایه قوانین دقیق و صحیح پایه‌گذاری می‌شود. وضع قوانین مناسب و به هنگام می‌تواند سبب پیشرفت یک کشور شود. هر قانون یک عبارت متنی است که پس از طی فرایندی با تصویب مجلس به مجموعه قوانین موجود اضافه می‌شود. در بررسی هر قانون جدید، از میان مجموعه قوانین موجود، قوانین مرتبط استخراج و مورد تحلیل قرار می‌گیرد. در این مقاله، یک راهکار نوین برای استخراج قوانین مرتبط برای یک عبارت مورد بحث از میان مجموعه قوانین موجود با استفاده از تکنیک‌های ارتباط معنایی و یادگیری عمیق مبتنی بر مدل برت ارائه شده است. در روش پیشنهادی، جملات یا پاراگراف‌های متنی را در یک بردار با طول ثابت (فضای برداری متراکم) رمزگذاری کرده سپس از آن بردارها برای ارزیابی و امتیازدهی به ارتباط معنایی جملات با مقیاس اندازه‌گیری فاصله کسینوسی استفاده می‌شود. در این روش، ماشین می‌تواند معنا و مفهوم جملات را با استفاده از روش کدگذاری مدل برت، با در نظر گرفتن موقعیت موجودیت‌های به کار برده شده در جملات درک کند. و روابط معنایی اسناد را کشف و میزان ارتباط اسناد آنها را با یک موضوع محاسبه و شباهت معنایی آنها را تشخیص دهد. نتایج بدست آمده از نمونه کوچک تستی دیناست نشان دهنده صحت و دقت روش پیشنهادی در تشخیص روابط معنایی اسناد قانونی مرتبط با مجلس شورای اسلامی می‌باشد و دستیابی به میزان صحت و دقت عملکرد بالای ۹۰ درصد را نشان می‌دهد.



Improved Performance Analysis and Design of Dual Metal Gate FinFET for Low Power Digital Applications

P. Padmaja^a, D. Vemana Chary^a, R. Erigela^a, G. Sirisha^a, S. K. ChayaDevi^b, M. C. Pedapudi^c, B. Balaji*^d, S. Cheerala^d, V. Agarwal^d, Y. Gowthami^d

^a Department of Electronics and Communication Engineering, Teegala Krishna Reddy Engineering College, Meerpet, Hyderabad, India

^b Department of information Technology, Vasavi College of Engineering, Hyderabad, India

^c Department of Electronics and Communications Engineering, Vignan's Foundation for Science Technology & Research (Deemed to be University), Vadlamudi, Guntur District, A.P, India

^d Department of Electronics and Communication Engineering, Koneru Lakshmaiah Education Foundation, Green Fields, Vaddeswaram, Andhra Pradesh, India

PAPER INFO

Paper history:

Received 30 October 2023

Received in revised form 08 January 2024

Accepted 08 February 2024

Keywords:

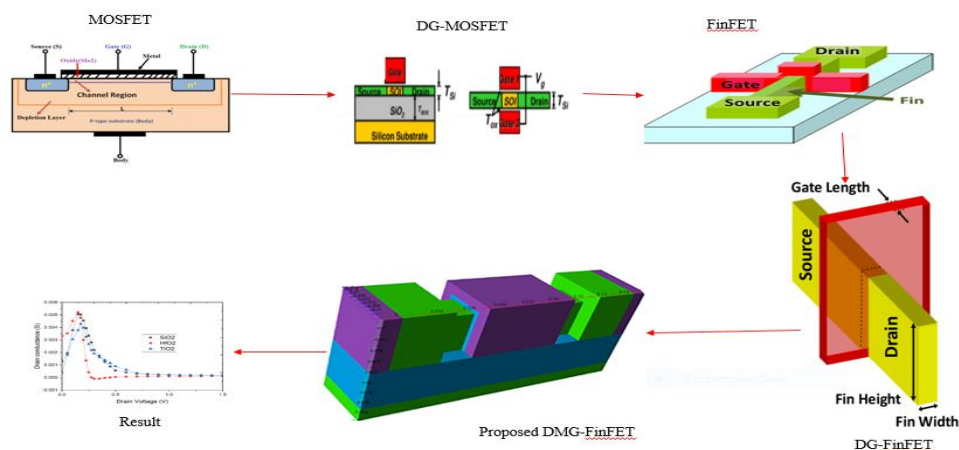
Dielectric Material
On Current
Off Current
Silicon Dioxide
Nano Technology

ABSTRACT

A High-K Dielectric Dual Metal Gate FinFET (DMG-FinFET) is proposed in this work to improve the drain current and electrical characteristics of the device. The proposed device employing dielectric materials such as Silicon dioxide, Hafnium oxide and Titanium oxide and investigated in 10 nm technology. The architecture represents a critical advancement in transistor design, addressing challenges posed by traditional high-K gate dielectric materials being HfO₂ and TiO₂. This work employs a comprehensive approach, incorporating simulation techniques to evaluate the performance metrics of DMG FinFET. This investigation encompasses key aspects being transistor characteristics, power consumption, and reliability. This high-k dielectric (HfO₂) Dual material Gate –FinFET device achieving improved performance parameters such as I_{on}= 32.12 mA, I_{off}= 33 μA, G_m(max) = 0.045 S, G_{ds}(max) = 0.024 S and R_{on}(max) = 32.87 kΩ. Therefore this work is suitable for designing high performance devices with high-k dielectric materials being HfO₂ and TiO₂. The impact of dual metal gate materials on I_{on}, I_{off}, G_m (max), G_{ds}(max) and R_{on}(max) is calculated and improved 64% compared to conventional device.

doi: 10.5829/ije.2024.37.06c.02

Graphical Abstract



*Corresponding Author Email: yahividi@gmail.com (B. Balaji)

Please cite this article as: Padmaja P, Vemana Chary D, Erigela R, Sirisha G, ChayaDevi SK, Pedapudi MC, Balaji B, Cheerala S, Agarwal V, Gowthami Y, Improved Performance Analysis and Design of Dual Metal Gate FinFET for Low Power Digital Applications. International Journal of Engineering, Transactions C: Aspects. 2024;37(05):1059-66.

1. INTRODUCTION

The Metal-Oxide-Semiconductor Field-Effect Transistor (MOSFET) is a crucial component in modern electronics, serving as a fundamental building block for digital and analog circuits. Developed as a successor to the bipolar junction transistor (BJT), MOSFETs play a pivotal role in integrated circuits, enabling the amplification and switching of electrical signals with remarkable efficiency (1). The MOSFET's design leverages the principles of semiconductor physics, offering advantages such as low power consumption, high integration density, and compatibility and comparison with complementary metal oxide-semiconductor (CMOS) technology (2).

The MOSFET has a metal gate that acts as a control electrode. This gate is separated from the semiconductor material by a thin insulating layer, typically made of low-k dielectric materials and high-k dielectric materials such as silicon dioxide (SiO_2), hafnium oxide (HfO_2) and Titanium dioxide (TiO_2) (3). The insulating oxide layer isolates the gate from the semiconductor. Its thinness is crucial for facilitating effective control of the transistor. The MOSFET consists of a semiconductor material, often silicon, which forms the channel region where the flow of charge carriers is controlled by the electric field applied by the gate (4). The MOSFET relies on the modulation of the conductivity of the channel region between the source and drain terminals. This modulation is achieved by applying a voltage to the gate terminal, creating an electric field that controls the flow of charge carriers. In an n-type MOSFET, electrons are the majority carriers, and applying a positive voltage to the gate repels electrons, reducing the conductivity of the channel (5). In a p-type MOSFET, holes are the majority carriers, and a negative voltage on the gate serves a similar purpose. MOSFETs are extensively used in digital and analog circuits, serving roles in amplification, signal switching, and as key components in integrated circuits (6). MOSFETs consume minimal power due to their inherent voltage-driven drain current operation and are compatible with CMOS technology, allowing for the integration of large numbers of transistors on a single chip (7). MOSFETs exhibit fast and improved switching characteristics, making them suitable for high-speed digital applications. Therefore, MOSFET is a foundational present trend semiconductor device that has revolutionized the field of electronics. Its versatility, efficiency, and compatibility with integrated circuit technologies have contributed significantly to the miniaturization and performance improvement of electronic devices.

As the quest for more energy-efficient and high-performance electronic devices continues, researchers and engineers are exploring the present novel transistor architectures, and one promising candidate is the Tunnel Field-Effect Transistor (TFET). TFET represents a

departure from traditional MOSFETs by leveraging quantum tunneling phenomena to achieve enhanced energy efficiency and reduced power consumption (8, 9). This innovative transistor design holds great potential for applications in low-power integrated circuits and emerging technologies. TFETs operate based on quantum tunneling phenomenon in quantum mechanics where particles can pass through energy barriers that classical physics would consider insurmountable. In the case of TFETs, electrons or holes tunnel through a thin barrier in the transistor's channel region employing with low-k dielectric materials and high-k dielectric materials such as silicon dioxide (SiO_2), hafnium oxide (HfO_2) and titanium dioxide (TiO_2). Similar to MOSFETs, TFETs have source and drain terminals, defining the direction of current flow through the channel. However, the operation of TFETs involves tunneling rather than traditional drift or diffusion of charge carriers (10).

The TFET's energy band diagram plays a crucial role in its operation. With low-k dielectric materials and high-k dielectric materials such as SiO_2 , HfO_2 and TiO_2 engineering the bandgap and the tunneling barrier, TFETs can achieve steep subthreshold slopes, a key metric for low-power performance. TFETs have the potential to achieve sub-60 mV/decade subthreshold slopes, surpassing the physical limitations of traditional MOSFETs (11, 12). This characteristic makes them highly attractive for applications where minimizing power consumption is critical. TFETs can operate efficiently at lower supply voltages, contributing to energy savings and enabling the design of circuits with extended battery life in portable devices. TFETs show promise in various applications, including low-power integrated circuits, energy-efficient processors, and devices where extended battery life is crucial (13, 14).

In semiconductor technology, the continual pursuit of smaller transistor sizes and improved performance has led to the development of advanced transistor structures. One such innovation is the Dual Metal Gate FinFET with high-K dielectric materials, a cutting-edge technology implemented in 10nm semiconductor nodes (15). This high-K advanced dielectric materials and transistor architecture addresses the challenges posed by traditional transistor scaling, such as leakage currents and power consumption, thereby enhancing the overall efficiency and performance of integrated circuits (16).

The conventional FinFET technology is widely used in semiconductor manufacturing, particularly in advanced nodes for digital integrated circuits. The process begins with a silicon wafer, which serves as the substrate for the semiconductor device and a thin layer of silicon is deposited on the substrate. A gate dielectric layer is deposited over the fins to control the current.

FinFET (Fin Field-Effect Transistor) is a 3D transistor design that overcomes some limitations of traditional planar transistors. It involves the use of a fin-

like structure for the channel region, enabling better control over the flow of electrical current (17). The dual metal gate refers to the incorporation of two distinct metal layers in the gate structure of the FinFET. This dual-layer design enhances control over the transistor's conductivity and allows for improved performance, reduced leakage currents, and enhanced reliability. The semiconductor industry has witnessed a relentless pursuit of improved miniaturization to enhance performance and energy efficiency (18). As the semiconductor industry progresses towards smaller nodes, the 10nm process emerges as a promising device. This study focuses on the qualitative performance analysis of dual metal gate (DMG) FinFET (DMG-FinFET) in the 10 nm technology node (19).

Power efficiency is a critical concern in modern semiconductor design. The analysis delves into the power consumption patterns of DMG FinFETs under various operating conditions being dynamic power consumption during switching events and static power dissipation in idle states (20). This work investigates the robustness of DMG FinFETs in the face of process variations and environmental factors, providing insights into their long-term performance related to low-K dielectric materials and high-K dielectric materials such as SiO₂, HfO₂ and TiO₂ (21).

Traditional transistors use silicon dioxide (SiO₂) as the gate dielectric. However, as transistors shrink, the insulating properties of silicon dioxide diminish. High-K dielectric materials, characterized by a higher dielectric constant (K), are employed to counteract this effect. Common high-K materials include hafnium oxide (HfO₂)-based compounds, which offer better insulation and allow for further downscaling of transistor dimensions. The high-K dielectric materials help minimize leakage currents, enhancing the energy efficiency of the transistors. The dual metal gate design provides better control over the transistor's conductance, resulting in improved speed and performance. The 10nm technology allows for the fabrication of smaller, more densely packed transistors, contributing to increased device integration and overall performance. The DMG FinFET with high-K dielectric materials in 10nm technology finds applications in a wide range of electronic devices, including smartphones, tablets, high-performance computing systems, and other advanced electronic devices demanding higher processing power and energy efficiency (22).

2. DEVICE STRUCTURE AND MODELLING

The fabrication process for FinFETs is more complex compared to traditional planar transistors, requiring additional manufacturing materials and increased process control. The complexity of the FinFET fabrication

process, along with the need for advanced materials and equipment, can lead to higher manufacturing costs. Variability in the height of the fin structures can occur during the fabrication process, leading to performance variations among transistors. This variability can affect the overall yield and reliability of the semiconductor device.

The design of a DMG FinFET with high-K dielectric material such as silicon dioxide (SiO₂), hafnium oxide (HfO₂) and titanium dioxide (TiO₂) involves several key considerations to optimize device performance, reduce power consumption, and ensure manufacturability. In this proposed HfO₂ DMG-FinFET, employing a suitable semiconductor material for the fin structure as silicon and gate dielectric materials as HfO₂ and TiO₂ as shown in Figure 1. The fin provides the channel through which the current flows. The high-K dielectric material, such as hafnium oxide (HfO₂), to replace traditional silicon dioxide as the gate dielectric. High-K materials enable effective gate control and minimize leakage currents. The proposed high-K FinFET architecture to enhance control over the channel. The fin structure allows for better electrostatic control of the channel, reducing leakage current and improving overall transistor performance. Design a gate stack in the proposed device that includes the high-K dielectric layer and the metal gates. Optimize the thickness and composition of each layer to achieve the desired electrical characteristics, such as threshold voltage and subthreshold slope (23).

The high-K dielectric material, HfO₂ device fin for optimal carrier mobility and electrostatic control. Consider the fin width, height, and doping concentration to achieve the desired device characteristics. In this proposed device spacer engineering dielectric material being TiO₂ helps in achieving better control over the transistor characteristics and mitigating issues related to process variations. The integration of the DMG FinFET into the semiconductor fabrication process must be seamless to enable large-scale production and 10nm, to leverage the advantages of this high-K dielectric materials being HfO₂ and TiO₂ manufacturing processes (24).

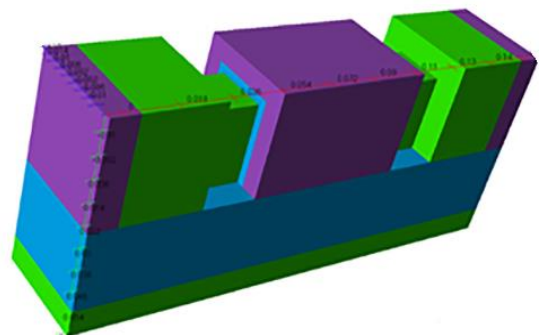


Figure 1. Proposed DMG- FinFET

Utilized the simulation and modeling TCAD tool to predict and optimize the device characteristics before actual fabrication. This aids in fine-tuning the design parameters for optimal performance. Therefore, the proposed device design of DMG-FinFET with high-K dielectric materials, engineers can create transistors that offer improved qualitative performance, reduced power consumption, and enhanced reliability for advanced semiconductor technologies (25, 26). High-K dielectric materials and the FinFET architecture help achieve lower subthreshold slopes, reducing power consumption in subthreshold operation (27). This is particularly advantageous for applications requiring energy-efficient operation in low-power states. The use of high-K dielectric materials contributes to improved temperature stability. This is vital for maintaining consistent device performance across a range of operating conditions, ensuring reliability in various environments (28).

Table 1 shows the proposed device utilized parameters for the simulation in 10nm technology. The improved performance parameters of proposed device compared with existing devices are shown in Table 2.

3. PROPOSED DEVICE ALGORITHM

The algorithmic proposed FinFET design determining the materials for the dual gate structure. This could involve optimizing the properties of each SiO₂ and HfO₂ material to achieve higher drain current and lower leakage current performance characteristics. Developing algorithms for the precise placement and control of the dual materials within the gate structure. This may involve considerations for thickness, composition, and other

TABLE 1. Used parameters of the proposed device

Device Parameter	Value
Length of device(W_L)	60 nm
Gate Length(L_G)	10 nm
Source Length(L_S)	30 nm
Drain Length(L_D)	30 nm
Channel Length(L_C)	10 nm
Source Doping(N_D)	10^{18} cm^{-3}
Drain Doping (N_D)	10^{18} cm^{-3}
Channel Doping	10^{20} cm^{-3}
Gate Work Function	4.3eV
Low-k material	SiO ₂
High-k material	HfO ₂
Fin width	10nm
Fin height	14nm

TABLE 2. Used Modelling for the proposed structure

Model	Description
conmob	Specifies the concentration mobility
fldmob	Calculation of the field dependent mobility
evsatmod=1	implements the carrier temperature mobility
hcte.el	to enable energy balance for electrons
taurel.el	specifies the relaxation time in the
taumob.el	specifies the relaxation time for electrons

material properties. Implementing algorithms to optimize the manufacturing process, including deposition, etching, and other steps involved in creating the dual material gate FinFET. The development of algorithms to model the electrical characteristics and performance of the dual material gate FinFET. This could include simulations and analyses to predict behavior under various dielectric materials. The algorithms may be developed to seamlessly incorporate the dual material gate FinFET into existing fabrication processes.

The novelty in semiconductor technology often involves improvements in performance, power efficiency and transistor design. In DMG FinFET is a recent development with gate length of 22 nanometer and thickness of Fin is 2nm. The unique features of this device is improved drain current, reduced leakage current and lower sub threshold swing about 64 percent. Therefore, this device is suitable for low power applications.

4. RESULTS AND DISCUSSION

4. 1. Drain Current Vs Drain Voltage Characteristics

Analyzing the characteristics of the drain current (I_d) as a function of the drain-to-source voltage (V_{ds}) for a DMG FinFET with high-K dielectric materials being hafnium oxide (HfO₂) and titanium dioxide (TiO₂) involves at low V_{ds} values, below the threshold voltage (V_{th}), the proposed device is in the subthreshold region. In this region, the drain current is exponentially dependent on V_{ds} . The subthreshold slope is a crucial parameter, and the use of high-K dielectric materials (HfO₂) helps in achieving lower subthreshold slopes, contributing to lower power consumption in subthreshold operation as shown in Figure 2. The threshold voltage is the gate voltage at which the I_d begins to conduct. In the I_d Vs V_{ds} plot, this is the point where the curve starts to rise. DMG design can impact the threshold voltage, allowing for better tuning and control. As V_{ds} increases beyond V_{th} , the transistor enters the saturation region. In this region, the drain current becomes relatively independent of V_{ds} (29, 30).

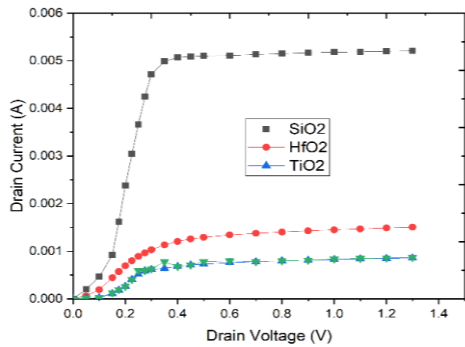


Figure 2. Id Vs Vds characteristics of Proposed device with HfO₂ and TiO₂ high-K dielectric mater

4. 2. Drain Current Vs Gate Voltage Characteristics

The drain current (I_d) as a function of gate-to-source voltage (V_{gs}) measured in volts (V) for DMG FinFET with high-K dielectric materials provides valuable insights into the transistor's behavior. The threshold voltage (V_{th}) is the gate voltage at which the transistor just starts to conduct. In the I_d vs V_{gs} plot, where the curve begins to rise. High-K dielectric materials such as hafnium oxide (HfO₂) and titanium dioxide (TiO₂) and the dual metal gate design influence V_{th} , allowing for better control and optimization. At lower V_{gs} (V) values (below V_{th}), the transistor is in the subthreshold region. The drain current in this region is exponentially dependent on V_{gs} . High-K dielectric materials (HfO₂ and TiO₂) help in achieving lower subthreshold slopes, contributing to lower power consumption in subthreshold operation. As V_{gs} increases beyond V_{th} , the transistor enters the saturation region. In this region, the drain current becomes relatively independent of further increases in V_{gs} (V). The dual high-K metal gate design contributes to improved electrostatic control, reducing the impact of gate voltage on the drain current as shown in Figure 3.

4. 3. Drain Conductance Characteristics The drain conductance is an important parameter in the

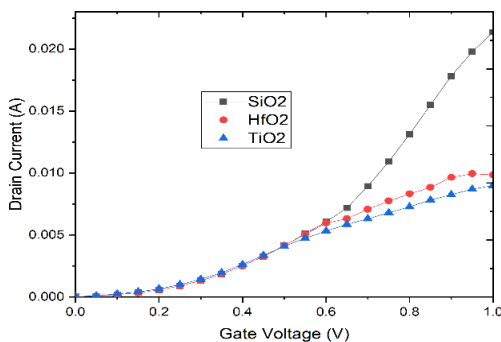


Figure 3. Id Vs Vgs characteristics of Proposed device with HfO₂ and TiO₂ high-K dielectric materials

operation of a proposed DMG-FinFET, employing with high-K gate dielectric materials being HfO₂ and TiO₂. It is a measure of how easily current can flow from the source to the drain terminal of the device. The drain conductance is influenced by high-K dielectric materials as HfO₂ and TiO₂. The drain conductance of a DMG FinFET would be influenced by the specific characteristics of the dual metal gate structure. The choice of high-K dielectric materials and spacer materials, and the overall design of the transistor impact how efficiently current can be conducted from the source to the drain as shown in Figure 4.

4. 4. Transconductance Characteristics

The transconductance (g_m) of a DMG FinFET with high-K dielectric materials high-K gate dielectric materials being HfO₂ and TiO₂ is a crucial parameter that indicates how effectively the transistor amplifies small input signals. The transconductance of this device is mathematically expressed as the derivative of the drain current (I_d) with respect to the gate-source voltage (V_{gs}) and it is highly dependent on the gate-source voltage. As V_{gs} increases, the transistor enters the saturation region, where the slope of the I_d vs V_{gs} curve determines the transconductance. In the saturation region of the transistor operation, the slope of the I_d vs V_{gs} curve represents the transconductance. A steeper improved slope corresponds to a higher transconductance and indicates better amplification capability as shown in Figure 5.

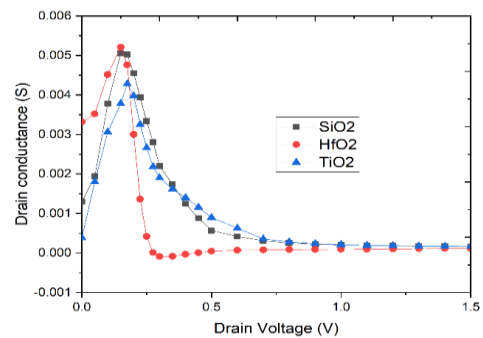


Figure 4. Gd Vs Vds characteristics of Proposed device with HfO₂ and TiO₂ high-K dielectric materials

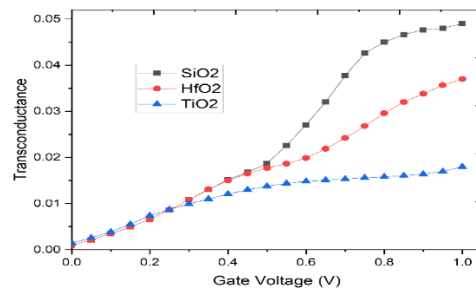


Figure 5. 5 Gm Vs Vgs characteristics of the proposed device with HfO₂ and TiO₂ high-K dielectric materials

The resistance characteristics of a DMG FinFET with high-K dielectric materials are important for understanding the device's behavior in various operating conditions. The channel resistance is a crucial component of the total resistance in a transistor as shown in Figure 6. It is influenced by the properties of the semiconductor material forming the channel and the dimensions of the fin structure. In a FinFET, the 3D fin structure provides better electrostatic control, reducing channel resistance compared to traditional planar transistors. The overlap between the gate and source regions can contribute to resistance. Design considerations, such as optimizing the gate-source overlap and using appropriate materials can impact this resistance as shown in Figure 6. The series resistance of the source and drain regions, including the contact resistances, can significantly affect the overall transistor resistance. Techniques such as silicidation are often employed to reduce source and drain contact resistances.

The reduction of sub threshold slope increases the off-current and power dissipation in the device. These characteristics are essentials for low power portable devices. The amount of gate voltage needed for variation of drain current defined as sub threshold slope given in Equation 1:

$$\text{Subthreshold slope (SS)} = \frac{\partial V_{gs}}{\partial(\log(I_{ds}))} \tag{1}$$

Silicon dioxide (SiO₂) is a key material in semiconductor manufacturing, particularly in the fabrication of integrated circuits. SiO₂ has a high dielectric constant, making it an excellent insulator. This property is crucial for the gate dielectric in metal-oxide-semiconductor (MOS) transistors, where SiO₂ has historically been used and the thickness of SiO₂ is 2nm is proposed in this simulations

4. 5. Main Achievement of the Prposed Device

The DMG-FinFET device contributes to improved electrostatic control, reducing the impact of drain voltage

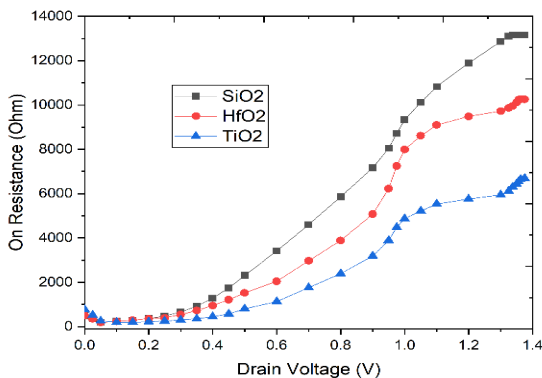


Figure 6. Ron characteristics of Proposed device with HfO₂ and TiO₂ high-K dielectric materials

TABLE 3. Performance parameters comparison with various devices based on literatures work

Parameters	C FinFET	SG FinFET	DG FinFET	HD-DMG FinFET	Proposed Device
Ion (A/μm)	4.13	5.84	5.9	5.93	8.2
Ioff (A/μm)	8.20	8.90	6.22	6.20	2.27
Ion/Ioff	2.29	2.9	3.1	3.81	3.841
Gm (S/mm)	2.31	2.34	2.6	2.61	3.81
Gd (S/mm)	2.1	1.19	1.84	2.8	2.01
Ron (Ωmm)	3.1	2.6	2.14	2.17	3.15

on the drain current. The higher V_{ds} values, the transistor enter a linear region where the drain current increases linearly with V_{ds}. This region is generally not desirable for digital applications but may relevant in certain analog circuit configurations also based on higher drain current, lower leakage current and lower sub threshold swing. The block diagram of proposed device as shown in Figure 7.

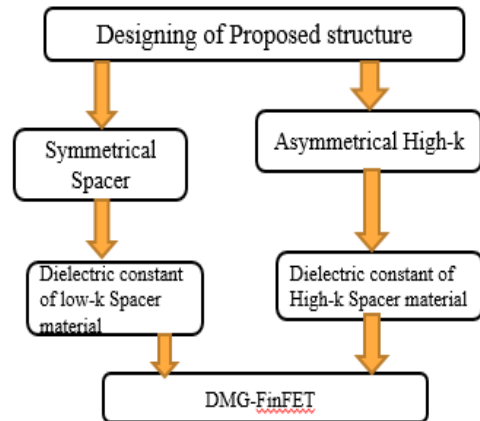


Figure 7. Block diagram of Proposed device

5. CONCLUSION

The integration of Dual Metal Gate FinFET with high-K Dielectric Materials in 10nm technology represents a significant advancement in semiconductor technology, offering a range of benefits for modern electronic devices. The proposed device employing high-K dielectric materials such as hafnium oxide (HfO₂) and titanium oxide (TiO₂) and investigated in 10 nm technology. The dual metal gate design enhances electrostatic control over the channel, reducing leakage currents and improving overall device performance. The incorporation of high-K dielectric materials in the gate stack replaces traditional HfO₂ and TiO₂. The proposed

high-K dielectric materials DMG-FinFET has improved performance over silicon dioxide (SiO₂) gate stack and notable enhancement in device performance and subthreshold slope. The advantages of the proposed structure have the improvement performance compared to existed devices such as drain current and reduced leakage current and switching ratio about ~ 12 times is reported. The most recent innovation in this proposed structure lies in the Fin thickness, which is now 2nm and enables precise control of the current across the entire device. The limitations of this proposed structure is SS, which can be reduced in submicron node. The future scope in this proposed device can introduce advanced structural modifications in the optimized FinFET to enhance device further features for very lower applications.

6. REFERENCES

- Howldar S, Balaji B, Srinivasa Rao K. Design and Analysis of Hetero Dielectric Dual Material Gate Underlap Spacer Tunnel Field Effect Transistor. *International Journal of Engineering, Transactions C: Aspects*. 2023;36(12):2137-44. 10.5829/ije.2023.36.12c.01
- Krishnamurthya A, Reddy DV, Radhammac E, Jyothirmayeed B, Raoc DS, Agarwale V, et al. Design and Performance Analysis of 6H-SiC Metal-Semiconductor Field-Effect Transistor with Undoped and Recessed Area under Gate in 10nm Technology. *International Journal of Engineering, Transactions C: Aspects*. 2023;36(12):2264-71. 10.5829/ije.2023.36.12c.16
- Mehrabani AH, Fattah A, Rahimi E. Design and Simulation of a Novel Hetero-junction Bipolar Transistor with Gate-Controlled Current Gain. *International Journal of Engineering, Transactions C: Aspects*. 2023;36(03):433. 10.5829/ije.2023.36.03c
- Rohith Sai K, Girija Sravani K, Srinivasa Rao K, Balaji B, Agarwal V. Design and Performance Analysis of High-k Gate All Around Fin-field Effect Transistor. *International Journal of Engineering, Transactions C: Aspects*. 2024;37(3):476-83. 10.5829/ije.2024.37.03c.04
- Howldar S, Balaji B, Srinivasa Rao K. Gate Oxide Thickness and Drain Current Variation of Dual Gate Tunnel Field Effect Transistor. *International Journal of Engineering, Transactions C: Aspects*. 2024;37(3):520-8. 10.5829/ije.2024.37.03c.09
- Yadav S, Kumar H, Negi CMS. Extensive analysis of gate leakage current in nano-scale multi-gate MOSFETs. *Transactions on Electrical and Electronic Materials*. 2022;23(6):658-65. <https://doi.org/10.1007/s42341-022-00404-w>
- Kaur G, Gill SS, Rattan M. Lanthanum Doped Zirconium Oxide (LaZrO₂) High-k Gate Dielectric FinFET SRAM Cell Optimization. *Transactions on Electrical and Electronic Materials*. 2021;1-12. <https://doi.org/10.1007/s42341-021-00296-2>
- Radhamma E, Vemana Chary D, Krishnamurthy A, Venkatarami Reddy D, Sreenivasa Rao D, Gowthami Y, et al. Performance analysis of high-k dielectric heterojunction high electron mobility transistor for rf applications. *International Journal of Engineering, Transactions C: Aspects*. 2023;36(9):1652-8. 10.5829/ije.2023.36.09c.09
- Gowthami Y, Balaji B, Srinivasa Rao K. Performance Analysis and Optimization of Asymmetric Front and Back Pi Gates with Dual Material in Gallium Nitride High Electron Mobility Transistor for Nano Electronics Application. *International Journal of Engineering, Transactions A: Basics* 2023;36(7):1269-77. 10.5829/ije.2023.36.07a.08
- Raushan RK, Ansari MR, Chauhan U, Khalid M, Mohapatra B. Implementation of 12T and 14T SRAM bitcell using FinFET with optimized parameters. *Transactions on Electrical and Electronic Materials*. 2021;22:328-34. <https://doi.org/10.1007/s42341-020-00243-7>
- Chung H. Analysis of Electrical Characteristics of Shielded Gate Power MOSFET According to Design and Process Parameters. *Transactions on Electrical and Electronic Materials*. 2018;19:245-8. <https://doi.org/10.1007/s42341-018-0049-1>
- Gowthami Y, Balaji B, Rao KS. Design and performance evaluation of 6nm hemt with silicon sapphire substrate. *Silicon*. 2022;14(17):11797-804. <https://doi.org/10.1007/s12633-022-01900-7>
- Kumar PK, Balaji B, Rao KS. Performance analysis of sub 10 nm regime source halo symmetric and asymmetric nanowire MOSFET with underlap engineering. *Silicon*. 2022;14(16):10423-36. <https://doi.org/10.1007/s12633-022-01747-y>
- Howldar S, Balaji B, Srinivasa Rao K. Design and Qualitative Analysis of Hetero Dielectric Tunnel Field Effect Transistor Device. *International Journal of Engineering, Transactions C: Aspects* 2023;36(6):1129-35. 10.5829/ije.2023.36.06c.11
- Anvarifard MK, Orouji AA. Enhancement of a nanoscale novel Esaki tunneling diode source TFET (ETDS-TFET) for low-voltage operations. *Silicon*. 2019;11(6):2547-56. <https://doi.org/10.1007/s12633-018-0043-6>
- Dixit A, Gupta N. A compact model of gate capacitance in ballistic gate-all-around carbon nanotube field effect transistors. *International Journal of Engineering, Transactions A: Basics*. 2021;34(7):1718-24. 10.5829/IJE.2021.34.07A.16
- Sharma S, Chaujar R. Band gap and gate metal engineering of novel hetero-material InAs/GaAs-based JLTFTFET for improved wireless applications. *Journal of Materials Science: Materials in Electronics*. 2021;32(3):3155-66. <https://doi.org/10.1007/s10854-020-05064-1>
- Chakrabarty R, Roy S, Pathak T, Kumar Mandal N. Design of Area Efficient Single Bit Comparator Circuit using Quantum dot Cellular Automata and its Digital Logic Gates Realization. *International Journal of Engineering, Transactions C: Aspects*. 2021;34(12):2672-8. 10.5829/ije.2021.34.12c.13
- Jaiswal NK, Ramakrishnan V. Vertical GaN reverse trench-gate power MOSFET and DC-DC converter. *Transactions on Electrical and Electronic Materials*. 2021;22:363-71. <https://doi.org/10.1007/s42341-020-00248-2>
- Roy A, Mitra R, Kundu A, editors. Influence of channel thickness on analog and RF performance enhancement of an underlap DG AlGaIn/GaN based MOS-HEMT device. 2019 *Devices for Integrated Circuit (DevIC)*; 2019: IEEE.
- Gedam A, Acharya B, Mishra GP. Junctionless silicon nanotube TFET for improved DC and radio frequency performance. *Silicon*. 2021;13:167-78. <https://doi.org/10.1007/s12633-020-00410-8>
- Mehrabani AH, Fattah A, Rahimi E. Design and Simulation of a Novel Hetero-junction Bipolar Transistor with Gate-Controlled Current Gain. *International Journal of Engineering, Transactions C: Aspects* 2023;36(03):433. 10.5829/ije.2023.36.03c.01
- Rafiee A, Nickabadi S, Nobarian M, Tagimalek H, Khatami H. Experimental investigation joining al 5083 and high-density polyethylen by protrusion friction stir spot welding containing nanoparticles using taguchi method. *International Journal of Engineering, Transactions C: Aspects*. 2022;35(6):1144-53. 10.5829/ije.2022.35.06c.06

24. Misra S, Biswal SM, Baral B, Pati SK. Study of DC and Analog/RF Performances Analysis of Short Channel Surrounded Gate Junctionless Graded Channel Gate Stack MOSFET. Transactions on Electrical and Electronic Materials. 2023;1-10. <https://doi.org/10.1007/s42341-023-00455-7>
25. Sahu SA, Goswami R, Mohapatra S. Characteristic enhancement of hetero dielectric DG TFET using SiGe pocket at source/channel interface: proposal and investigation. Silicon. 2020;12(3):513-20. <https://doi.org/10.1007/s12633-019-00159-9>
26. Balaji B, Srinivasa Rao K, Giriya Sravani K, Bindu Madhav N, Chandras K, Jaswanth B. Improved drain current characteristics of hfo2/sio2 dual material dual gate extension on drain side-tfet. Silicon. 2022;14(18):12567-72. <https://doi.org/10.1007/s12633-022-01955-6>
27. Kumar PK, Balaji B, Rao KS. Halo-Doped Hetero Dielectric Nanowire MOSFET Scaled to the Sub-10 nm Node. Transactions on Electrical and Electronic Materials. 2023;1-11. <https://doi.org/10.1007/s42341-023-00448-6>
28. Emami N, Kuchaki Rafsanjani M. Extreme learning machine based pattern classifiers for symbolic interval data. International Journal of Engineering, Transactions B: Applications. 2021;34(11):2545-56. 10.5829/IJE.2021.34.11B.17
29. Fouladinia F, Gholami M. Decimal to excess-3 and excess-3 to decimal code converters in QCA nanotechnology. International Journal of Engineering, Transactions C: Aspects. 2023;36(9):1618-25. 10.5829/ije.2023.36.09c.05
30. Gowthami Y, Balaji B, Rao KS. Design and Analysis of a Symmetrical Low- κ Source-Side Spacer Multi-gate Nanowire Device. Journal of Electronic Materials. 2023;52(4):2561-8. <https://doi.org/10.1007/s11664-023-10217-z>

COPYRIGHTS

©2024 The author(s). This is an open access article distributed under the terms of the Creative Commons Attribution (CC BY 4.0), which permits unrestricted use, distribution, and reproduction in any medium, as long as the original authors and source are cited. No permission is required from the authors or the publishers.



Persian Abstract

چکیده

یک FinFET دو دروازه فلزی دی الکتریک بالا (DMG-FinFET) در این کار برای بهبود جریان تخلیه و ویژگی های الکتریکی دستگاه پیشنهاد شده است. دستگاه پیشنهادی با استفاده از مواد دی الکتریک مانند دی اکسید سیلیکون، اکسید هافنیوم و اکسید تیتانیوم و در فناوری 10 نانومتر بررسی شده است. این معماری نشان دهنده یک پیشرفت حیاتی در طراحی ترانزیستور است که به چالش های ناشی از مواد دی الکتریک دروازه سنتی با پتاسیم بالا (TiO₂ و HfO₂) رسیدگی می کند. این کار از یک رویکرد جامع استفاده می کند، که هر دو تکنیک شبیه سازی را برای ارزیابی معیارهای عملکرد DMG FinFET ترکیب می کند. این بررسی جنبه های کلیدی مانند ویژگی های ترانزیستور، مصرف برق و قابلیت اطمینان را در بر می گیرد. این دستگاه دی الکتریک با کیفیت بالا (HfO₂) دو ماده گیت FinFET - که به پارامترهای عملکردی بهبود یافته مانند $G_{ds}(max) = 0.024 S$ ، $G_m(max) = 0.045 S$ ، $I_{off} = 33 \mu A$ ، $I_{on} = 32.12 mA$ ، $R_{on} = 32.87 \Omega$ دست می یابد. کیلو اهم. بنابراین این کار برای طراحی دستگاه های با کارایی بالا با مواد دی الکتریک با k بالا که TiO₂ و HfO₂ هستند مناسب است. تاثیر مواد دروازه فلزی دوگانه بر روی I_{off} ، $G_m(max)$ ، $R_{on}(max)$ و $G_{ds}(max)$ محاسبه شده و 64 درصد نسبت به دستگاه معمولی بهبود یافته است.



A Novel Ensemble Deep Learning Model for Building Energy Consumption Forecast

M. Khodadadi^a, L. Riazi^{*a}, S. Yazdani^b

^a Department of Information Technology Management, Science and Research Branch, Islamic Azad University, Tehran, Iran

^b Department of Computer Engineering, Tehran North Branch, Islamic Azad University, Tehran, Iran

PAPER INFO

Paper history:

Received 08 November 2023

Received in revised form 18 December 2023

Accepted 28 December 2023

Keywords:

Energy Consumption

Stacking

Regression

Deep Learning

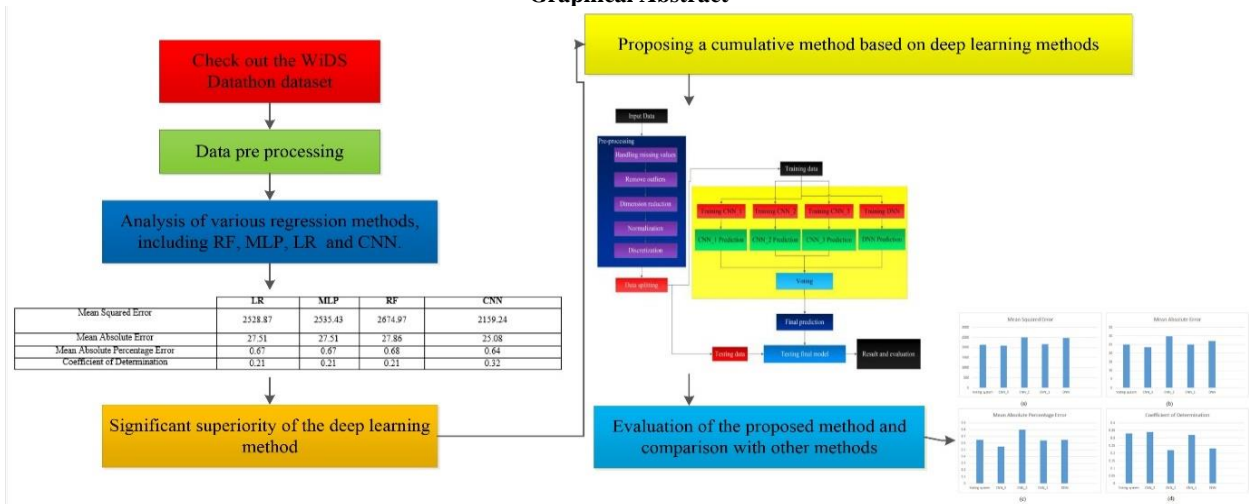
Artificial Intelligence

ABSTRACT

The issue of energy limitation has gained attention as a crisis faced by societies. Buildings play a major role, in energy consumption making it crucial to accurately predict their energy usage. This prediction problem has led researchers to explore machine learning techniques in the field of energy efficiency. In this study we investigated the performance of used machine learning methods like Random Forest (RF) Multi Layer Perceptron (MLP) Linear Regression (LR) and deep learning methods for predicting building energy consumption. The findings revealed that deep learning outperformed methods in solving this problem. To address this we proposed a voting based solution that combines three CNN models with structures and a Deep Neural Network (DNN) method. We applied our proposed method to the WiDS Datathon dataset and achieved promising results. Each of the deep learning methods used in the proposed method provide suitable results and finally, the voting them is done by the averaging. Due to the fact that the proposed method obtains the final result from voting regression models with high accuracy, it is considered a robust model that will be able to provide a suitable prediction against new data.

doi: 10.5829/ije.2024.37.06c.03

Graphical Abstract



1. INTRODUCTION

The increasing energy consumption at the global level has led to many environmental problems, such as air

pollution, global warming, and climate change. Therefore, the management of human activities is necessary to preserve life on earth [1]. In addition, the limitation of energy reserves is a problem that has caused

*Corresponding Author Email: Lriazi@gmail.com (L. Riazi)

many concerns in many countries. Conventional energy sources are not sustainable and obtaining and using fresh reserves is becoming more challenging day by day [2].

These problems have drawn the attention of researchers to the prediction of energy consumption in different fields [3]. Since the contribution of buildings in energy consumption is significant (36 % of the total global energy), predicting building energy consumption and optimizing energy consumption has become a fundamental issue [4].

The building sector is a major energy consumer, accounting for a significant percentage of global energy consumption of CO₂ emissions, and over time its annual growth rate increases. The increase in building energy consumption has been due to population growth and increased demand for building comfortable environments. This increased use of energy consumption in the building sector raises concerns about supply issues and global environmental impacts. Therefore, energy efficiency in this sector is needed to reduce carbon emissions and reduce supply problems, and it serves as the basis for many advanced building energy management techniques, such as safety monitoring, demand response and optimization control.

Hence, a precise method for predicting building energy consumption for energy management systems is important and challenging. However, building energy consumption data often shows nonlinear and non-stationary patterns that make forecasting more difficult.

With the increasing demand for energy consumption, the necessity of activity in this field is still ongoing, as well as up-to-date articles in this field are presented in prestigious journals. In order to address the mentioned problems, in this research, a new approach to predicting energy consumption using artificial intelligence techniques has been presented in order to increase accuracy. In this research, the combination of deep learning and artificial intelligence techniques will be used to develop a solution to the problem that offers both good accuracy and efficiency.

The innovations of this research can be expressed as follows:

- Integrated use of deep learning methods in predicting energy consumption in the building field which includes various networks such as torsion, recursive network, etc. Was.
- Optimize the parameters of several deep learning methods simultaneously in order to achieve higher accuracy. This optimization is applied with the help of a successive halving method.
- Feature selection with the help of recursive feature removal to achieve higher performance.
- Apply the voting process between the results of applying different deep models based on the weights assigned to each model.

In addition, increasing urbanization and the development of cities is one of the issues that aggravates this concern in many countries [5]. One of the available solutions to control this problem is to predict the energy consumption of the building before designing and building the structure. This prediction can lead to the optimal construction of buildings and energy saving. Building energy prediction is related to several factors such as the behavioral characteristics of the building occupants, physical characteristics of the structure, environmental conditions and weather. These cases have complicated the accurate prediction of this issue. Various tools have been provided to simulate building energy consumption and their performance depends on many input parameters. In fact, for the correct use of this tool, accurate and extensive information must be available. In practice, this issue itself has become a new challenge and the unavailability of this information leads to the poor performance of these tools [6]. One of the available solutions to solve this problem is the use of machine learning techniques that are used in various fields [7]. These methods do not require a lot of information and can provide a suitable forecast using the historical data of each region.

Machine learning algorithms and models use patterns and inference to learn, rather than using clear instructions. In this way, they easily identify trends and patterns without the need for human intervention. The widespread use of machine learning methods in various fields to manage multidimensional and complex data in a short time and using limited resources is significant. In addition, researchers' attention to this field has led to the continuous improvement of its techniques.

In this way, it is possible to predict the building's energy needs in any area by using the available data and using the machine learning technique, and avoid possible future problems. The proper performance of machine learning methods largely depends on the models used for learning and the available data. In this research, an approach based on deep learning techniques is used, which processes data in a way inspired by the human brain and recognizes complex patterns. In addition, this research will use a standard data set that has been collected and used by several research teams in recent years, and will keep the possibility of comparing the results for future research.

In the continuation of this research, in section 2, the recent work done in the field of using machine learning and deep learning techniques in the problem of predicting building energy consumption are presented. In section 3, the proposed voting-based system is discussed and its details are explained. In section 4, explanations about the data set used are provided. The results of the implementation of the proposed method and its components are presented in section 5, and finally, conclusion is stated in section 6.

2. RELATED WORK

Currently machine learning and deep learning algorithms have proven their ability to manage sequential data and are used to solve many data-driven problems [8, 9]. In Yazdan et al. [10] used RNN to predict energy consumption. The results of this research showed that the proper efficiency of this method is obtained by increasing the number of courses and setting the parameters properly. Olu-Ajayi and Alaka [11] introduced machine learning techniques including artificial neural network, support vector machine and decision tree; they have applied on a dataset of multiple buildings and were able to predict the average amount of energy consumption in buildings.. The results obtained from this research showed that the artificial neural network showed the best performance among the evaluated methods and achieved values of 2.80 and 7.85 in RMSE and MSE criteria, respectively.

A building energy consumption prediction model called SSA-CNNBiGRU was proposed by Wei and Bai [12] which combines SSA, CNN and BiGRU methods. Actual data is used from a number of office buildings in the UK. The obtained results and comparison with other machine learning techniques showed the appropriate accuracy of the proposed method of this research. So that in the MAE criterion, the values of 76.85 and 77.70 were obtained for the prediction of electricity consumption and gas consumption, respectively. A new architecture based on hybrid deep learning was proposed by Jogunola et al. [13] using two layers of CNN and BLSTM and LSTM. This method was used to predict energy consumption in commercial and residential buildings in areas such as Canada and the United Kingdom, and satisfactory results were obtained.

An electric load forecasting model was proposed by Alsharekh et al. [14] in which the input data which includes spatial and temporal features is pre-processed. After that, a method based on R-CNN and MLLSTM is used to learn patterns in two steps. The results of implementing the proposed method on the IHEPC and PJM datasets showed a relative reduction in the error rate.

Khan et al. [15] investigated several deep learning methods and finally a CNN-based model was proposed to extract new features from the analyzed data to predict the energy required in residential and commercial buildings. The features extracted in the previous step are used by the LSTM encoder and decoder to generate prediction sequences. Khan et al. [16] presented a framework for predicting short-term electric energy consumption; which first deals with data preprocessing and cleaning. In the continuation of this research, CNN is used to extract the pattern. The output obtained from this section is sent to a stacked LSTM. Evaluation of this system on the IHEPC and PJM datasets provided good results.

Amalou et al. [17] investigated a number of deep learning methods, such as RNN, LSTM and GRU to solve the problem of energy consumption management and prediction. The results of this research on the SGSC data set showed that among the mentioned methods, GRU provides the best performance., LSTM, GRU and combined LSTM-GRU learning methods were used by Çetiner [18] to predict energy consumption. The proposed method of this research was applied to the dataset published by ENTSO-E (European Distribution Authority). The results of the research showed that the combined LSTM-GRU method has relatively higher training time, however, it has achieved appropriate accuracy.

Wang et al. [19], a multi-scale recurrent neural network (MCRNN) was proposed that uses multi-scale convolution units to gather information about temperature, air pressure, light data. Bi-RNN is used to obtain the dependence between the expressed factors. In the proposed method of this research, a recurrent convolutional connection is used to filter useful multi-scale and long-term information. Lei et al. [20] first used the rough sets theory to reduce the effective factors. In the following, the extracted features were used as the input of a deep neural network to predict the energy consumption of the building in the short and medium term. The results of the proposed method with other methods proved the appropriate accuracy of this method.

El Alaoui et al. [21] focused on predicting the energy consumption of an administrative building through the utilization of machine learning and statistical techniques. The study aims to develop accurate and efficient models for forecasting energy usage, which can contribute to energy management and conservation efforts. They collect and analyze historical energy consumption data from an administrative building, along with relevant external variables like weather conditions and occupancy patterns. This data is then utilized to develop predictive models using machine learning algorithms, such as artificial neural networks and support vector regression. Additionally, statistical methods, including autoregressive integrated moving average models, were employed for benchmarking purposes and model comparison. The models' performances were compared based on three statistical indicators: normalized root mean square error (nRMSE), mean average error (MAE), and correlation coefficient (R). The results show that all studied models have good accuracy, with a correlation coefficient of $0.90 < R < 0.97$. The artificial neural network outperforms all other models ($R=0.97$, $nRMSE=12.60\%$, $MAE= 0.19$ kWh).

3. PROPOSED METHOD

In this study, several machine learning regression

TABLE 1. Comparison of previous works

Evaluation	Data collection	Method	Reference
RMSE / 0.084	OPSD, Germany	RNN	(10)
RMSE / 2.80	MHCLG + Meteostat	ANN	(11)
MAE/ 76.85 MAE/ 77.70	Real office buildings in the UK	SSA-CNNBiGRU	(12)
MSE / 0.09	commercial and domestic building in Canada and UK	CBLSTM-AE	(13)
MSE / 0.002 MSE / 0.0005	IHEPC and PJM datasets	R-CNN + ML-LSTM	(14)
MSE / 0.19 RMSE / 0.47	UCI residential building dataset	CNN + LSTM-AE b	(15)
RMSE / 14.85 RMSE / 3.4	IHEPC and PJM datasets	CNN + stacked LSTM	(16)
RMSE / 0.034	SGSC	GRU	(17)
MSE / 0.0013	Germany energy consumption data set	LSTM-GRU	(18)
RMSE / 38.3016	Residential building in Belgium	MCRNN	(19)
Relative error/ 7%	Civil public and laboratory building	RS-DBN	(20)

methods, including Random Forest (RF), Multi-Layer Perceptron (MLP), Linear Regression (LR), and Convolutional Neural Networks (CNN) were used to analyze the investigated data set. The results showed that the CNN method has a significant superiority over the other investigated techniques. Since deep learning methods can detect complex patterns in data with appropriate accuracy, in this research, deep learning methods were further investigated. Different structures of CNN and Deep Neural Network (DNN) were investigated and finally a method based on voting was proposed to predict building energy consumption. The proposed method of this research is shown in Figure 1. Since deep learning methods work well on data and perform well, it is difficult to choose the best method among them. To get better results in the proposed method of this research, voting technique has been used. The proposed voting regression-based method is a meta-estimator that averages the predictions of individual models and provides a final prediction. In this method, instead of providing a strong model, a combination of several models is used. In the proposed method, each model examines aspects of the data structure and the result of the final model will be more robust. In methods with appropriate robustness, one can be sure that the performance of the model does not change and does not deviate significantly when using new data compared to the training data. As can be seen in the figure, in the proposed research system, three different versions of CNN and a DNN models are applied to the training data after the pre-processing of the obtained data. The specifications of the CNNs used in the proposed method

are given in Table 2. The results obtained from voting methods will be presented as the final prediction.

We examined different methods of deep learning approaches with different parameters; finally, the architecture proposed in this article has provided the best results.

4. DATA SET

In this research, the WiDS Datathon dataset is used to check the energy consumption prediction model. WiDS Datathon has been created in collaboration with various institutions and universities such as Stanford University, Harvard University and the WiDS Datathon Committee. This continuously developing dataset is collected by research teams and university researchers around the world for climate change mitigation and energy efficiency. The WiDS Datathon 2022 used in this research contains approximately 100k observations of building energy consumption records, and each record represents the energy consumption information of a building over the course of one year. This information was collected over 7 years from several different states of the United States. In each record, information related to 31 features is recorded, which includes building characteristics, climate characteristics of the region (the region where the building is located), geographical characteristics of the region, the year in which the information was checked, and the amount of energy consumption. Among the things that are checked for building specifications are things like the type of

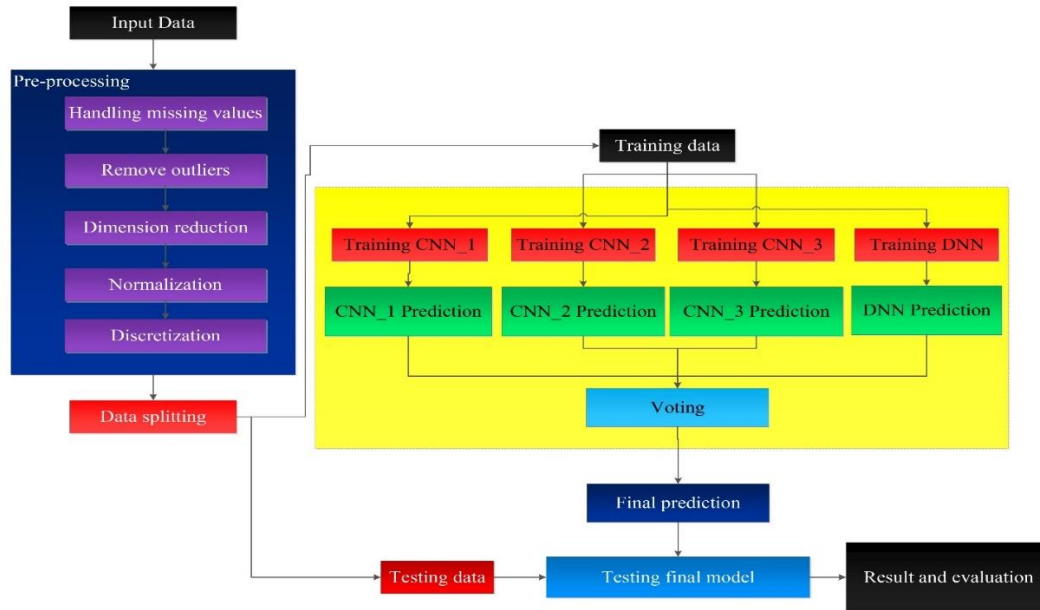


Figure 1. Flowchart of the proposed method

TABLE 2: The specifications of the CNNs used in the proposed method

	Layer (type)	Output Shape	Param #
CNN_1	Conv1D_1 (Conv1D)	(None, 54, 64)	640
	dropout_2 (Dropout)	(None, 54, 64)	0
	Conv1D_2 (Conv1D)	(None, 52, 32)	6176
	Conv1D_3 (Conv1D)	(None, 51, 16)	1040
	MaxPooling1D(MaxPooling1D)	(None, 25, 16)	0
	flatten_2 (Flatten)	(None, 400)	0
	Dense_1 (Dense)	(None, 64)	25664
	Dense_2 (Dense)	(None, 1)	65
CNN_2	Conv1D_1 (Conv1D)	(None, 58, 32)	192
	dropout_1 (Dropout)	(None, 58, 32)	0
	Conv1D_2 (Conv1D)	(None, 56, 32)	3104
	MaxPooling1D (MaxPooling1D)	(None, 28, 32)	0
	flatten_1 (Flatten)	(None, 896)	0
	Dense_1 (Dense)	(None, 32)	28704
CNN_3	Dense_2 (Dense)	(None, 1)	33
	Conv1D_1 (Conv1D)	(None, 56, 64)	512
	dropout (Dropout)	(None, 56, 64)	0
	Conv1D_2 (Conv1D)	(None, 54, 32)	6176
	Conv1D_3 (Conv1D)	(None, 53, 16)	1040
	MaxPooling1D (MaxPooling1D)	(None, 26, 16)	0
	flatten (Flatten)	(None, 416)	0
	Dense_1 (Dense)	(None, 32)	13344
	Dense_2 (Dense)	(None, 1)	33

building, the floor area of the building and the year of its construction. Among the climatic and geographical data recorded in this dataset, we can mention things like minimum, average and maximum temperature, annual rainfall in the building site, maximum wind speed and its direction. More information about this dataset is available on the Kaggle site.

In order to use the WiDS Datathon data set in this research, pre-processing operations were first applied to the data. Management of missing values, removal of outliers, dimensionality reduction, normalization and discretization are among the things that have been done in the pre-processing of the data set investigated in this research.

5. RESULTS AND DISCUSSION

In order to better compare the performance of the proposed method in this research, the performance of the basic regression methods that are used in many researches are first examined. In the first experiment, RF, MLP, LR, and CNN methods were applied separately on the training data set, and the results obtained from their application on the test data set are given in Table 3. As can be seen from the results of this table, the results obtained from the CNN method are significantly superior to other methods. Among RF, MLP and LR regression methods, LR regression method has the best performance. However, the CNN method has performed better than it in terms of MSE, MAE, MAPE and

Coefficient of Determination by 369.63, 2.43, 0.03 and 0.11, respectively. The comparison of the methods in different criteria in Figure 2 clearly shows the superiority of the CNN.

In the continuation of this section, the performance results of the proposed method of this research and the deep learning methods used in it were compared. As stated in the previous section, three regression models based on CNN that have different structures and one regression model based on DNN have been used in the proposed method. The results recorded by each of them are given in Table 4. Figure 3 shows the comparison of the efficiency of deep learning methods and the implemented basic methods (LR, MLP and RF). Comparison of the graphs obtained from this figure show that deep learning methods are superior in various criteria.

TABLE 3. Comparison of the results obtained from LR, MLP, RF, and CNN

	LR	MLP	RF	CNN
Mean Squared Error	2528.87	2535.43	2674.97	2159.24
Mean Absolute Error	27.51	27.51	27.86	25.08
Mean Absolute Percentage Error	0.67	0.67	0.68	0.64
Coefficient of Determination	0.21	0.21	0.21	0.32

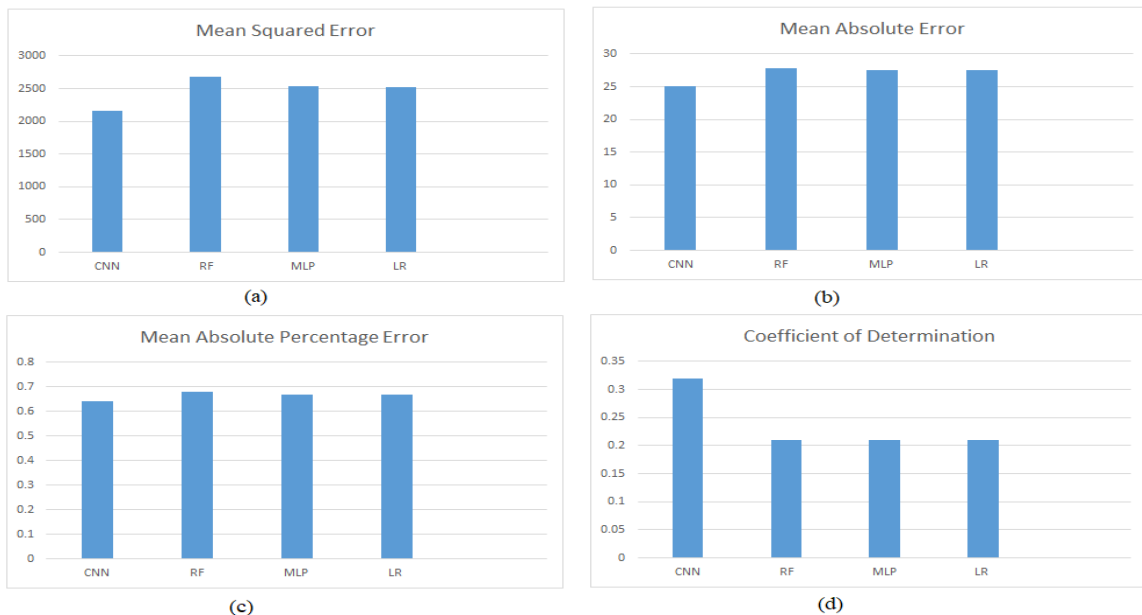
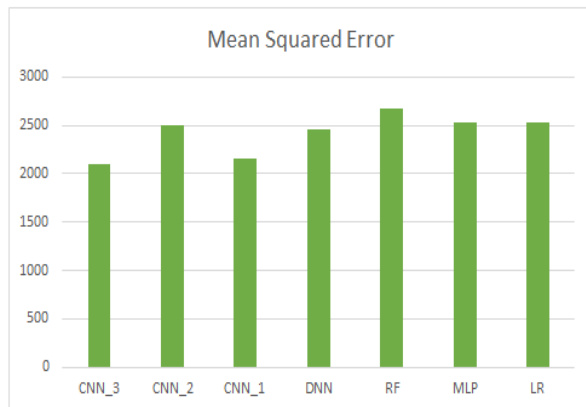


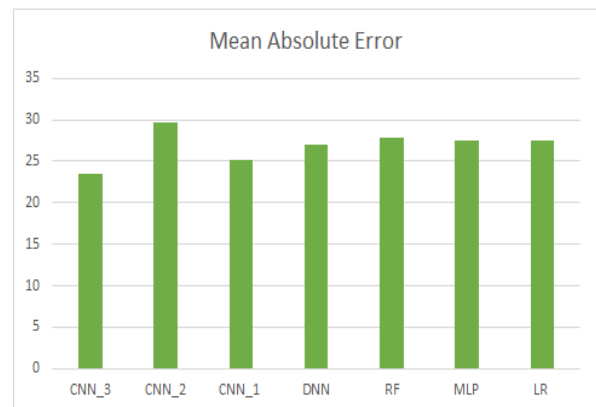
Figure 2. Performance comparison of LR, MLP, RF, and CNN in (a): Mean Squared Error (b): Mean Absolute Error (c): Mean Absolute Percentage Error and (d): Coefficient of Determination

TABLE 4. Comparison of the results obtained from DNN, CNN_1, CNN_2, CNN_3 and Voting system

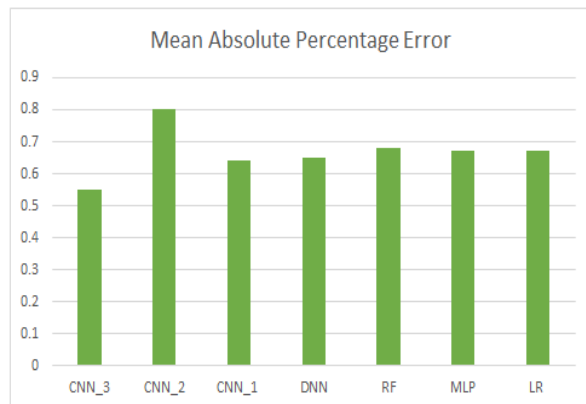
	DNN	CNN_1	CNN_2	CNN_3	Voting system
Mean Squared Error	2457.63	2159.24	2495.87	2092.89	2126.62
Mean Absolute Error	27.02	25.08	29.72	23.45	25.00
Mean Absolute Percentage Error	0.65	0.64	0.80	0.55	0.65
Coefficient of Determination	0.23	0.32	0.22	0.34	0.33



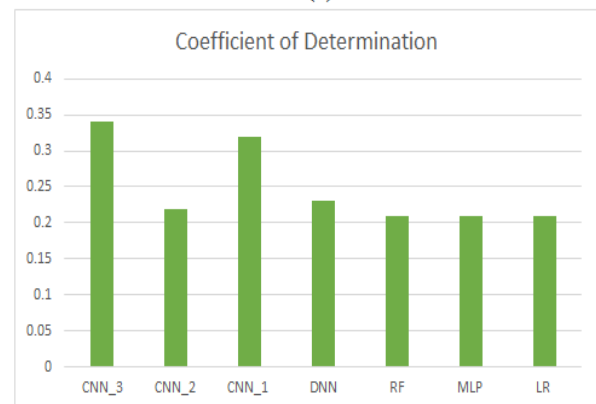
(a)



(b)



(c)



(d)

Figure 3. Performance comparison of LR, MLP, RF, CNN_1, CNN_2, CNN_3 and DNN in (a): Mean Squared Error (b): Mean Absolute Error (c): Mean Absolute Percentage Error and (d): Coefficient of Determination

Figure 4 shows the comparison of deep learning methods and the proposed voting-based method. The results of this study show that the CNN_3 method is the best available method and the proposed method of this research is the second best method in the results with a small difference. The proposed method consists of voting regression models and the average of the methods used

in it is used to obtain the final result. In this way, the final result obtained is directly related to the results of the basic methods used, and the final result will be less than the best available method among the basic methods. This small difference in the accuracy of the system can be ignored compared to the more robustness of the proposed method.

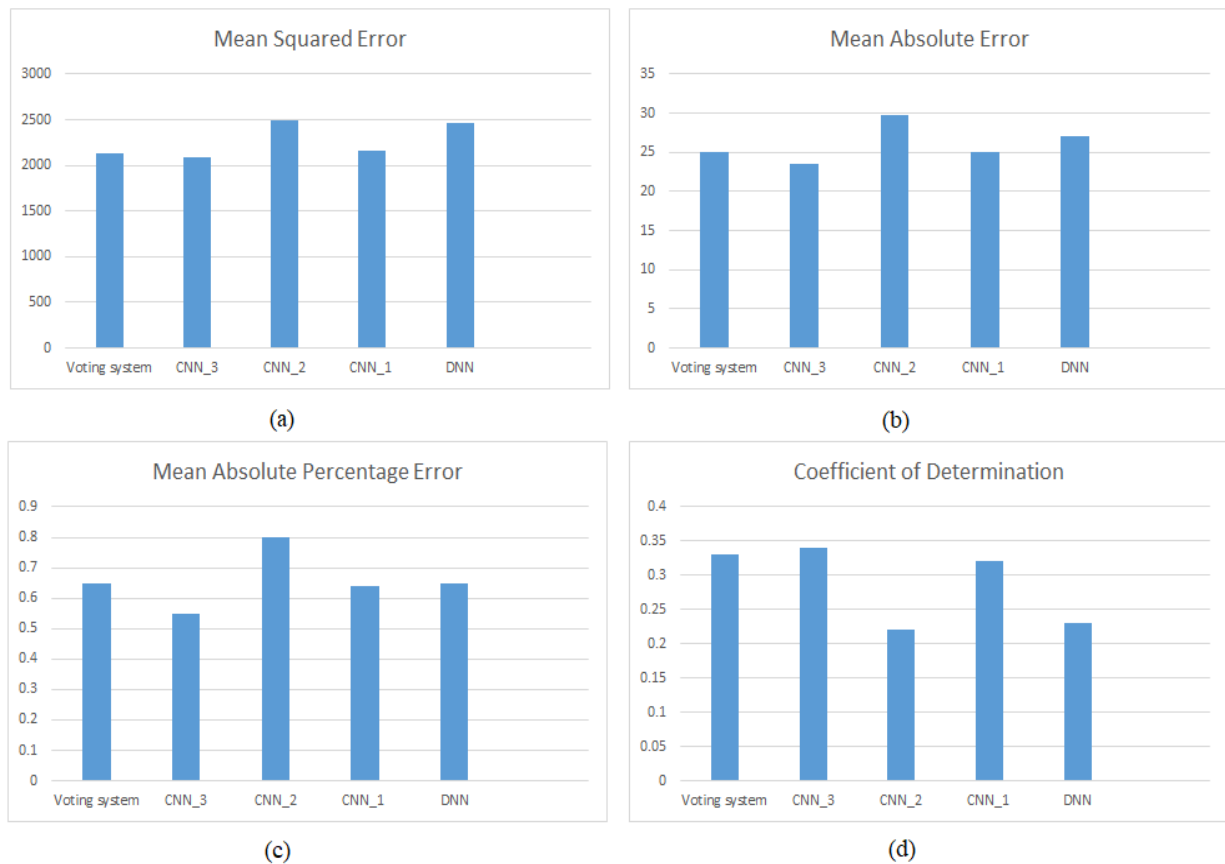


Figure 4. Performance comparison of DNN, CNN_1, CNN_2, CNN_3 and Voting system in (a): Mean Squared Error (b): Mean Absolute Error (c): Mean Absolute Percentage Error and (d): Coefficient of Determination

6. CONCLUSION

In this research, first, a number of machine learning regression models were used to predict building energy consumption. For appropriate review of the methods, the WiDS Datathon data set was used, which is available to all researchers and makes it possible to compare the results for future research. The results of the investigations showed that the compared deep learning method recorded relatively more appropriate results in all the investigated criteria, including MAE, MSE, MAPE and R². In this way, in the continuation of this research, a method based on voting of deep learning methods was proposed. Each of the deep learning methods used in the proposed method provide suitable results and finally, the voting between these regression methods is done by the averaging. Due to the fact that the proposed method obtains the final result from voting regression models with high accuracy, it is considered a robust model that will be able to provide a suitable prediction against new data.

7. REFERENCES

1. Zabihian F, Fung A. Fuel and GHG emission reduction potentials by fuel switching and technology improvement in the Iranian electricity generation sector. *International Journal of Engineering (IJE)*. 2009;3(2):159.
2. Al-johani H, Saleh Z, Almalki A, Almalki A, AbdelMeguid H. Advancements in Green Hydrogen Production using Seawater Electrolysis in Tabuk, Saudi Arabia. *International Journal of Engineering (IJE)*. 2023;15(3):42.
3. Olu-Ajayi R, Alaka H, Owolabi H, Akanbi L, Ganiyu S. Data-Driven Tools for Building Energy Consumption Prediction: A Review. *Energies*. 2023;16(6):2574. <https://doi.org/10.3390/en16062574>
4. Khalil M, McGough AS, Pourmirza Z, Pazhoohesh M, Walker S. Machine Learning, Deep Learning and Statistical Analysis for forecasting building energy consumption—A systematic review. *Engineering Applications of Artificial Intelligence*. 2022;115:105287. <https://doi.org/10.1016/j.engappai.2022.105287>
5. Yu J, Chang W-S, Dong Y. Building energy prediction models and related uncertainties: A review. *Buildings*. 2022;12(8):1284. <https://doi.org/10.3390/buildings12081284>
6. Runge J, Zmeureanu R. Forecasting energy use in buildings using artificial neural networks: A review. *Energies*. 2019;12(17):3254. <https://doi.org/10.3390/en12173254>

7. Sheikhi S, Kheirabadi MT, Bazzazi A. An effective model for SMS spam detection using content-based features and averaged neural network. *International Journal of Engineering*. 2020;33(2):221-8. <https://doi.org/10.5829/ije.2020.33.02b.06>
8. Amasyali K, El-Gohary NM. A review of data-driven building energy consumption prediction studies. *Renewable and Sustainable Energy Reviews*. 2018;81:1192-205. <https://doi.org/10.1016/j.rser.2017.04.095>
9. Ardabili S, Abdolalizadeh L, Mako C, Torok B, Mosavi A. Systematic review of deep learning and machine learning for building energy. *Frontiers in Energy Research*. 2022;10:786027. <https://doi.org/10.3389/fenrg.2022.786027>
10. Yazdan MMS, Khosravia M, Saki S, Al Mehedi MA. Forecasting Energy Consumption Time Series Using Recurrent Neural Network in Tensorflow. 2022. <https://doi.org/10.20944/preprints202209.0404.v1>
11. Olu-Ajayi R, Alaka H, editors. Building energy consumption prediction using deep learning. EDMIC 2021 CONFERENCE PROCEEDINGS ENVIRONMENTAL DESIGN & MANAGEMENT INTERNATIONAL CONFERENCE: Confluence of Theory and Practice in the Built Environment: Beyond Theory into Practice; 2021: Obafemi Awolowo University, Ile-Ife. Retrieved from <https://oauife.edu.ng/>
12. Wei S, Bai X. Multi-Step Short-Term Building Energy Consumption Forecasting Based on Singular Spectrum Analysis and Hybrid Neural Network. *Energies*. 2022;15(5):1743. <https://doi.org/10.3390/en15051743>
13. Jogunola O, Adebisi B, Hoang KV, Tsado Y, Popoola SI, Hammoudeh M, Nawaz R. CBLSTM-AE: a hybrid deep learning framework for predicting energy consumption. *Energies*. 2022;15(3):810. <https://doi.org/10.3390/en15030810>
14. Alsharekh MF, Habib S, Dewi DA, Albattah W, Islam M, Albahli S. Improving the Efficiency of Multistep Short-Term Electricity Load Forecasting via R-CNN with ML-LSTM. *Sensors*. 2022;22(18):6913. <https://doi.org/10.3390/s22186913>
15. Khan ZA, Hussain T, Ullah A, Rho S, Lee M, Baik SW. Towards efficient electricity forecasting in residential and commercial buildings: A novel hybrid CNN with a LSTM-AE based framework. *Sensors*. 2020;20(5):1399. <https://doi.org/10.3390/s20051399>
16. Khan ZA, Ullah A, Haq IU, Hamdy M, Mauro GM, Muhammad K, et al. Efficient short-term electricity load forecasting for effective energy management. *Sustainable Energy Technologies and Assessments*. 2022;53:102337. <https://doi.org/10.1016/j.seta.2022.102337>
17. Amalou I, Mouhni N, Abdali A. Multivariate time series prediction by RNN architectures for energy consumption forecasting. *Energy Reports*. 2022;8:1084-91. <https://doi.org/10.1016/j.egy.2022.07.139>
18. ÇETİNER H. Recurrent Neural Network Based Model Development for Energy Consumption Forecasting. *Bitlis Eren Üniversitesi Fen Bilimleri Dergisi*. 2022;11(3):759-69. <https://doi.org/10.17798/bitlisfen.1077393>
19. Wang H, Ma W, Wang Z, Lu C. Multiscale convolutional recurrent neural network for residential building electricity consumption prediction. *Journal of Intelligent & Fuzzy Systems*. 2022;43(3):3479-91. <https://doi.org/10.3233/jifs-213176>
20. Lei L, Chen W, Wu B, Chen C, Liu W. A building energy consumption prediction model based on rough set theory and deep learning algorithms. *Energy and Buildings*. 2021;240:110886. <https://doi.org/10.1016/j.enbuild.2021.110886>
21. El Alaoui M, Chahidi LO, Rougui M, Lamrani A, Mechaqrane A. Prediction of Energy Consumption of an Administrative Building using Machine Learning and Statistical Methods. *Civil Engineering Journal*. 2023 May 1;9(5):1007-22. <http://dx.doi.org/10.28991/CEJ-2023-09-05-01>

COPYRIGHTS

©2024 The author(s). This is an open access article distributed under the terms of the Creative Commons Attribution (CC BY 4.0), which permits unrestricted use, distribution, and reproduction in any medium, as long as the original authors and source are cited. No permission is required from the authors or the publishers.

**Persian Abstract****چکیده**

مسئله محدودیت انرژی به عنوان بحرانی که جوامع با آن روبرو هستند مورد توجه قرار گرفته است. ساختمان‌ها نقش مهمی در مصرف انرژی دارند و پیش‌بینی دقیق مصرف انرژی آنها بسیار مهم است. این مشکل پیش‌بینی باعث شده است که محققان تکنیک‌های یادگیری ماشین را در زمینه بهره‌وری انرژی کشف کنند. در این مطالعه عملکرد روش‌های یادگیری ماشینی مورد استفاده مانند جنگل تصادفی (RF) شبکه عصبی چند لایه کاملاً متصل (MLP) رگرسیون خطی (LR) و یادگیری عمیق برای پیش‌بینی مصرف انرژی ساختمان مورد بررسی قرار گرفت. یافته‌ها نشان داد که یادگیری عمیق در حل این مشکل از روش‌های دیگر بهتر عمل می‌کند. برای رسیدگی به این موضوع، ما یک راه حل مبتنی بر رای گیری را پیشنهاد کردیم که سه مدل شبکه‌های عصبی پیش‌بینی CNN را با ساختارها و روش شبکه عصبی عمیق DNN ترکیب می‌کند. ما روش پیشنهادی خود را به مجموعه داده‌های WiDS Datathon اعمال کردیم و به نتایج امیدوارکننده‌ای دست یافتیم. هر یک از روش‌های یادگیری عمیق مورد استفاده در روش پیشنهادی نتایج مناسبی را ارائه می‌دهند و در نهایت رای گیری آنها با میانگین انجام می‌شود. با توجه به اینکه روش پیشنهادی نتیجه نهایی را از مدل‌های رگرسیون رای گیری با دقت بالا به دست می‌آورد، یک مدل قوی محسوب می‌شود که قادر به ارائه پیش‌بینی مناسب در برابر داده‌های جدید خواهد بود.



Improvement of Sand Soil with Bio-micropiles and Bio-grout Injection in Reinforced Soils

M. Nouranbakhsh, K. Barkhordari*, S. Ghasemi

Department of Civil Engineering, Yazd University, Yazd, Iran

PAPER INFO

Paper history:

Received 27 October 2023

Received in revised form 26 January 2024

Accepted 16 February 2024

Keywords:

Microbially Induced Carbonate Precipitation

Bio-micropile

Reinforced Soil

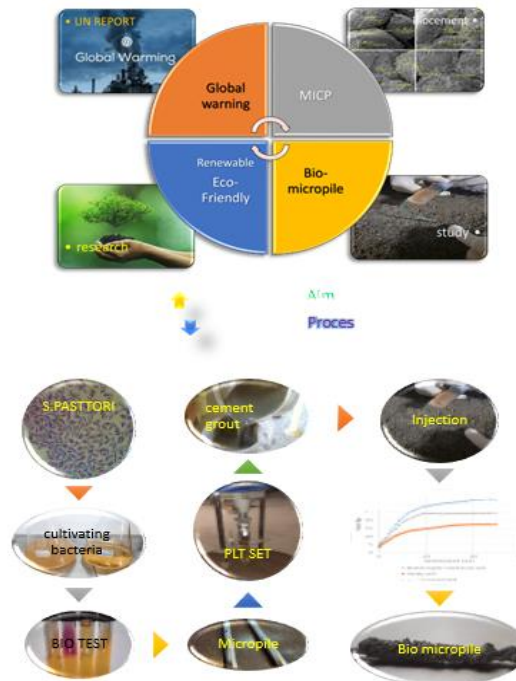
Bio-grout

ABSTRACT

The production of Portland cement, one of the most used materials in the construction industry, has increased environmental pollution and global warming. Soil bio-improvement is an eco-friendly and renewable method that has recently received attention. Microbially induced carbonate precipitation (MICP) has been the most researched for bio-geotechnical issues. *Sporosarcina pasteurii* is a micro-organism that produces urease enzymes and was used for sand soil improvement in this study. Also, the type of grout and injection method were selected as variables. The result of the test showed that the use of bio-grout had a significant effect on increasing the bearing capacity of soil. Bio-micropiles increased the bearing capacity by more than 94%. This increase was 126% in the case of cement-grouted micropile. Also, the results of the tests showed that the bearing capacity of bio-improved soil and reinforced soil increased by 54% and 125%, respectively. This research showed that bio-micropile could be a suitable method to replace cement-grouted micropile.

doi: 10.5829/ije.2024.37.06c.04

Graphical Abstract

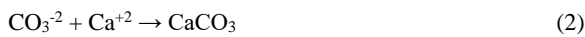
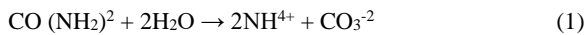


*Corresponding Author Email: kbarkhordari@yazd.ac.ir (K. Barkhordari)

Please cite this article as: Khodadadi M, Riazi L, Yazdani S. A Novel Ensemble Deep Learning Model for Building Energy Consumption Forecast. International Journal of Engineering, Transactions C: Aspects. 2024;37(06):1076-84.

1. INTRODUCTION

The biological improvement of soils is a permanent, eco-friendly method that improves their mechanical properties (1). Soil Microorganisms have been active, renewable, anti-pathogenic, and eco-friendly on the earth for millions of years, but classical geotechnical engineering did not pay attention to this manner (2). The chemical reaction of urea hydrolysis is carried out so slowly in nature. Bacteria such as *Sporosarcina pasteurii* that produce urease enzymes increase the rate of urea hydrolysis up to 10^{14} times (3). Equations 1 and 2 showed calcium carbonate precipitation occurs on soil particles and bio-cementation. Finally, the soil's shear strength and stiffening increase. Also, its permeability and settlement decrease (Figure 1).



The potential applications for bio-cementation include soil strengthening for slope stability, liquefaction mitigation, seepage reduction, erosion prevention, and contaminant immobilization (4). Also, bio-grout is a bio-mineralization product that improves its mechanical properties. The bio-grout reaction is so slower than the chemical grout reaction. This solidification rate reduction allows the bio-grout to spread through soil species (5). Also, previous research showed that bio-grout helped to control soil permeability and bio-improve soil with bio-cementation (6). Bio-grout's other workability is wind erosion resistance. Bio-coating methods can control this problem (7). In addition, the generation of bio-denitrification from bio-grout injection and microbial metabolic activity affects the bulk modulus of the pore fluid. It thus reduces the generation of excess pore water

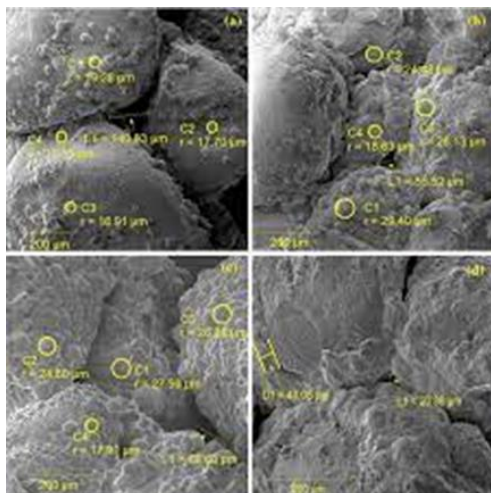


Figure 1. Microbially induced calcium carbonate precipitation (MICP) in sand particles

pressure during shearing. Furthermore, microorganisms can form bio-film and bio-polymers by bio-grout injection, which may clog the pore space, reducing the permeability of the soil (8).

Moreover, soil reinforcing with micropiles, as a soil improvement method, has been used significantly since their conception in the 1950s (9). Micropiles used as foundations support elements to resist static and seismic load to a lesser extent, as in-situ reinforcements to soil improvement or provide stabilization of slopes and excavations of soil (10). Grouting operations have an impact on micropile bearing capacity (Figure 2).

Injected grout increases the bearing capacity of the micropile while protecting it from corrosion (11). The grout usually comprises a neat cement mix W/C ratio of 0.45. Cement production, as one of the most consumed construction materials, requires high energy and creates high pollution. Air emissions such as oxides of carbon dioxide, NO_x, sulfur dioxide, polychlorinated dibenzo-p-dioxins, dibenzofurans, and their compounds increase environmental problems (10). The effect of bio-grout injection in micropile compared to cement-grouted micropile in this research is studied.

2. MATERIALS AND METHODOLOGY

2. 1. Sandy Soil Properties The tested soils of this research were the Mashhad Kashafroud River sand. The particle size distribution curve is shown in Figure 3; which is classified as poorly graded sand (SP) at the Unified Soil (USCS). Research showed that SP soil bio-precipitation amount is five times more than that of graded sandy soil (SW) with the same moisture and density (12).

The test soil had a specific gravity (G_s) of 2.65, a mean particle size (D_{50}) of 0.8 mm, and a maximum and minimum void ratio (E_{max} and E_{min}) of 0.90 and 0.57, respectively. The soil was non-cohesive, its cohesion was

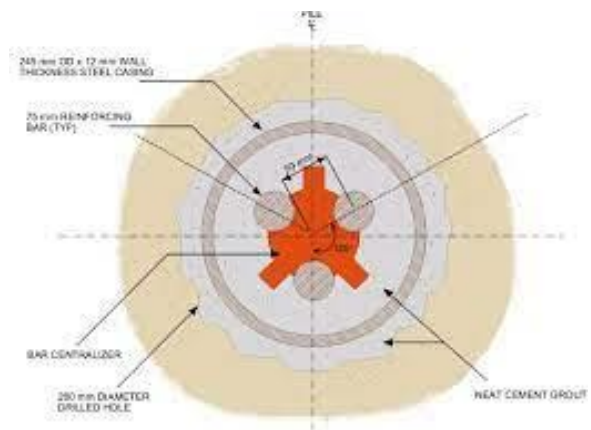


Figure 2. Grout-injected micropile general section

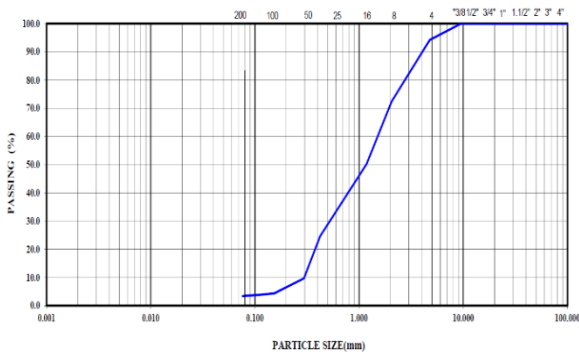


Figure 3. Kashafroud sand gradation graph

zero, and its internal friction angle was 30° in the speed direct shear test (Figure 4). Also, soil pH is effective as a chemical characteristic in soil bio-precipitation. The research showed that MICP in an alkaline soil mass, with a pH between 7.5 and 9.5, had better function. The sample soil pH was 8.5.

2. 2. Bacteria Cultivation and Growth Condition

The most crucial parameter in microorganism choice for the MICP process is its ability to produce urease enzymes. Enzymes, as a bio-catalyst, significantly reduces the time of bio-precipitation. Research showed that the *Sporosarcina pasteurii* has the highest performance in urease enzyme production. Therefore, these microorganisms are used in the tests.

Bacterial cultures grew in an ATCC-specified medium. These bacteria are added to a Nutrient Agar culture medium containing 2% urea. First, 20 g of urea was dissolved in a liter poor water and about 8 g of nutrient broth culture, along with 100 mg of calcium chloride, was poured into Erlen and stirred well by a shaker (13). The liquid cultures were placed on a hot plate to have a solid culture medium. Then, nutrient agar was added to the solution (Figure 5). So, solid and liquid culture areas were prepared for the activation and cultivation of bacteria (14).

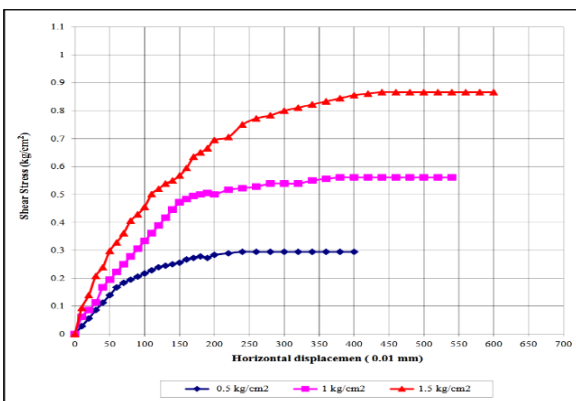


Figure 4. The result of Samples direct shear test graph

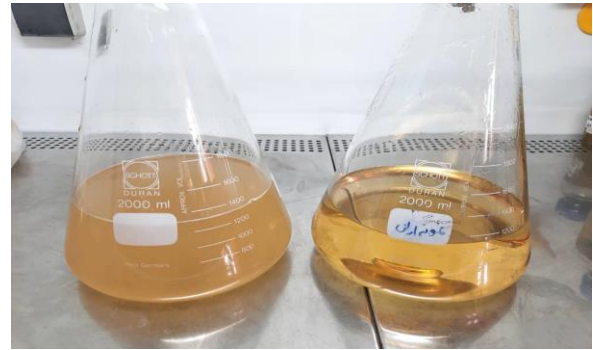


Figure 5. Bacterial cultures medium

The calcium chloride and urea reagents are needed to complete the reaction and precipitation of calcium carbonate. This cementing solution increases the process of bio-precipitation like a catalyst.

2. 3. PLT Set and Parameters

Plate loading tests set are used to determine the ultimate bearing capacity and the probable soil settlement. The FHWA recommends that the thickness of the loading plate be more than ten times the maximum soil particles. Therefore, in research, the rigid steel loading plate with dimensions of $8*8*2 \text{ cm}^3$. Also, According to The Boussinesq approximation, for the distribution of stress bubbles under the loading plate to ignore the boundary condition, the diameter and height of the tank were 55 and 60 cm. The sand soil was compacted to prepare the specimens in three 15 cm layers with a moisture content of about 6% (Figure 6).

2. 4. Micropile and its variable parameters

The reinforced soil with four types of bio-micropile, cement-grouted, non-grout micropile, and reinforced soil with bio-grout injection, was tested in this research, and the steel core of micropiles were ST37 thin-walled steel tubes. Also, according to FHWA's recommendation, the



Figure 6. Plate loading tests set

micropile diameter was 0.8 mm, and its length was 200 mm. For better infiltration of the grout in the soil around the micropile wall and the formation of the grout sheath, the micropile was drilled in two perpendicular directions and at 4 cm intervals (Figure 7).

Cement grout prepared with FHWA recommendation. In this instruction, the executive classification of micropiles with gravity injection of grout with W/C 0.4 to 0.5 is placed in executive group A (15). Cement grout prepared with 20% micro-silica and 1% super plasticizer. Micro-silica, like other amorphous pozzolans, increases the mechanical properties of grout. The compressive strength and grout shrinkage amount in the first 2 hours tested. The results were 20.1, 28.6, and 31.2 MPa in 2, 7, and 28 days.

2. 5. Qualitative Test of Urease Enzyme Production Capacity

The urease enzyme production capacity qualitative test is done in a solid culture medium. Due to the decomposition of urea and conversion to ammonia, the pH increases, and within 24 hours, the color of the cultivated area changes from yellow to pink (16). So, the culture areas are used for the isolation of urease-producing microorganisms. One liter of UAB culture area needs 20 g urea, 5 g sodium chloride, 1 g peptone, 1 g glucose, 2 g mono potassium phosphate, 12 mg red phenol, and 15 g agar. So, except urea, all of the materials were mixed in a laminar hood and placed in an autoclave (Figure 8).

After autoclaving, it cooled to a temperature of 38°C, dissolved urea was added to the area through a sterile filter, and then kept in an incubator at 25 to 30°C for 24 hours. During this period, the development of pink color was recorded in the culture medium.

2. 6. The Solution Concentration Control

Continuous dilution method used for determining the



Figure 7. Non-grouted micropiles used in the tests

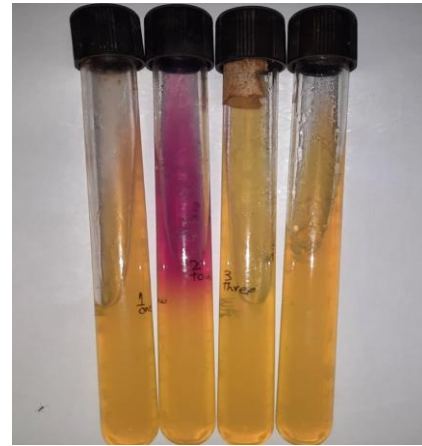


Figure 8. Qualitative test of urease enzyme production capacity

bacterium. First, 6 test tubes containing 9 ml of distilled water or sterile normal saline were placed consecutively, and 1 ml of the solution of the first test tube was transferred from the container containing cultured bacteria. The concentration of bacteria in the first tube is 10^{-1} of the source solution. This process continued until, at the last one, the solution concentration reached 10^{-6} of the main one. Then, 1 ml of solution was transferred into Petri dishes containing solid culture bacteria medium (17).

These were placed inside the incubator for 24 hours. After that period, bacterial cells are seen as colonies inside the culture medium. Then, the contents of each test tube are poured into the cells of the spectrophotometer that shows a number OD in the ABS part of the device by passing light and determining a specific wavelength. In this research, at the wavelength of 650 nm, the bio-grout OD was between 0.8 and 1.0.

2. 7. Reinforced Specimen Preparation and Grout Injection Process

Research target was based on investigating the behavior of micropile-reinforced sand. In this part, the grout was injected at a slow and constant gravity injection rate inside the micropile. To drain the excess grout in this test, install a drain valve at the bottom of the tank. One-stage cement grout and two-stage bio-grout were injected into the micropile. Observations of the tests showed that micropile grout cover is dependent on the viscosity and type of grout. The amount of penetration of cement grout around the micropile was 15 mm. In bio-grout injection, Due to its fluid movement, was about 24 mm (Figure 9). In the other part, we studied bio-improved reinforced soil. In this research, bio-grout was injected in two stages. First, bio-grout was injected inside the micropile. So, it penetrated soil particles around the micropile. After 6 hours, we drained the soil by closing the drainage valve. After 2 hours of draining to bio-mineralization, calcium chloride is added to the soil. So, bio-cementation happened. The second step

duplicates the first one. The tests showed that the grout penetration in the soil decreased by 35% in the second step injection. Previous research showed that, by increasing the six stages of injections, the penetration rate decreased by 75% (18).

2. 8. Reinforced and Bio-improved Soil Equalization Method

The injection of bio-grout in soil with or without micropile changes the physical and mechanical characteristics of the soil. Micropile and bio-grout injection create a composite cross-section by increasing the soil stiffness and strength. The bio-grout injection also improves its conditions in interaction with micropiles and soil. There are various methods to check composite sections as bio-improved reinforced soil. The Transformed-Section Method is one of the most used methods to explain this situation. This theory is one of the methods used for bending stress analysis in composite sections (19).

This method is based on general relationships for linear or non-linear elastic materials. In this method, the cross-sectional area of the composite element with different stiffness is converted into the cross-sectional area consisting of a hypothetical equivalent material. This new cross-section is called a transformed cross-section (20). In this method use the dimensionless parameters. The equivalent stiffness and mechanical properties are shown in Equations 3 to 5.

$$\frac{A_{soil}}{a \times b} = \alpha \quad \& \quad \frac{A_{biocement}}{a \times b} = \beta \quad \& \quad \frac{A_{steel}}{a \times b} = \gamma \tag{3}$$

$$E_q = E_{soil} \left(\frac{A_{soil}}{a \times b} \right) + E_{biocement} \left(\frac{A_{biocement}}{a \times b} \right) + E_{steel} \left(\frac{A_{steel}}{a \times b} \right) \tag{4}$$

$$E_q = E_{soil} \times \alpha + E_{biocement} \times \beta + E_{steel} \times \gamma \tag{5}$$



Figure 9. Bio-grout injection in micropile

3. TEST RESULT ANALYSE

3. 1. Unreinforced Soil Test Results The results of the PLT test for unreinforced soil in Figure 10 showed that the unreinforced soil carried a 17.3 kg load at a 50 mm settlement. According to the plate dimensions, loose sandy soil, and without surcharge condition of the test, the bearing capacity was about 0.27 kg/cm². This amount was nearly according to experimental relationships such as Terzaghi's method, whose value showed a bearing capacity of about 0.26 kg/cm².

3. 2. Bio-improved Soil Test Results Results showed that bio-cement can be either solid or liquid. In liquid form, the bio-grout has a much lower viscosity and can flow like water. Thus, the delivery of bio-cement into soil is much easier compared with that of cement or chemicals. Furthermore, when using bio-cement, one usually must wait weeks for the stiffening, whereas when using bio-grout, the reaction time can be reduced if required.

The test results showed that the soil-bearing capacity increased with bio-improvement. The results showed that the bio-remedied soil had a growth rate of 54.1% with an increase in the final load equivalent to a 50 mm settlement compared to the sandy soil. The formation of connecting bridges and bio-calcite cementation between sand particles increased the bearing capacity (Figure 11).

3. 3. Reinforced Soil and Grouted-Micropile Result

The injection of grout into the micropile and its penetration into the surrounding sand particles cements the soil and increases its mechanical properties by forming a composite section. In this research, cement-grout and bio-grout. The results of the tests showed that the non-grouted micropile increased the bearing capacity by 55%. The reinforced soil with micropile behaves as a composite specimen with higher characteristics than the

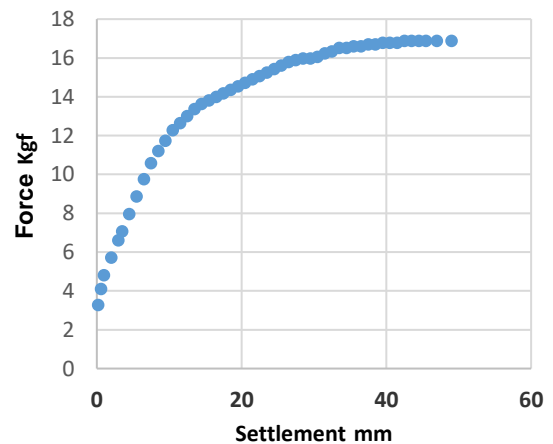


Figure 10. Unreinforced-soil PLT test result

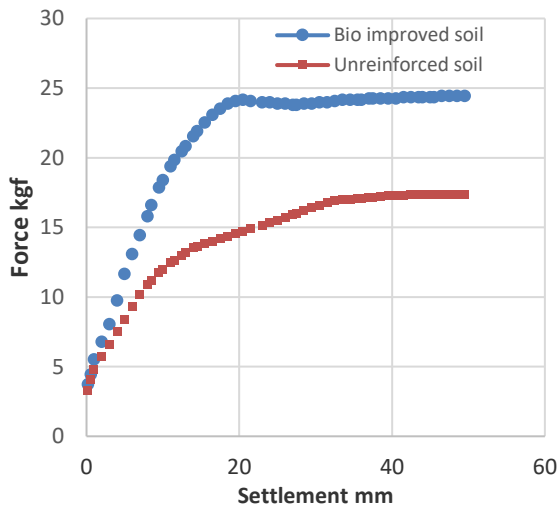


Figure 11. Bio-improved soil PLT test result

original soil. The cement grout injection inside the micropile created a suitable interlock between the grout, soil, and micropile. These increased the bearing capacity by 126%. While increasing the diameter and hardness of the micropile, the grout increased the frictional resistance between the sand particles and the rough surface of the micropile with cement grout.

Also, the results of the tests showed that the bio-grout injected into the bio-micropile penetrated the sand soil particles and increased the bearing capacity of the soil by 96% through bio-cementation. The comparison of these results showed that using bio-micropile can be a sustainable and Eco-friendly replacement for cement-grouted micropile. Soil reinforcement and the injection grout test results are shown (Figure 12).

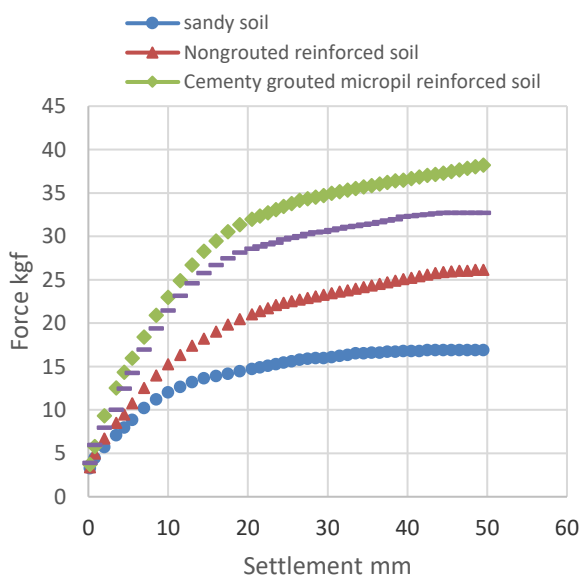


Figure 12. Reinforcing and grouting test result

3. 4. Bio-grout Injection Effect on Soil Reinforcement and Improvement

The results showed that bio-micropiles increased the soil characteristics more than the bio-improving ones. The results showed that the bio-micropile case created a strong adhesion between the micropile wall and the bio-improved soil. Also, the injection of bio-grout in the micropile prevents the corrosion of the steel wall by creating a suitable cover with self-healing ability.

The research results showed that the bearing capacity in bio-micropile reinforced soil is 88.36% higher than in bio-improved soils. So, it has resulted in a transformed soil with a cross-section. Also, the test results in bio-improved soil showed that the bearing capacity of the soil increased by 40.55%. The selected method for soil improvement depends on the Problematic soil type and the required improvement amount (Figure 13).

3. 5. Bio-micropile Numbers Effect in Reinforced Soil

Another influential parameter in increasing the bearing capacity of reinforced soil is the number and type of bio-micropile arrangement. In previous research, according to the dimension of micropile in soil reinforcement, the study is usually done on the micropile group. The number and arrangement of bio-micropiles in soil improvement are related to other parameters such as dimensioning, execution method, bio-micropiles distance from each other, and type of soil granulation. In this research, according to Figure 14, one, three, and five bio-micropiles were used under the arrangement shown.

The results of this research showed that, according to Figure 15, in the case of reinforcing soil with bio-micropiles with 8mm diameter and 14cm length, an increase in the bearing capacity of the soil compared to sand soil in the number of one, three and five bio-

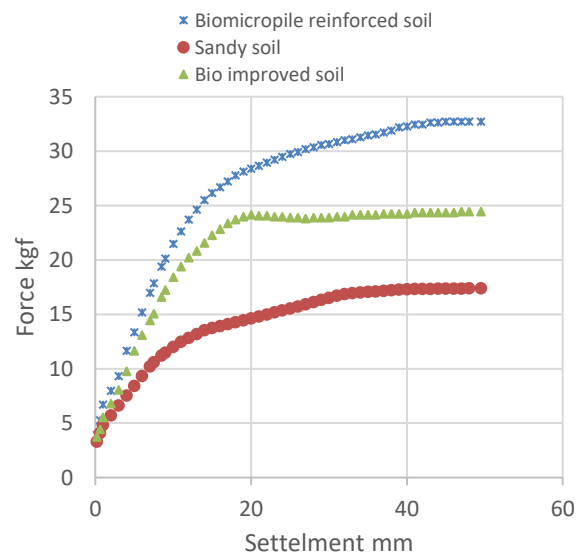


Figure 13. Reinforcing and bio-grouting test result



Figure 14. Five bio-micropile arrangement

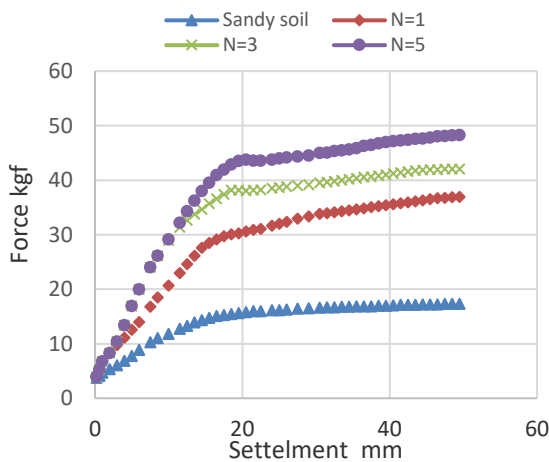


Figure 15. Five bio-micropiles arrangement results

micropiles because of stress distribution curves in the soil and the efficiency of the bio-micropile group are 113.4, 142.3 and 178.9%.

3. 6. Bio-improvement Reinforced-soil Test

This research studied the effect of bio-improvement on the soil-bearing capacity in reinforced and unreinforced soils. In the previous tests, bio-grout was injected into the micropile, and sand particles were cemented within a limited radius around the bio-micropile. In this test, all the soil is bio-improved by surface injection in two stages. The test results showed that bio-cemented soil has high stiffness and bearing capacity. The homogeneity of the residual resistance of this soil can be neglected due to the breaking of the bio-cement bond due to loading. In Figure 8, it was shown that an increase in the bearing capacity of the soil in unreinforced and reinforced bio-improved conditions was 41.1% and 127.6%, respectively. The improvement percentage of reinforced to unreinforced soil strength was 54.9% and 161.6%, respectively. Figure 16 illustrates the bio-improved reinforced soil test result. The coincidental integration of

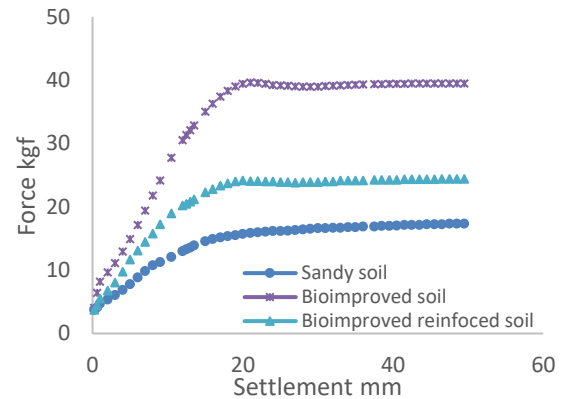


Figure 16. Bio-improved reinforced soil test result

the overall bio-improvement of the reinforced soil caused a more advantageous result in increasing the mechanical characteristics, including its bearing capacity.

4. CONCLUSION

With bacterial sources, which can be a suitable alternative to micropile chemical grout injection. The injection causes bio-cementation of the soil and increases the stiffness and strength of the composite soil. Also, the following results were the output of this process:

- Bio-grout with low viscosity and energy consumption is prepared from renewable sources, and after injection into the soil, it causes soil particles bio cementation.
- Bio-improved soil, with bio-grout injection, caused the connection between the soil particles and increased its bearing capacity by 54.1%. This increase in soil stiffness was also noticeable.
- In the reinforced soil case, the bio-grout injection increased the bearing capacity of the soil by 94% by creating a cover around the bio-micropile. While the non-grouted micropile only increased it by 55%. Also, superplasticizer cement grout injection in micropiles increased its bearing capacity by 112%.
- In a comparative study showed that soil reinforcing with bio-micropiles improved their mechanical characteristics. The bio-grout injection is a renewable and eco-friendly method arison of bio-grout with cement grout, despite the creation of enough cover in micropile due to the stability of bio-grout production resources, its eco-friendliness, the possibility of self-healing of cracks over time in bio-cement cover, bio-grout benefited from better advantages.
- The results of the experiment showed that the bio-improvement method in reinforced soil caused a significant increase in the bearing capacity of the soil. The force-settlement curve showed that the soil stiffness also grew. In this method, the soil's bearing capacity increased by 124%.

•Bio-grout with low viscosity makes gravity injection possible. This injection method is low-cost and reduces energy consumption. However, injecting chemical grout consumes energy while causing environmental pollution.

•According to the warnings of the U.N regarding Global Warning, research to find eco-friendly and sustainable methods is necessary. The bio-micropile usage method can be a suitable alternative to micropile with chemical grout.

5. REFERENCES

- Aggarwal S, Hozalski RM. Determination of biofilm mechanical properties from tensile tests performed using a micro-cantilever method. *Biofouling*. 2010;26(4):479-86. <https://doi.org/10.1080/08927011003793080>
- Taghavi L, Emedzadeh M. Experimental study on the factors affecting hexavalent chromium bioreduction by *Bacillus cereus*. *International Journal of Engineering, Transactions B: Applications*. 2016;29(2):152-9. 10.5829/idosi.ije.2016.29.02b.03
- Liu B, Zhu C, Tang C-S, Xie Y-H, Yin L-Y, Cheng Q, et al. Bio-remediation of desiccation cracking in clayey soils through microbially induced calcite precipitation (MICP). *Engineering geology*. 2020;264:105389. <https://doi.org/10.1016/j.enggeo.2019.105389>
- Cheng L, Cord-Ruwisch R. Upscaling effects of soil improvement by microbially induced calcite precipitation by surface percolation. *Geomicrobiology Journal*. 2014;31(5):396-406. <https://doi.org/10.1080/01490451.2013.836579>
- Achal V, Kawasaki S. Biogrout: A novel binding material for soil improvement and concrete repair. *Frontiers in microbiology*. 2016;7:179226. <https://doi.org/10.3389/fmicb.2016.00314>
- Chou C-W, Seagren EA, Aydilek AH, Lai M. Biocalcification of sand through ureolysis. *Journal of Geotechnical and Geoenvironmental Engineering*. 2011;137(12):1179-89. [https://doi.org/10.1061/\(ASCE\)GT.1943-5606.0000532](https://doi.org/10.1061/(ASCE)GT.1943-5606.0000532)
- Chae SH, Chung H, Nam K. Evaluation of microbially Induced calcite precipitation (MICP) methods on different soil types for wind erosion control. *Environmental Engineering Research*. 2021;26(1). <https://doi.org/10.4491/eer.2019.507>
- Hemayati M, Nikooee E, Habibagahi G, Niazi A, Afzali SF. New non-ureolytic heterotrophic microbial induced carbonate precipitation for suppression of sand dune wind erosion. *Scientific Reports*. 2023;13(1):5845. <https://doi.org/10.1038/s41598-023-33070-w>
- Abdraham MA, El Naggar MH. Axial performance of micropile groups in cohesionless soil from full-scale tests. *Canadian Geotechnical Journal*. 2020;57(7):1006-24. 10.1139/cgj-2018-0695
- Chandiwala A, Vasanwala S. Experimental study of lateral loading on piled raft foundations on sandy soil. *International Journal of Engineering, Transactions A: Basics*. 2023;36(1):28-34. 10.5829/ije.2023.36.01a.04
- Shahmandi A, Ghazavi M, Barkhordari K, Hashemi M. The Effect of Using Reinforced Granular Blanket and Single Stone Column on Improvement of Sandy Soil: Experimental Study. *International Journal of Engineering, Transactions B: Applications*. 2023;36(8):1532-47. 10.5829/ije.2023.36.08b.13
- Goudar S, Kamatagi A. An experimental evaluation of axial load bearing capacity of belled and straight piles embedded in sand. *International Journal of Engineering, Transactions B: Applications*. 2022;35(8):1599-607. 10.5829/ije.2022.35.08b.16
- Fry M. Cement, carbon dioxide, and the 'necessity' narrative: A case study of Mexico. *Geoforum*. 2013;49:127-38. <https://doi.org/10.1016/j.geoforum.2013.06.003>
- Rebata-Landa V. Microbial activity in sediments: effects on soil behavior: Georgia Institute of Technology; 2007.
- Van Wijngaarden W, Vermolen F, Van Meurs G, Vuik C. Modelling biogrout: a new ground improvement method based on microbial-induced carbonate precipitation. *Transport in porous media*. 2011;87:397-420. 10.1007/s11242-010-9691-8
- Lin H. Microbial modification of soil for ground improvement: Lehigh University; 2016.
- Veludo J, Júlio E, Dias-da-Costa D. Compressive strength of micropile-to-grout connections. *Construction and Building Materials*. 2012;26(1):172-9. <https://doi.org/10.1016/j.conbuildmat.2012.06.003>
- Karami A, Shooshpasha I, Alikhani H. Optimum Bacteria Suspension Volume for Stabilizing Silty Sand Soils by *Sporosarcina pasteurii* Bacteria. *International Journal of Engineering, Transactions A: Basics*. 2022;35(10):1820-9. 10.5829/ije.2022.35.10a.02
- Henze J, Randall DG. Microbial induced calcium carbonate precipitation at elevated pH values (> 11) using *Sporosarcina pasteurii*. *Journal of Environmental Chemical Engineering*. 2018;6(4):5008-13. <https://doi.org/10.1016/j.jece.2018.07.046>
- Peng J, Liu Z. Influence of temperature on microbially induced calcium carbonate precipitation for soil treatment. *PLoS One*. 2019;14(6):e0218396. <https://doi.org/10.1371/journal.pone.0218396>

COPYRIGHTS

©2024 The author(s). This is an open access article distributed under the terms of the Creative Commons Attribution (CC BY 4.0), which permits unrestricted use, distribution, and reproduction in any medium, as long as the original authors and source are cited. No permission is required from the authors or the publishers.

**Persian Abstract****چکیده**

تهیه و تولید سیمان پرتلند، به‌عنوان یکی از پرمصرف‌ترین مواد در صنعت ساختمان، موجب افزایش آلودگی محیط زیست و تشدید خطر گرمایش جهانی شده است. بهسازی زیستی خاک، یک روش کاملاً تجدیدپذیر و سازگار با محیط زیست می‌باشد که در سالیان اخیر مورد توجه پژوهشگران قرار گرفته است. ترسیب کربنات کلسیم ناشی از فرایند زیستی (M.I.C.P) بیشترین سهم تحقیق را برای مسائل بیو-ژئوتکنیکی داشته است. *Sporosarcina Pasteurii*، یک میکروارگانیسم تولیدکننده آنزیم اوره‌آز است که در این پژوهش برای بهسازی زیستی خاک ماسه‌ای مورد استفاده قرار گرفت. در این تحقیق مقایسه چگونگی عملکرد دوغاب زیستی و دوغاب سیمانی، در تزریق به درون و اطراف ریزشمع‌های مسلح‌کننده خاک صورت گرفت. همچنین بهسازی زیستی موضعی و کلی خاک، که تشکیل دهنده یک مقطع مرکب در خاک می‌باشد، مورد پژوهش قرار گرفت. نتایج آزمایش‌ها نشان داد که استفاده از دوغاب زیستی تأثیر بسزایی در افزایش ظرفیت باربری خاک داشت. مسلح کردن خاک با ریزشمع زیستی ظرفیت باربری را بیش از ۹۴ درصد افزایش داد. این افزایش در مورد ریزشمع سیمانی ۱۲۶ درصد بود. همچنین نتایج آزمایش‌ها نشان داد که ظرفیت باربری خاک بهسازی کامل زیستی شده و خاک مسلح به ترتیب ۵۴ و ۱۲۵ درصد افزایش یافت. این تحقیق نشان داد که استفاده از ریزشمع‌های زیستی می‌تواند روش مناسبی برای جایگزینی مسلح سازی خاک با ریزشمع‌های با تزریق دوغاب سیمانی باشد.



Deep Reinforcement Learning with Immersion- and Invariance-based State Observer Control of Wave Energy Converters

H. Mohammadian KhalafAnsara, J. Keighobadi*

Faculty of Mechanical Engineering, University of Tabriz, East Azerbaijan, Iran

PAPER INFO

Paper history:

Received 10 November 2017

Received in revised form 23 December 2017

Accepted 04 January 2018

Keywords:

Wave Energy Converter

Extended State Observer

Immersion- and Invariance-based Control

Deep Reinforcement Learning

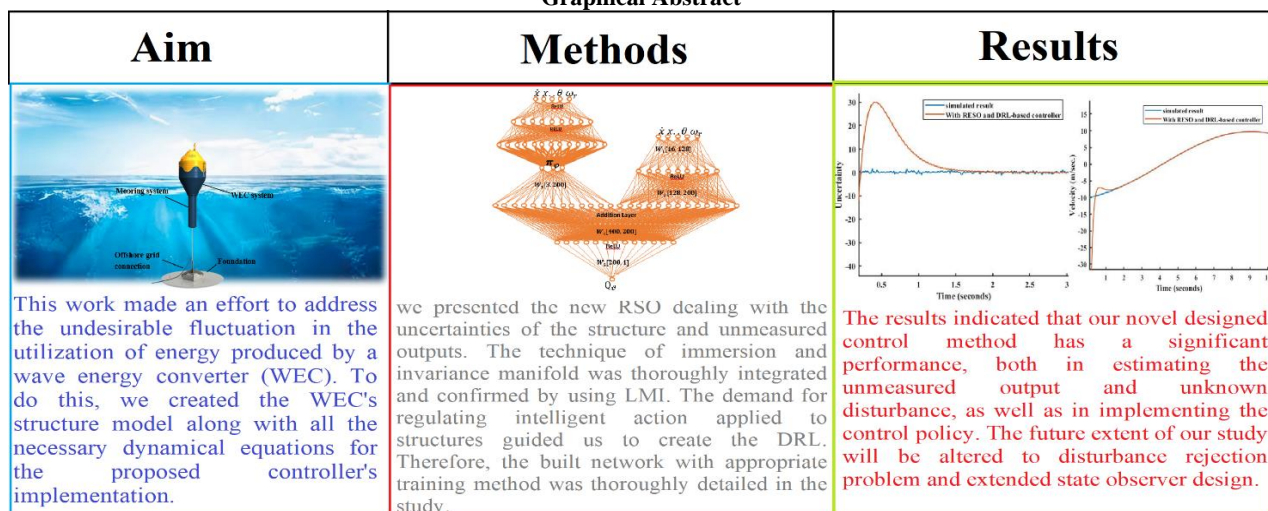
Uniform Energy

ABSTRACT

Composable life under the extensive global warming of the Earth encourages the progress of renewable energy devices and the adoption of new technologies, such as artificial intelligence. Regarding enormous potential of wave energy and its consistency, wave energy converter (WEC) plays vital role in uniform energy harvesting field. In this paper, the significant environmental changes in the ocean prompt us to propose an intelligent feedback control system to mitigate the impact of disturbances and variable wind effects on the efficacy of WECs. Deep reinforcement learning (DRL), as a powerful machine intelligence technique, is capable of identifying WECs as black-box models. Therefore, based on the DRL model, the disturbance and unmeasured state variables are simultaneously estimated in the extended state observer section. Leakage in identification data and real-time application requirements of limited number of layers in the deep neural networks are compensated by implementation of immersion and invariance-based extended state observer which improves coping with the unwanted exogenous noises as well. In the overall intelligent control system, the estimated parameters are inputted into the DRL as the actor-critic networks. The initial actor network is responsible for predicting the control action, while the subsequent critic network determines the decision criterion for evaluating the accuracy of the actor's estimated amount. Next, the output value of the critic stage is backpropagated through the layers to update the network weights. The simulation test results in MATLAB indicate the convergence of unmeasured parameters/states to the corresponding true values and the significance of newly designed intelligent DRL method.

doi: 10.5829/ije.2024.37.06.c.05

Graphical Abstract



*Corresponding Author Email: keighobadi@tabrizu.ac.ir (J. Keighobadi)

Please cite this article as: Mohammadian KhalafAnsara H, Keighobadi J. Deep Reinforcement Learning with Immersion- and Invariance-based State Observer Control of Wave Energy Converters. International Journal of Engineering, Transactions C: Aspects. 2024;37(06):1085-97.

NOMENCLATURE

WEC	Wave energy converter	ESO	Extended state observer
DRL	Deep reinforcement learning	RSO	reduced state observer
BEM	Boundary element method	m_s	mass of the buoy(kg)
MPC	Model predictive control	z_w	water level(m)
DOF	Degree of freedom	f_s	lateral restoring force(N)
ADRC	Adaptive disturbance rejection control	ρ	water's density(kg/m ³)
g	gravity acceleration(m/s ²)	f_r	radiation force(N)
A	cross-section of the float(m ²)	m_e	extra mass(kg)
z_v	heave motion of the float(m)	h_r	core of the radiation force
w	unknown disturbance	PTO	power take-off

1. INTRODUCTION

Global warming, a major consequence of the increasing use of fossil fuels, has led to a growing tendency among people to seek benefits from renewable energy sources. Accordingly, offshore energy converter devices such as wind turbines and WECs are developed to generate consistent energy for everyday needs. In this paper, we propose an artificial intelligence algorithm in the form of a closed-loop control system for the WEC plant to mitigate obstacles to achieving uniform clean energy production. As a means of reducing test platform costs, it is recommended to employ dynamic modeling of the WEC and simulate it along with the proposed control algorithms. The boundary element method (BEM) employs a linear potential theory, assuming small displacements of the structure relative to the wavelength in the presence of non-rotational flows. Hence, the performance of BEM solutions in stormy seas is restricted (1). The theoretical maximum energy has been determined to be roughly 3.1013 kWh/year, which is equivalent to almost 20% of the total-energy consumption in 2019. But the usable resource is roughly ten times smaller due to technical and budgetary restrictions. WECs convert wave energy into electrical current. While there have been efforts to generalize wave power as a regularly used source since 1890, it is not currently being widely utilized. Around 16 MW of operational wave power were globally generated in 2020, which is approximately five times less than about 2 TW, required to fully reach of the world's wave energy potential. One important aspect is the production costs per kWh, which in 2020 were approximately 10 times higher than those of offshore wind projects.

In the last three decades, various ways for conversion of wave power have been created, resulting in hundreds of patents in recent years. Diversity of wave energy ideas are now being explored by industry and academic research organizations all across the globe. Despite the fact that various operational designs have been built and validated, only a few concepts have incorporated modeling and wave tank testing into the sea.

Wave energy is still a crucial source of clean and renewable energy, even though it won't likely ever correspond with the global power output of wind and solar energy. Wave energy has the ability to deliver the electricity in hard-to-reach locations like coastal communities and remote islands that today depend on expensive, carbon-intensive diesel imports as it is more predictable and stable than solar / wind energy. Also, military tasks that need access to deeper seas, offshore fishing, and marine research may all be powered by wave energy devices. Waves in the US provide nearly 80% of the energy required by the country. The industry may access part of that energy, albeit not all of it, to make it simpler for the country to move to 100% clean energy. WECs, also known as point absorbers, are buoy-style devices that collect wave energy from all directions. They are positioned at or near the surface of the ocean. Wave energy is captured by a vertically submerged buoy and then converted into power by a piston or linear generator. Among numerous research studies in the field of control for WECs, Nielsen et al. proposed a model predictive control (MPC) approach to demonstrate its superiority in terms of collecting up to 25% more energy compared to conventional reactive controllers. These reactive controllers take into account the power losses during the conversion from mechanical to electrical energy (2). Also, the authors showed the hydrodynamic and economic performance of an oscillating wave surge energy converter is significantly influenced by the installation depth and height of the incident wave (3). In (4), the authors introduced a novel configuration for a linear permanent magnet Vernier machine, specifically tailored for harnessing wave energy and enhancing the operational efficiency of the existing Vernier machine prototype. Bayani et al. presented an overview of an offshore point-absorber WEC developed by the Hydrodynamics, Acoustics and Marine Propulsion Group at Babol Noshirvani University of Technology (5). Alizadeh Kharkehi et al. assessed the effectiveness of dimensionless coefficients in multi-reservoirs within a hydrodynamic oscillating column converter for sea water waves. The experiment, which took place in Mazandaran, involved extracting

parameters that influence the system's behavior in order to conduct a hydrodynamic analysis of the oscillating water column (6). Son and Yeung conducted experimental tests to validate the nonlinear MPC using a solid-state electrical relay with pulse-width modulation to simulate analog current flow (7). Korde explored the sub-optimal time-domain responsive control of WECs and contrasted the increased reactive energy consumption for the submerged buoy (8). Anderlini et al. gave the wave altitude, wave energy span, and the power take-off damping as an input data to the artificial neural network to assess the lack of confidence in linear model (9). Latching control for heave motion of wave converter was developed to extremize the motion's measurement irrespective of the wave's frequency (10). Wu et al. devised the simultaneous latching control for the single Duck WEC in unbalanced waves to increase the act of structure in sea conditions distant from the normal frequency (11). Using MPC, Faedo et al. examined several methods of implementing a latching control system in the context of WEC (12). Upper limit value for wave excitation force was determined using Kalman filter to monitor energy absorption with 90% of the ideal constrained optimal collected energy (13). Using limited MPC, O'Sullivan and Lightbody produced the large quantity of absorbed electrical power from the point absorber WEC working in heave mode independently, linked to a linear permanent magnet generator (14). Also, Li et al. developed the multilayer perceptron using the deep neural network's techniques to anticipate the temporary wave forces and transferred the output of network via MPC strategy to conduct online latching control action to a point absorber WEC (15). For maximum power extraction, a robust MPC using Laguerre polynomials was developed to alleviate the computational burden (16). A heave-pitch-surge 3-DOF WEC, with the pitch-surge optimization separated from heave, increased the gathered energy by more than three times compared to the captured energy from the lurch-only WEC (17). Investigation of blocked optimum control on a small asymmetrical float indicated that, despite the improvement in power capture achievable with the current control, the actuation forces are significant (18). Moreover, Burgaç and Yavuz implemented the discrete Fourier transform technique to estimate the dominant wave frequency in the fuzzy controller for defining the power take-off control settings (19). Zhan et al. (20) proposed a categorized adaptive optimum control framework for WECs to enhance energy conversion efficiency and reduce the modeling effort required for control design.

The newly built controller in this study was not adequately evaluated in the field of WEC and requires further investigation. The following summarizes the most crucial related works to our newly proposed

controller. In (21), Han J introduced an active disturbance rejection control that combines an error-driven control rule, state observer feature, and the power of a nonlinear controller. Zhejiang Gao proved that by unifying the controller and addressing the issue of disturbance rejection, the performance of traditional controllers when faced with disturbances is improved. The proposal of the paper was to improve the developed controller for the official model, with the aim of rejecting disturbances in the plant model (22). Zhao and Guo introduced the novel ADRC, which has the capacity to track reference signals, reject disturbances, and maintain closed-loop stability for a group of single-input single-output systems (23). Also, Feng and Guo have researched the output feedback stability for indefinite structures described by partial differential equations (24). Hosseini and Keighobadi developed an extended state observer-based robust active control to approximate both the speed and perturbation trajectories of the gyro's dynamics using the location signs (25). In (26), Guo and Zhao sought to demonstrate the stability issue of an extended state observer by utilizing the error equation. They aimed to decrease the influence of the disturbance by implementing a high-gain approach. Li et al. (27) presented the necessary conditions for the convergence of the quantized nonlinear extensible state observer using linear matrix inequality. Zhao and Guo developed a temporally varying gain ESO to reduce the peaking effect near the main time caused by the constant high gain technique (28).

In this research work, to obtain a nearly compatible model with real plant, the development of the overall dynamics of a WEC with detailed consideration of acting forces on the structure is explained. Next, the paper proposes a new estimation technique for the disturbance and unmeasured parameters of WEC, specifically the immersion and invariance-based extended state observer. Through mapping of considered observer manifold, the unmeasured variables are estimated and are fed as input to the intelligent controller presumed DRL, which consists of two networks named actor-critic. The output of the actor network is the input of the main plant. The Q_value , which represents the output of the critic network, is used to update the weights and biases of the networks using the backpropagation method. To prove the convergence of the control system, the direct stability method of the Lyapunov is assessed. The results of the controller are evaluated for the reduced state observer (RSO) as well. The RSO focuses on estimating unmeasured states and accounting for exogenous inputs. The simulation is conducted to design a linear observer for these unmeasured variables. The wide range simulation results are assessed with the noisy data to guarantee the strength and robustness of the suggested controller.

2. MATERIAL AND METHODS

In this paper, the software simulation of WEC is conducted using the point absorber model to demonstrate the effectiveness of the proposed control system. To achieve this, we assume the nominal second-order model of the WEC, considering all acting forces, in order to obtain an accurate model. The model contains an immersed object with a cylinder on the surface of the sea. Wave energy is gathered through the use of a power take-off system.

2. 1. State Space Model of WEC The state space calculations of the proposed system include forces, where \mathbf{z}_w represents the water level and \mathbf{z}_v represents the heave movement of the middle point of the float. The power generated by the generator is proportional to the force \mathbf{f}_u applied to the piston. Therefore, the obtained power will be equal to $\mathbf{P} = \mathbf{f}_u \mathbf{v}$, with the value of $\mathbf{v} = \dot{\mathbf{z}}_v$. By applying Newton's second law, the dynamics of the system can be determined:

$$m_s \ddot{z}_v = -f_s - f_r + f_e + f_u \quad (1)$$

where m_s represents the mass of the buoy. The following describes the definition of the forces present in Equation 1.

f_s is the lateral restoring force.

$$f_s = \rho g A z_v \quad (2)$$

In the given equation, ρ stands for the density of water, g represents the acceleration due to gravity, A shows the cross-section of the float, and z_v is the heave motion of the float.

The radiation force f_r is obtained as follows.

$$f_r = m_\infty \ddot{z}_v + \int_{-\infty}^{\infty} h_r(\tau) \dot{z}_v(t-\tau) d\tau \quad (3)$$

where m_∞ indicates the additional mass and h_r represents the core of the radiation force. Using a finite-dimensional state-space model, the convolutional term in the force value is estimated as follows.

$$\begin{aligned} \dot{x}_r &= A_r x_r + B_r \dot{z}_r \\ f_r &= C_r x_r \approx \int_{-\infty}^t h_r(\tau) \dot{z}_v(t-\tau) d\tau \end{aligned} \quad (4)$$

Now, considering the equivalent state-space representation $D_r \sim (A_r, B_r, C_r, 0)$ leads to the $f_r \approx D_r(s) \dot{z}_v$.

Exterior perturbation force acting on the float is determined as $f_e = D_e(s) z_w$, where D_e is the equivalent representation of the following realization:

$$\begin{aligned} \dot{x}_e &= A_e x_e + B_e z_w \\ f_e &= C_e x_e \approx \int_{-\infty}^t h_e(\tau) z_w(t-\tau) d\tau \end{aligned} \quad (5)$$

By applying the force amounts, the state-space model of WEC is derived.

$$\begin{aligned} \dot{x} &= A_c x + B_{uc} u + B_{wc} w \\ z &= C_z x \end{aligned} \quad (6)$$

where $w = z_w$, $z = z_v$. $y = \dot{z}_v$, $x = [z_v, \dot{z}_v]^T$ and

$$A_c = \begin{bmatrix} 0 & 1 \\ -\frac{k_s}{m} & -\frac{D_r(\delta_r)}{m} \end{bmatrix}, B_{uc} = \begin{bmatrix} 0 \\ \frac{D_e(\delta_e)}{m} \end{bmatrix}, B_{wc} = \begin{bmatrix} 0 \\ \frac{1}{m} \end{bmatrix}, C_z = [1 \ 0] \quad (7)$$

The value of m is $m_a + m_\infty$. Additionally, the dynamics of the radiation and excitation forces include structure uncertainties, represented by δ_r and δ_e , respectively. The state space form of a dynamic model is commonly referred to as:

$$\begin{aligned} \dot{x}_1 &= x_2 \\ \dot{x}_2 &= -\frac{k_s}{m} x_1 + \frac{1}{m} u - \frac{D_r}{m} x_2 + \frac{D_e}{m} w \end{aligned} \quad (8)$$

Therefore, we will estimate the amount of x_2 as unmeasured output and the quantity of w as an unknown disturbance value. The viscosity force, assuming the negligible velocity of WEC compared to the wave velocity, only includes constant terms that refer to $D_e(\delta_e)$ as an uncertainty term. The characteristics of the sea required for the training of DRL were discussed in Section 3. Moreover, Table 1 includes a detailed table about this process and some training data.

2. 2. Implementation of the Control System

Suppose an n-dimensional lower-triangular nonlinear system with definition as follows (25).

$$\dot{\xi}_i(t) = \xi_{i+1}(t) + f_i(\xi_1(t), \dots, \xi_i(t), u(t)), \quad i = 1 : n-1, \quad (9)$$

where, $\xi_i \in \mathbb{R}$ denotes the state variables belonging to a compact set Ω , $u \in \mathcal{C}^1(\mathbb{R}_{\geq 0}, \mathbb{R})$ shows the input with an upper bound namely u_0 , $w \in \mathcal{C}^1(\mathbb{R}_{\geq 0}, \mathbb{R})$ demonstrates the unknown disturbance with an upper bound of w_1 , $f_i \in \mathcal{C}^0(\mathbb{R}^{i+1}, \mathbb{R})$ are defining parts of the system that are locally Lipschitz, and $g \in \mathcal{C}^0(\mathbb{R}^{n+1}, \mathbb{R})$ stands for the uncertainty section.

TABLE 1. Target sea characteristic data

Wave height	Wave period	Wavelength
0.024	0.870	1.186
0.030	1.008	1.581
0.036	1.178	2.109
0.032	1.217	2.231
0.030	1.260	2.367
0.022	1.385	2.761
0.018	1.510	3.152

We define the measurable output as y , and the other trajectories and disturbances go into the aggregated variable vector x . Therefore, the following representation of overall system is expressed.

$$\begin{aligned} y &= \xi_i \\ x_i &= \xi_{i+1}, \quad i = 1 : n-1 \\ x_n &= g(y, x_1, \dots, x_{n-1}, w) \end{aligned} \quad (10)$$

By introducing the following definition as a new state variables vector:

$$\begin{aligned} \bar{x}_i &= [x_1, \dots, x_i]^T \in \mathbb{R}^i, \quad i = 1 : n \\ x &= \bar{x}_n \in \mathbb{R}^n \end{aligned} \quad (11)$$

Equation 9 is transferred as:

$$\begin{aligned} \dot{y}(t) &= Cx(t) + f_1(y(t), u(t)) \\ \dot{x}(t) &= Ax(t) + \sum_{i=1}^{n-1} B_i f_{i+1}(y(t), \bar{x}_i(t), u(t)) \\ &+ B_n h(y(t), x(t), u(t), w(t), \dot{w}(t)) \end{aligned} \quad (12)$$

$$A = \begin{bmatrix} 0 & 1 & 0 & \dots & 0 \\ 0 & 0 & 1 & \dots & 0 \\ \vdots & \vdots & \vdots & \ddots & \vdots \\ 0 & 0 & 0 & \dots & 1 \\ 0 & 0 & 0 & \dots & 0 \end{bmatrix} \in \mathbb{R}^{n \times n}, \quad B_i = [\delta_{1i}, \dots, \delta_{in}]^T \in \mathbb{R}^{n \times 1}, \quad C = [1 \ 0 \ \dots \ 0] \in \mathbb{R}^{1 \times n}, \quad i = 1 : n$$

$$\begin{aligned} h(y, x, u, w, \dot{w}) &= \frac{\partial g(y, \bar{x}_{n-1}, w)}{\partial y} (x_1 + f_1(y, u)) + \\ &\sum_{i=1}^{n-1} \frac{\partial g(y, \bar{x}_{n-1}, w)}{\partial x_i} (x_{i+1} + f_{i+1}(y(t), \bar{x}_i(t), u(t))) \\ &+ \frac{\partial g(y, \bar{x}_{n-1}, w)}{\partial w} \dot{w} \end{aligned} \quad (13)$$

Along with the measurable output as first input to the estimator, the produced control action by the DRL is the second input. Accordingly, the proposed estimator gives the unmeasurable part of the output vector, the matched uncertainty and disturbance values as well. In this regard, the dynamical system is defined as:

$$\dot{\xi} = \alpha(\xi, y, u, t) \quad (14)$$

where ξ belongs to the n -dimensional space and α is a continuous function from the $(n+3)$ -dimensional space to the n -dimensional kind.

If there exists the left-invertible mapping ϕ_1 then the system of Equation 14 is called a reduced order observer with the following manifold:

$$M_1 = \{(y, x, \xi, u, t) \in \mathbb{R}^{2n+3} \mid \phi_1(x, y, u, t) = \beta_1(\xi, y, u, t)\} \quad (15)$$

Therefore, the reduced order ESO is paraphrased as the dynamical system of Equation 14 along with manifold introduced by Equation 15. Now, imagine the mapping ϕ_1 is of the form:

$$\phi_1(x, y, u, t) = x + \psi_1(y, u, t) \quad (16)$$

Considering this case, the defined manifold is replaced by:

$$M_1 = \{(y, x, \xi, u, t) \in \mathbb{R}^{2n+3} \mid x + \psi_1(y, u, t) = \beta_1(\xi, y, u, t)\} \quad (17)$$

In the equality of the set in Equation 17, by replacing the function as estimation of x :

$$\eta_1(\xi, y, u, t) = \beta_1(\xi, y, u, t) - \psi_1(y, u, t) \quad (18)$$

By assuming a manifold coordinate of Equation 7 to describe the distance of the routes of systems in Equations 13 and 14:

$$z = x - \eta_1(\xi, y, u, t) \quad (19)$$

Considering the $\eta_1(\xi, y, u, t)$ as \hat{x} , the difference between x and \hat{x} is obtained as error estimation of the state variable. The derivative of the Equation 19 and the substitution of corresponding parameters in Equation 13 lead to:

$$\begin{aligned} \dot{z}(t) &= \left(A - \frac{\partial \eta_1}{\partial y} C\right) z(t) + \left(A - \frac{\partial \eta_1}{\partial y} C\right) \eta_1(\xi(t), y(t), u(t), t) \\ &+ \sum_{i=1}^{n-1} B_i f_{i+1}(y(t), \bar{x}_i(t), u(t)) + \\ &B_n h(y(t), x(t), u(t), w(t), \dot{w}(t)) \\ &- \frac{\partial \eta_1}{\partial y} f_1(y(t), u(t)) - \frac{\partial \eta_1}{\partial u} \dot{u}(t) - \frac{\partial \eta_1}{\partial t} \\ &\frac{\partial \eta_1}{\partial \xi} \alpha(\xi(t), y(t), u(t), t) \end{aligned} \quad (20)$$

If $\frac{\partial \eta_1}{\partial \xi}$ doesn't have the zero determinant, we introduce the expression for α to simplify Equation 20:

$$\begin{aligned} \alpha(\xi, y, u, t) &= \left(\frac{\partial \eta_1}{\partial \xi}\right)^{-1} \left(\left(A - \frac{\partial \eta_1}{\partial y} C\right) \eta_1(\xi, y, u, t) + \sum_{i=1}^{n-1} B_i f_{i+1}(y, \hat{x}_i, u) \right) + \\ &\left(\frac{\partial \eta_1}{\partial \xi}\right)^{-1} \left(-\frac{\partial \eta_1}{\partial y} f_1(y, u) - \frac{\partial \eta_1}{\partial u} \dot{u} - \frac{\partial \eta_1}{\partial t} \right) \end{aligned} \quad (21)$$

where \hat{x} is defined as component-wise based on \hat{x} . Consequently, the system of Equation 20 is reduced as 25:

$$\begin{aligned} \dot{z}(t) &= \left(A - \frac{\partial \eta_1}{\partial y} C\right) z(t) + \\ &\sum_{i=1}^{n-1} B_i \left(f_{i+1}(y(t), \bar{x}_i(t), u(t)) - \right. \\ &\left. f_{i+1}(y(t), \hat{x}_i(t), u(t)) \right) + \\ &B_n h(y(t), x(t), u(t), w(t), \dot{w}(t)) \end{aligned} \quad (22)$$

The matrix inequality of Equation 22 to be stable is as follows:

$$P_1 \left(A - \frac{\partial \eta_1}{\partial y} C \right) + \left(A - \frac{\partial \eta_1}{\partial y} C \right)^T P_1 + \frac{2}{\epsilon} P_1 \leq 0 \quad (23)$$

Theorem 1. Considering the prolonged system of Equation 13, the system of Equation 14 with given dynamics in Equation 21 is a reduced order ESO and the corresponding state estimation is obtained as $\hat{x} = \eta_1(\xi, y, u, t)$.

Proof. We present the following Lyapunov function as:

$$V_1(z) = z^T P_1 z \tag{24}$$

Taking the time derivative of Equation 24 and using the equivalent amounts of Equations 22 and 23 gives:

$$\begin{aligned} \dot{V}_1(z(t)) \leq & -\frac{2}{\epsilon_1} V_1(z(t)) + \\ & 2z^T(t) \sum_{i=1}^{n-1} P_1 B_i \left(f_{i+1}(y(t), \hat{x}_i(t), u(t)) - \right. \\ & \left. f_{i+1}(y(t), \hat{x}_i(t), u(t)) \right) + \\ & 2z^T(t) P_1 B_n h(y(t), x(t), u(t), w(t), \dot{w}(t)) \end{aligned} \tag{25}$$

Assuming $h(\cdot)$ is restricted to an upper bound as:

$$|h(y, x, u, w, \dot{w})| \leq h_0 \tag{26}$$

Locally Lipschitz assumption of f with l_{fi} multiplier gives 21:

$$f_i(y, \hat{x}_{i-1}, u) - f_i(y, \hat{x}_{i-1}, u) \leq l_{fi} z, \quad i = 2:n \tag{27}$$

Now, the inequality (25) is rewritten as:

$$\begin{aligned} \dot{V}_1(z(t)) \leq & -\left(\frac{2}{\epsilon_1} - 2l_f \frac{\lambda_{\max}(P_1)}{\lambda_{\min}(P_1)}\right) V_1(z(t)) + \\ & 2h_0 \frac{\lambda_{\max}(P_1)}{\sqrt{\lambda_{\min}(P_1)}} \sqrt{V_1(z(t))} \end{aligned} \tag{28}$$

To complete the proof, the Λ_r -attractivity of the manifold \mathcal{M}_1 is explained as follows.

Λ_r -attractivity: For each $t_0 \in \mathbb{R}_{\geq 0}$, r_0 is available such that if $z(t_0) \in \Lambda_{r_0}$, then $z(t)$ is bounded for all $t \geq t_0$ and moreover, the positive r_1 and its finite reaching time are as $t_r = t_r(r_0, r_1)$, in this sense $z(t) \in \Lambda_{r_1}$ for all $t \geq t_0 + t_r$.

Now, assuming:

$$\epsilon_1 < \epsilon'_1 = \frac{\lambda_{\min}(P_1)}{l_f \lambda_{\max}(P_1)} \tag{29}$$

Application of the comparison lemma on 28 yields in:

$$\begin{aligned} z(t) \leq & \sqrt{\frac{\lambda_{\max}(P_1)}{\lambda_{\min}(P_1)}} \left(z(t_0) - \sqrt{\frac{\lambda_{\max}(P_1)}{\lambda_{\min}(P_1)}} \lambda(\epsilon_1) h_0 \right) \\ & \times \exp\left(-\frac{t-t_0}{\lambda(\epsilon_1)} + \frac{\lambda_{\max}(P_1)}{\lambda_{\min}(P_1)} \lambda(\epsilon_1) h_0\right) \end{aligned} \tag{30}$$

$$\lambda(\epsilon_1) = \frac{1}{1 - \frac{1}{\epsilon_1}} \tag{31}$$

The inequality 30 implies that the trajectories starting in Λ_{r_0} stay bounded. Furthermore, the reaching time is of the form:

$$t_r = \lambda(\epsilon_1) \ln \left(\frac{1}{r_2} \sqrt{\frac{\lambda_{\max}(P_1)}{\lambda_{\min}(P_1)}} \left(z(t_0) - \sqrt{\frac{\lambda_{\max}(P_1)}{\lambda_{\min}(P_1)}} \lambda(\epsilon_1) h_0 \right) \right) \tag{32}$$

With the positive scalars $r_2 < r_1 < r_0$ gives:

$$\epsilon_1 < \frac{r_1 - r_2}{h_0 \frac{\lambda_{\max}(P_1)}{\lambda_{\min}(P_1)} + \frac{r_1 - r_2}{r_1}} \tag{33}$$

Noting that $\epsilon''_1 < \epsilon'_1$, and Equation 33 holds for the selected parameters, then the manifold \mathcal{M}_1 is Λ_r -attractive for any $r_1 < r_0$. So, the system of Equation 14 with defined dynamics of Equation 21 is a reduced order ESO. ■

Corollary 1. If Theorem 1 satisfied, so $\lim_{\substack{t \rightarrow \infty \\ (\epsilon_1 \rightarrow 0)}} z(t) = 0$.

Proof. Taking the supremum of Equation 30 leads to:

$$\lim_{t \rightarrow \infty} z(t) \leq \frac{\lambda_{\max}(P_1)}{\lambda_{\min}(P_1)} \lambda(\epsilon_1) h_0 \tag{34}$$

Since $\lim_{\epsilon_1 \rightarrow 0} \lambda(\epsilon_1) = O(\epsilon_1)$, the ultimate bound of $\|z(t)\|$ approaches to zero as $\epsilon_1 \rightarrow 0$. ■

Convergence analysis via LMIs

Considering the i^{th} component of $\frac{\partial \eta}{\partial v}$ as a_i :

$$\begin{aligned} a_i(t) &= a_i^0 + a_i^1 \theta_i(t), \\ a_i^{min} &\leq a_i(t) \leq a_i^{max}, \\ a_i^0 &= (a_i^{max} + a_i^{min})/2, \\ a_i^1 &= (a_i^{max} - a_i^{min})/2 \\ |\theta_i(t)| &\leq 1 \end{aligned} \tag{35}$$

Based on Equation 35, we obtain the following representation of coefficient of $z(t)$ in Equation 22,

$$A - \frac{\partial \eta}{\partial v}(t)C = A_0 + A_1 \theta(t)A_2 \tag{36}$$

With the assumptions:

$$\begin{aligned} A_0 &= \begin{bmatrix} -a_1^0 & 1 & 0 & \dots & 0 \\ -a_2^0 & 0 & 1 & \dots & 0 \\ \vdots & \vdots & \vdots & \ddots & \vdots \\ -a_{n-1}^0 & 0 & 0 & \dots & 1 \\ -a_n^0 & 0 & 0 & \dots & 0 \end{bmatrix} \in \mathbb{R}^{n \times n}, \\ A_1 &= [A_{11}, \dots, A_{1n}], \quad A_{1j} = \begin{bmatrix} -a_1^1 \delta_{1j} & 0 & 0 \dots 0 \\ -a_2^1 \delta_{2j} & 0 & 0 \dots 0 \\ \vdots & \vdots & \vdots \dots \vdots \\ -a_{n-1}^1 \delta_{(n-1)j} & 0 & 0 \dots 0 \\ -a_n^1 \delta_{nj} & 0 & 0 \dots 0 \end{bmatrix} \in \mathbb{R}^{n \times n} \end{aligned} \tag{37}$$

$$\Theta(t) = \text{diag}(\Theta_j(t))_{j=1}^n, \quad \Theta_j(t) = \theta_j(t) \in \mathbb{R}^{n \times n},$$

$$A_2 = [A_{21}, \dots, A_{2n}]^T,$$

$$A_{2j} = \begin{bmatrix} 1 & 0 & 0 \dots 0 \\ 0 & 0 & 0 \dots 0 \\ \vdots & \vdots & \vdots \dots \vdots \\ 0 & 0 & 0 \dots 0 \\ 0 & 0 & 0 \dots 0 \end{bmatrix} \in \mathbb{R}^{n \times n}$$

Theorem 2. Suppose that Equation 37 is valid for the components of $\frac{\partial \eta}{\partial v}$ and the matrix P is available as following:

$$\begin{bmatrix} PA_0 + A_0^T P + \frac{2}{\circ} P & PA_1 & A_2^T \\ A_1^T P & -I & 0 \\ A_2 & 0 & -I \end{bmatrix} \leq 0 \quad (38)$$

Then, Equation 23 holds with positive $\epsilon_1 = \epsilon$ and matrix P .

Proof. Considering Equation 36, the inequality 23 is written as:

$$P(A_0 + A_1\Theta(t)A_2) + (A_0 + A_1\Theta(t)A_2)^T P + \frac{2}{\circ} P \leq 0 \quad (39)$$

According to Young's inequality together with constraint $\Theta^T(t)\Theta(t) \leq I$,

$$PA_1\Theta(t)A_2 + A_2^T\Theta^T(t)A_1^T P \leq \frac{1}{\mu} PA_1A_1^T P + \mu A_2^T A_2 \quad (40)$$

where μ is a positive constant. The inequality 40 satisfies if the following is true.

$$PA_0 + A_0^T P + \frac{2}{\circ} P + \frac{1}{\mu} PA_1A_1^T P + \mu A_2^T A_2 \leq 0 \quad (41)$$

Therefore, inequality 41 is equivalent to the viability of LMI 38 for a non-negative P . ■

Assuming fixed values of $\frac{\partial \eta}{\partial v}$ as k_i :

$$\frac{\partial \eta^{(i)}}{\partial v} = k_i, \quad i=1,2,\dots,n \quad (42)$$

where $\eta^{(i)}$ stands for the i^{th} component of η . Therefore, η is written as:

$$\eta^{(i)}(\xi, v) = k_i v + \varpi_i(\xi) \quad (43)$$

where the functions $\varpi_i(\xi)$ satisfy the condition of non-zero determinant of $\frac{\partial \eta^{(i)}}{\partial v}$. The fixed $\frac{\partial \eta^{(i)}}{\partial v}$ reduces LMI 38 to:

$$PA_0 + A_0^T P + \frac{2}{\circ} P \leq 0 \quad (44)$$

Now, using the generalized eigenvalue solvers, the solution of P is obtained.

3. NUMERICAL RESULTS

The Simulink diagram of the designed control model in MATLAB is illustrated in Figure 1. The figure shows that the first step is to simulate the system in order to

calculate the outputs. Then, the measured output along with the assigned value for input are fed to the observer block to estimate the unmeasured output and the unknown disturbances. Besides, our main block including the DRL controller will suggest the action u and it tries to reach the optimal input action along with correct estimation of the mentioned parameters with use of the immersion- and invariance-based extended state observer. The implemented DRL has the structure as shown in Figure 2. In this figure, the actor and critic networks are stacked in a row. The lagged version of two main networks is not shown but they are necessary to avoid the divergence during the updating process step. The pseudo code of the DRL as clarification is brought in Table 2. The output function for getting the optimal control action is described as:

$$y_j = \begin{cases} r_j & \text{terminates at step } j+1 \\ r_j + \gamma \max_{a'} Q_{g'}(s_{j+1}, a; g') & \text{otherwise} \end{cases} \quad (45)$$

where, the $Q_{g'}$ stands for the lagged version of the main critic network, γ is the coefficient and r_j indicates the cumulative reward during processing time. DRL, in every sea state based on the environment's observed conditions, learns the required optimal force on the piston of PTO to capture the uniform energy, i.e., the structure faces the waves instead of internal models. At each processing time, the control system determines a change in the action, which is carried out by the hydraulic PTO unit as the agent. Through accumulating rewards as the function of the produced electrical power and in an alteration of environment's state, where the state is indicated by the substantial wave altitude, H_s , the average zero-crossing span, T , and the PTO damping factor. For the oscillatory essence of sobriety waves, it is essential to average the captured power in the reward function over a horizon, H , in one wave cycle during which the state s_n and action a_{n-1} are fixed. Next, a new action a_n is designated in an instant modification of state to s_{n+1} and a new mean progression. The process of DRL is described in detail as follows.

State Space: As noted before, the circumstances variables are supposed to be the effective wave height, average zero-crossing span, and PTO damping multiplier so that the assumed RL state space is:

$$S = \left\{ s \mid s_{j,k,l} = H_{s,j} + T_{z,k} + B_{PTO,l} \begin{matrix} j=1:J, \\ k=1:K, \\ l=1:L \end{matrix} \right\} \quad (46)$$

Action Space: The action series consists of three amounts based on the selected state space as following:

$$A = \{a \mid (-B_{PTO}, 0, +B_{PTO})\} \quad (47)$$

where $\Delta B_{PTO} = B_{PTO,k+1} - B_{PTO,k}$. Equivalent states to

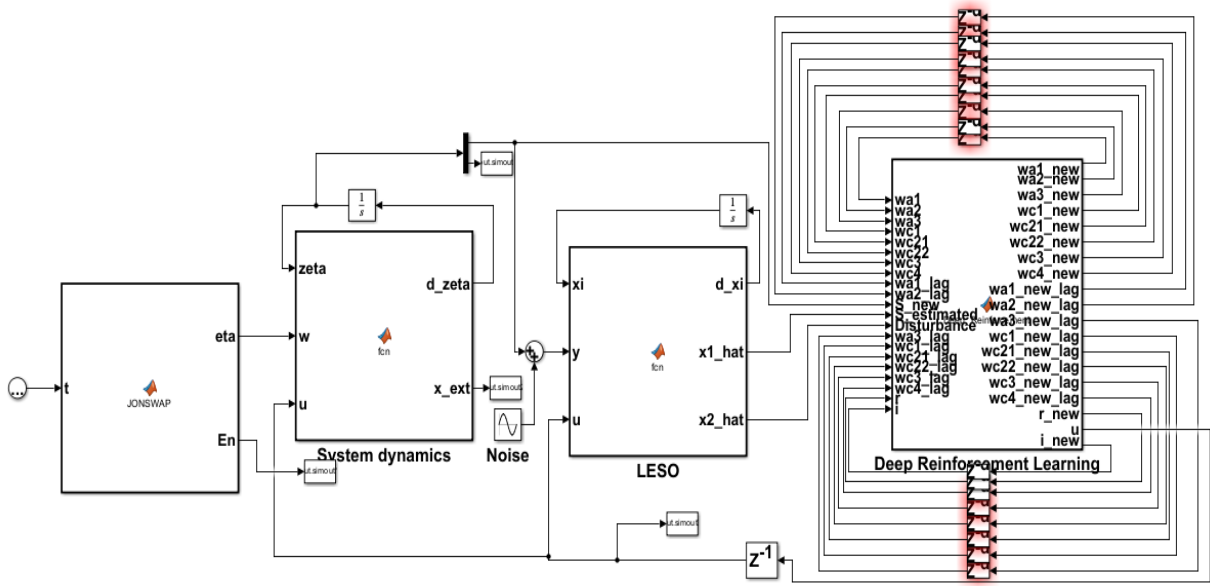


Figure 1. Block diagram of the entire observer and controller in MATLAB

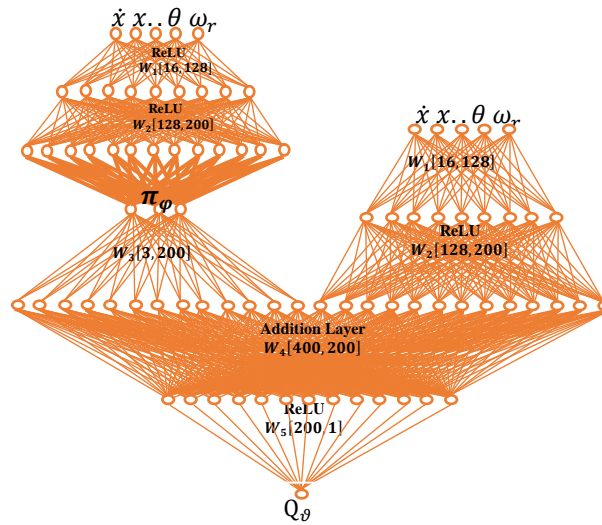


Figure 2. Stacked critic-actor network in DRL (29)

the extreme damping constants, i.e., $B_{PTO,1}$ and $B_{PTO,L}$, have some actions so as to preclude the controller from surpassing the boundary of state space. For example, for $B_{PTO,1}$ case, the candidate $+\Delta B_{PTO}$ is left out.

Reward: In DRL field, the aim to propose a reward function is to optimize the performance of the agent through negative reward for incorrect action or positive for correct one, and the reward function is maximized at the end of processing time. Hence, for the I&I RSO control system of WECs, the compensation function is considered to be pertinent to the captured power. The effect of variations in the momentous wave height on the average produced power, P_{avg} , is more than

variations in the PTO restraining constant. Considering the harvested power proportional to the square of the substantial wave elevation, the reward function is well-defined as P_{avg}/H_s^2 to obtain a dimensionless function. Additionally, owing to the stiff quantization of the condition variables and the random environment of periodic waves, the reward function is alleviated by averaging a number M of P_{avg}/H_s^2 values for each state along with the average captured power over a horizon H . Keeping the M recent P_{avg}/H_s^2 quantities for each state in a matrix, R , whose magnitude is as a maximum $n_s \times M$, with $n_s = J \times K \times L$ as the number of states.

TABLE 2. Pseudo code of the training process of the Deep Deterministic Policy Gradient (DDPG) algorithm

Algorithm 1: DDPG algorithm

Randomly initialization of weights ϑ and φ in critic network $\mathbf{Q}_\vartheta(s, a | \vartheta)$ and actor $\pi_\varphi(s | \varphi)$.

Initialization of target lagged network $\mathbf{Q}'_{\vartheta'}$ and $\pi'_{\varphi'}$ with weights $\vartheta' \leftarrow \vartheta, \varphi' \leftarrow \varphi$

Replay buffer R Initialization

for incident = 1. M ensure

Take initial state s_1

for t = 1. T do

Choose action $a_t = \mu(s_t | \theta^\mu)$ based on the current policy

Accomplish action a_t to detect reward r_t and new-fangled state s_{t+1}

Save evolution (s_t, a_t, r_t, s_{t+1}) in R

Sample a spontaneous small group of N transitions (s_i, a_i, r_i, s_{i+1}) from R

Set $y_i = r_i + \gamma \mathbf{Q}'_{\vartheta'}(s'_i, \pi'_{\varphi'}(s'_i))$

Update critic by differentiation of the loss: $L = \frac{1}{N} \sum (\mathbf{Q}_\vartheta(s_i, \mathbf{a}_i) - y_i(s_i, \mathbf{a}_i, r_i, s'_{i+1}))^2$ with respect to weights

Revise the performer procedure employing the sampled policy slope:

$$\nabla_{\varphi} J \approx \frac{1}{N} \sum_i \nabla_a Q(s, a | \vartheta) \Big|_{s=s_i, a=\pi_\varphi} \Big|_{s_i} \nabla_\varphi \pi_\varphi(s | \varphi) \Big|_{s_i}$$

Update the target networks:

$$\begin{aligned} \vartheta'^{(t+1)} &\leftarrow \tau \vartheta + (1 - \tau) \vartheta'^{(t)} \\ \varphi'^{(t+1)} &\leftarrow \tau \varphi + (1 - \tau) \varphi'^{(t)} \end{aligned}$$

end for

end for

Therefore, the average amount in each state is described with the vector $\mathbf{m} = \langle R(s, \mathbf{m}) \rangle_{m=1:(M \text{ vend})}$ of size n_s . The states of the vector \mathbf{m} include the vector-oriented version of Equation 46, such that the discrete quantities of B_{PTO} , H_s and T_z represent the inner-most, middle and outermost loop of vectorization, respectively.

Regarding the values of ΔB_{PTO} , for $B_{PTO} > 0$, there exists a bit of difference between the averages of adjacent damping coefficients of PTO, which yields extreme problems for the confluence of the Q-learning process. Hence, the benefit of desiring the optimum balancing multiplier in piece sea condition is obvious to detour the convergence issues. Assignment of a factor as the power of the values in vector \mathbf{m} deals with the close amounts in the neighboring coefficients. Furthermore, with the mentioned mathematical operation, the excessive memory is required to keep the reward values. Therefore, it is essential from a

mathematical point of view to primarily regularize the quantity of the vector for every individual condition concerning the highest amount for each sea condition. Regarding s_n , we should find the maximum quantity between the indexes $o = \text{floor} \left(\frac{s_n - 1}{L} \right) L + 1$ and $p = \text{floor} \left(\frac{s_n - 1}{L} \right) L + L$ of the vector \mathbf{m} . Also, the power factor, k , is considered an odd digit to maintain the sign of the produced power. The smoother the quantization of PTO balancing value, the superior k is considered to expedite the learning process. On the other hand, very great values for k result in convergence issues especially with noise affected power in irregular wave. Furthermore, selecting the optimum damping value by itself makes the structure destruction i.e., submergence or emergence, if not complete failure. So, the penalty amount should be considered to avoid exceeding the upper bound limitation of translational movement of the structure, Z_{max} . The reward function is defined as following with arbitrary chosen amount the same as $p = -4$ for penalty:

$$r_{n+1} = \begin{cases} \left[\frac{m(s_n)}{\max_{i=o:p} m(i)} \right]^k & \text{if } |\max(z)| \leq z_{\max} \\ -4 & \text{if } |\max(z)| > z_{\max} \end{cases}$$

The system is acting in the presence of wave with the following regular form:

$$\xi = \xi_a \sin(\omega t - kx) \quad (48)$$

We can describe the irregular wave by using the superposition principle consisting of n regular waves with variant amplitude, frequency, and phase. Therefore, the wave elevation ξ_n is given as:

$$\xi(x, t) = \xi_{An} \sin(\omega_n t - k_n x + \epsilon_n) \circ \quad (49)$$

where the value ϵ_n stands for the stochastic phase that its value is distributed between 0 and 2π . If all elevations are summed up, the following shows the total elevation of the proposed wave structure:

$$\xi(x, t) = \sum_{n=1}^N \xi_{An} \sin(\omega_n t - k_n x + \epsilon_n) \circ \quad (50)$$

The sea state is typically described in terms of the wave spectrum $S(\omega)$, which explains information about the wave energy for various frequencies. E_n , the energy in each component is defined as follows.

$$s(\omega_n) \Delta \omega = \frac{E_n}{\rho g} = \frac{1}{2} \xi_{An}^2 \quad (51)$$

Therefore, the value of the amplitude is found:

$$\xi_n = \sqrt{2S(\omega_n) \Delta \omega} \cos(\omega_n t - k_n x + \epsilon_n) \quad (52)$$

A standardized wave spectrum to model the sea states is JONSWAP, which is developed for the North Sea. The formula of this spectrum is:

$$S(\omega) = \frac{\alpha g^2}{\omega^5} e^{-\frac{5}{4} \left(\frac{\omega_p}{\omega}\right)^4} \gamma e^{-\frac{1}{2} \left(\frac{\omega - \omega_p}{\sigma \omega_p}\right)^2} \quad (53)$$

where γ is peak number, σ decides the form of the spectrum in the high frequency part and with assuming T_p as peak frequency. The value of the parameter ω_p is:

$$\omega_p = \frac{2\pi}{T_p} \quad (54)$$

The simulated disturbance and uncertainty assuming JONSWAP spectrum is shown in Figure 3 in which the randomness of the proposed wave spectrum is vivid. The measured output of the system is illustrated as Figure 4 showing the stability of the desired state. With application of the above assumptions, the simulated results in MATLAB are as follows. Through adding the measurement noise, we tried to show the efficacy of the proposed controller. The results of Figure 5 illustrate that only one second takes to achieve the exact value of the unmeasured output and no effect of fluctuation due to the noise is seen.

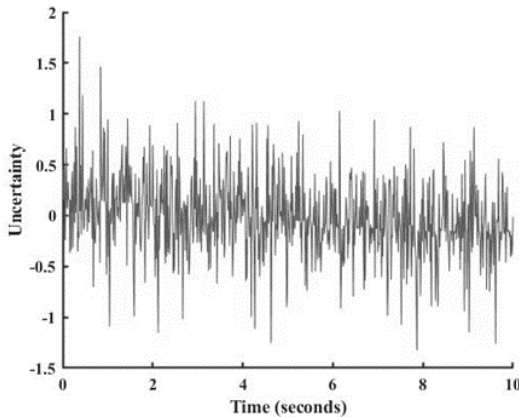


Figure 3. Uncertainty analysis based on the JONSWAP spectrum

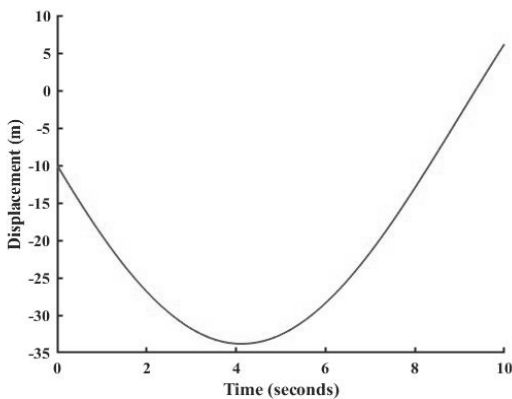


Figure 4. Simulation result for the displacement state variable

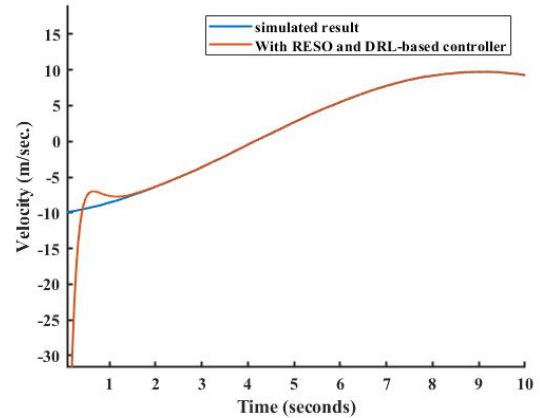


Figure 5. Comparison of unmeasured velocity in simulated and estimated phase

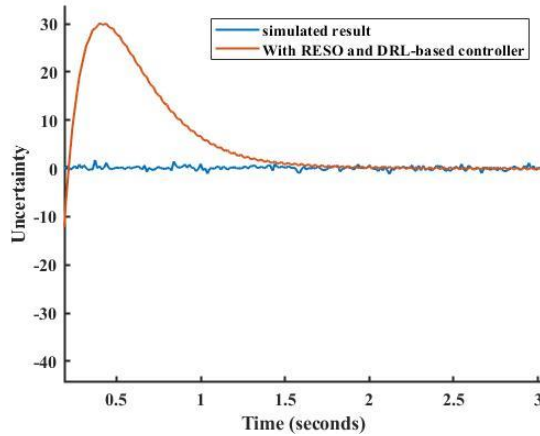


Figure 6. Unknown disturbance and uncertainty with simulated and estimated scenario

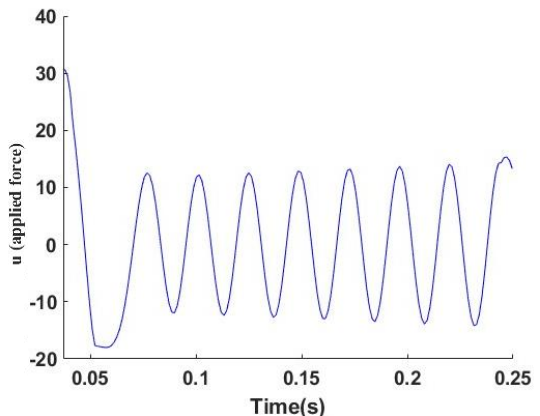


Figure 7. Control action applied on the PTO with DRL

As shown in Figure 6, the uncertainty of the problem is tracked quickly so that the tracking error approaches to zero after two seconds. The estimated results can be

used in the other control purposes including disturbance rejection. The significant point of the correct estimation with low settling time refers to the application of the concise control action. Figure 7 illustrates the applied force required to reach the uniform and maximum amount of energy and correct tracking. The accumulated reward during the processing time is demonstrated in Figure 8. The accumulated reward is increased so that its final value stands for the optimum control policy applied by the actor network and also, the maximum amount of energy. The captured energy during this task is demonstrated as Figure 9. Although, the fluctuation in some periods is clear, oscillation is not bothersome and is in the acceptable range for the consumer.

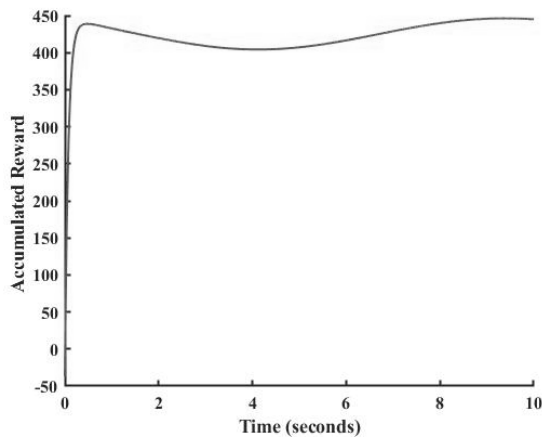


Figure 8. Captured energy during the processing time by DRL

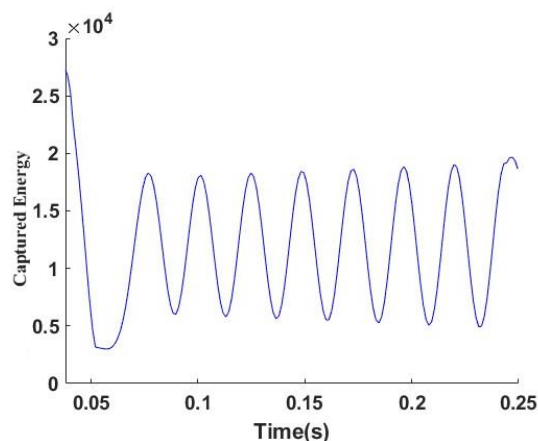


Figure 9. Captured energy during the processing time by DRL

4. CONCLUSION AND REMARKS

This work made an effort to address the undesirable fluctuation in the utilization of energy produced by a WEC. To do this, we created the WEC's structure model

along with all the necessary dynamical equations for the proposed controller's implementation. Next, we presented the new RSO dealing with the uncertainties of the structure and unmeasured outputs. The technique of immersion and invariance manifold was thoroughly integrated and confirmed by using LMI. The demand for regulating intelligent action applied to structures guided us to create the DRL. Therefore, the built network with appropriate training method was thoroughly detailed in the study. Finally, the numerical results carried out using MATLAB to examine and verify the performance of the suggested control system. The results indicated that our novel designed control method has a significant performance, both in estimating the unmeasured output and unknown disturbance, as well as in implementing the control policy. The future extent of our study may be altered to disturbance rejection problem and extended state observer design.

CREDIT AUTHOR STATEMENT

Hadi Mohammadian KhalafAnsar and Jafar Keighobadi: Conceptualization, Methodology, Data testing, Writing original draft, and editing.

DECLARATION OF COMPETING INTEREST

The authors declare no financial interests/personal relationships which may be considered as potential competing interests.

DATA AVAILABILITY

The data is accessible with request.

ACKNOWLEDGMENTS

This work was supported by University of Tabriz.

5. REFERENCES

1. Keighobadi J, KhalafAnsar HM, Naseradinmousavi P. Adaptive neural dynamic surface control for uniform energy exploitation of floating wind turbine. *Applied Energy*. 2022;316:119132. <https://doi.org/10.1016/j.apenergy.2022.119132>
2. Nielsen KM, Pedersen TS, Andersen P, Ambühl S. Optimizing control of wave energy converter with losses and fatigue in power take off. *IFAC-PapersOnLine*. 2017;50(1):14680-5. <https://doi.org/10.1016/j.ifacol.2017.08.2497>
3. Sadripour G, Shafaghat R, Alizadeh Kharkeshi B, Tabassom R, Mahmoudi A. Installation Depth and Incident Wave Height Effect on Hydrodynamic Performance of a Flap Type Wave Energy Converter: Experimental Analysis. *International Journal of Engineering*. 2022;35(12):2283-90. <https://doi.org/10.5829/ije.2022.35.12c.02>

4. Arish N, Marignetti F. Evaluation of Linear Permanent Magnet Vernier Machine Topologies for Wave Energy Converters. *International Journal of Engineering*. 2021;34(2):403-13. <https://doi.org/10.5829/ije.2021.34.02b.12>
5. Bayani R, Farhadi M, Shafaghat R, Alamian R. Experimental evaluation of irwec1, a novel offshore wave energy converter. *International Journal of Engineering*. 2016;29(9):1292-9. <https://doi.org/10.5829/idosi.ije.2016.29.09c.15>
6. Alizadeh Kharkeshi B, Shafaghat R, Jahanian O, Alamian R. Experimental evaluation of the effect of dimensionless hydrodynamic coefficients on the performance of a multi-chamber oscillating water column converter in laboratory scale. *Modares Mechanical Engineering*. 2021;21(12):823-34. <http://mme.modares.ac.ir/article-15-52993-en.html>
7. Son D, Yeung RW. Real-time implementation and validation of optimal damping control for a permanent-magnet linear generator in wave energy extraction. *Applied energy*. 2017;208:571-9. <https://doi.org/10.1016/j.apenergy.2017.09.097>
8. Korde UA. Preliminary consideration of energy storage requirements for sub-optimal reactive control of axisymmetric wave energy devices. *Annual Reviews in Control*. 2015;40:93-101. <https://doi.org/10.1016/j.arcontrol.2015.08.004>
9. Anderlini E, Forehand D, Bannon E, Xiao Q, Abusara M. Reactive control of a two-body point absorber using reinforcement learning. *Ocean Engineering*. 2018;148:650-8. <https://doi.org/10.1016/j.oceaneng.2017.08.017>
10. Babarit A, Duclos G, Clément AH. Comparison of latching control strategies for a heaving wave energy device in random sea. *Applied Ocean Research*. 2004;26(5):227-38. <https://doi.org/10.1016/j.apor.2005.05.003>
11. Wu J, Yao Y, Zhou L, Götteman M. Real-time latching control strategies for the solo Duck wave energy converter in irregular waves. *Applied Energy*. 2018;222:717-28. <https://doi.org/10.1016/j.apenergy.2018.04.033>
12. Faedo N, Olaya S, Ringwood JV. Optimal control, MPC and MPC-like algorithms for wave energy systems: An overview. *IFAC Journal of Systems and Control*. 2017;1:37-56. <https://doi.org/10.1016/j.ifacsc.2017.07.001>
13. Hals J, Falnes J, Moan T. Constrained optimal control of a heaving buoy wave-energy converter. 2011. <https://doi.org/10.1115/1.4001431>
14. O'Sullivan AC, Lightbody G. Co-design of a wave energy converter using constrained predictive control. *Renewable energy*. 2017;102:142-56. <https://doi.org/10.1016/j.renene.2016.10.034>
15. Li L, Yuan Z, Gao Y. Maximization of energy absorption for a wave energy converter using the deep machine learning. *Energy*. 2018;165:340-9. <https://doi.org/10.1016/j.energy.2018.09.093>
16. Jama M, Wahyudie A, Noura H. Robust predictive control for heaving wave energy converters. *Control Engineering Practice*. 2018;77:138-49. <https://doi.org/10.1016/j.conengprac.2018.05.010>
17. Zou S, Abdelkhalik O, Robinett R, Korde U, Bacelli G, Wilson D, et al. Model Predictive Control of parametric excited pitch-surge modes in wave energy converters. *International journal of marine energy*. 2017;19:32-46. <https://doi.org/10.1016/j.ijome.2017.05.002>
18. Korde UA, Lyu J, Robinett III RD, Wilson DG, Bacelli G, Abdelkhalik OO. Constrained near-optimal control of a wave energy converter in three oscillation modes. *Applied Ocean Research*. 2017;69:126-37. <https://doi.org/10.1016/j.apor.2017.10.004>
19. Burgaç A, Yavuz H. Fuzzy Logic based hybrid type control implementation of a heaving wave energy converter. *Energy*. 2019;170:1202-14. <https://doi.org/10.1016/j.energy.2018.12.090>
20. Zhan S, Wang B, Na J, Li G. Adaptive optimal control of wave energy converters. *IFAC-PapersOnLine*. 2018;51(29):38-43. <https://doi.org/10.1016/j.ifacol.2018.09.466>
21. Han J. From PID to active disturbance rejection control. *IEEE transactions on Industrial Electronics*. 2009;56(3):900-6. <https://doi.org/10.1109/TIE.2008.2011621>
22. Gao Z. On the centrality of disturbance rejection in automatic control. *ISA transactions*. 2014;53(4):850-7. <https://doi.org/10.1016/j.isatra.2013.09.012>
23. Zhao Z-L, Guo B-Z. On convergence of nonlinear active disturbance rejection control for SISO nonlinear systems. *Journal of Dynamical and Control Systems*. 2016;22(2):385-412. <https://doi.org/10.1007/s10883-015-9304-5>
24. Feng H, Guo B-Z. Active disturbance rejection control: Old and new results. *Annual Reviews in Control*. 2017;44:238-48. <https://doi.org/10.1016/j.arcontrol.2017.05.003>
25. Hosseini-Pishrobat M, Keighobadi J. Extended state observer-based robust non-linear integral dynamic surface control for triaxial MEMS gyroscope. *Robotica*. 2019;37(3):481-501. <https://doi.org/10.1017/S0263574718001133>
26. Guo B-Z, Zhao Z-l. On the convergence of an extended state observer for nonlinear systems with uncertainty. *Systems & Control Letters*. 2011;60(6):420-30. <https://doi.org/10.1016/j.sysconle.2011.03.008>
27. Li J, Xia Y, Qi X, Wan H. On convergence of the discrete-time nonlinear extended state observer. *Journal of the Franklin Institute*. 2018;355(1):501-19. <https://doi.org/10.1016/j.jfranklin.2017.11.019>
28. Zhao Z-L, Guo B-Z. Extended state observer for uncertain lower triangular nonlinear systems. *Systems & Control Letters*. 2015;85:100-8. <https://doi.org/10.1016/j.sysconle.2015.09.004>

COPYRIGHTS

©2024 The author(s). This is an open access article distributed under the terms of the Creative Commons Attribution (CC BY 4.0), which permits unrestricted use, distribution, and reproduction in any medium, as long as the original authors and source are cited. No permission is required from the authors or the publishers.

**Persian Abstract****چکیده**

زندگی در دنیای گرمتر زمین، باعث ترغیب و پیشرفت دستگاه‌های تولید انرژی تجدیدپذیر و بهره‌گیری از فناوری‌های جدید مانند هوش مصنوعی می‌شود. با توجه به پتانسیل بالای انرژی امواج دریا و تطابق آن با محیط زیست، مبدل‌های انرژی موج نقش حیاتی در برداشت انرژی یکنواخت ایفا می‌کنند. در این مقاله، تغییرات زیست محیطی چشمگیر در اقیانوس‌ها را در نظر گرفته‌ایم تا یک سیستم کنترل فیدبک هوشمند را برای کاهش تأثیر اغتشاشات و اثرات باد متغیر بر عملکرد مبدل‌های انرژی امواج پیشنهاد دهیم. یادگیری تقویتی عمیق به عنوان یک تکنیک هوش مصنوعی قدرتمند، توانمند به تشخیص مبدل‌های امواج مانند مدل‌های جعبه سیاه است. بنابراین، با استفاده از یادگیری تقویتی عمیق، متغیرهای حالتی که نمی‌توان به طور مستقیم اندازه‌گیری کرد و اغتشاش‌ها به طور همزمان در بخش نظارت بر حالت تخمین زده می‌شوند. ضعف در داده‌های اندازه‌گیری و نیاز به کاربرد بلادرنگ تعداد محدودی از لایه‌ها در شبکه‌های عصبی عمیق را با پیاده‌سازی مشاهده‌گر حالت توسعه یافته مبتنی بر روش غوطه‌وری و تغییر ناپذیری که مقابله با نویزهای خارجی ناخواسته را بهبود می‌بخشد، جبران می‌شود. در سیستم کنترل هوشمند کلی، پارامترهای تخمینی به عنوان شبکه‌های عملگر-منتقد وارد مدل یادگیری تقویتی عمیق می‌شوند. شبکه عملگر اولیه مسئول پیش‌بینی ورودی کنترل است، در حالی که شبکه منتقد بعدی معیار تصمیم‌گیری برای ارزیابی دقت مقدار پیش‌بینی عملگر را تعیین می‌کند. سپس، مقدار خروجی مرحله منتقد از طریق لایه‌ها به عقب برگردانده می‌شود تا وزن‌های شبکه به‌روز شوند. نتایج آزمون شبیه‌سازی در نرم‌افزار متلب نشان‌دهنده هم‌گرایی پارامترها/حالت‌های اندازه‌گیری نشده با مقادیر واقعی متناظر و اهمیت روش یادگیری تقویتی عمیق هوشمندانه طراحی شده جدید است.



Peculiarities of Abrasive Finishing of Surfaces of Parts Made of Aluminium Alloy of AMts Grade in Magnetic Field

A. I. Keksin^{*a}, N. I. Sorokopud^a, N. N. Zakirov^b

^a Empress Catherine II Saint Petersburg Mining University, St. Petersburg, Russia

^b Tyumen Industrial University, Tyumen, Russia

PAPER INFO

Paper history:

Received 10 November 2023

Received in revised form 23 January 2024

Accepted 10 February 2024

Keywords:

Aluminum Alloy AMts

Surface Roughness

Abrasive Finishing

Abrasive Finishing in a Magnetic Field

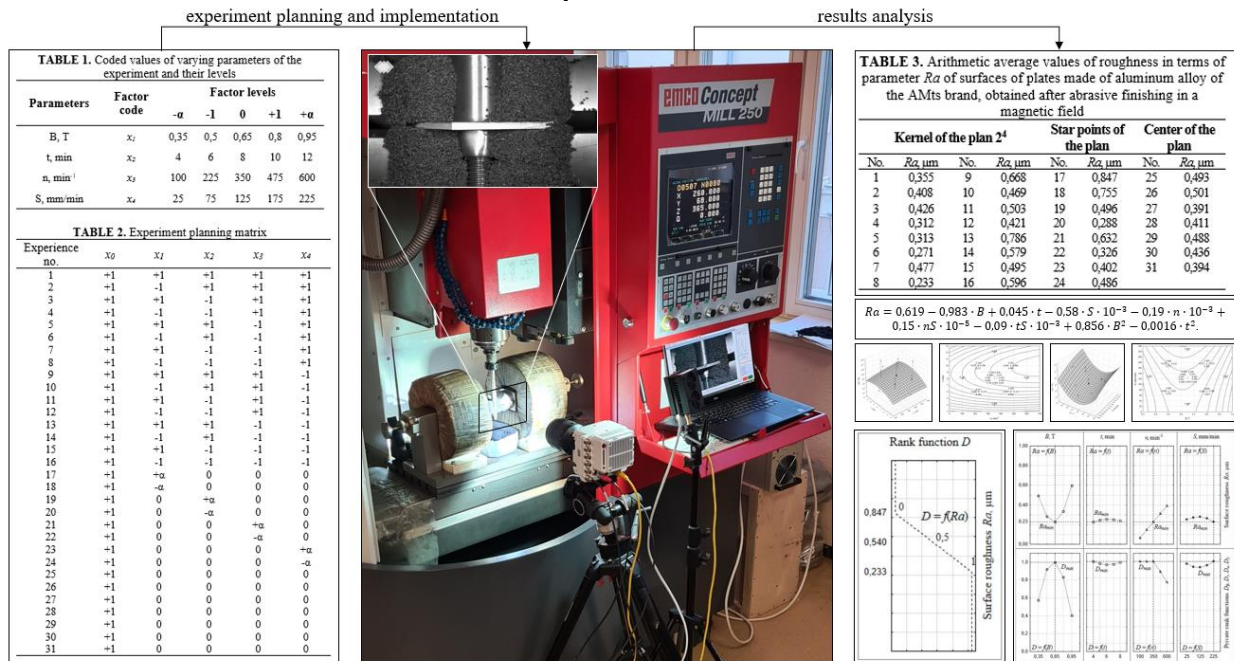
Finishing of Surfaces

ABSTRACT

The scientific article presents the results of research to identify the regularities arising from the abrasive finishing of the surfaces of parts made of aluminium alloy grade (AMts) in a magnetic field. As a result of conducted experiments the relations between variable factors of abrasive finishing in a magnetic field and quality indicators of surfaces of parts from aluminium alloy of mark AMts which have been expressed by means of physical and statistical model of graphic dependences of functions defined as $Ra = f(t, n)$ and $Ra = f(B, S)$. It has been established that abrasive finishing in a magnetic field allows for an insignificant amount of time $t = 4...12$ min to reduce surface roughness from initial $Ra = 1.3...1.9 \mu\text{m}$ to $Ra = 0.23...0.85 \mu\text{m}$ (depending on processing conditions). In addition, the optimization problem of determining the optimal conditions of abrasive finishing in a magnetic field, providing the achievement of the minimum value of roughness $Ra_{min} = 0.23 \mu\text{m}$ of the surfaces of parts made of aluminium alloy grade AMts was solved.

doi: 10.5829/ije.2024.37.06c.06

Graphical Abstract



*Corresponding Author Email: keksin.a@mail.ru (A.I. Keksin)

1. INTRODUCTION

Currently, there is a tendency to expand the scale of machine building industries (1, 2). This is primarily due to the need to provide oil and gas (3-5), energy (6, 7), mining (8, 9) and other industries with high-performance machinery and process equipment (10, 11).

Improvement of machine-building production in accordance with modern challenges cannot be realized without a deeper study of the issues of mechanical processing of materials (12, 13). It is connected first of all with the fact that the level of machine-building productions, the quality of products manufactured by them, as well as the rationality of decisions taken in the development of technological processes of machining largely depends on the degree of study of these issues (14).

Today, special attention is paid to the machining of materials with special physical and mechanical properties (15, 16), including aluminium-based alloys (17-19). The machining of aluminium and its alloys is a rather labour-intensive process. For example, the high thermal conductivity of aluminium and its alloys causes oxidation during heating, which is accompanied by the formation of cold cracks in the material (20); increased temperature during machining of aluminium products causes structural changes in the surface of the machined material.

An effective solution to this problem is the use of finishing methods with low temperature in the cutting zone when machining aluminium material. The most promising finishing methods include abrasive finishing in a magnetic field (21), at which the temperature in the micro-cutting zone is of the order of $T = 30 \div 40^\circ\text{C}$. This type of finishing consists in the creation of a technological tool, consisting of a magnetic field and abrasive powder, and its subsequent use for impact during a certain period of time on the machined surfaces of parts. In this case, to implement magnetic and abrasive impacts, the machined part, pole tips or the part and pole tips together are given different combinations of movements (rotational, oscillating, reciprocating) (22).

Studies of abrasive finishing of aluminium and its alloys in a magnetic field have received considerable attention in literature (23, 24). For example, in the work of Khomich (23) the influence of technological tool on the number of inclusions, micro-sharpening and removal of oxide film from the flanks of sheets from aluminium alloy of *Al-Mg* system (grades 1560 (AMg-6)) was studied. It is noted that rational selection of mode parameters and type of technological tool allows to perform defect-free abrasive finishing of sheet edges in a magnetic field. The criteria of surface roughness and its morphology after abrasive finishing in a magnetic field of surfaces of parts made of aluminium alloy of *Al-Cu-Mg* system (grades 2024 (D16)) has been analyzed in the work of Anjaneuli and Venkatesh (24). It was revealed that the following factors have the main influence on the

quality of parts surfaces: stress, allowing to change the stiffness of the technological tool; feed rate, providing the process of micro-cutting. The influence of rotation speed and abrasive material composition on the quality of machined surfaces of parts made of aluminium alloy of *Al-Mg-Si* system (grades 6061 (AD33)) was studied by Li et al. (25). It was experimentally established that as a result of abrasive finishing in a magnetic field, the roughness value of parts surfaces by *Ra* parameter can be improved by 97%.

The conducted researches were focused on finishing of aluminium alloy systems: *Al-Mg* (grades 1560 (AMg-6)), which belongs to deformable alloys and used in the manufacture of hull parts and transport tanks; *Al-Cu-Mg* (grades 2024 (D16)), which is most commonly used in sub-zero and cryogenic temperatures in aircraft and aerospace applications; *Al-Mg-Si* (grades 6061 (AD33)), which is a corrosion-resistant alloy and is used for the manufacture of pipes and profiles of various cross-sections. However, the parts made of aluminium alloy of *Al-Mn* system (grades 3003 (AMts)), which are used in gas-insulated transformers and sensitive elements of electric tachometers (26), were not subjected to abrasive finishing in a magnetic field, despite the high surfaces quality requirements ($Ra = 0.25 \div 0.63 \mu\text{m}$) for these parts.

In this connection, the research presented in the scientific article is aimed at studying the peculiarities of abrasive finishing in the magnetic field of surfaces of parts made of aluminium alloy of *Al-Mn* system (grades 3003 (AMts)).

2. MATERIALS AND METHODS

Studies on abrasive finishing of AMts aluminium alloy parts surfaces in a magnetic field were carried out on a specially designed complex. The developed experimental complex included a technological system of abrasive finishing in a magnetic field (27-29), created on the basis of an upgraded machining centre *Emco Concept Mill 250* with CNC (Figure 1) and a mobile computerized information-measuring system (Figure 2), consisting of an optical bench, profilometer *Mitutoyo SJ-210* and a laptop with the appropriate software.

As experimental samples plates from aluminium alloy of AMts grade with dimensional parameters $30 \times 30 \times 2 \text{mm}$ with initial surface roughness $Ra_{initial} = 1,3 \dots 1,9 \mu\text{m}$ were used. Fixing of plates was made by means of a fixture (Figure 1), which was installed in the mandrel of an upgraded machining centre *Emco Concept Mill 250* with CNC.

The technological tool for abrasive finishing in a magnetic field of AMts aluminium alloy plate surfaces was a combination of magnetic field, abrasive powder and coolant (30-32). The magnetic field was constant and



Figure 1. Experimental complex for abrasive finishing in a magnetic field

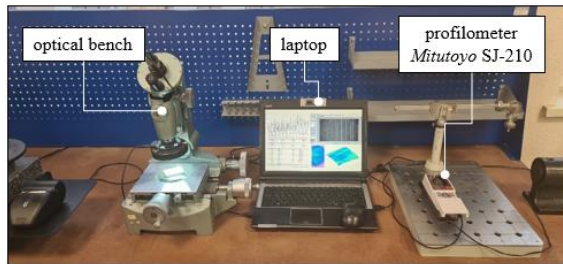


Figure 2. Mobile computerised information and measurement system

was generated by electromagnetic coils of the abrasive finishing in a magnetic field system (33-35). A homogeneous abrasive of PR10P6M5 grade with fraction $\Delta = 0.25 \div 0.16 \mu\text{m}$, consisting of high-speed steel P6M5 particles with increased carbon content of rounded splinter shape, was used as an abrasive powder. Cooling lubricant Global was used to ensure clean surfaces of plates made of aluminium alloy of AMts grade and to prevent abrasive material inclusions in the processed samples.

Abrasive finishing in the magnetic field of the surfaces of plates made of aluminium alloy of AMts grade was carried out according to the central composite rotatable plan (Tables 1 and 2). This plan consisted of 31 experiments: 16 experiments were the core of the plan and corresponded to the planning matrix of the full-factorial experiment 2^4 ; 8 experiments were the «star» points; 7 experiments were the centre of the plan.

The variable factors during abrasive finishing in a magnetic field of the surfaces of plates made of

TABLE 1. Coded values of varying parameters of the experiment and their levels

Parameters	Factor code	Factor levels				
		$-\alpha$	-1	0	+1	$+\alpha$
B, T	x_1	0,35	0,5	0,65	0,8	0,95
t, min	x_2	4	6	8	10	12
n, min^{-1}	x_3	100	225	350	475	600
S, mm/min	x_4	25	75	125	175	225

TABLE 2. Experiment planning matrix

Experience no.	x_0	x_1	x_2	x_3	x_4
1	+1	+1	+1	+1	+1
2	+1	-1	+1	+1	+1
3	+1	+1	-1	+1	+1
4	+1	-1	-1	+1	+1
5	+1	+1	+1	-1	+1
6	+1	-1	+1	-1	+1
7	+1	+1	-1	-1	+1
8	+1	-1	-1	-1	+1
9	+1	+1	+1	+1	-1
10	+1	-1	+1	+1	-1
11	+1	+1	-1	+1	-1
12	+1	-1	-1	+1	-1
13	+1	+1	+1	-1	-1
14	+1	-1	+1	-1	-1
15	+1	+1	-1	-1	-1
16	+1	-1	-1	-1	-1
17	+1	$+\alpha$	0	0	0
18	+1	$-\alpha$	0	0	0
19	+1	0	$+\alpha$	0	0
20	+1	0	$-\alpha$	0	0
21	+1	0	0	$+\alpha$	0
22	+1	0	0	$-\alpha$	0
23	+1	0	0	0	$+\alpha$
24	+1	0	0	0	$-\alpha$
25	+1	0	0	0	0
26	+1	0	0	0	0
27	+1	0	0	0	0
28	+1	0	0	0	0
29	+1	0	0	0	0
30	+1	0	0	0	0
31	+1	0	0	0	0

aluminum alloy of the AMts brand were: the value of magnetic induction $B = 0.35 \div 0.95$ T; finishing time $t = 4 \div 12$ min; plate rotation speed $n = 100 \div 600$ min⁻¹; plate feed along the pole pieces $S = 25 \div 225$ mm/min (Table 1). The controlled parameter was the surface roughness of the plates according to the Ra parameter, which was monitored using a *Mitutoyo SJ-210* profilometer (Figure 2).

The roughness values obtained in the course of experimental studies in terms of the Ra parameter of the surfaces of plates made of aluminum alloy of the AMts brand were subjected to statistical processing in order to construct a physical-statistical model, which can be generally represented by means of a response function in the form of a complete polynomial of the second degree expressed in Equation 1:

$$y_i = b_0 + \sum_{1 \leq i \leq k} b_i x_i + \sum_{1 \leq i \leq j \leq k} b_{ij} x_i x_j + \sum_{1 \leq i \leq k} b_{ii} x_i^2. \quad (1)$$

where y_i is i -th quality parameter (roughness according to the Ra parameter) of the surfaces of the part after finishing; x_i is i -th factor of abrasive finishing in a magnetic field; b_0, b_i, b_{ij} are values of model coefficients.

The construction of a physical-statistical model 1 of the influence of varying factors of abrasive finishing in a magnetic field on the roughness in terms of the parameter Ra of plate surfaces was carried out in accordance with the calculation algorithm, which is described in detail. The main stages of the calculation algorithm were: coding the levels of factors x_i , calculating the coefficients b_0, b_i, b_{ij} model, estimating the dispersion of the reproducibility of the experiment S_y^2 , estimating the dispersion of the model coefficients S_b^2 and their root-mean-square errors S_b , calculating confidence intervals Δb_i and determining the statistical significance of the coefficients b_0, b_i, b_{ij} models, calculation of the variance of model inadequacy SS_{inad}^2 , calculation of the F_{calc} calculation model criterion and testing the hypothesis about the adequacy of the model $F_{calc} < F_{table}$, decoding the levels of factors x_i .

The physical-statistical model 1 of the influence of abrasive finishing factors in a magnetic field on the roughness in the Ra parameter of the surfaces of plates made of aluminum alloy of the AMts brand will make it possible to predict quality indicators with sufficient accuracy depending on the processing conditions. This is especially important when the complexity of the occurrence of physical phenomena in processes creates significant difficulties in creating analytical models.

All mathematical calculations necessary to construct a physical and statistical model 1 of the influence of abrasive finishing factors in a magnetic field on the quality indicators of plate surfaces, and the subsequent conversion of the obtained data into graphical form, were carried out in an automated mode using *Microsoft Office Excel* and *Statistica 12* programs.

3. RESULTS AND DISCUSSION

As a result of experimental studies on abrasive finishing in a magnetic field of the surfaces of plates made of aluminum alloy of the AMts brand, the roughness values for the parameter Ra were obtained. The calculated arithmetic average roughness values are summarized in Table 3 and divided according to the 3 parts of the central compositional rotatable plan.

Based on the mathematical calculations performed following the calculation algorithm previously summarized, a physical-statistical model was built in the form of a response function, which makes it possible to predict the roughness values in terms of the Ra parameter of the surfaces of plates made of aluminum alloy of the AMts brand, depending on the conditions of abrasive finishing in a magnetic field stated in Equation 2:

$$Ra = 0,619 - 0,983 \cdot B + 0,045 \cdot t - 0,58 \cdot S \cdot 10^{-3} - 0,19 \cdot n \cdot 10^{-3} + 0,15 \cdot nS \cdot 10^{-5} - 0,09 \cdot tS \cdot 10^{-3} + 0,856 \cdot B^2 - 0,0016 \cdot t^2. \quad (2)$$

A more visual representation of the response function 2 can be presented using its geometric analogue - the response surface. However, a geometric representation is only appropriate when there are no more than two factors influencing the output parameter. Taking this fact into account, the response surface was geometrically depicted in three-dimensional and two-dimensional spaces in two combinations: the influence of finishing time and rotation speed on the roughness parameter Ra (Figure 3, a, c); the influence of magnetic induction and feed on the roughness in terms of the Ra parameter (Figure 3, b, d).

The constructed physical-statistical model and graphical dependences of the functions $Ra = f(t, n)$ and $Ra = f(B, S)$ make it possible to determine the main tendency of the influence of varying factors of abrasive finishing in a magnetic field on the quality, in particular

TABLE 3. Arithmetic average values of roughness in terms of parameter Ra of surfaces of plates made of aluminum alloy of the AMts brand, obtained after abrasive finishing in a magnetic field

Kernel of the plan 24				Star points of the plan		Center of the plan	
No.	$Ra, \mu\text{m}$	No.	$Ra, \mu\text{m}$	No.	$Ra, \mu\text{m}$	No.	$Ra, \mu\text{m}$
1	0,355	9	0,668	17	0,847	25	0,493
2	0,408	10	0,469	18	0,755	26	0,501
3	0,426	11	0,503	19	0,496	27	0,391
4	0,312	12	0,421	20	0,288	28	0,411
5	0,313	13	0,786	21	0,632	29	0,488
6	0,271	14	0,579	22	0,326	30	0,436
7	0,477	15	0,495	23	0,402	31	0,394
8	0,233	16	0,596	24	0,486		

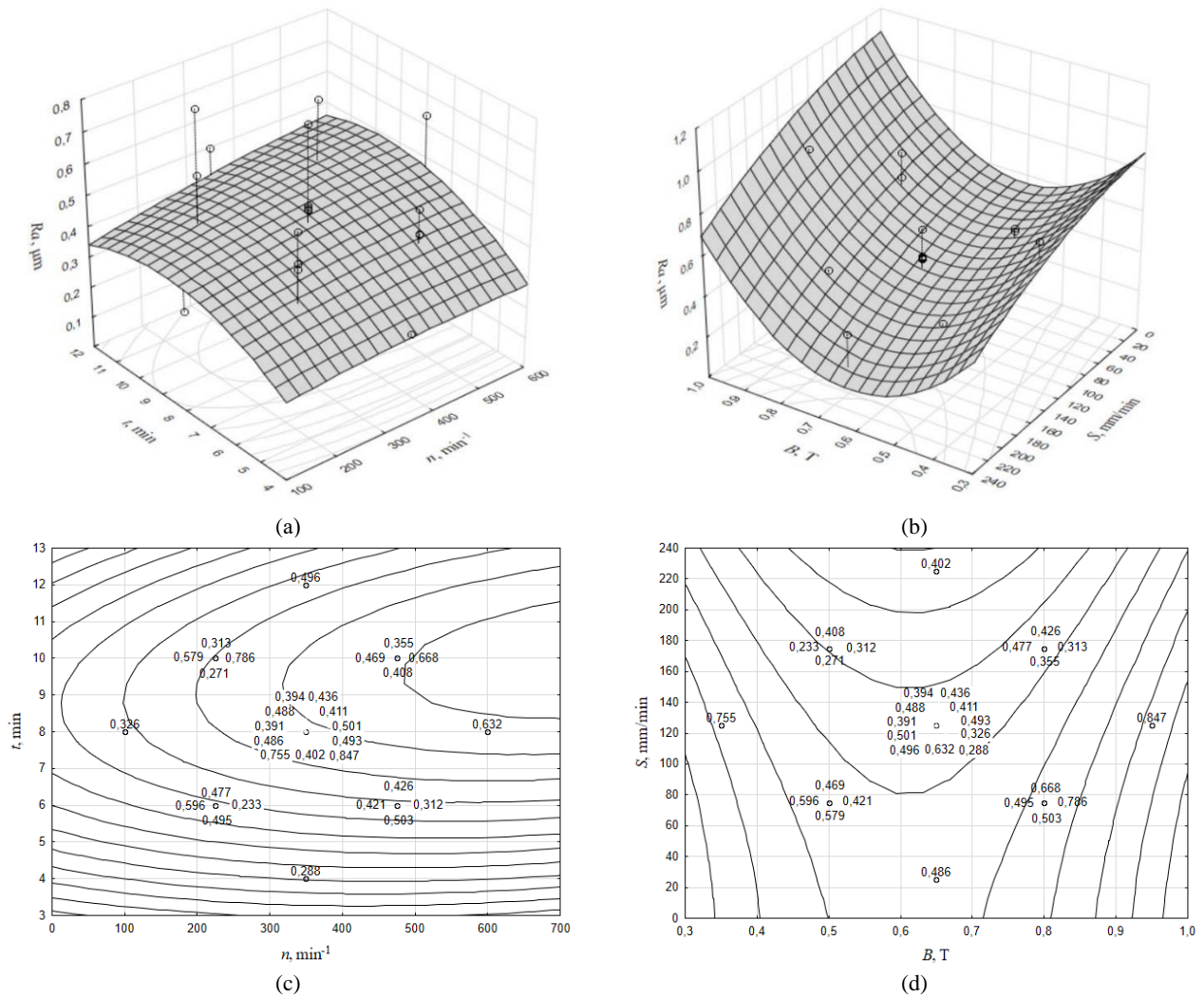


Figure 3. Graphic dependences of the influence of abrasive finishing factors in a magnetic field on the roughness in terms of the Ra parameter of the surfaces of plates made of aluminum alloy grade AMTs

on the roughness in the parameter Ra , of plate surfaces made of aluminum alloy AMTs brand. However, in this case, it is not possible to offer the most optimal conditions for abrasive finishing in a magnetic field for practice. For this reason, the obtained data were subjected to additional analysis in order to solve the optimization problem.

The criterion for optimal conditions for abrasive finishing in a magnetic field was the ability, under appropriate conditions, to form the minimum value of roughness Ra_{min} of the surfaces of plates made of aluminum alloy of the AMTs brand. The process of searching for optimal conditions was carried out on the basis of a rank approach, in which a generalized rank function $D = f(Ra)$ (Figure 4), was initially constructed, subsequently converted into private rank functions of the levels of abrasive finishing factors in a magnetic field D_B

$= f(B)$, $D_t = f(t)$, $D_n = f(n)$, $D_S = f(S)$ (Figure 5). Subsequently, these functions $D_B = f(B)$, $D_t = f(t)$, $D_n = f(n)$, $D_S = f(S)$ were compared with the profiles of the influence of abrasive finishing factors in a magnetic field on the roughness of plate surfaces $Ra = f(B)$, $Ra = f(t)$, $Ra = f(n)$, $Ra = f(S)$ and the optimal conditions for abrasive finishing in a magnetic field were determined (Figure 5).

When constructing the generalized rank function $D = f(Ra)$ three ranks «0», «0,5» and «1» were assigned experimental roughness values obtained during experimental studies (Table 3), Ra_{max} , Ra_{medium} and Ra_{min} respectively (Figure 4). The generalized rank function $D = f(Ra)$ shows the preference for minimum roughness values Ra_{min} of plate surfaces in comparison with values close to Ra_{max} .

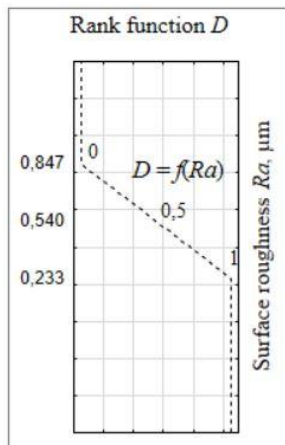


Figure 4. Generalized rank function plot $D = f(Ra)$

Based on the generalized rank function $D = f(Ra)$ partial rank functions were constructed from the levels of abrasive finishing factors in a magnetic field $D_B = f(B)$, $D_t = f(t)$, $D_n = f(n)$, $D_S = f(S)$ and compared with the profiles of the influence of abrasive finishing factors in a magnetic field on the surface roughness of plates $Ra = f(B)$, $Ra = f(t)$, $Ra = f(n)$, $Ra = f(S)$. This comparison showed that the minimum value of the surface roughness of the plates, within the studied range of changes in abrasive finishing factors in a magnetic field, is equal to

$Ra_{min} = 0,19 \mu\text{m}$ and is formed under the following conditions: $B = 0,65 \text{ T}$, $t = 12 \text{ min}$, $n = 475 \text{ min}^{-1}$, $S = 225 \text{ mm/min}$.

A more detailed study of the partial function $D_t = f(t)$ allowed to conclude that there are two preferred finishing times: $t = 4 \text{ min}$ and $t = 12 \text{ min}$. In this regard, the range of values from $t = 4 \div 12 \text{ min}$ to $t = 4 \div 8 \text{ min}$ of the private rank function $D_t = f(t)$ was adjusted and the partial functions $D_B = f(B)$, $D_t = f(t)$, $D_n = f(n)$, $D_S = f(S)$ were again compared with profiles of the influence of abrasive finishing factors in a magnetic field on the roughness of plate surfaces $Ra = f(B)$, $Ra = f(t)$, $Ra = f(n)$, $Ra = f(S)$ (Figure 5). As a result, it was found that the minimum value of the surface roughness of the plates is $Ra_{min} = 0,23 \mu\text{m}$ and is formed under the following conditions: $B = 0,65 \text{ T}$, $t = 4 \text{ min}$, $n = 350 \text{ min}^{-1}$, $S = 225 \text{ mm/min}$ (Figure 5).

Despite the insignificant difference $\Delta = 0,04 \mu\text{m}$ in the minimum values of the formed surface roughness of plates made of aluminum alloy of the AMts brand, the following conditions will be considered the most rational conditions for abrasive finishing in a magnetic field for their recommendation for production: $B = 0,65 \text{ T}$, $t = 4 \text{ min}$, $n = 350 \text{ min}^{-1}$, $S = 225 \text{ mm/min}$. These conditions of abrasive finishing in a magnetic field make it possible to ensure the surface roughness of plates made of aluminum alloy of the AMts brand equal to $Ra = 0,23 \mu\text{m}$.

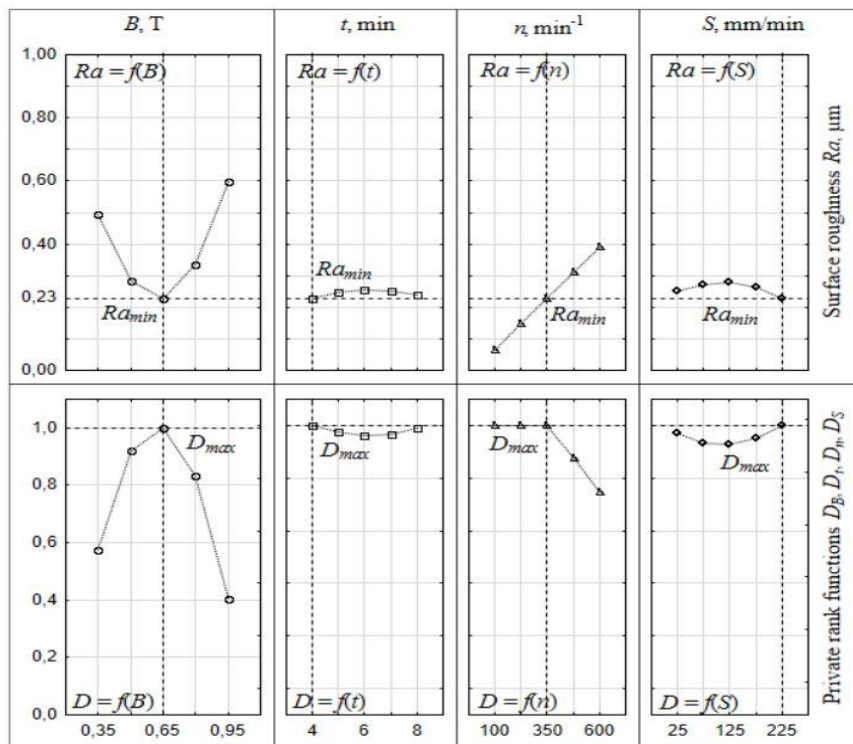


Figure 5. Determination of optimal conditions for abrasive finishing of the surfaces of plates made of aluminum alloy grade AMts in a magnetic field

4. CONCLUSION

Studying the peculiarities of abrasive finishing in the magnetic field of the surfaces of parts made of aluminium alloy grade AMz, the authors presented the following conclusions based on the results of the study:

- The finishing method of abrasive finishing in a magnetic field is an effective method for recommending it in practice for the purpose of final processing of the surfaces of parts made of aluminum alloy grade AMts. Since in a short time $t = 4...12$ min, it allows to reduce the roughness of the surfaces of parts from the original equal $Ra = 1,3...1,9 \mu\text{m}$ to $Ra = 0,23...0,85 \mu\text{m}$ (depending on processing conditions).
- Solving the optimization problem allows to determine the optimal conditions for abrasive finishing in a magnetic field of the surfaces of plates made of aluminum alloy of the AMts brand with achieving a minimum roughness value of $Ra_{min} = 0,23 \mu\text{m}$; the optimal conditions are: $B = 0,65 \text{ T}$, $t = 4 \text{ min}$, $n = 350 \text{ min}^{-1}$, $S = 225 \text{ mm/min}$.

5. REFERENCES

1. Admakin M, Khalimonenko A, Zakharova V, Nguen VD. Machinability of cutting of low-magnetic high-manganese steels. *Chernye Metally*. 2023;2023(2):82-7. 10.17580/chm.2023.02.12
2. Leong K, Jaafar H, Tajul L, Zailani Z, Hamidon R, Zain M. Effect of Inclined Angle in Trimming of Ultra-high Strength Steel Sheets Having Inclined and Curved Shapes. *International Journal of Engineering*. 2023;36(11):2004-14. 10.5829/IJE.2023.36.11B.06
3. Fetisov V, Shalygin AV, Modestova SA, Tyan VK, Shao C. Development of a numerical method for calculating a gas supply system during a period of change in thermal loads. *Energies*. 2022;16(1):60. 10.3390/en16010060
4. Nikolaev A, Samigullin G, Samigullina L, Fetisov V, editors. Non-stationary operation of gas pipeline based on selections of travel. IOP conference series: Materials Science and Engineering; 2018: IOP Publishing. 10.1088/1757-899X/327/2/022074
5. Gafur S, Andrey S, Liliya S, Vadim F. Assessment of damage of metallic elements in oil and gas facilities using small punch test. *International Journal of Applied Engineering Research*. 2017;12(21):11583-7. https://www.ripublication.com/ijaer17/ijaerv12n21_148.pdf
6. Nikolaev A, Dokoukin V, Lykov Y, Fetisov V, editors. Research of processes of heat exchange in horizontal pipeline. IOP Conference Series: Materials Science and Engineering; 2018: IOP Publishing. 10.1088/1757-899X/327/3/032041
7. Fetisov V, Davardoost H, Mogylevets V. Technological aspects of methane-hydrogen mixture transportation through operating gas pipelines considering industrial and fire safety. *Fire*. 2023;6(10):409. 10.3390/fire6100409
8. Teplyakova A, Azimov A, Alieva L, Zhukov I. Improvement of manufacturability and endurance of percussion drill assemblies: Review and analysis of engineering solutions. *MIAB Mining Inf Anal Bull*. 2022;9:120-32. 10.25018/0236_1493_2022_9_0_120
9. Шишляльников Д, Зверев В, Муравский А, Звонарев И, Королев И. МЕТОДИКА ОПРЕДЕЛЕНИЯ СРЕДНЕВЗВЕШЕННОЙ ПРОИЗВОДИТЕЛЬНОСТИ МЕХАНИЗИРОВАННЫХ КОМБАЙНОВЫХ КОМПЛЕКСОВ КАЛИЙНЫХ РУДНИКОВ. Горный информационно-аналитический бюллетень (научно-технический журнал). 2021(7):125-33. 10.25018/0236_1493_2021_7_0_125
10. Khrustaleva IN, Lyubomudrov SA, Larionova TA, Brovkina YY. Increasing the efficiency of technological preparation for the production of the manufacture components equipment for the mineral resource complex. *Записки Горного института*. 2021;249:417-26. 10.31897/PMI.2021.3.11
11. Pshenin VV, Zakirova GS. Improving the efficiency of oil vapor recovery units in the commodity transport operations at oil terminals. *Journal of Mining Institute*. 2024;265:121-8. 10.31897/PMI.2023.29
12. Maksarov V, Efimov A, Olt J. Improving the quality of hole processing in welded products made of dissimilar materials with a new boring tool. *The International Journal of Advanced Manufacturing Technology*. 2022;118(3):1027-42. 10.1007/s00170-021-07975-7
13. Mahmoodi M, Tagimalek H, Maraki M, Karimi S. Experimental and Numerical Investigation of the Formability of Cross and Accumulative Roll Bonded 1050 Aluminum Alloy Sheets in Single Point Incremental Forming Process. *International Journal of Engineering*. 2022;35(9):1707-15. 10.5829/ije.2022.35.09C.05
14. Yamilev M, Pshenin V, Matveev D, Podlesniy D, Bezimyannikov T. The use of compact inspection devices for monitoring the technical condition of pipelines in protective cases (Russian). *Oil Industry Journal*. 2022;2022(02):106-10. 10.24887/0028-2448-2022-2-106-110
15. Bennabi A, Adjeloua A, Ameer H, Boualem N, Younsi M. Influence of Multiple Repairs on the Quality of Duplex Welded Joints. *International Journal of Engineering, Transactions A: Basics*. 2022;35(4):675-84. 10.5829/IJE.2022.35.04A.06
16. Jadhav SP, Sawant SH. Dry Sliding Behaviour Study of Novel Low-metallic Friction Materials by using DoE-Taguchi Method. *International Journal of Engineering, Transactions C: Aspects*. 2024;37(3):452-9. 10.5829/ije.2024.37.03c.01
17. Tandel K, Menghani J. Fabrication of Aluminum 5083/SiC Surface Composite on Tungsten Inert Gas Weld Joint by Novel Direct Friction Stir Processing Technique. *International Journal of Engineering, Transactions C: Aspects*. 2023;36(3):523-31. 10.5829/IJE.2023.36.03C.12
18. Stepanov SN, Larionova TA, Stepanov SS. Study of Aluminum Influence on the Adhesion of Stainless Steel in Flame Spraying. *Записки Горного института*. 2020;245:591-8. 10.31897/PMI.2020.5.11
19. Bazhin VY, Ustinova YV, Fedorov SN, Shalabi MEK. Improvement of energy efficiency of ore-thermal furnaces in smelting of aluminosilic raw materials. *Записки Горного института*. 2023(261 (eng)):384-91. <https://pmi.spmi.ru/pmi/article/view/16128/16112>
20. Drits A, Ovchinnikov V. Properties of the welded joints of cast aluminum alloys formed by friction stir welding. *Tsvetn Met*. 2020(1):925. 10.17580/tsm.2020.01.11
21. Olt J, Maksarov V, Petrishin G, Panteleyenkov E, Liskovich M. Magnetic Abrasive Machining of Hard Workpieces by New Diffusion-Alloyed Materials. *Russian Engineering Research*. 2023;43(2):190-4. 10.3103/S1068798X23030243
22. Maksarov V, Popov M, Zakharova V. Influence of magnetic-abrasive machining parameters on ceramic cutting tools for technological quality assurance of precision products from cold-resistant steels. *Chernye Metally*. 2023(1):67. 10.17580/chm.2023.01.10
23. Khomich N. *Magnitno-abrazivnaya obrabotka izdelii (Magnetic Abrasive Treatment of Products)*, Minsk: Beloruss. Nats Tekh Univ. 2006.

24. Anjaneyulu K, Venkatesh G. Surface texture improvement of magnetic and non magnetic materials using magnetic abrasive finishing process. Proceedings of the Institution of Mechanical Engineers, Part C: Journal of Mechanical Engineering Science. 2021;235(19):4084-96. 10.1177/0954406220970590
25. Li W, Li X, Yang S, Li W. A newly developed media for magnetic abrasive finishing process: Material removal behavior and finishing performance. Journal of Materials Processing Technology. 2018;260:20-9. 10.1016/j.jmatprotec.2018.05.007
26. Davis JR. Aluminum and aluminum alloys: ASM international; 1993.
27. Mosavat M, Rahimi A. Numerical-experimental study on polishing of silicon wafer using magnetic abrasive finishing process. Wear. 2019;424:143-50. 10.1016/j.wear.2019.02.007
28. Malpotra A, Singh B, Singh L. Electrolytic magnetic abrasive finishing process—a review. Materials Today: Proceedings. 2023. 10.1016/j.matpr.2023.03.237
29. Modi KP, Bhavsar SN. Multi-response optimization of magnetic abrasive finishing process parameters on AISI H13 hot die steel using grey relational analysis. Materials Today: Proceedings. 2023. 10.1016/j.matpr.2023.01.381
30. Heng L, Kim JS, Mun SD, Song JH. Effect of strong flexible polycrystalline diamond abrasive tools in magnetic abrasive finishing of V-grooved ceramic guide rollers. Materials Today Communications. 2022;33:104333. 10.1016/j.mtcomm.2022.104333
31. Wei C, Tian Y, Chowdhury S, Han J, Gu Z. Investigation on high-shear and low-pressure grinding characteristics for zirconia ceramics using newly developed flexible abrasive tool. Ceramics International. 2023;49(6):8725-35. 10.1016/j.ceramint.2022.10.265
32. Kumar R. Study the effect of concentration ratio (magnetic abrasive powder and castor oil) in magnetic abrasive finishing process. Materials Today: Proceedings. 2021;37:3706-8. 10.1016/j.matpr.2020.10.160
33. Gao Y, Zhao Y, Zhao G, Zhang G, Zhang H. Achieving polycrystalline diamond magnetic abrasive tools via double-stage gas atomization. Materials & Design. 2022;224:111423. 10.1016/j.matdes.2022.111423
34. Bahrami M, Moradi A, Maljaei MD. Periodic magnetic finishing machine. Invention Disclosure. 2022;2:100007. 10.1016/j.inv.2022.100007
35. Faba A, Rimal HP, Laudani A, Chilosi F, Cardelli E. Measurements of magnetic characteristics of laminated Fe-Si steel filter inductors in grid interface converters. Measurement. 2022;195:111108. 10.1016/j.measurement.2022.111108

COPYRIGHTS

©2024 The author(s). This is an open access article distributed under the terms of the Creative Commons Attribution (CC BY 4.0), which permits unrestricted use, distribution, and reproduction in any medium, as long as the original authors and source are cited. No permission is required from the authors or the publishers.

**Persian Abstract****چکیده**

این مقاله علمی نتایج تحقیقات را برای شناسایی نظم های ناشی از پرداخت ساینده سطوح قطعات ساخته شده از آلیاژ آلومینیوم (AMTs) در میدان مغناطیسی ارائه می کند. در نتیجه آزمایش های انجام شده، روابط بین عوامل متغیر پرداخت ساینده در میدان مغناطیسی و شاخص های کیفی سطوح قطعات از آلیاژ آلومینیوم علامت AMTs که با استفاده از مدل فیزیکی و آماری وابستگی های گرافیکی توابع تعریف شده به عنوان $Ra = f(t, n)$ بیان شده است، $Ra = f(B, S)$ ثابت شده است که پرداخت ساینده در یک میدان مغناطیسی به مدت زمان ناچیزی اجازه می دهد تا زبری سطح را از ۱.۳...۱.۹ میکرومتر اولیه به $Ra = 0.23 \dots 0.85$ میکرومتر کاهش دهد. بسته به شرایط پردازش). علاوه بر این، مشکل بهینه سازی تعیین شرایط بهینه پرداخت ساینده در میدان مغناطیسی، با ارائه حداقل مقدار زبری رامین $= 0.23$ میکرومتر از سطوح قطعات ساخته شده از آلیاژ آلومینیوم AMTs حل شد.



Functional Model of Integrated Maintenance in Petrochemical Industries

S. M. Seyed Hosseini^{*a}, K. Shahanaghi^a, S. Shasfand^b

^a Department of Industrial & Civil Engineering, Iran University of Science and Technology, Tehran, Iran

^b Iran University of Science and Technology, Tehran, Iran, and Maintenance manager of Tabriz Petrochemical Company, Tabriz, Iran

PAPER INFO

Paper history:

Received 11 November 2023

Received in revised form 20 January 2024

Accepted 21 January 24

Keywords:

Integrated Maintenance Model

Human-Management-cost

Manpower

Petrochemical Industry

Knowledge

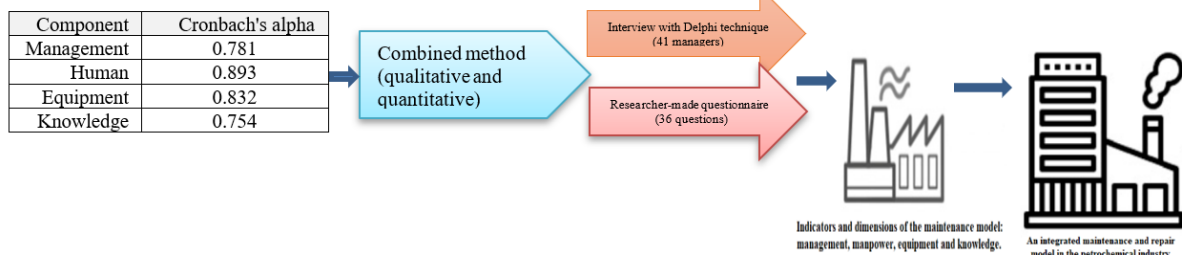
Energy Cost

A B S T R A C T

The purpose of this research is to provide an integrated maintenance model in the petrochemical industry. The current research is applied in terms of purpose and descriptive survey in terms of data collection method. A mixed method (qualitative and quantitative) has been used to conduct the research. The tools used in this research are researcher-made questionnaires (36 Questions), dialog with domestic and foreign professors in the field of maintenance and production, the Delphi technique (41 Maintenance managers), Field investigations (20 internal and 7 overseas petrochemical companies), and experiences and evidence obtained from 12 overhauls during 30 years. The validity was determined through experts' opinions and reliability through Cronbach's alpha evaluation. The results showed that the questionnaire has high validity and reliability. The statistical population includes experts in the field of Maintenance in industry and university, among whom 110 people were selected by targeted sampling. To conduct the research in the first stage, first by using the documentary method and content analysis and interviews with experts, the indicators and dimensions of the strong integrated maintenance and repair model were extracted and given to the experts in the form of a Likert scale for scoring; After conducting the survey, 36 components were selected, and each component of management, manpower, equipment, and knowledge had 9 sub-components. In the next step, the components and sub-components were scored and ranked using the questionnaire and the Analytical hierarchy process method. In this research, the following three results have been obtained: 1. Four main roots (Human, Management, Knowledge, and Equipment) and thirty-six sub-roots of effective maintenance. 2. The essential elements of the formula for measuring the criticality index of equipment. 3. Five indicators for measuring integrated maintenance performance. According to the calculations, the inconsistency between the vectors of each matrix is less than 0.10. Therefore, the constituent vectors of each of the formed matrices are consistent with the three results of the research and the stability of the respective comparisons is acceptable.

doi: 10.5829/ije.2024.37.06c.07

Graphical Abstract



1. INTRODUCTION

Maintenance is one of the basic concepts in advanced organizations and moving towards world-class and has a

special position among industrial managers. Today, maintenance care of particular importance with the demand for productivity, quality, and availability of equipment (1). Maintenance systems directly affect the

*Corresponding Author Email: seyedhosseini@iust.ac.ir
(S. M. Seyed Hosseini)

budget and profitability of industries, and the lack of proper planning of maintenance in the organization reduces the useful life of the equipment (2). Great attention to science of maintenance is necessary to respond to the expectations of industries, which is due to the limited resources such as energy, manpower, and capital, with suitable planning and its principled implementation, can lead to an increase in productivity, efficiency. Finally, the goals will be achieved (3).

Petrochemical industries are among the sensitive and complex industries that require efficient and practical maintenance due to the high volume of production, high added value, technical and safety risks, the need to comply with international standards, and high competition (4). Maintenance in petrochemical industries can improve performance, reduce costs, increase equipment life, reduce breakdowns, increase reliability, increase productivity, reduce waste, preserve the environment, and improve employee safety (5).

As the holder of first place in the country's non-oil exports, the petrochemical industry plays an essential role in the direction of economic prosperity, sustainable development, localization of technology, development of downstream industries, job creation, etc. The main advantages of this industry in Iran are the variety of feed, access to water resources, young and expert manpower. The petrochemical industry is one of the industries in which oil and gas are processed from the oil field region (6).

Considering that currently, Iran is considered the second gas-producing country and the fourth country in the field of crude oil production in the world. Iran is susceptible to the growth and development of the petrochemical industry. Thus, the development of the petrochemical industry is considered one of the important and strategic categories of development of the country. The petrochemical sector produces a variety of products, and among the products produced, polyethylene is very important due to its large volume, as well as its use and importance in the production of various of plastic appliances and food industries. So far, the countries of India, China, the Middle East and Far East, Europe, and Southeast Asia have been among the importers of Iranian petrochemical products (7).

A petrochemical complex is a complex combination of advanced equipment, machinery, and arteries. All kinds of valves, heat exchangers, steam boilers, distillation towers, hydraulic and gas turbines, separators, pumps and compressors, industrial valves, precision instruments, dryers, and blowers can be seen in a petrochemical complex. It takes years and sometimes decades to engineer and build a petrochemical complex, time, energy, and capital. In this complex, right after the start of operation, an important part of the costs is the maintenance of the refinery. Stopping production in a petrochemical complex can bring irreparable costs to the

complex (5). Access to specialized manpower, identification system for maintenance, and planning of these matters, along with issues related to the supply of required parts and consumables, is one of the challenges of this field (7).

To better use and increase the useful life of equipment and optimal use of resources, it is necessary to have a proper system of planning, analysis, control, and applying correct management methods (8).

Therefore, developing an effective and dynamic maintenance and repair system is very important. Neglecting the maintenance and repair of equipment, especially complex, sensitive, and expensive devices, imposes a lot of costs on the petrochemical industry and causes many problems for that organization. The environmental conditions of the studied industry, expensive equipment, and the problems of its replacement have increased the importance of this issue and the need to pay attention to maintenance and increase the effectiveness of the equipment (9). Therefore, considering the importance of Maintenance in the current research, we present a functional model of integrated maintenance in the petrochemical industry. Building upon the foundation established, we will delve into the definitions, categorizations, and models of maintenance and repairs, exploring their diverse applications. We will also outline the methodology and tools employed for data collection, introduce the research community involved in this field, and then embark on a comprehensive data analysis process. The culmination of this endeavor will be a presentation of the research outcomes and a proposed model that encapsulates the findings.

2. LITERATURE REVIEW

The continuous growth of industrial operations and the increasing complexity of production processes have fueled the development of maintenance and repair practices. Traditionally, maintenance has been associated with preserving and restoring capital assets to ensure their ability to perform desired tasks. The term "maintenance and repair" is defined in the EN 13306 standard as the combination of technical, administrative, and managerial actions throughout the lifecycle of an item to maintain or restore it to an optimal state for performing its intended function. The EN 13306 standard also defines maintenance management as the set of all activities that prioritize maintenance goals, set basic goals for the maintenance and repair department, determine the maintenance and repair strategies, and implement them through planning, control, support, and continuous improvement (10). In today's advanced and dynamic organizations, maintenance and repair strategies play a crucial role in optimizing asset utilization, enhancing productivity, and achieving organizational

objectives. Effective maintenance practices can lead to significant cost savings, improved product quality, and reduced downtime (11).

The management system of maintenance and repairs encompasses the comprehensive management of all physical assets within an organization, aiming to maximize capital utilization efficiency. By effectively managing inputs such as human resources, equipment, tools, and associated costs, and outputs such as the performance of devices and equipment during planned operations, maintenance management techniques like preventive inspections, schedule maintenance, and performance monitoring play a vital role in achieving desired performance levels (12). The maintenance and repair management process can be divided into two key phases: strategy definition and its implementation. Strategy definition involves establishing clear maintenance and repair goals, which serve as the foundation for other activities in the process, such as planning, scheduling, progress control, and indirect cost reduction. The correct implementation of maintenance and repair strategies effectively minimizes direct costs associated with labor and resources, aligning with the concept of efficiency (13).

Orrù et al. (14), Labib (15) and Mowbray (16) emphasized the complexity involved in developing and implementing effective maintenance and repair programs. They highlight that organizations often lack a systematic approach, leading to the adoption of various maintenance models, even among similar organizations. Similarly, consultants from different countries may present different maintenance models to their clients. To address these challenges and optimize asset utilization, a comprehensive system integrating planning, analysis, control, and sound management principles is essential. Neglecting maintenance and repair, especially for complex, sensitive, and expensive equipment, can incur significant costs and operational disruptions. The harsh environmental conditions in petrochemical industries, the high cost of equipment, and the challenges associated with replacement further underscore the importance of prioritizing maintenance and enhancing equipment effectiveness (17). In summary, maintenance and repair management encompasses activities aimed at maintaining or restoring production systems to ensure their efficient and economic operation. Key objectives include:

1. Ensuring system performance (availability, efficiency, and product quality)
2. Prolonging system life (asset management)
3. Maintaining safety
4. Promoting worker well-being (18).

In the world of manufacturing, the importance of efficient production planning is undeniable, particularly in the face of increasing competition. The high cost of equipment and the associated expenses of replacing damaged machinery necessitate effective maintenance

and repair strategies (19). As industries rapidly transition towards automation, the need for skilled personnel to manage and maintain equipment intensifies. Additionally, rising investment levels, production speeds, and spare part costs underscore the significance of integrating maintenance and repair processes into production systems (20). This approach aims to minimize repair costs and overall production expenses by employing techniques like regular inspections, scheduling maintenance tasks, and utilizing advanced monitoring systems (21). The strategies adopted in the petrochemical industry for maintenance and repairs have undergone significant transformations, particularly in terms of mindset and management style (22). However, a notable segment of experts, managers, and operations and maintenance executives still view production, maintenance, and repair processes as separate entities. This perspective fails to recognize the interconnectedness of these aspects and the potential benefits of adopting a holistic approach. In advanced industries worldwide, the concept of breakdown maintenance has gradually faded, replaced by a combination of preventive, predictive, and condition monitoring strategies (23). Experts strive to minimize or eliminate process disruptions, leading to the development of comprehensive maintenance and repair frameworks that optimize unit performance while minimizing costs and maximizing added value (24).

Reliability-centered maintenance (RCM) has emerged as a leading approach in the industry, providing a systematic method for determining the most appropriate maintenance strategy for equipment (systems). By analyzing factors like equipment criticality, failure modes, and potential consequences, RCM helps organizations make informed decisions about maintenance activities, ensuring optimal performance and minimizing disruptions (25). In summary, effective maintenance and repair strategies are crucial for manufacturing industries to thrive in the competitive landscape. By adopting a holistic approach that integrates maintenance and repair processes into production systems, organizations can achieve significant cost savings, enhance productivity, and safeguard their equipment's longevity. Reliability-centered maintenance (RCM) provides a valuable framework for making informed decisions about maintenance activities, ensuring that equipment is maintained in a condition that maximizes its availability, efficiency, and overall performance (21).

The maintenance and repair management system seeks to minimize repair costs and overall production expenses by implementing strategies such as regular inspections, scheduled maintenance, and advanced monitoring techniques. These measures contribute to reducing the financial burden associated with equipment breakdowns and enhancing overall operational efficiency.

In parallel, environmental concerns have gained prominence in recent years, recognized as a critical aspect of sustainable development. The escalating issues of air pollution and climate change have propelled governments worldwide to formulate policies aimed at curbing greenhouse gas emissions. These initiatives include imposing limits on carbon emissions and levying penalties for exceeding these thresholds (25, 26).

In summary, both economic and environmental considerations necessitate effective maintenance and repair practices. By optimizing equipment performance, organizations can reduce repair costs, minimize environmental impact, and contribute to sustainable development goals.

3. METHODOLOGY

The current research is applied in terms of fundamental purpose and descriptive survey in terms of the data collection method. A mixed method (qualitative and quantitative) was used to conduct the research. In the qualitative stage, the indicators and dimensions of the model were extracted using library studies, and a questionnaire was designed for the survey in the form of four areas human resources, equipment, knowledge, and management. Using the Delphi technique, the dimensions and components were approved by experts. The statistical population is experts in the field of maintenance industry and university, and 110 of them were selected as a sample by simple random sampling. The indicators extracted from the qualitative stage were provided to the sample in the form of a questionnaire. The validity of the questionnaire was confirmed by experts in the qualitative stage and its reliability was determined through Cronbach's alpha.

The method used in this research, which is based on the arithmetic mean of experts' opinions, is carried out in the following steps:

The arithmetic mean of the opinions of decision-makers was calculated in the form of a matrix and the relationship was calculated.

$$\bar{A} = \begin{bmatrix} (1, 1, 1) & \tilde{a}_{12} & \tilde{a}_{1n} \\ \tilde{a}_{21} & (1, 1, 1) & \tilde{a}_{2n} \\ \vdots & \vdots & \vdots \\ \tilde{a}_{n1} & \tilde{a}_{n2} & (1, 1, 1) \end{bmatrix}$$

$$\alpha_{ij} = \sum_{k=1}^{p_{ij}} a_{ijk} \quad i, j = 1, 2, \dots, n$$

Calculate the sum of row elements

$$S_i = \sum_{j=1}^n \alpha_{ij} \quad i = 1, 2, \dots, n$$

to normalize

$$M_i = s_i \otimes [\sum_{i=1}^n s_i] - 1 \quad i = 1, 2, \dots, n$$

Determining the degree of probability of being larger

$$V(M_2 > M_1) = \text{Sub}_{y \geq x} [\min(\mu_{M_1}(x), \mu_{M_2}(y))]$$

This relationship can be expressed synonymously as follows:

$$V(M_2 > M_1) = \text{hgt}(M_2 \cap M_1) = \mu_{M_2}(d)$$

$$m_2 \geq m_1$$

$$l_2 \geq u_1$$

Normalized weights are obtained by normalizing the vector of weights.

$$W = \left[\frac{d(A_1)}{\sum_{i=1}^n d(A_i)}, \frac{d(A_2)}{\sum_{i=1}^n d(A_i)}, \dots, \frac{d(A_n)}{\sum_{i=1}^n d(A_n)} \right] t$$

By combining the weights of the option and the criteria, the final weights are obtained.

$$U_i = \sum_{j=1}^n w_i r_{ij}$$

Finally, the inconsistency rate should be calculated. If the inconsistency rate is less than 0.10, the consistency of the comparisons is acceptable, and otherwise, the comparisons should be revised.

The results of Table 1 and Figure 1 shows that among the experts in the research community, 2 of them are experts, 3 are masters, 5 are deputy directors, 12 are maintenance managers, 4 are operations managers, 3 are Deputy complex, and 1 person has also been the manager of the petrochemical complex.

TABLE 1. Related to the organizational post of the respondents

The organizational post	Absolute abundance	Abundance percentage
Expert	2	6.7
Master expert	3	10
Deputy Director	5	10
Maintenance Manager	12	40
Operation Manager	4	13
Deputy complex	3	10
Complex Manager	1	3.3
Sum	30	100

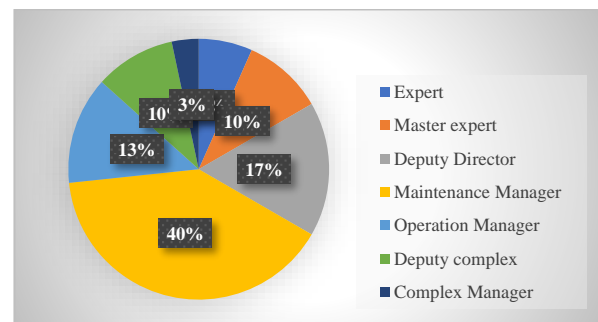


Figure 1. Related to the organizational post of the respondents

3. 2. Confirmatory Factor Analysis The most important goal of confirmatory factor analysis is to determine the power of the predefined factor model with a set of observed data. In other words, confirmatory factor analysis tries to determine whether the number of factors and variable loadings measured on these factors are consistent with what was expected based on the theory and theoretical model. In other words, this type of factor analysis tests the degree of conformity between the theoretical construct and the empirical construct of the research. In this method, the relevant variables and indicators were first selected based on the primary theory and after factor analysis, they were used to check whether these variables and indicators were loaded on the predicted factors as expected. Or that their composition has been changed and loaded on other factors. The second-order confirmatory factor analysis of management, knowledge, equipment and human variables were reported in Tables 2 to 5, respectively.

In the following, we will examine the statistical indicators to confirm the research data, which is given in Table 6.

TABLE 2. Second-order confirmatory factor analysis of the management variable

Component	Dimensions	Factor load	Estimation error	T statistic	The result of the path analysis
Management	MA1	0.7891	0.0113	36.9816	meaningful
	MA2	0.8145	0.0190	43.0050	meaningful
	MA3	0.8070	0.0219	39.1956	meaningful
	MA4	0.7801	0.0293	26.3816	meaningful
	MA5	0.8445	0.0186	22.7059	meaningful
	MA6	0.8333	0.0209	32.1956	meaningful
	MA7	0.7991	0.0222	35.9516	meaningful
	MA8	0.8145	0.0196	40.5059	meaningful
	MA9	0.8270	0.0198	41.0621	meaningful

TABLE 3. Second-order confirmatory factor analysis of the knowledge variable

Component	Dimensions	Factor load	Estimation error	T statistic	The result of the path analysis
Knowledge	KN1	0.8391	0.0213	29.3816	meaningful
	KN2	0.8944	0.0293	12.0330	meaningful
	KN3	0.8022	0.0119	19.4946	meaningful

KN4	0.8801	0.0283	26.3416	meaningful
KN5	0.8441	0.0196	21.7559	meaningful
KN6	0.8535	0.0229	22.1226	meaningful
KN7	0.8996	0.0233	34.9661	meaningful
KN8	0.8445	0.0177	30.0059	meaningful
KN9	0.8362	0.0244	29.5463	meaningful

TABLE 4. Second-order confirmatory factor analysis of the equipment variable

Component	Dimensions	Factor load	Estimation error	T statistic	The result of the path analysis
Equipment	EQ1	0.8032	0.0139	36.9816	meaningful
	EQ2	0.8801	0.0163	43.0050	meaningful
	EQ3	0.8241	0.0226	39.1956	meaningful
	EQ4	0.8323	0.0219	26.3816	meaningful
	EQ5	0.8801	0.0283	22.7059	meaningful
	EQ6	0.8311	0.0200	32.1956	meaningful
	EQ7	0.8981	0.0222	35.9516	meaningful
	EQ8	0.8845	0.0206	40.5059	meaningful
	EQ9	0.8181	0.0022	15.1511	meaningful

TABLE 5. Second-order confirmatory factor analysis of the human variable

Component	Dimensions	Factor load	Estimation error	T statistic	The result of the path analysis
Human	HU1	0.7899	0.0213	16.1816	meaningful
	HU2	0.8143	0.0290	13.0350	meaningful
	HU3	0.8323	0.0259	29.1056	meaningful
	HU4	0.8801	0.0243	26.3006	meaningful
	HU5	0.8313	0.0201	20.7012	meaningful
	HU6	0.8335	0.0219	22.1922	meaningful
	HU7	0.7999	0.0112	15.9916	meaningful
	HU8	0.8145	0.0096	10.5779	meaningful
	HU9	0.7960	0.0206	20.5510	meaningful

TABLE 6. Indicators and Current Situation

Indicator	Measurement criteria	Current situation
2X (k squared)	The smaller the better	178.15

(Degree of freedom)	Greater than Zero	29
(The significance level) P- Value	-	0.0000
(Squared error) RMSEA	Smaller than 0.8	0.138
GFI (Fitness index)	Greater than 0.9	0.98
(adjusted fitness index) AGFI	Greater than 0.9	0.93

According to the results of Table 6 and the level of significance and the degree of freedom, it can be concluded that the research data is normal, and since the significance level is less than 5%. It can be concluded that the chance of this difference or relationship is very low. It was concluded that the difference or relationship in question is significant. When the results of structural equations are presented, the resulting reports include several indicators to show the degree of model fit, usually the distribution of these indicators is X2. In the current research, the degree of freedom is equal to 178.15, which indicates the fit of the current research model.

In this research, Cronbach's alpha was used to check the reliability of the research questions. As shown in Table 7, considering that Cronbach's alpha of all the questions of the upper components is 0.7, it can be concluded that all the questions are valid.

After fitting the structural model (SEM), the reliability of the structure (conceptual variables) can be calculated. Construct reliability can be calculated based on composite reliability (CR) and variance extracted (AVE). Whenever one or more characteristics are measured through two or more methods, the correlation between these measurements provides two important indicators of reliability. If the correlation between the scores of tests that measure a single trait is high, the questionnaire has convergent validity. The existence of this correlation is necessary to ensure that the test measures what it is supposed to measure. According to the obtained results, it can be concluded that the existing sub-components have convergent validity, divergent validity, and reliable construct validity.

4. FINDINGS

In this part of the research, we will present the findings of the research considering that the four main

TABLE 7. Reliability of the first questionnaire

Component	Number of Questions	Cronbach's alpha
Management	9	0.781
Human	9	0.893
Equipment	9	0.832
Knowledge	9	0.754

components of management, knowledge, equipment, and manpower have been used in this research to examine the importance of evaluation indicators. Therefore, in the first place, we will introduce the main components of the research in the structural model of the research.

In this step, the dimensions and components of management and knowledge were extracted by studying the models and studies presented in the subject of research. The results show that each of the four main components of management, knowledge, equipment, and manpower under investigation has 9 sub-axis which are mentioned in the table above. In the continuation of the research, each of the sub-components was examined to check their weight and importance from the point of view of experts, and the results are shown in Tables 8 and 9.

The sub-components of income and cost, mission and strategy, risk and change, human resources and energy, planning and scheduling, efficiency and effectiveness, condition monitoring and foresight, corrective action and continuous improvement, control, and evaluation were selected. Regarding the knowledge component, the following components of standards and regulations, software, books and articles, research and development, less and practice, procedures, work orders, technical data and maintenance, and inherent knowledge of the expert were selected.

To determine the sub-component of equipment and manpower, by studying the models and studies conducted in the field of research, their dimensions and sub-

TABLE 8. Introducing management and knowledge sub-components in the strong integrated Maintenance model

Management	Income & Cost	MA1
	Mission & Strategy	MA2
	Risk & Change	MA3
	Human & Energy Resources	MA4
	Planning & Scheduling	MA5
	Efficiency & Effectiveness	MA6
	Condition Monitoring & Foresight	MA7
	Corrective action and continuous improvement	MA8
	Control & Evaluation	MA9
Knowledge	Standards & Regulation	KN1
	Software	KN2
	Books & Articles	KN3
	Research & Development	KN4
	Lessens & Practices	KN5
	Procedures	KN6
	Work orders	KN7
	Technical & Maintenance Data	KN8
	Expert's inherent knowledge	KN9

TABLE 9. Introducing the sub-components of equipment and manpower in the strong integrated Maintenance model

Equipment	Criticality Analysis	EQ1
	Condition Monitoring	EQ2
	Life Cycle Cost	EQ3
	Risk Based Inspection	EQ4
	Optimized Risk & Cost	EQ5
	Overall Equipment Effectiveness	EQ6
	Root cause failure Analysis	EQ7
	Reliability Centered Maintenance	EQ8
	Availability and Maintainability	EQ9
Human	Motivation & Effort	HU1
	Commitment & Ethical	HU2
	Education & Learning	HU3
	Expertise & Experience	HU4
	Flexibility & Creativity	HU5
	Responsibility & Loyalty	HU6
	Mental Model & Behavior	HU7
	Encouragement & Appreciation	HU8
	Culture & Teamwork	HU9

components were determined, as shown in Table 3, the sub-components of equipment include critical analysis, condition monitoring, cycle cost life, risk-based inspection, optimized risk and cost, the overall effectiveness of equipment, root cause analysis of failure, maintenance based on reliability and availability and maintenance, and the sub-components of human resources include motivation and effort, commitment and ethics, education and learning, expertise and experience, flexibility and creativity, responsibility and loyalty, mental model and behavior, encouragement and appreciation, and culture and teamwork.

The results of the investigations in Table 10 show that the sig (significance level) of all variables is greater than 0.05. Therefore, at the 95% confidence level, it can be said that the distribution of all data is normal.

In Table 11 and Figure 2 the ranking of the criteria for evaluating the quality of maintenance and production

TABLE 10. Checking the normality of population distribution

Variables	Average	The significance level
Human	4.41	0.22
Equipment	3.33	0.41
Management	3.87	0.08
Knowledge	4.95	0.90
The whole questionnaire	4.12	0.20

TABLE 11. Friedman's test ranks the importance of each of the quality evaluation criteria of the new model

Evaluation criteria	Average rank	Statistics χ^2
Cost	6.97	47.773
Production	6.54	
Reliability	6.79	
Availability	6.70	
Operational Risk	6.52	
Safety	6.72	
Quality	6.49	
Environment	6.43	
Maintainability	6.52	
Energy	6.12	

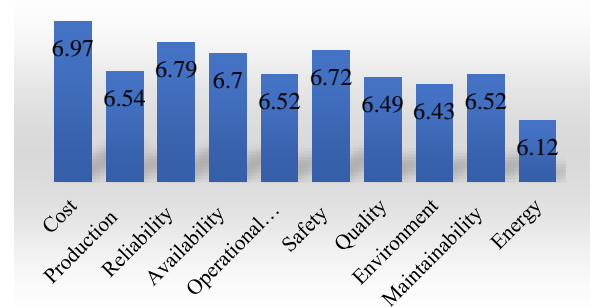


Figure 2. Friedman's test ranks the importance of each of the quality evaluation criteria of the new model

from the point of view of experts was discussed, among which the cost component is the first important criterion with an average of 6.97. The energy component with an average of 6.12 ranks last in service quality evaluation criteria. The important features and sub-features should be considered in choosing a Maintenance strategy, including determining the criteria that are involved in the decision-making process for choosing maintenance and repair strategies. The analysis should be done in such a way that the maintenance and repair strategy that is chosen will achieve the desired goals, improve the availability, and reduce the number of failures.

The top and most important according to a survey conducted in the field of maintenance and repair of the petrochemical industry, from the point of view of experts, the most important factors are cost, reliability, and availability, respectively, with coefficients of 6.97, 6.79, and 6.70. The repair of machinery in the petrochemical field has been selected.

To obtain the equipment criticality index and coefficients of its essential elements, we used the Likert preferences of 75 experts using the AHP method. Equation 1 and Table 13 present the results.

$$ECI=0.116Q+0.105P+0.117S+0.099E+0.089OR+0.104R+0.089A+0.105M+0.077ES+0.105C \quad (1)$$

Pairwise comparison scale for AHP preferences by 64 judges are stated in Table 14.

The matrix for the calculation of the inconsistency rate is reported in Table 15. Weight Coefficients of Integrated Maintenance obtained from geometric mean is stated in Table 16.

TABLE 12. The judgment of 75 experts on the coefficients of the 10 elements of determining the sensitivity of equipment its calculations based on Satya's (AHP)

No.	Judgment by	Judgment by										No.	Judgment by	Judgment by									
		Quality	Capacity	Safety	Environment	Operation Risk	Reliability	Availability	Maintainability	Energy	Cost			Quality	Capacity	Safety	Environment	Operation Risk	Reliability	Availability	Maintainability	Energy	Cost
1	Main. Manag.*7	12	9	12	10	9	10	8	11	8	11	38	MR-2	10	5	10	22	5	10	10	10	10	20
2	Planning	12	10	12	9	6	12	10	10	7	12	39	Jam-DOPM	13	10	10	9	10	12	10	10	7	10
3	Mechanical	12	11	11	10	9	10	7	11	8	12	40	JPC	11	8	12	9	8	13	10	11	8	11
4	R&D	12	9	10	11	9	11	9	10	10	10	41	PPC	10	10	14	12	8	11	12	5	6	12
5	HRM	12	10	11	9	11	9	10	10	9	9	42	MR-4	14	10	13	9	10	11	9	10	9	10
6	DOCM	11	12	8	10	13	11	8	12	8	9	43	Razak MD	12	10	10	10	10	10	9	10	9	10
7	Percurment	12	11	13	7	11	10	8	9	8	11	44	DOCM-Jam	8	15	10	8	8	10	10	8	8	15
8	Shift head	12	10	11	8	10	10	9	12	10	9	45	MM1	8	8	15	10	15	10	9	15	10	15
9	Feed head	9	12	12	10	12	9	7	10	7	12	46	MM2	12	8	12	10	10	10	8	12	9	12
10	CM	10	10	12	11	9	10	8	10	10	10	47	MM3	10	10	14	8	8	10	10	12	8	10
11	IT	11	8	14	13	9	8	12	11	8	7	48	-MOTS KHPC	15	7	12	8	8	10	10	8	8	10
12	Electrical	12	10	12	10	9	10	8	11	8	11	49	MOP-AKPC	12	9	11	10	10	9	10	10	9	10
13	SSD	12	11	11	9	10	11	8	11	9	9	50	MM4	10	10	14	10	6	10	8	12	7	11
14	DOM	11	10	12	11	9	10	8	11	9	10	51	MM5	12	9	11	9	9	10	9	8	10	13
15	Shift manager	15	8	11	12	8	9	9	10	8	11	52	MM6	12	9	12	10	9	12	6	11	8	11
16	Security	11	10	11	9	10	11	9	10	8	11	53	MM7	12	9	13	9	9	10	8	11	9	10
17	Exc &IT	10	12	12	8	10	12	11	10	6	10	54	MM8	12	10	13	10	9	10	10	12	7	12
18	Planning	12	12	8	6	10	12	12	11	8	12	55	MM9	10	11	12	8	9	12	10	11	8	11
19	Supervisour1	12	14	10	12	12	9	9	9	13	12	56	-MOM	10	10	13	11	10	10	10	10	8	10
20	Supervisour2	12	11	10	8	9	11	9	10	10	13	57	-DOMM	12	10	12	11	9	9	8	12	8	11
21	Supervisour3	15	15	8	12	10	8	8	8	6	12	58	MM10	10	9	15	9	12	10	10	9	8	11
22	Supervisour4	10	10	15	15	11	15	1	10	10	5	59	MM11	12	8	14	9	10	12	10	10	8	9
23	M.S.S1	12	10	14	10	10	10	6	10	9	10	60	MM12	12	9	15	7	9	10	10	11	8	11
24	M.S.S2	12	9	12	9	9	10	11	10	8	11	61	MM13	11	9	15	12	9	10	7	11	7	10
25	M.S.S3	18	9	12	10	4	10	8	11	7	11	62	MM14	13	9	11	8	9	10	8	11	1	12
26	M.S.S4	12	9	12	8	8	10	10	11	10	11	63	-MOM	10	9	10	11	10	9	8	12	10	11
27	M.S.S5	14	12	10	7	7	12	9	12	7	10	64	BIPC	11	8	15	12	8	10	8	10	8	10
28	M.S.S6	14	8	10	10	10	10	10	12	5	10	65	MOM-REPC	12	8	12	12	7	10	8	10	10	11
29	M.S.S7	12	9	12	11	8	10	8	11	9	9	66	-MOM	12	11	12	10	10	11	9	11	6	10
30	M.S.S8	12	8	12	10	8	10	9	10	10	11	67	Pars MM	12	9	12	10	9	10	8	11	7	12
31	M.S.S9	12	10	12	10	8	10	7	11	11	9	68	ARYA_S_MM	10	13	13	10	9	8	8	10	8	10
32	M.S.S10	12	11	12	10	10	11	8	8	8	9	69	MM15	12	9	12	10	9	10	8	12	7	11
33	M.S.S11	12	11	12	10	10	11	8	10	8	8	70	MM16	11	9	13	11	8	10	9	11	7	11
34	M.S.S12	12	8	12	10	8	11	9	11	8	11	71	MS.SA	10	10	13	11	9	9	10	11	8	10
35	M.S.S13	13	9	12	10	9	10	9	12	8	11	72	TRC-MM	10	10	12	10	10	10	8	13	7	10
36	M.S.S14	10	10	12	10	9	10	9	12	8	11	73	TRC-S-1	12	10	11	10	10	10	8	10	9	10
37	MR-1	9	12	10	12	9	10	11	8	11	8	74	TRC-S-2	12	9	12	9	10	9	9	13	8	10
												75	TRC-S-3	11	9	12	10	9	10	9	10	9	11

TABLE 13. Equipment criticality elements and related coefficients

Item	Quality	Production	Safety	Environment	Operational Risk
Coefficient	0.116 - Q	0.105 - P	0.117 - S	0.099 - E	0.089 - OR
Item	Reliability	Availability	Maintainability	Energy Saving	Cost
Coefficient	0.104 - R	0.089 - A	0.105 - M	0.077 - ES	0.105 - C

TABLE 14. Pairwise comparison scale for AHP preferences by 64 judges (OEE, OLE, EEE, HSE, and OCE)

Pairwise comparison scale for AHP prefe						64 Judges							
Judgment By	OEE	OLE	EEE	HSE	OCE	Judgment By	OEE	OLE	EEE	HSE	OCE		
J1	Inspection Head	7	5	4	7	9	J33	Instrument Engineer	3	5	7	5	9
J2	Deputy of Complex M	8	6	7	7	6	J34	Inspection Engineer	7	4	6	4	4
J3	Reliability Engineer	7	9	9	6	8	J35	Workshop Manager	3	5	7	5	8
J4	Planning engineer	8	8	9	7	7	J36	Instrument Manager	4	4	6	5	4
J5	Planning Manager	9	7	5	7	9	J37	Professor	9	4	6	5	9
J6	O/H Head	8	9	8	7	6	J38	Professor	3	4	7	3	3
J7	CM Head	7	8	6	6	9	J39	Professor	5	3	6	4	8
J8	Instrument Head	5	9	8	5	5	J40	Professor	9	4	6	5	5
J9	Service	8	9	7	5	5	J41	Professor	3	4	7	4	3
J10	Planning Head	9	8	7	6	5	J42	Deputy of Complex M-J	4	4	6	5	5
J11	Electrical Head	7	9	8	5	6	J43	Professor	3	4	6	4	4
J12	Packaging Head	9	8	8	5	7	J44	Professor	4	8	6	4	4
J13	Maint. Manager	8	8	7	7	7	J45	Project Manager	7	5	4	7	9
J14	Machinery Head	9	8	8	9	7	J46	PHD-Student	8	6	7	7	6
J15	Electrical Manager	8	9	5	6	7	J47	Mechanical. Eng.	7	9	9	6	8
J16	Coplex Manager	4	4	6	5	4	J48	Mechanical. Eng.	8	8	8	7	7
J17	IT manager	4	5	6	5	4	J49	electrical eng.	9	7	5	7	9
J18	DOMM	4	4	6	9	3	J50	electrical eng.	8	9	8	7	7
J19	R&D Maneger	5	6	8	7	6	J51	Project eng.	7	8	6	6	8
J20	Process	4	4	6	4	3	J52	Human Resource Manager	5	9	8	5	5
J21	Planning	4	4	6	5	5	J53	Contractor Manager	8	9	7	5	6
J22	Inspection Manager	5	4	6	5	5	J54	Master.S .Student	9	8	7	6	5
J23	Production Manager	4	3	5	4	4	J55	Energy control head	7	9	8	5	6
J24	Technical Ser. Mang.	3	4	6	4	9	J56	Maint. Manager-PPC	9	8	8	5	7
J25	Maintenance shift Head	3	8	9	5	5	J57	Maint. Manager-OPC	8	8	7	7	6
J26	Maintenance shift Head	5	6	9	7	9	J58	Maint. Manager-BIPC	9	8	8	9	7
J27	Manitenance Ser. Manage	4	4	6	5	4	J59	Plan. Manager-AKPC	8	9	5	6	7
J28	CM. Engineer	3	5	6	3	3	J60	DOMM-ARPC	5	4	6	3	3
J29	Electrical Engineer	4	4	6	4	4	J61	Eng.Manager-NPC	4	4	6	4	4
J30	Civil Engineer	2	7	9	3	3	J62	Maint. Manager-TPC	4	4	6	4	3
J31	Engeneering Head	3	4	6	5	5	J63	Maint. Manager-Arya	4	4	7	5	4
J32	Machinery Engineer	3	5	6	3	3	J64	Maint. Manager-KHPC	8	8	7	7	9

OEE: Overall Equipment Effectiveness;
 OLE: Overall Labor Effectiveness;
 EEE: Endogeneity, Extroversion, and Exogenous;
 HSE: Health, Safety, and Environment;
 OCE: Overall Cost Effectiveness

TABLE 15. The matrix for the calculation of the inconsistency rate

	A1	A2	A3	A4	A5
WF	0.190	0.202	0.232	0.182	0.194
A1	0.190	1.000	0.941	1.044	0.979
A2	0.202	1.063	1.000	1.110	1.041
A3	0.232	1.221	1.149	1.000	1.196
A4	0.182	0.958	0.901	1.000	0.938
A5	0.194	1.021	0.960	0.836	1.000

$\Pi = (\lambda_{max} - n) / 4 = (5.255 - 5) / 4 = 0.6375$

$Ci = \Pi / (Cr \text{ or } R.I), n=5 \rightarrow Cr \text{ or } R.I = 1.12 \Rightarrow Ci = 0.057 '0.1$

TABLE 16. Weight Coefficients of Integrated. Maintenance obtained from geometric mean

Coefficient	Item	AHP
A1	OEE	0.190
A2	OLE	0.202
A3	EEE	0.232
A4	HSE	0.182
A5	OCE	0.194

Considering the results, the inconsistency rate is less than 0.10, as a result, the matrix is compatible and the stability of the comparisons is acceptable.

5. RESULT

The findings showed that the establishment of an integrated net system can lead to the improvement of related indicators. One of the most important reasons for this is to design and provide written implementation methods for each step of the hierarchy of stopping. Because the stoppage is not a routine operation and the probability of problems related to process safety is higher in these situations than in normal operation times.

Another reason is that the system created to prevent the wear and tear of machine components can reduce unplanned breakdowns and, as a result, machines being out of reach. On the other hand, in the implemented system, the failure times of the parts are predicted. Therefore, these parts are purchased in advance, which leads to a reduction in procurement time and an improvement in the average repair time after the installation of the system compared to before.

Considering that petrochemical industries usually use old equipment and machinery that are usually at least 15 years old in their upstream, middle, and downstream operations. Therefore, an integrated system of maintenance is necessary to keep this relatively old equipment operational. In such a situation, adopting a reactive maintenance and repair tactic does not provide any guarantee that sudden and unplanned outages will not occur. The working nature of these complexes is vital and at the same time very dangerous. For this reason, it needs double care and supervision. In the petrochemical industry, many accidents such as fire and explosion or even the stoppage of some equipment lead to huge damages, which is generally due to the failure of the parts used in the equipment and processes. It is vital to know and how these failures occur to prevent them from increasing system reliability, optimizing process performance and profitability.

6. CONCLUSION

In today's competitive industrial landscape, organizations must prioritize maintenance and repair strategies to safeguard their performance, efficiency, and productivity. These strategies play a crucial role in maintaining equipment reliability, availability, and product quality while mitigating risks and reducing downtime. As investments in industries surge, the efficient utilization of resources and raw materials becomes paramount for industrial owners and responsible managers. This is particularly critical in the face of intense competition in both domestic and global markets.

A growing number of engineers and managers are recognizing the significance of maintenance and repair engineering, often referred to as 'Net' in technical and engineering terms. Modern net engineering departments in industrial units have adopted statistical and mathematical methods to enhance their planning capabilities, transforming net into a knowledge-based discipline. Numerous companies have employed various net strategies, including corrective net, preventive net, comprehensive productive net, reliability-based net, and status-based net. However, the primary challenge faced by those involved in maintenance and repair lies not only in applying these techniques but also in making informed decisions regarding the selection of the most suitable and effective maintenance and repair strategies for their organization's specific needs. This research delves into the development of an integrated maintenance and repair management model tailored to the unique needs of the petrochemical industry. The study's initial phase involved identifying the key components of the maintenance management model through theoretical discussions and expert interviews. By analyzing the findings, the dimensions, components, and sub-components of the model were extracted, yielding a four-component structure.

The research focused on four key components: management, manpower, equipment, and knowledge. The results indicated that knowledge is the most critical component (importance coefficient of 0.90), followed by equipment (0.41), manpower (0.22), and management (0.08) in terms of their impact on implementing an integrated maintenance and repair system.

The subsequent stage involved evaluating maintenance and repair quality using expert opinions. The cost component emerged as the most significant criterion (average score of 6.97), while the energy component ranked lowest (average score of 6.12). These rankings highlight the importance of prioritizing cost-effectiveness and energy efficiency in establishing a robust maintenance and repair system.

The study identifies human incentives, management, equipment, and knowledge as the key components for establishing an integrated maintenance model in the petrochemical industry. Based on these findings, the following suggestions are proposed: Formulate comprehensive guidelines and regulations for integrated maintenance in Iranian petrochemical companies to shift the mindset of senior, middle management, and employees from traditional maintenance to integrated maintenance practices. Provide comprehensive training programs for managers and employees to cultivate integrated maintenance thinking and instill a long-term vision of the benefits of integrated maintenance, recognizing its potential to enhance petrochemical industries' economic, social, and environmental performance, leading to increased competitiveness and market success.

Develop maintenance sustainability strategies based on a thorough assessment of internal and external environmental factors, including opportunities, threats, strengths, and weaknesses. Prioritize product quality and quantity by closely monitoring key indicators such as OEE (Overall Equipment Effectiveness), OCE (Overall Cycle Effectiveness), OLE (Overall Logistics Effectiveness), HSE (Health, Safety, and Environment), and EEE (Energy Efficiency).

Implement industry-standardized maintenance procedures that encompass safety, health, environment, energy, production, quality, cost, revenue, export, stress, risk, maintainability, reliability, availability, replacement cost, motivation, and satisfaction. Embrace appropriate maintenance tools like Total Productive Maintenance (TPM), Reliability-Centered Maintenance (RCM), Risk-Based Inspection (RBI), Industry 4.0 technologies, Artificial Intelligence (AI), and the Internet to enhance maintenance efficiency and effectiveness. For future research, the following areas are recommended: Explore the intricate relationship between maintenance, the Internet, business environment, Industry 4.0, and Artificial Intelligence (AI) to optimize maintenance strategies. Develop effective mechanisms for managing conflicts, interactions, and the impact of various organizational units' activities (e.g., top management, operations, maintenance, safety, procurement, finance, human resources, and education) to ensure seamless and coordinated maintenance operations.

Investigate the potential of Internet-based failure detection and artificial intelligence-based condition monitoring systems to enhance maintenance proactiveness and reduce downtime.

Conduct research on the application of integrated maintenance practices in the context of pandemics (such as COVID-19), warfare, embargos, and uncertainty to develop resilient and adaptable maintenance strategies.

7. REFERENCES

- Hadidi LA, Ghaithan A, Mohammed A, Alhwoaikan N. A Markov-based model to mitigate human errors occurrence during maintenance activities in petrochemical systems. *International Journal of System Assurance Engineering and Management*. 2023;14(6):2146-59. <https://doi.org/10.1007/s13198-023-02045-5>
- Rahimi Komijani H, Shahin M, Jabbarzadeh A. Optimal policy of condition-based maintenance considering probabilistic logistic times and the environmental contamination issues. *International Journal of Engineering, Transactions B: Applications*. 2018;31(2):357-64. 10.5829/ije.2018.31.02b.21
- O'Neil R, Khatab A, Diallo C, Venkatadri U. Optimal joint maintenance and orienteering strategy for complex mission-oriented systems: A case study in offshore wind energy. *Computers & Operations Research*. 2023;149:106020. <https://doi.org/10.1016/j.cor.2022.106020>
- Tong L, Pu Z, Chen K, Yi J. Sustainable maintenance supplier performance evaluation based on an extend fuzzy PROMETHEE II approach in petrochemical industry. *Journal of Cleaner Production*. 2020;273:122771. <https://doi.org/10.1016/j.jclepro.2020.122771>
- Tutubalin P, editor Method of increasing information security of petrochemical industry enterprises using NFC technology. 2021 International Conference on Industrial Engineering, Applications and Manufacturing (ICIEAM); 2021: IEEE.
- Diallo C, Venkatadri U, Khatab A, Liu Z. Optimal selective maintenance decisions for large serial k-out-of-n: G systems under imperfect maintenance. *Reliability Engineering & System Safety*. 2018;175:234-45. <https://doi.org/10.1016/j.res.2018.03.023>
- Yazdanparast S, Sadegheih A, Fallahnezhad M, Abooe M. Modelling and decision-making on deteriorating production systems using stochastic dynamic programming approach. *International Journal of Engineering, Transactions B: Applications*. 2018;31(12):2052-8. 10.5829/ije.2018.31.12c.09
- Ajmi AA, Mahmood NS, Jamaludin KR, Talib HHA, Sarip S, Kaidi HBM. WITHDRAWN: An efficient framework for identifying current open issues to prevent human errors in maintaining power plants: Research gap. Elsevier; 2021.
- Shou W, Wang J, Wu P, Wang X. Lean management framework for improving maintenance operation: Development and application in the oil and gas industry. *Production Planning & Control*. 2021;32(7):585-602. <https://doi.org/10.1080/09537287.2020.1744762>
- Wari E, Zhu W, Lim G. Maintenance in the downstream petroleum industry: A review on methodology and implementation. *Computers & Chemical Engineering*. 2023;172:108177. <https://doi.org/10.1016/j.compchemeng.2023.108177>
- Alkough A, Keddar KA, Alatefi S. Revolutionizing Repairability of Industrial Electronics in Oil and Gas Sector: A Mathematical Model for the Index of Repairability (IOR) as a Novel Technique. *Electronics*. 2023;12(11):2461. <https://doi.org/10.3390/electronics12112461>
- Kaveh Pishghadam H, Esmaeeli H. A system dynamics model for evaluating the firms' capabilities in maintenance outsourcing and analyzing the profitability of outsourcing. *Scientia Iranica*. 2023;30(2):712-26. <https://doi.org/10.24200/sci.2021.55108.4080>
- Salehi V, Zarei H, Shirali GA, Hajizadeh K. An entropy-based TOPSIS approach for analyzing and assessing crisis management systems in petrochemical industries. *Journal of Loss Prevention*

- in the Process Industries. 2020;67:104241. <https://doi.org/10.1016/j.jlp.2020.104241>
14. Orrù PF, Zoccheddu A, Sassu L, Mattia C, Cozza R, Arena S. Machine learning approach using MLP and SVM algorithms for the fault prediction of a centrifugal pump in the oil and gas industry. *Sustainability*. 2020;12(11):4776. <https://doi.org/10.3390/su12114776>
 15. Labib AW. World-class maintenance using a computerised maintenance management system. *Journal of Quality in Maintenance Engineering*. 1998;4(1):66-75. <https://doi.org/10.1108/13552519810207470>
 16. Moubray J. *Reliability-centered maintenance*: Industrial Press Inc.; 2001.
 17. Crespo Márquez A, Moreu de Leon P, Gomez Fernandez J, Parra Marquez C, López Campos M. The maintenance management framework: A practical view to maintenance management. *Journal of Quality in Maintenance Engineering*. 2009;15(2):167-78. <https://doi.org/10.1108/13552510910961110>
 18. Ahmad R, Kamaruddin S. An overview of time-based and condition-based maintenance in industrial application. *Computers & industrial engineering*. 2012;63(1):135-49. <https://doi.org/10.1016/j.cie.2012.02.002>
 19. Ding S-H, Kamaruddin S. Maintenance policy optimization—literature review and directions. *The International Journal of Advanced Manufacturing Technology*. 2015;76:1263-83. <https://doi.org/10.1007/s00170-014-6341-2>
 20. Ahuja IPS, Khamba JS. Total productive maintenance: literature review and directions. *International journal of quality & reliability management*. 2008;25(7):709-56. <https://doi.org/10.1108/02656710810890890>
 21. Alaswad S, Xiang Y. A review on condition-based maintenance optimization models for stochastically deteriorating system. *Reliability engineering & system safety*. 2017;157:54-63. <https://doi.org/10.1016/j.res.2016.08.009>
 22. Shahriar A, Sadiq R, Tesfamariam S. Risk analysis for oil & gas pipelines: A sustainability assessment approach using fuzzy based bow-tie analysis. *Journal of loss prevention in the process Industries*. 2012;25(3):505-23. <https://doi.org/10.1016/j.jlp.2011.12.007>
 23. Allal A, Sahnoun Mh, Adjoudj R, Benslimane SM, Mazar M. Multi-agent based simulation-optimization of maintenance routing in offshore wind farms. *Computers & Industrial Engineering*. 2021;157:107342. <https://doi.org/10.1016/j.cie.2021.107342>
 24. Chaabane K, Khatab A, Diallo C, Aghezaf E-H, Venkatadri U. Integrated imperfect multitemission selective maintenance and repairpersons assignment problem. *Reliability Engineering & System Safety*. 2020;199:106895. <https://doi.org/10.1016/j.res.2020.106895>
 25. Petronio B, Pietrantonio M, Pietroletti M, Cardellicchio N, editors. *Environmental science and pollution research. proceedings Seventh FECS Conference, Metal speciation and bio-availability in marine sediments of Northern Adriatic sea*; 2000.
 26. WANG MY, HYTOWITZ R, GOLDBERG K, LUH PB, VISWANADHAM N, VOLZ R, et al. *IEEE Transactions on Automation Science and Engineering*. Science & Technology.852:3469-2544.

COPYRIGHTS

©2024 The author(s). This is an open access article distributed under the terms of the Creative Commons Attribution (CC BY 4.0), which permits unrestricted use, distribution, and reproduction in any medium, as long as the original authors and source are cited. No permission is required from the authors or the publishers.

**Persian Abstract**

چکیده

هدف از پژوهش حاضر ارائه یک مدل نگهداری و تعمیرات یکپارچه در صنعت پتروشیمی می باشد. تحقیق حاضر از نظر هدف، کاربردی و از نظر روش گردآوری داده ها، توصیفی-پیمایشی است. برای انجام پژوهش از روش ترکیبی (کیفی و کمی) استفاده شده است. ابزار مورد استفاده در این تحقیق، پرسشنامه محقق ساخته (۳۶ سوال)، گفتگو با اساتید داخلی و خارجی در زمینه نگهداری و تولید، تکنیک دلفی (۴۱ مدیر تعمیر و نگهداری)، تحقیقات میدانی (۲۰ شرکت پتروشیمی داخلی و ۷ شرکت پتروشیمی خارج از کشور)، تجربیات و شواهد به دست آمده از ۱۲ تعمیرات اساسی در طول ۳۰ سال است. که روایی پرسشنامه از طریق نظرات خبرگان و پایایی آن از طریق ارزیابی آلفای کرونباخ تعیین شده است. نتایج نشان می دهد که پرسشنامه دارای روایی و پایایی بالا می باشد. جامعه آماری شامل، متخصصان حوزه نگهداری و تعمیرات در صنعت و دانشگاه می باشد که از بین آنها ۱۱۰ نفر به روش نمونه گیری هدفمند انتخاب شده اند. جهت انجام تحقیق در مرحله اول، ابتدا با استفاده از روش اسنادی، تحلیل محتوا و مصاحبه با خبرگان، شاخص ها و ابعاد مدل نگهداری و تعمیرات یکپارچه قوی استخراج گردید و به صورت طیف لیکرت جهت امتیاز دهی در اختیار خبرگان قرار گرفت؛ بعد از انجام بررسی تعداد ۳۶ زیر مولفه انتخاب گردید که هر یک از مولفه های اصلی: مدیریت، نیروی انسانی، تجهیزات و دانش دارای ۹ زیر مولفه بودند. در مرحله بعد با استفاده از پرسشنامه و به روش فرآیند تحلیل سلسله مراتبی به امتیاز دهی و رتبه بندی مولفه ها و زیر مولفه ها پرداخته شد. در این تحقیق سه نتیجه زیر به دست آمده است: ۱- چهار ریشه اصلی (انسان، مدیریت، دانش و تجهیزات) و سی و شش ریشه فرعی نگهداشت اثر بخش. ۲- عناصر ضروری فرمول اندازه گیری شاخص بحرانی تجهیزات. ۳- پنج شاخص برای اندازه گیری عملکرد تعمیر و نگهداری یکپارچه. با توجه به محاسبات، مقدار ناسازگاری بین بردارهای هر ماتریس کمتر از ۰.۱۰ است. بنابراین، بردارهای تشکیل دهنده هر یک از ماتریس های تشکیل شده برای نتایج سه گانه تحقیق سازگار بوده و همچنین پایدار می باشد. مقایسه های مربوطه قابل قبول هستند.



Stone Architecture in Abruzzo: Seismic Risk Analysis of Bell Tower of the Church of San Lorenzo in San Buono

F. Marchione*

Dipartimento di Ingegneria Civile, Edile e Architettura (DICEA), Università Politecnica delle Marche, via B. Bianche, Ancona, Italy

PAPER INFO

Paper history:

Received 11 November 2023

Received in revised form 16 December 2023

Accepted 06 January 2024

Keywords:

Masonry Structures

Seismic Risk Analysis

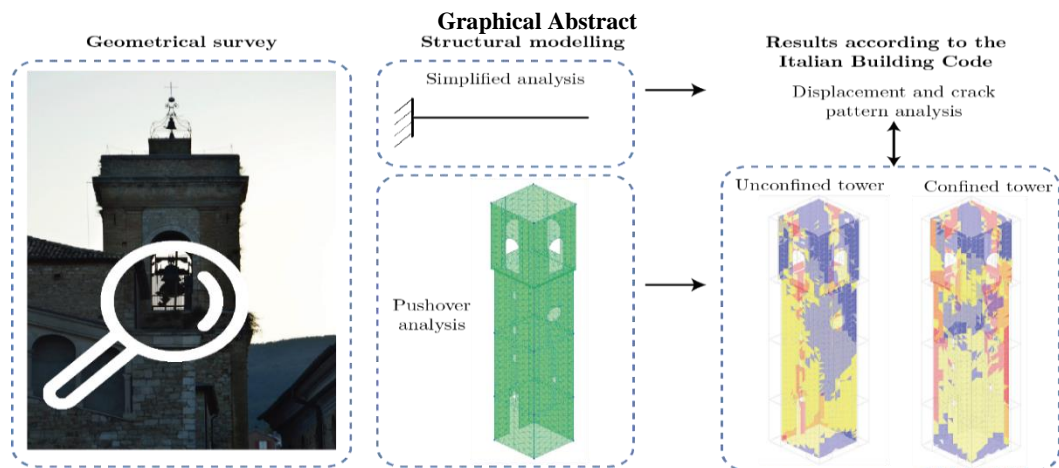
Masonry Tower

Seismic Assessment

ABSTRACT

The church of San Lorenzo in San Buono (Italy) is unique in the local landscape due to its technical, and architectural features. The building, whose construction dates from the 14th century to the mid-20th century, was realized by the most important designers in the region. The bell tower is an element characterized by refined neoclassicism and testifies to a remarkable episode of the permanence of the neoclassical style in Abruzzo until the first decades of the 20th century. The present study illustrates both a technological-constructive analysis of the building and an assessment of the seismic risk of the bell tower, to present an important point for the knowledge of the artefact with regard to possible conservative restoration works. The seismic risk analyses are carried out for two different structural configurations and two different typologies allowed by the Italian building codes for monumental masonry buildings: simplified linear and non-linear static. The study illustrates how the presence of the adjacent structure significantly alters the structural behavior of the masonry tower, both in terms of displacement and propagation of the crack pattern. The differences in the results of the non-linear calculation and the expeditious methods suggested by the standard are highlighted as well.

doi: 10.5829/ije.2024.37.06c.08



1. INTRODUCTION

Neoclassicism refers to an eclectic movement that spanned the entire European cultural landscape and was

based on both aesthetic considerations and matters of taste (1). In architecture, there was indeed a revival of Roman and Greek architectural principles. While searching for the architectural archetypes that had

*Corresponding Author Institutional Email:
f.marchione@pm.univpm.it (F. Marchione)

favoured the emergence and development of classical architecture, rationality, applied to previous architectural experiences, led to the definition of the concepts of typology and style (1, 2).

The neoclassic architecture, which origins in the 18th century, found a new home in the 19th century when it contributed to the “Empire” style (3). Although it is possible to identify certain historical and cultural-historical circumstances to locate its development, a precise spatial and temporal definition is not possible. Despite the fact that the European architectural scene at the beginning of the 20th century was oriented towards Art Nouveau and the new modern building systems that were becoming more and more prevalent, neoclassical orientations continued to shape the artistic culture of the 19th century. Moreover, it preserved an essential homogeneity of theoretical and speculative premises that formed the basis for mid-20th century monumentalism and the rationalist architecture that followed (4).

The present study illustrates both a technological-constructive analysis of the building and an assessment of the seismic risk of the bell tower, in order to present an important point for the knowledge of the artifact with regard to possible conservative restoration works.

Ozturk (5) studied the seismic behavior of two monumental masonry buildings in Cappadocia. The effect of structural walls on their seismic behavior was highlighted through dynamic analyses.

In the analysis of the damage, the decisive role played by the layout of the floors in the pattern of damage in the dome roofs was described. Guney et al. (6) studied the effect of seismic action on earthen buildings affected by the earthquake in Turkey in 2010 and 2011. The study has focused on the main parameters for describing the seismic behavior of buildings affected by the earthquake (i.e., foundations, type of masonry, geometry of the building, roofing).

Li (7) proposed an optimized macroseismic analysis, integrating the traditional macroseismic intensity scale and evaluation models of resilience and empirical vulnerability of regional buildings. In another work, Li (8) studied the seismic vulnerability of regional group structures, establishing empirical vulnerability matrices of six building groups in different seismic intensity zones. A series of zonal fragility prediction models of six typical regional structure groups is established. Li (9, 10) highlighted the importance of measuring seismic intensity to evaluate and predict seismic risk and vulnerability of structures, proposing an improved equation for instrumental intensity. The innovation introduced consists of an improved model compared to traditional techniques for assessing the seismic risk of regional structures.

The correct assessment of the seismic risk of an existing structure - important for economic and occupant safety considerations - cannot ignore the nonlinear

structural behavior of the material. The most appropriate methods for such analyses are: nonlinear static analysis (pushover) and nonlinear time history analysis. The second method can determine the non-linear behavior of the structure in a more realistic way; however it is complex to solve. Therefore pushover analysis is preferable for its computational advantages.

2. DESCRIPTION

The church of San Lorenzo is an ancient building, mentioned in the tithe books from the 14th century. It was only rebuilt in the middle of the 20th century. It represents a valuable architectural element in the area and is an important example of late 19th century neoclassicism, which is only expressed in the interior and the bell tower, as the main façade was remodelled more recently.

In the transformation of the above mentioned building, many important designers of the area follow one another, from the architects Di Rienzo and Aloisio in the early 19th century to the engineer Castelli and the more recent Genio Civile of Chieti in the mid-20th century (11). The church in its present form is a fusion of various earlier buildings. It is the result of the Caracciolo-Pisquizi princes’ desire for renewal. Figure 1 shows the main view of the building.

The building is - like the entire historic centre - a masonry building made of local river stone. It measures 10.70 m in width and 29 m in length up to the presbytery. The dome is decorated with stucco; from the ground floor a descent leads into the crypt where the body of the patron saint Buono is kept. The crypt, added in 1774, compensates for the difference in height between the floor of the church and the square behind it and also provides an entrance from there.



Figure 1. Main elevation

The exterior façades are simple and unadorned, with the exception of the main façade and the bell tower.

The bell tower which was restored in 1893 by the engineer Castelli, rises more than 40 metres above the main square. Its height is divided into four registers. The earth extension consists of a steep ashlar base: this is the only part in which this material is used. The first register consist of projecting brick rectangular cornices that delimit the masonry. The third register is completely empty and houses the bell tower with arches on all four sides framed by composite-style brick pilasters.

The church has a simple floor plan, consisting of a single vaulted hall in the shape of a Latin cross, with a lowered domed roof in the choir area. In the floor plan, it is noticeable that the width of the space is determined by the diameter of the dome.

The elevation is divided into two registers: a lower one, consisting of the side altars framed by round arches supported by semi-columns of the giant Corinthian order, and an upper one, consisting of the claristorium and the barrel vault. To the right and left of the liturgical hall, Corinthian semi-columns frame three niches in which three side altars are located. The area enclosed by the dome is flanked by two other smaller altars, which are larger than the previous ones. In the wall opposite the entrance wall is the main altar, which is dedicated to the patron saint of the small center. Figure 2 **Error! Reference source not found.** shows the elevation view of the belltower.

3. DESIGN FEATURES

The construction of the church extended over a considerable period of time: therefore, there are overlaps



Figure 2. Belltower: elevation view

in the technical and architectural solutions and languages.

An analysis of the historical sources shows that the search for building materials followed the classic criterion of maximum cost-and-time savings. The semi-finished stonework that characterises the church is shown in an arrangement that follows continuous rows, with a finished mortar joint that is much thinner compared to the rustic architecture that characterises the urban area, testifying to the richness of the construction.

More specifically, the masonry technique can be defined as being characterised by blocks of different sizes, some of which have been worked; discontinuous mortar layers with brick fragments (11). The lithological setting consists of irregular blocks of quarry limestone, pebbles and erratic material from river beds. The state of preservation of the masonry is good and no cracks or active kinematics can be observed.

All the walls consist of masonry with the features just described and a bag profile with inserted diatons. The thickness of the perimeter walls is between 1 and 2 metres. The masonry of the building consists of vaults and domes. In the liturgical area, a structure similar to that typical of the Latin development of the eastern basilicas can be observed. It consists of a series of repeating masonry structures that frame the barrel vaults and on which they rest. These arches relieve the weight of the roof and the vaults themselves on the inner buttresses, which are represented by the masonry areas with the semi-columns of the giant order.

4. MATERIAL CONDITION ANALYSIS

The building features technical solutions and material choices typical of traditional architecture in Abruzzo at the end of the 19th century, although there are no particular innovations at the technological level.

As there are no signs of foundation or structural cracks, it can be assumed that the deterioration of the materials is due to other causes. The main problems that the building suffers from concern the low resistance of the materials to weathering, which is due both to the typological characteristics and to the lack of experimentation with new materials, as reported in literature (12).

As far as typological characteristics are concerned, the domed roof which, despite its expert construction, shows a slight infiltration of rainwater. Other elements exposed to decay are the plaster cladding and the paintwork. The main causes are exposure to drive rain in areas that are not protected by waterproofing, the use of non-breathable paints or coatings and inadequate rainwater disposal solutions. On the outer wall, especially in the upper part of the bell tower, the decay affects the mortar. This is located in the most superficial area.

5. SIMPLIFIED SEISMIC ANALYSIS

Tower structures such as a bell tower can be compared to a system of distributed masses with an infinite number of degrees of freedom and consequently an infinite number of vibration modes. In reality, it is only the first modes of vibration that define the true seismic response of the system. In this section, the results of the simplified calculation model provided by Italian standard (13) are presented.

The equation of motion of a shelf with distributed mass embedded in the ground can be written as follows (12):

$$m^*q'' + K^*q = 0 \quad (1)$$

where:

$$m^* = \int \mu \phi^2(z) dz \quad (2)$$

$$K^* = \int EI(\phi^2(z))^2 dz \quad (3)$$

where:

- $\phi(z)$ is the oscillation waveform;
- μ is the mass distributed over height;
- q'' is the second derivative of displacement as a function of time

Considering a quadratic waveform of the type:

$$\phi(z) = \frac{z^2}{H^2} \quad (4)$$

It is obtained from previous Equations:

$$m^* = \mu \frac{H}{5} \quad (5)$$

$$K^* = 4 \frac{EI}{H^3} \quad (6)$$

$$c^* = \mu \frac{H}{3} \quad (7)$$

The expressions for the maximum displacement of the cantilever and the load distribution as a function of elevation can be derived.

$$y_{max} = \mu g H^4 \frac{S_e}{g 12 EI} \quad (8)$$

$$p(z) = \frac{5}{3} \mu \frac{g}{H^2} \frac{S_d}{g} z^2 \quad (9)$$

5.1. Structural Modeling The modelling of the belfry was carried out by varying the boundary conditions (i.e., constraints), offered in this case by the presence of the adjacent bodies (e.g., presbytery). The effects of two calculation models, different in terms of constraint conditions, are thus considered:

- Model A - isolated tower, with a height of 42 m;
- Model B - tower constrained in the portions adjacent to the church, which interact with the tower itself. In this case the free span of the church is lower and equal to 30 m.

5.2. Seismic Parameters

The geometric-mechanical parameters adopted in the calculation are summarised in Table 1.

The maximum displacement obtained for the unconfined tower model (i.e., Model A) with linear calculation assumptions is 9.12 cm.

The maximum displacement obtained for the confined tower model (i.e., Model B) with linear calculation assumptions is 2.37 cm.

The confinement offered by the adjacent structures of the church makes it possible to reduce the free span of the ideal cantilever that schematises the tower, thus considerably reducing the maximum displacements.

6. PUSHOVER ANALYSIS

This section describes the second evaluation level considered. The pushover analysis considers a non-linear numerical model of the tower, in which the external forces are increased in a linear manner until the structure collapses. The mechanical parameters of the materials, knowledge of the construction technology of the time and the state of preservation of the material play a fundamental role in this type of analysis.

6.1. Mechanical Parameters of Masonry

The mechanical parameters adopted in the calculation were taken from the guidance provided by Circular 2019 - NTC2018 (13). This regulation presents a collection of

TABLE 1. Geometrical-mechanical parameters for simplified calculation

Parameter	Value	Units
Tower height	42 – 30	m
Elastic modulus	12000	daN/cm ²
Base length	7.00	m
Base height	6.80	m
Wall thickness	1.30	m
P _s	2000	daN/m ³
$\tau_{vk,0}$	3.50	daN/cm ²
γ_M	2.40	-
FC	1.35	-
q	3	-
T*	0.451	s
C _c	1.37	-
T _D	2	s
ag	0.113	g
S	1.50	-
F ₀	2.569	s

the most recurring mechanical parameters of masonry. For the model under consideration, the following typology was considered: “masonry with rough-hewn ashlar, with faces of uneven thickness”.

Table 2 shows the main mechanical parameters of this masonry type.

Figure 3 shows the constitutive law for the masonry material.

The nonlinear parameters are summarized in Table 3.

6. 2. Levels of Knowledge Considered

According to the Italian regulations (NTC2018), the knowledge level (LC) influence the values of the mechanical parameters adopted. In fact, each knowledge level (i.e., LC) corresponds to a confidence factor (i.e., FC) that is used to reduce the values of the mechanical properties of the materials considered according to following equation:

TABLE 2. Mechanical properties of the material considered [15]

$f_{cm(k)}$ [MPa]	$f_{vm(k),0}$ [MPa]	$f_{tm(k)}$ [MPa]	$f_{cm(k),0}$ [MPa]
2	0.035	0.035	2
Γ_m [-]	τ_0 [MPa]	M [-]	Λ [-]
2.50	0.035	0.40	20

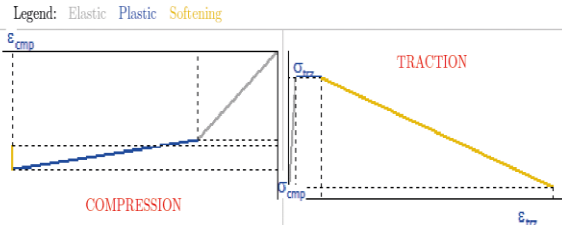


Figure 3. Constitutive law of masonry

TABLE 1. Nonlinear parameters of masonry

Phase	Parameter	Unit	Value
Elastic stage	Max compression stress	MPa	1.50
	Corr. deformation	%	1.22
	Max tensile stress	MPa	0.04
	Corr. elongation	%	0.03
Plastic stage	Max compression stress	MPa	2.00
	Corr. deformation	%	4.00
	Max tensile stress	MPa	0.04
	Corr. elongation	%	0.13
Softening stage	Max compression stress	MPa	4.00
	Corr. deformation	%	1.60
	Max tensile stress	MPa	1.00
	Corr. elongation	%	0.00

$$R_d = \frac{R}{FC} \quad (10)$$

As the level of knowledge increases, the FC factor will be lower. The Italian building regulations identify three knowledge levels.

In the present study, knowledge level LC1 was chosen due to limited investigations (i.e. visual and documentary). The confidence factor is 1.35. For the resistances, the minimum values of the intervals indicated by Circular 2019 are considered; for the elastic moduli, the average values indicated by the same Circular are used.

6. 3. FE Modeling

The modelling of the steeple was carried out using the finite element method (FEM), employing TESSYS software (MS-DOS solver) [16]. In addition to the mechanical parameters outlined above, further determining factors for the result of the analysis are the degrees of constraint of the structure, offered in this case by the presence of the adjacent blacksmith's bodies (i.e., presbytery). The effects of two calculation models, differing in their constraint conditions, are thus studied:

- Model A - isolated tower;
- Model B - tower constrained in the portions adjacent to the church, which interact with the tower itself.

The tower is modelled with two-dimensional linear triangular elements (CST - Constant Strain Triangle), and is considered constrained to the ground by non-yielding joints.

Table 4 summarizes the results of the pushover analysis.

It can be seen that the isolated (ideal) tower model is not able to sustain the expected displacement demand, in contrast to the real tower model (C/D Index always greater than one).

6. 4. Analysis of the Crack Pattern

The evolution of the response of the structure analysed in

TABLE 4. Pushover analysis

Model	Seismic direction	Seismic demand [d _{max} in cm]	Seismic capacity [d _e in cm]	C/D Index
Isolated tower	+x	15.032	6.197	0.412
	-x	14.958	6.577	0.440
	+y	15.104	14.095	0.933
	-y	15.492	15.717	1.015
Confined tower	+x	18.403	21.199	1.152
	-x	8.587	8.671	1.010
	+y	9.787	46.681	4.770
	-y	9.166	37.063	4.044

terms of the crack framework is shown below. In particular, for a bell tower wall, the cracking frameworks for the main points of the capacity curve are shown.

Figure 4 shows the typical trend for a masonry capacity curve.

The points considered are as follows:

- i. Point 1: Linear branch of the curve, where the material still exhibits elastic behaviour;
- ii. Point 2: yielding of the structure; at some points, plasticisation of the material is observed and the first cracks begin to spread;
- iii. Point 3: plastic stretch, where cracks increase and almost the entire structure is in the plastic phase;
- iv. Point 4: collapse of the structure.

Figure 5 shows the evolution of the crack pattern for the unconfined tower, with force distribution proportional to the first mode of vibration (-x direction).

Figure 6 shows the evolution of the crack pattern for the confined tower, with force distribution proportional to the first mode of vibration (-x direction).

The results shown both refer to the wall adjacent to the square, for the analysis in the -x direction. For both models, the first cracks appear at the belfry due to the geometric singularities of the structure. The cracks then

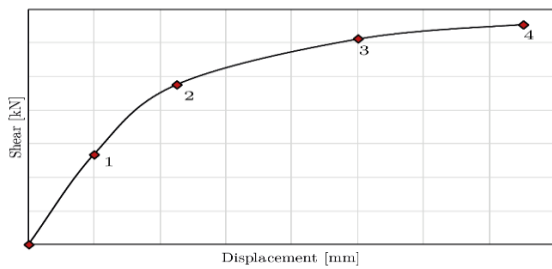
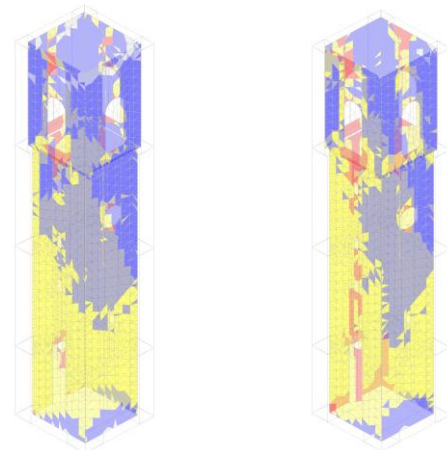
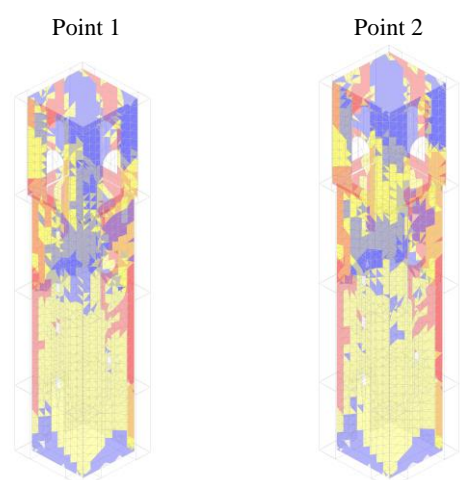
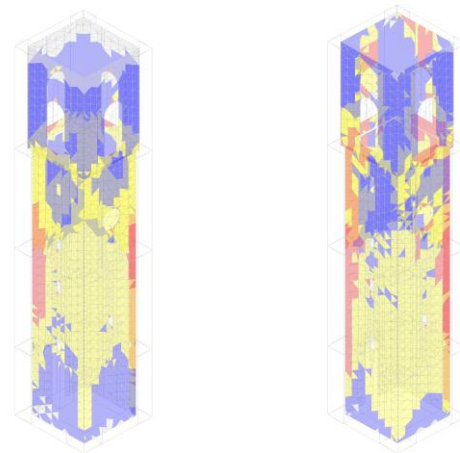


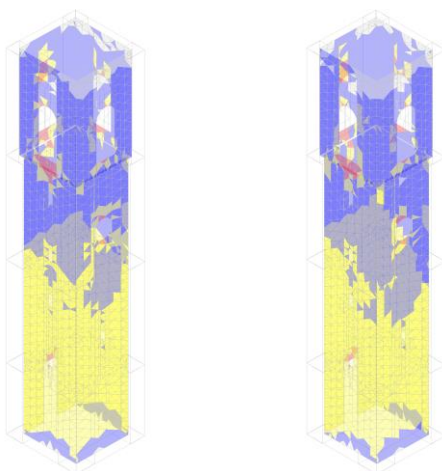
Figure 1. Capacity curve (qualitative)



Point 3 Point 4
Figure 5. Damage evolution: unconfined tower with distribution proportional to the I mode of vibration and earthquake direction -x



Point 1 Point 2
Point 3 Point 4
Figure 6. Damage evolution: confined tower with distribution proportional to the I mode of vibration and earthquake direction -x



Point 1 Point 2

propagate from intermediate structural weaknesses (i.e. internal staircase lighting slits), until they reach collapse (Point 4), with cracks spreading along almost the entire shaft of the tower.

It can be seen how the influence of the degree of constraint is fundamental for the structure's crisis fashion: neglecting the interaction of the adjacent building (i.e., isolated tower) results in a different crack pattern at collapse. In fact, in the first case a brittle crisis mode can be considered, while in the second case there is a more diffuse plasticity behaviour, with cracks localized at the top of the structure instead of at the base (generalised collapse).

To validate the crack evolution model, it is possible to observe the two real cases that occurred in Italy (Figure 7 and 8).

The crack patterns observed in the real cases reflects the patterns obtained by the nonlinear static analysis. Figure 9 shows the Capacity Basket for the C/D index (i.e., capacity/demand) of the tower displacement.



Figure 2. Belltower in Castelsantangelo, damaged by the earthquake in 2016 (confined tower)



Figure 8. Belltower in Amatrice, damaged by the earthquake in 2016 (unconfined tower)

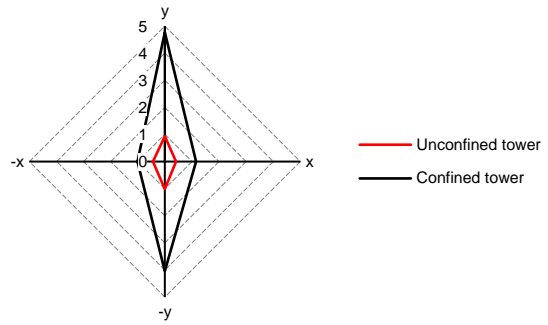


Figure 9. Capacity basket for the Capacity/Demand index with proportional distribution at I mode of vibration and earthquake direction -x

It can be observed that in the x-direction the confinement offered by the surrounding walls has the positive effect of doubling the ratio considered and increasing it significantly (+480%) in the y-direction, allowing the structure to meet the displacement requirements for both directions in the confined configuration.

Figure 10 shows the comparison between the maximum displacement results for the 4 nodes at the top of the tower according to the simplified linear model and the pushover analysis.

It can be observed that the linear model allows the displacement of the free cantilever to be predicted with good approximation (i.e., Model-A), while it significantly underestimates the maximum displacement in the case of the confined tower (i.e., Model-B). The effect of the confinement offered by the surrounding masonry is reflected more in the stress distribution in the masonry than in the maximum displacements. In fact, the greatest influence is observed in the mode of propagation of the crack pattern.

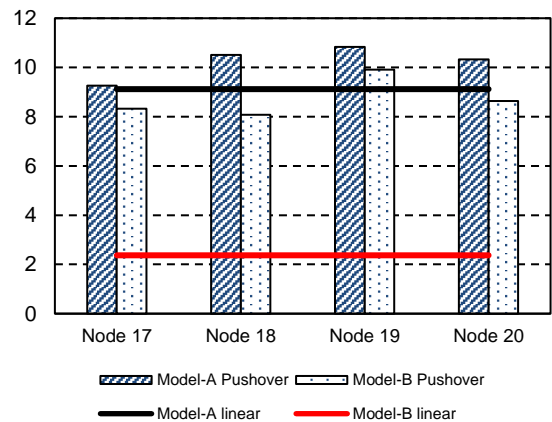


Figure 10. Comparison of the displacement (cm) from simplified linear and pushover analyses

7. CONCLUSIONS

The present study illustrates and compares two different seismic analyses allowed by Italian code on existing masonry monumental buildings (13).

In particular, the effect of the different degrees of constraint on the structure of the bell tower of the church of San Lorenzo in San Buono (Chieti, Italy) has been analyzed. It is chosen as a case study because of the peculiar characteristics of the area on which it stands.

The numerical analyses take into account the uncertainty of the type of material used, considering the various semi-probabilistic factors offered by the Italian technical regulations on existing buildings. The numerical analyses illustrated the difference between the different types of constraint (isolated tower and constrained tower), showing how this factor can significantly influence both the building's failure mode and the possibility of predicting possible hazard scenarios.

The main results are:

- The linear analysis closely approximates the behaviour of the tower structure only in the case of an unconfined structure (i.e., Model-A). The displacement values obtained are comparable in this case;
- The non-linear static analysis (pushover) allows the evolution of the structure's crack pattern to be highlighted;
- The confined tower configuration (Model-B) satisfies the requirements of the structure's seismic demand in all directions and highlights the beneficial effect of confinement offered by adjacent structures;
- The free tower (Model-A) or corbelled configuration is overly cautious.

8. REFERENCES

1. Biraghi MS. *Storia dell'architettura contemporanea I 1750-1945*: Einaudi; 2008.
2. Curl JS. Lawrence Weaver (Book Review). *RSA Journal*. 1989;138(5401):63. <https://doi.org/10.1080/13556207.1996.10785173>
3. Raycheva R. An Empire Style Furniture Set at Nedkovich House, Old Town Plovdiv. *Architecture and Urban Planning*. 2015;10(1):49-54. <https://doi.org/10.1515/aup-2015-0007>
4. Zevi B, Zevi B, Zevi B, Architect I, Zevi B. *Storia dell'architettura moderna*: Einaudi Turin; 1953.
5. Ozturk B. Seismic behavior of two monumental buildings in historical Cappadocia region of Turkey. *Bulletin of Earthquake Engineering*. 2017;15:3103-23. <https://doi.org/10.1007/s10518-016-0082-6>
6. Güney D, Aydın E, Öztürk B, editors. The evaluation of damage mechanism of unreinforced masonry buildings after Van (2011) and Elazığ (2010) Earthquakes. *Journal of Physics: Conference Series*; 2015: IOP Publishing.
7. Li S-Q. Empirical resilience and vulnerability model of regional group structure considering optimized macroseismic intensity measure. *Soil Dynamics and Earthquake Engineering*. 2023;164:107630. <https://doi.org/10.1016/j.soildyn.2022.107630>
8. Li S-Q, Chen Y-S, Liu H-B, Del Gaudio C. Empirical seismic vulnerability assessment model of typical urban buildings. *Bulletin of Earthquake Engineering*. 2023;21(4):2217-57. <https://doi.org/10.1007/s10518-022-01585-8>
9. Li S-Q. Improved seismic intensity measures and regional structural risk estimation models. *Soil Dynamics and Earthquake Engineering*. 2024;176:108256. <https://doi.org/10.1016/j.soildyn.2023.108256>
10. Li S-Q, Gardoni P. Empirical seismic vulnerability models for building clusters considering hybrid intensity measures. *Journal of Building Engineering*. 2023;68:106130. <https://doi.org/10.1016/j.job.2023.106130>
11. Varagnoli C. *La costruzione tradizionale in Abruzzo. Fonti materiali e tecniche costruttive dalla fine del Medioevo all'Ottocento*, Roma. 2008. <https://books.google.it/books?id=ks-C2XRFKH4C>
12. Rainieri C, Fabbrocino G, editors. *Il periodo elastico delle torri in muratura: correlazioni empiriche per la previsione*. XIV Congresso Nazionale L'Ingegneria Sismica in Italia, Bari; 2011.
13. *Le Costruzioni NNTP*. NTC: Rome. Italy; 2018.

COPYRIGHTS

©2024 The author(s). This is an open access article distributed under the terms of the Creative Commons Attribution (CC BY 4.0), which permits unrestricted use, distribution, and reproduction in any medium, as long as the original authors and source are cited. No permission is required from the authors or the publishers.



Persian Abstract

چکیده

کلیسای سن لورنزو در سان بونو (ایتالیا) به دلیل ویژگی‌های فنی و معماری خود در منظر محلی منحصر به فرد است. این بنا که تاریخ ساخت آن از قرن چهاردهم تا اوایل قرن بیستم است، توسط مهم‌ترین طراحان منطقه محقق شد. برج ناقوس عنصری است که با نئوکلاسیسم پالایش شده مشخص می‌شود و گواه بخش قابل توجهی از ماندگاری سبک نئوکلاسیک در آبروزو تا دهه‌های اول قرن بیستم است. مطالعه حاضر هم تحلیلی فن‌آوری-سازنده از ساختمان و هم ارزیابی را نشان می‌دهد. خطر لرزه ای برج ناقوس، به منظور ارائه یک نکته مهم برای شناخت این اثر با توجه به کارهای مرمت محافظه کارانه احتمالی. تجزیه و تحلیل خطر لرزه ای برای دو پیکربندی ساختاری مختلف و دو نوع شناسی مختلف مجاز توسط کدهای ساختمان ایتالیایی برای ساختمان‌های بنایی بنای تاریخی انجام می‌شود: استاتیک خطی ساده و غیر خطی. این مطالعه نشان می‌دهد که چگونه حضور سازه مجاور به طور قابل توجهی رفتار ساختاری برج بنایی را هم از نظر جابجایی و هم از نظر انتشار الگوی ترک تغییر می‌دهد. تفاوت در نتایج محاسبه غیر خطی و روش‌های سریع پیشنهاد شده توسط استاندارد نیز برجسته شده است.



A Novel Sensor Integration Scheme for an Aided Inertial Navigation System Based on a Generalized PID Filter in the Presence of Observation Uncertainty

M. Ansari^a, J. Jamali^{*a}, M. H. Fatehi-Dindarlou^a, M. A. Rahgoshay^b, O. Mahdiyar^a

^a Islamic Azad University of Kazerun, Department of Electrical Engineering, Kazerun, Iran

^b Salman Farsi University of Kazerun, Department of Electrical Engineering, Kazerun, Iran

PAPER INFO

Paper history:

Received 24 November 2023

Received in revised form 26 January 2024

Accepted 15 February 2024

Keywords:

Integrated Navigation System

Inertial Navigation System

Global Positioning System

Data Fusion

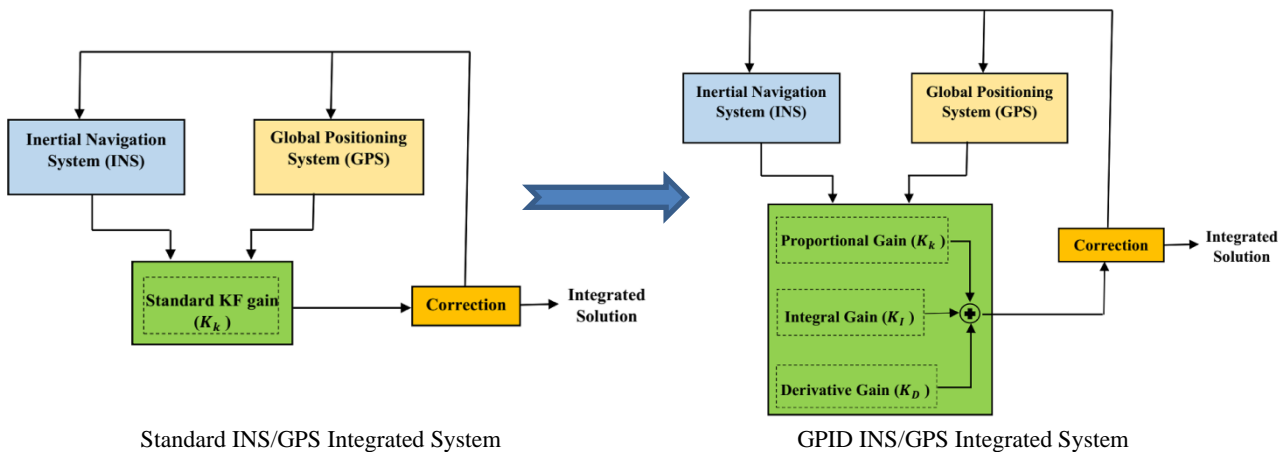
Kalman Filtering

ABSTRACT

Implementing a proper integration scheme plays an important role in the performance of integrated navigation systems. Not only does employing a more reliable estimation method improve the accuracy of the integrated navigation system, but this can lead to a more robust solution in the presence of different types of uncertainties. Implementing an integration scheme that has a robust and simple structure is a challenging issue in the design of integrated navigation systems. By inspiring from the concept of PID control, this paper proposes a robust integration scheme for aided inertial navigation systems in the presence of aiding sensor measurement uncertainties. The proposed filter combines the concept of proportional-integral-derivative control theory and the standard Kalman filter estimator to improve the performance of the integration scheme. Thanks to the integral and derivative parts added to the proposed scheme, the integrated system attains a faster and more robust solution in the presence of observation errors and uncertainties. The simulation case studies validate the superior efficacy and capability of the proposed scheme compared to the integration method based on the standard Kalman filter.

doi: 10.5829/ije.2024.37.06c.09

Graphical Abstract



1. INTRODUCTION

Navigation systems can function based on two different techniques: Dead Reckoning (DR) and Position Fixing

(PF) (1). DR-based systems utilize the measurements of the vehicle's motions via body-mounted inertial sensors and perform a series of computational tasks to obtain the navigation solution. On the other hand, PF-based systems

*Corresponding Author Email: j.jamali@kau.ac.ir (J. Jamali)

attain the navigation solution by exchanging data with the known position information of external sources. The solution obtained by the DR-based system usually has an appropriate performance in short-term intervals but the accumulative error caused by the integration operation deteriorates the accuracy and performance of the long-term solution. Unlike DR-based systems, PF-based systems represent a desirable long-term but noisy short-term solution. To benefit from the advantages and cover the drawbacks of the two aforementioned techniques, aided or integrated navigation systems utilize both DR and PF systems simultaneously, which leads to a more precise and reliable navigation solution (2). As the most well-known DR-based navigation system, the Inertial Navigation System (INS) usually uses external information of one or more PF-based systems as aiding sensors. For instance, INS-aided systems such as INS/Global Navigation Satellite System (GNSS) and INS/Doppler Velocity Log (DVL) are widely used in land, aerial and marine (3-5).

One of the most important parts of an integrated navigation system is the optimal state estimator, which continuously estimates the navigation system's errors during the initial alignment and navigation stages. The performance of an aided navigation system is directly affected by optimal state estimation techniques used in the integration or sensor fusion scheme. Kalman Filter (KF) is the most widely used optimal state estimator in many theoretical and industrial applications including integrated navigation systems (6-11). To achieve an optimal solution in the KF, determining proper models for the system and stochastic noises is a key factor problem (12). In the integrated navigation system, the system model is mostly deterministic and does not raise a serious issue in the KF-based estimator. However, determining a proper stochastic model for process and measurement noises (\mathbf{Q} and \mathbf{R}) is a challenging issue. In fact the statistical model of inertial sensors, gyroscopes and accelerometers, is specified by an error covariance matrix, \mathbf{Q} . Also, the measurement error of aided sensors which are utilized in the aided navigation system is specified by another error covariance matrix, \mathbf{R} .

A proper model for \mathbf{Q} is usually obtained according to the specification of inertial sensors and nominal dynamic motion which vehicle experiences. However, the modeling of \mathbf{R} is not as straightforward as \mathbf{Q} . In fact, the outputs of the PF-based system used as the measurement vector in the estimator can be corrupted by several sources of errors, which possibly decreases the performance of the integrated system. The GPS measurement, for instance, may suffer from different types of errors such as multipath, interference or jamming, receiver and satellite clock offsets, etc. Similarly, the velocity measurements of a DVL can also be associated with errors such as bias and noise due to installation misalignment, severe environmental

conditions, temporary failures, etc. Clearly, setting a fixed \mathbf{R} model for the optimal estimator may not be a viable option and does not attain an optimal solution for the integrated system.

2. RELATED WORK

In recent research, robust and adaptive solutions are proposed to resolve the lack of robustness issue in the KF estimator of the integrated navigation systems (13-15). However, these methods assume predetermined constraints on the signal uncertainty model and also add some complexity to the signal processing algorithms of the estimation procedure.

The concept of a combination of the PID control theory and the standard KF has recently been presented in some research (16-18). This idea leads to a simple structure and robust estimator named the Generalized Proportional Integral Derivative (GPID) filter. In addition to current measurement, the GPID filter also uses past and prediction of future measurements to estimate the current state and attains a more desirable performance compared to the standard KF. The GPID filter was used in the initial self-alignment of SINS for the first time (19, 20). The self-alignment process is performed by stationary or quasi-stationary assumptions without using any external aided measurements. This process usually utilizes measures of the Earth's rotation rate and the gravity vector in different frames as the measurement vector which are pure and do not have any uncertainties in them. Therefore, \mathbf{Q} modeling is much more important than \mathbf{R} modeling in the initial self-alignment process. On the other hand, in the integrated navigation systems, unlike the initial self-alignment process, \mathbf{R} modeling plays a critical role in the integrated system due to the existence of uncertainties in the observations (measurements) of aiding sensors. In the presence of these uncertainties, improper \mathbf{R} modeling can greatly decrease the performance of the integrated system.

In this paper, a robust integration scheme for the INS-aided system is proposed based on the GPID filter as the optimal estimator. Regarding the robustness property of the proposed approach, the performance of the integrated system is greatly improved in the presence of observation uncertainties compared with the standard KF-based integration scheme. The proposed scheme also has a simple structure and low computational burden compared to the robust and adaptive KF-based schemes. By conducting simulation case study tests, the efficacy and capability of the proposed method are demonstrated and compared with the standard KF-based integration scheme.

The contributions of the paper are as follows:

- Proposing a novel PID-based Kalman filter for the integrated navigation systems
- Proposing a simplified structure of GPID Filter for simple online implementation
- Presenting a detailed robustness analysis of the proposed integration scheme

The paper is divided into the following sections. In section 2, the process and measurement equations used in the integration scheme are introduced. The main contribution of the proposed method is expressed in section 3, which contains the introduction of the GPID filter for the integration scheme and also presents proof of the robustness of the proposed filter in the presence of the measurement uncertainty of the aiding sensor. Finally, in section 4, the proposed method has been evaluated through conducting a detailed simulation case study (section 5). The last part, this work is concluded in section 6.

3. THE ERROR DYNAMICS AND MEASUREMENT MODELS OF THE AIDED-INS

In this paper, a 9-state error dynamics model of Strapdown INS (SINS) is implemented. For most terrestrial applications, the simplified 9-state model is used without causing a considerable error. This model can be expressed as follows:

$$\dot{\mathbf{x}}(t) = \mathbf{F}\mathbf{x}(t) + \mathbf{G}\mathbf{w}_p(t) \quad (1)$$

Where

$$\mathbf{x} = [\delta\boldsymbol{\varphi}_{3 \times 1}^n \quad \delta\mathbf{v}_{3 \times 1}^n \quad \delta\mathbf{p}_{3 \times 1}^n]^T \quad (2)$$

denotes the state vector with

$$\delta\boldsymbol{\varphi}^n = [\delta\varphi_E \quad \delta\varphi_N \quad \delta\varphi_U]^T \quad (3)$$

$$\delta\mathbf{v}^n = [\delta v_E \quad \delta v_N \quad \delta v_U]^T \quad (4)$$

$$\delta\mathbf{p}^n = [\delta L \quad \delta l \quad \delta h]^T \quad (5)$$

Equations 3 to 5 represents the attitude, velocity and position error vectors in the ENU local-level frame, respectively.

The process noise vector expressed as

$$\mathbf{w}_p = [\delta\omega^n \quad \delta\mathbf{a}^n]^T \quad (6)$$

where Equations 7 and 8 denote the projection of the stochastic parts of gyroscopes and accelerometers measurement into the ENU-frame, respectively.

$$\delta\boldsymbol{\omega}^n = [\delta\omega_E \quad \delta\omega_N \quad \delta\omega_U]^T \quad (7)$$

$$\delta\mathbf{a}^n = [\delta a_E \quad \delta a_N \quad \delta a_U]^T \quad (8)$$

and The matrices \mathbf{F} and \mathbf{G} are also as follows:

$$\mathbf{F} = \begin{bmatrix} \mathbf{0}_{3 \times 3} & \mathbf{F}_{\varphi v} & \mathbf{0}_{3 \times 3} \\ \mathbf{F}_{v\varphi} & \mathbf{0}_{3 \times 3} & \mathbf{0}_{3 \times 3} \\ \mathbf{0}_{3 \times 3} & \mathbf{F}_{pv} & \mathbf{0}_{3 \times 3} \end{bmatrix} \quad (9)$$

$$\mathbf{G} = \begin{bmatrix} -\mathbf{I}_{3 \times 3} & \mathbf{0}_{3 \times 3} \\ \mathbf{0}_{3 \times 3} & \mathbf{I}_{3 \times 3} \\ \mathbf{0}_{3 \times 3} & \mathbf{0}_{3 \times 3} \end{bmatrix} \quad (10)$$

where,

$$\mathbf{F}_{\varphi v} = \begin{bmatrix} 0 & \frac{1}{(R_M+h)} & 0 \\ -\frac{1}{(R_N+h)} & 0 & 0 \\ -\frac{\tan L}{(R_N+h)} & 0 & 0 \end{bmatrix} \quad (11)$$

$$\mathbf{F}_{v\varphi} = \begin{bmatrix} 0 & f_U & -f_N \\ -f_U & 0 & f_E \\ f_N & -f_E & 0 \end{bmatrix} \quad (12)$$

$$\mathbf{F}_{pv} = \begin{bmatrix} 0 & \frac{1}{(R_M+h)} & 0 \\ \frac{1}{(R_N+h)\cos L} & 0 & 0 \\ 0 & 0 & 1 \end{bmatrix} \quad (13)$$

In the INS/GPS integrated system, the estimator takes the difference between INS and GPS velocity and position outputs as the measurement vector. The measurement model used in the estimator can be expressed as the following equations:

$$\mathbf{z}(t) = \begin{bmatrix} \mathbf{v}_{INS} - \mathbf{v}_{GPS} \\ \mathbf{p}_{INS} - \mathbf{p}_{GPS} \end{bmatrix} = \mathbf{C}\mathbf{x}(t) + \mathbf{w}_m(t) \quad (14)$$

where

$$\mathbf{C} = \begin{bmatrix} \mathbf{0}_{3 \times 3} & \mathbf{I}_{3 \times 3} & \mathbf{0}_{3 \times 3} \\ \mathbf{0}_{3 \times 3} & \mathbf{0}_{3 \times 3} & \mathbf{I}_{3 \times 3} \end{bmatrix} \quad (15)$$

and \mathbf{w}_m is the measurement noise vector.

Similar to many other applications, the discrete form of the space-state model is commonly used in the estimation procedure of INS/GPS integration. The discrete-time form of Equations 1 and 14 are expressed as follows:

$$\mathbf{x}(k+1) = \mathbf{A}\mathbf{x}(k) + \mathbf{w}_p(k) \quad (16)$$

$$\mathbf{y}(k) = \mathbf{H}\mathbf{x}(k) + \mathbf{w}_m(k) \quad (17)$$

where $\mathbf{x}(k)$ and $\mathbf{y}(k)$ are the state and measurement vectors. \mathbf{A} and \mathbf{H} are the discrete representations of matrices \mathbf{F} and \mathbf{C} , respectively. \mathbf{w}_p and \mathbf{w}_m are assumed as a zero-mean stochastic vector with the covariance matrices of \mathbf{Q} and \mathbf{R} , respectively.

4. THE PROPOSED INTEGRATION SCHEME BASED ON GENERALIZED PID FILTER

In references, the standard KF is utilized as the estimator part of the integrated navigation systems. The block diagram of the INS/GPS integration based on the standard KF is depicted in Figure 1. According to this block diagram, the INS's computed velocity and position are compared with the GPS velocity and position

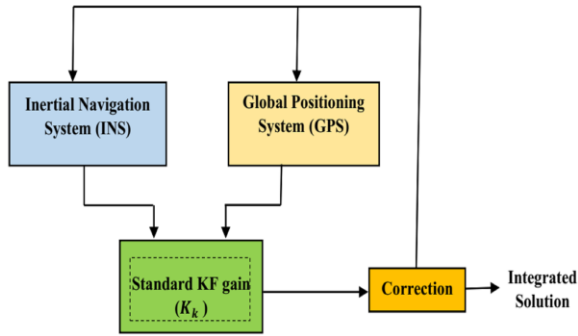


Figure 1. The block diagram of the INS/GPS integration based on the Standard KF

measurements, which are considered as the measurement vector in the KF estimator. At each cycle, the KF estimator computes an optimal Kalman gain K_k and estimates the errors related to INS and GPS. Finally, the estimated errors are feedback to INS and GPS systems and the integrated solution is attained.

As stated previously, the standard KF estimator is highly dependent on process and measurement models, which is the primary reason that motivated us to propose a robust integration scheme based on the combination of the PID control theory and the KF estimator. The block diagram of the proposed integration scheme is illustrated in Figure 2. Unlike the standard KF-based integration scheme, the proposed scheme utilizes two additional parts (integral and derivative parts) in its estimator block. The proposed scheme is the general form of the standard KF-based integration scheme and when the integral and derivative gains are set to zero, the GPID filter is identical to the standard KF.

Based on the error dynamics and measurement models of the INS/GPS integration described in Equations 1 to 17, the equations of the GPID estimator can be written as follows:

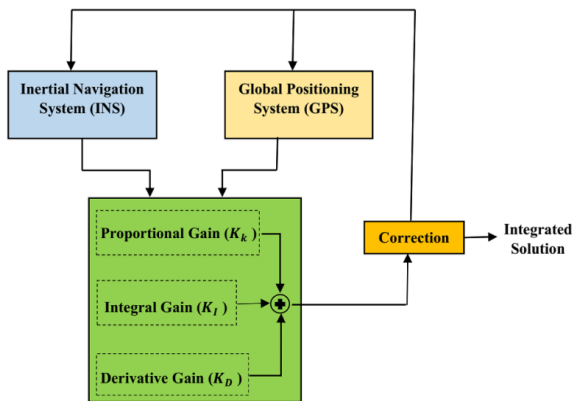


Figure 2. The block diagram of the INS/GPS integration based on the generalized PID filter

$$\hat{\mathbf{x}}(0|0) = \bar{\mathbf{x}}_0 \tag{18}$$

$$\mathbf{x}_I(0) = \mathbf{0} \tag{19}$$

$$\tilde{\mathbf{y}}(0) - \tilde{\mathbf{y}}(-1) = \mathbf{0} \tag{20}$$

$$\tilde{\mathbf{y}}(k) = \mathbf{y}(k) - \mathbf{H}\hat{\mathbf{x}}(k|k) \tag{21}$$

$$\hat{\mathbf{x}}(k|k-1) = \mathbf{A}\hat{\mathbf{x}}(k-1|k-1) \tag{22}$$

$$\mathbf{r}(k) = \mathbf{y}(k) - \mathbf{H}\hat{\mathbf{x}}(k|k-1) \tag{23}$$

$$\mathbf{x}_P(k) = \mathbf{K}_P(k)\mathbf{r}(k) \tag{24}$$

$$\mathbf{x}_I(k) = \mathbf{x}_I(k-1) + \mathbf{K}_I(k)\tilde{\mathbf{y}}(k-1) \tag{25}$$

$$\mathbf{x}_D(k) = \mathbf{K}_D(k)(\tilde{\mathbf{y}}(k-1) - \tilde{\mathbf{y}}(k-2)) \tag{26}$$

$$\hat{\mathbf{x}}(k|k) = \hat{\mathbf{x}}(k|k-1) + \mathbf{x}_P(k) + \mathbf{x}_I(k) + \mathbf{x}_D(k) \tag{27}$$

where \mathbf{K}_P , \mathbf{K}_I and \mathbf{K}_D denotes the proportional, integral and derivative gains used in computation of the proportional, integral and derivative parts of the estimator \mathbf{x}_P , \mathbf{x}_I and \mathbf{x}_D , respectively.

Based on Equation 18 to 27, we have proposed a simple structured PID filter which has a desirable robustness property and low computational burden for online implementation. The equations of the SRPIF are as follows:

$$\mathbf{P}(0|0) = \mathbf{P}_0 \tag{28}$$

$$\mathbf{P}(k|k-1) = \mathbf{A}\mathbf{P}(k-1|k-1)\mathbf{A}^T + \mathbf{W}(k-1) \tag{29}$$

$$\mathbf{K}_P(k) = \mathbf{P}(k|k-1)\mathbf{H}^T(\mathbf{H}\mathbf{P}(k|k-1)\mathbf{H}^T + \mathbf{R}(k))^{-1} \tag{30}$$

$$\mathbf{K}_I(k) = \mathbf{k}_I * \mathbf{K}_P(k) \tag{31}$$

$$\mathbf{K}_D(k) = \mathbf{k}_d * \mathbf{K}_P(k) \tag{32}$$

$$\mathbf{P}(k|k) = (\mathbf{I} - \mathbf{K}_P(k)\mathbf{C})\mathbf{P}(k|k-1) \tag{33}$$

$$\hat{\mathbf{x}}(k|k) = \hat{\mathbf{x}}(k|k-1) + \mathbf{x}_P(k) + \mathbf{x}_I(k) + \mathbf{x}_D(k) \tag{34}$$

where \mathbf{k}_I and \mathbf{k}_d are the integral and derivative constants and \mathbf{x}_P , \mathbf{x}_I and \mathbf{x}_D are determined by Equations 24 to 26, respectively.

4. 1. Robustness Analysis of the Proposed GPID Integration Scheme

Regarding the integral part employed in the generalized PID filter, the proposed integration scheme presents a robust solution, which successfully mitigates the undesirable effect of GPS signal uncertainties and errors on the integrated navigation system. To illustrate the effectiveness of the proposed scheme, the following robustness analysis is

presented based on the SRPIF estimator with $k_i=1$ and $k_a=0$. Because the GPS measurement uncertainties have a major effect on the performance of INS/GPS integration, the measurement noise is only considered in this analysis.

As mentioned before in the introduction, the main challenge in an integrated navigation system is detecting or eliminating the effect of aiding sensor measurement errors on the system performance. The specification of process noise is only related to inertial sensors used in the INS process and can be predetermined by some experimental laboratory tests. Therefore, the GPID integration scheme is proposed to eliminate the measurement error vector in aided INS. Hence, without loss of generality, we consider the state-space Equations 16 to 17 without the process noise vector :

$$\mathbf{x}(k+1) = \mathbf{A}\mathbf{x}(k) \quad (35)$$

$$\mathbf{y}(k) = \mathbf{H}\mathbf{x}(k) + \mathbf{w}_m(k) \quad (36)$$

Based on the Equations 23 to 36, the one-step estimator can be written as follows:

$$\hat{\mathbf{x}}(k+1|k+1) = \mathbf{A}\hat{\mathbf{x}}(k|k) + \mathbf{K}_p(\mathbf{y}(k) - \mathbf{H}\hat{\mathbf{x}}(k|k)) + \mathbf{x}_1(k) \quad (37)$$

The estimation error is also defined as:

$$\mathbf{e}(k+1) = \mathbf{x}(k+1) - \hat{\mathbf{x}}(k+1|k+1) \quad (38)$$

Substituting Equations 25 to 37 into Equation 38 gives:

$$\mathbf{e}(k+1) = \mathbf{A}\mathbf{x}(k) - \mathbf{A}\hat{\mathbf{x}}(k|k) - \mathbf{K}_p\mathbf{H}\mathbf{x}(k) + \mathbf{K}_p\mathbf{H}\hat{\mathbf{x}}(k|k) - \mathbf{K}_p\mathbf{w}_m(k) - \mathbf{x}_1(k) = (\mathbf{A} - \mathbf{K}_p\mathbf{H})\mathbf{e}(k) - \mathbf{K}_p\mathbf{w}_m(k) - \mathbf{x}_1(k) \quad (39)$$

The disturbance vector $\mathbf{d}(k)$ is defined as:

$$\mathbf{d}(k) = -\mathbf{K}_p\mathbf{w}_m(k) - \mathbf{x}_1(k) \quad (40)$$

Therefore, the error dynamics equation becomes:

$$\mathbf{e}(k+1) = (\mathbf{A} - \mathbf{K}_p\mathbf{H})\mathbf{e}(k) + \mathbf{d}(k) \quad (41)$$

The dynamic equation of $\mathbf{d}(k)$ can be also written using Equations 21 and 25:

$$\mathbf{d}(k+1) = -\mathbf{K}_p\mathbf{w}_m(k+1) - \mathbf{x}_1(k+1) = -\mathbf{K}_p\mathbf{w}_m(k+1) - \mathbf{x}_1(k) - \mathbf{K}_1\mathbf{C}\mathbf{e}(k) \quad (42)$$

Adding and subtracting $-\mathbf{K}_p\mathbf{w}_m(k)$ to Equation 42 gives:

$$\mathbf{d}(k+1) = \mathbf{d}(k) - \mathbf{K}_p(\mathbf{w}_m(k+1) - \mathbf{w}_m(k)) - \mathbf{K}_1\mathbf{C}\mathbf{e}(k) \quad (43)$$

According to Equations 41 and 43 the augmented error dynamics can be expressed as:

$$\begin{bmatrix} \mathbf{e}(k+1) \\ \mathbf{d}(k+1) \end{bmatrix} = \begin{bmatrix} (\mathbf{A} - \mathbf{K}_p\mathbf{C}) & \mathbf{I}_{9 \times 9} \\ -\mathbf{K}_1\mathbf{C} & \mathbf{I}_{9 \times 9} \end{bmatrix} \begin{bmatrix} \mathbf{e}(k) \\ \mathbf{d}(k) \end{bmatrix} + \begin{bmatrix} \mathbf{0}_{9 \times 9} \\ -\mathbf{K}_p(\mathbf{w}_m(k+1) - \mathbf{w}_m(k)) \end{bmatrix} \quad (44)$$

In INS, gyroscopes and accelerometer intrinsically attain their output measurements with a high rate (100Hz or higher) compared to low-rate updates of aiding sensors (21). Based on this realistic idea, there is a negligible difference between two consecutive outputs of the inertial sensors. Therefore, Equation 44 can be approximated as:

$$\begin{bmatrix} \mathbf{e}(k+1) \\ \mathbf{d}(k+1) \end{bmatrix} \approx \begin{bmatrix} (\mathbf{A} - \mathbf{K}_p\mathbf{C}) & \mathbf{I}_{9 \times 9} \\ -\mathbf{K}_1\mathbf{C} & \mathbf{I}_{9 \times 9} \end{bmatrix} \begin{bmatrix} \mathbf{e}(k) \\ \mathbf{d}(k) \end{bmatrix} \quad (45)$$

According to Equation 45, if the \mathbf{K}_p and \mathbf{K}_1 are chosen appropriately, $\begin{bmatrix} (\mathbf{A} - \mathbf{K}_p\mathbf{C}) & \mathbf{I}_{9 \times 9} \\ -\mathbf{K}_1\mathbf{C} & \mathbf{I}_{9 \times 9} \end{bmatrix}$ becomes a stable matrix and the augmented error dynamics vector tends to zero as $k \rightarrow \infty$. Tending $\mathbf{d}(k)$ to zero means that the integral part of estimator, $\mathbf{x}_1(k)$, eliminates the undesirable effect of vector $-\mathbf{K}_p\mathbf{w}_m(k)$ ■

5. SIMULATION CASE STUDY

To evaluate the performance of the proposed integration scheme, a comprehensive simulation case study is conducted in this section. In addition to the lack of access to a real experimental integrated navigation system, we conducted the simulation test to easily manipulate the GPS measurement and produce artificial errors in the GPS measurements in specific intervals. This paper uses the mathematical model and MATLAB simulation expressed by Zhang et al. (22) to generate the IMU and GPS measurements, which developed four different kinds of scenarios named static, straight line, circle, and s-shape trajectories. The specifications of the IMU and GPS errors added to the generated ideal measurements are shown in Table 1.

Inertial navigation systems are divided into different grades based on their accuracy and performance, which is directly related to the error specifications of inertial sensors implemented in the navigation system. In this paper, we assume that a tactical grade INS is used in the test with error specification in Table 1. However, choosing different grades of INS directly affects the performance of the integrated system, we implemented the same error specification in Table 1 to specifically evaluate the effect of the integration scheme on the performance of the aided navigation system. After

TABLE 1. Specification of the IMU and GPS errors

Gyro constant errors	0.01 deg / h
Gyro random errors	0.001 deg / \sqrt{h}
Accelerometer constant errors	$\pm 50 \mu\text{g}$
Accelerometer random errors	0.03 m/s/ \sqrt{h}
GPS receiver position error	5 m
GPS receiver velocity error	0.1 m/s

generating the IMU and GPS measurements, the integration schemes based on the standard KF and the proposed generalized PID filter are evaluated separately.

As we mentioned before, multipath error is the major source of GPS signal error that can happen in urban areas near tall buildings or dense jungles. To evaluate the performance of the proposed scheme, the GPS measurement is deliberately corrupted by multipath error in a specific time interval of the simulation test. The circle scenario is chosen for the motion trajectory of the INS/GPS integrated system. The total simulation time is considered as 1 hour (3600 seconds). It is assumed that the GPS signal is corrupted by some sources of multipath error in the interval of 600 to 1100 seconds. In this interval, the GPS position and velocity measurements are manipulated by multipath errors specified in Table 2.

In the simulation tests two different tunings of integral and derivative parts are used in the proposed integration:

scheme 1. ($k_i = 1$ & $k_d = 0$)

scheme 2. ($k_i = 1.5$ & $k_d = 3$).

However, other different options for these constants are viable and can be tested and utilized in the system, we choose these two different schemes to optimally illustrate the effect of integral and derivative parts with an acceptable response for the INS/GPS system.

The simulation test results for attitude errors are depicted in Figures 3 to 5. From these results and computed RMS attitude errors given in Table 3. It is clear that the standard KF estimator has an inaccurate solution in the presence of the GPS position and velocity error especially in the yaw angle, which converges more slowly after the error interval. However, the proposed method maintains the attitude errors near zero in the interval that the multipath error occurs. It can be concluded from the results that the proposed method can also be used in inertial gyrocompass systems where guaranteeing accurate angular positions is a critical issue, especially in marine applications.

TABLE 2. Specification of the IMU and GPS errors

GPS position error corrupted by multipath	50 m
GPS receiver velocity error corrupted by multipath	0.5 m/s

TABLE 3. Attitude errors for the standard KF and proposed PID KF integration schemes

Integration method	Roll RMS Error (degree)	Pitch RMS Error (degree)	Yaw RMS Error (degree)
Standard KF	0.0665	0.0683	0.1538
Proposed PID KF (scheme 1)	0.0176	0.0188	0.0441
Proposed PID KF (scheme 2)	0.0159	0.0169	0.0402

The simulation results for latitude, longitude and altitude errors are depicted in Figures 6 to 8, respectively. The total path trajectory in the 2-D plane of longitude-latitude is also depicted individually in Figure 9 for both the standard KF and the proposed method with respect to the ideal trajectory. A detailed position error comparison is also given in Table 4 for both integration schemes. The results indicate that the positioning results of the proposed method have a more accurate and robust solution in response to the GPS multipath error. Based on the PID control theory, increasing the derivative constant, k_d , can result in the improvement of rapidness but also increase the oscillations in the response. On the other hand, the integral constant directly influences the accuracy of the response. The higher the integral constant k_i , the less error can be obtained in the response. Different tunings of the integral and derivative constants directly affect the performance of the proposed filter, which is reflected in the oscillation, rapidness, and accuracy of the solution. By a proper tuning of the integral and derivative constants, an acceptable filter performance can be achieved for a specific aided inertial navigation system. As is clear from the results, the proposed GPID filter of scheme 2 has a more accurate but more oscillatory response compared to the proposed GPID of scheme 1.

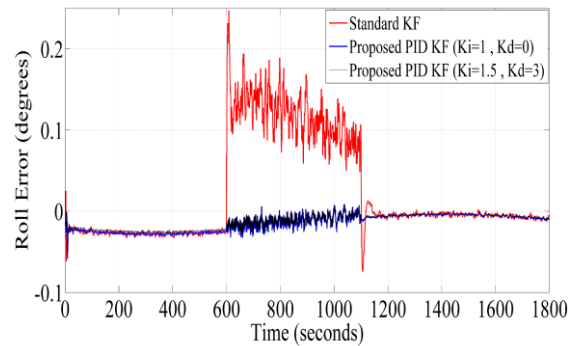


Figure 3. Roll angle error of the standard KF and the proposed GPID filter schemes

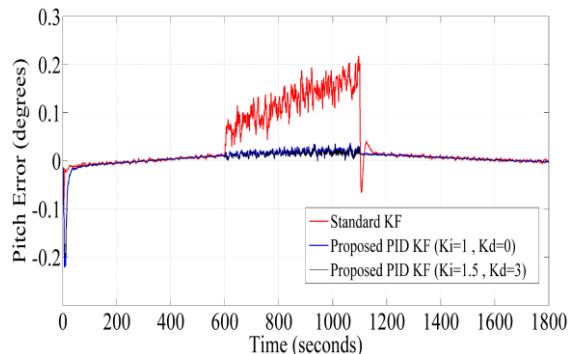


Figure 4. Pitch angle error of the standard KF and the proposed GPID filter schemes

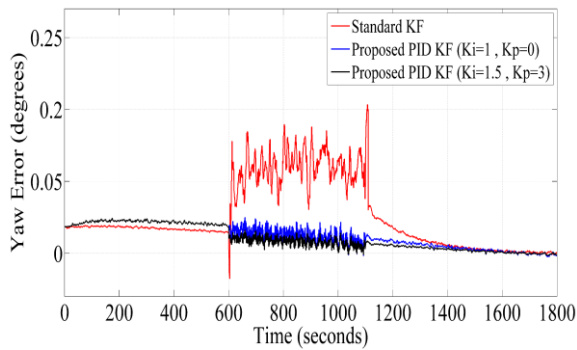


Figure 5. Yaw angle error of the standard KF and the proposed GPID filter schemes

TABLE 4. Position errors for the standard KF and proposed PID KF integration methods

Integration method	Latitude RMS Error (degree)	Longitude RMS Error (degree)	Altitude RMS Error (meter)	Horizontal Position Error (Km)
Standard KF	10.6 e-05	18.8 e-05	61.39	1.37
Proposed PID KF (scheme 1)	4.25 e-05	5.58 e-05	16.49	0.44
Proposed PID KF (scheme 2)	2.61 e-05	3.95 e-05	11.04	0.30

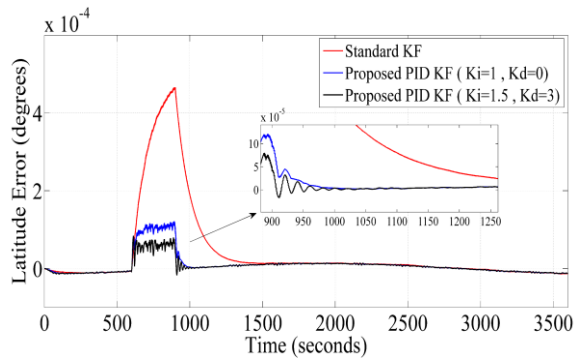


Figure 6. Latitude error of the standard KF and the proposed GPID filter schemes

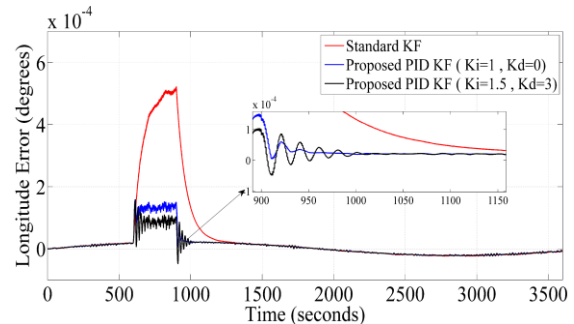


Figure 7. Longitude error of the standard KF and the proposed GPID filter schemes

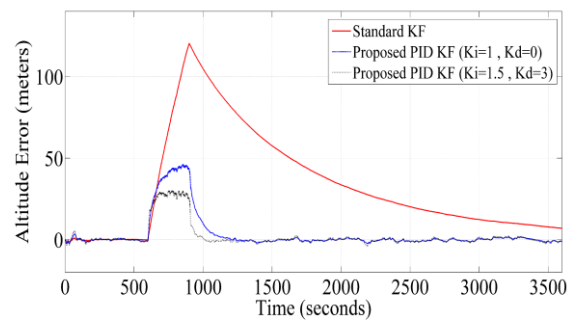


Figure 8. Altitude error of the standard KF and the proposed GPID filter schemes

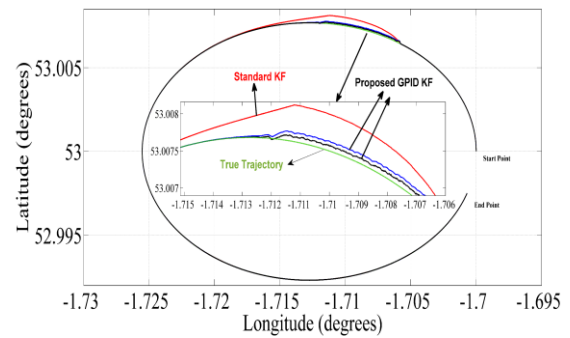


Figure 9. The 2-D trajectory for the KF and proposed GPID filter schemes

6. CONCLUSION

The performance of conventional estimators based on the standard Kalman filter is highly dependent on the accuracy of system and sensor modeling, which leads to performance reduction in the solution of the integrated navigation systems when the aiding sensor's information is corrupted by different sources of errors. To solve this problem, this paper has presented a robust simple structure integration scheme based on the combination of the PID control theory with the Kalman filter estimator. Adding two additional integral and derivative parts to the standard KF integration scheme can significantly boost the performance of the integrated navigation system. The proposed integration scheme is capable of eliminating the adverse effects of the measurement error of the aiding sensor in comparison to the standard KF scheme. The simulation results have illustrated that the proposed method has an acceptable performance in the presence of GPS measurement uncertainties in an INS/GPS navigation system. While The proposed integration scheme attains a robust solution with a very simple structure, which is suitable for online implementation with a low complexity burden, some primary tests are needed to tune the filter parameters. Implementing an adaptive or intelligent approach to tune the filter parameters can be taken into consideration for future research.

7. REFERENCES

1. Noureldin A, Karamat TB, Georgy J. Fundamentals of inertial navigation, satellite-based positioning and their integration: Springer Science & Business Media; 2012. <https://doi.org/10.1007/978-3-642-30466-8>
2. El-Sheimy N, Youssef A. Inertial sensors technologies for navigation applications: State of the art and future trends. *Satellite Navigation*. 2020;1(1):1-21. <https://doi.org/10.1186/s43020-019-0001-5>
3. Farhangian F, Benzerrouk H, Landry Jr R. Opportunistic in-flight INS alignment using LEO satellites and a rotatory IMU platform. *Aerospace*. 2021;8(10):280. <https://doi.org/10.3390/aerospace8100280>
4. Ghaderi F, Toloei A, Ghasemi R. Quadrotor Control for Tracking Moving Target, and Dynamic Obstacle Avoidance Based on Potential Field Method. *International Journal of Engineering, Transactions A: Basics*. 2023;36(10):1720-32. <https://doi.org/10.5829/IJE.2023.36.10A.01>
5. Wang Q, Liu K, Cao Z. System noise variance matrix adaptive Kalman filter method for AUV INS/DVL navigation system. *Ocean Engineering*. 2023;267:113269. <https://doi.org/10.1016/j.oceaneng.2022.113269>
6. Siddharth D, Saini D, Singh P. An efficient approach for edge detection technique using kalman filter with artificial neural network. *International Journal of Engineering, Transactions C: Aspects*. 2021;34(12):2604-10. <https://doi.org/10.5829/IJE.2021.34.12C.04>
7. Valizadeh A, Hamidi H. Improvement of navigation accuracy using tightly coupled kalman filter. *International Journal of Engineering, Transactions B: Applications*. 2017;30(2):215-23. <https://doi.org/10.5829/idosi.ije.2017.30.02b.08>
8. Hooshmand M, Yaghobi H, Jazaeri M. Irradiation and Temperature Estimation with a New Extended Kalman Particle Filter for Maximum Power Point Tracking in Photovoltaic Systems. *International Journal of Engineering, Transactions C: Aspects*. 2023;36(6):1099-113. <https://doi.org/10.5829/IJE.2023.36.06C.08>
9. Morales LA, Fabara P, Pozo DF. An Intelligent Controller Based on LAMDA for Speed Control of a Three-Phase Inductor Motor. *Emerging Science Journal*. 2023;7(3):676-90. <https://doi.org/10.28991/ESJ-2023-07-03-01>
10. Bagherzadeh SZ, Toosizadeh S. Eye tracking algorithm based on multi model Kalman filter. *HighTech and Innovation Journal*. 2022;3(1):15-27. <https://doi.org/10.28991/HIJ-2022-03-01-02>
11. Wirawan IMA, Wardoyo R, Lelono D, Kusrohmaniah S. Modified Weighted Mean Filter to Improve the Baseline Reduction Approach for Emotion Recognition. *Emerging Science Journal*. 2022;6(6):1255-73. <http://dx.doi.org/10.28991/ESJ-2022-06-06-03>
12. Rahgoshay MA, Karimaghiaie P. Robust in-field estimation and calibration approach for strapdown inertial navigation systems accelerometers bias acting on the vertical channel. *IET Radar, Sonar & Navigation*. 2020;14(3):407-14. <https://doi.org/10.1049/iet-rsn.2019.0359>
13. Rocha KD, Terra MH. Robust Kalman filter for systems subject to parametric uncertainties. *Systems & Control Letters*. 2021;157:105034. <https://doi.org/10.1016/j.sysconle.2021.105034>
14. Wang D, Dong Y, Li Z, Li Q, Wu J. Constrained MEMS-based GNSS/INS tightly coupled system with robust Kalman filter for accurate land vehicular navigation. *IEEE Transactions on Instrumentation and Measurement*. 2019;69(7):5138-48. <https://doi.org/10.1109/TIM.2019.2955798>
15. Zhu H, Zhang G, Li Y, Leung H. An adaptive Kalman filter with inaccurate noise covariances in the presence of outliers. *IEEE Transactions on Automatic Control*. 2021;67(1):374-81. <https://doi.org/10.1109/TAC.2021.3056343>
16. Farhangian F, Landry Jr R. Accuracy improvement of attitude determination systems using EKF-based error prediction filter and PI controller. *Sensors*. 2020;20(14):4055. <https://doi.org/10.3390/s20144055>
17. Setoodeh P, Habibi S, Haykin S. Kalman Filter. 2022. <https://doi.org/10.1002/9781119078166.ch5>
18. Zhang J, He X, Zhou D. Generalised proportional–integral–derivative filter. *IET Control Theory & Applications*. 2016;10(17):2339-47. <https://doi.org/10.1049/iet-cta.2015.0610>
19. Rahgoshay MA, Karimaghiaie P, Shabaninia F. Robust inertial frame-based alignment of fiber-optic gyro strapdown inertial navigation systems using a generalized proportional–integral–derivative filter. *Optical Engineering*. 2017;56(9):095102-. <https://doi.org/10.1117/1.OE.56.9.095102>
20. Rahgoshay MA, Karimaghiaie P, Shabaninia F. Initial alignment of fiber-optic inertial navigation system with large misalignment angles based on generalized proportionalintegral-derivative filter. *International Journal on Smart Sensing & Intelligent Systems*. 2017;10(3). <https://doi.org/10.21307/ijssis-2017-226>
21. Aggarwal P. MEMS-based integrated navigation: Artech House; 2010. <https://doi.org/10.1186/s43020-019-0001-5>
22. Zhang W, Ghogho M, Yuan B. Mathematical model and matlab simulation of strapdown inertial navigation system. *Modelling and Simulation in Engineering*. 2012;2012. <https://doi.org/10.1155/2012/264537>

COPYRIGHTS

©2024 The author(s). This is an open access article distributed under the terms of the Creative Commons Attribution (CC BY 4.0), which permits unrestricted use, distribution, and reproduction in any medium, as long as the original authors and source are cited. No permission is required from the authors or the publishers.



Persian Abstract

چکیده

بکارگیری یک روش موثر تلفیق داده در سیستم های ناوبری تلفیقی نقش موثری در عملکرد و دقت سیستم دارد. استفاده از یک روش موثر در تخمین نه تنها می تواند باعث بهبود دقت کلی سیستم گردد، بلکه در افزایش خاصیت مقاوم بودن سیستم در مواجهه با بروز خطا و نامعینی های اندازه گیری نیز موثر خواهد بود. مساله طراحی و بکارگیری یک روش تخمین بهینه حالت و تلفیق داده که بتواند بطور همزمان دارای خاصیت مقاوم بودن و ساختار ساده برای پیاده سازی عملی باشد به یک مساله داغ در سیستم های ناوبری و موقعیت یابی بدل شده است. در این مقاله با الهام از اصول تئوری کنترل کننده های تناسبی-انتگرالی-مشتقی و ترکیب آن با تخمین گر مرسوم فیلتر کالمن، یک روش تلفیق داده مقاوم در برابر نامعینی های اندازه گیری سنسورهای کمکی در سیستم های ناوبری تلفیقی ارائه شده است. به لطف اضافه شدن ترم های انتگرالی و مشتقی به تخمین گر ساده فیلتر کالمن، سیستم ناوبری تلفیقی پیشنهادی دارای عملکرد سریع تر و دقیق تر در مقایسه با سیستم های ناوبری تلفیقی بر پایه فیلتر کالمن ساده می باشد. نتایج شبیه سازی ها نشان دهنده کارایی و برتری روش پیشنهادی نسبت به روش تلفیق مرسوم بر پایه فیلتر کالمن است.



Flanges' Impact on Persian Historical Masonry Walls: Modeling Safety Factors

M. Ghamari^a, M. S. Karimi^b, P. B. Lourenço^c, H. S. Sousa^d

^a School of Computing, Engineering and the Built Environment, Edinburgh Napier University, Edinburgh EH10 5DT, United Kingdom

^b Assistant Professor, Faculty of Civil Engineering, Semnan University, Semnan, Iran

^c Professor, ISISE, Department of Civil, University of Minho, Guimarães, Portugal

^d Postdoctoral Researcher, ISISE, Department of Civil, University of Minho, Guimarães, Portugal

PAPER INFO

Paper history:

Received 20 November 2023

Received in revised form 06 January 2024

Accepted 05 February 2024

Keywords:

Persian Historical Masonry Walls

Partial Safety Factors

In-plane Behavior

Flanged Walls

Macro-modeling

ABSTRACT

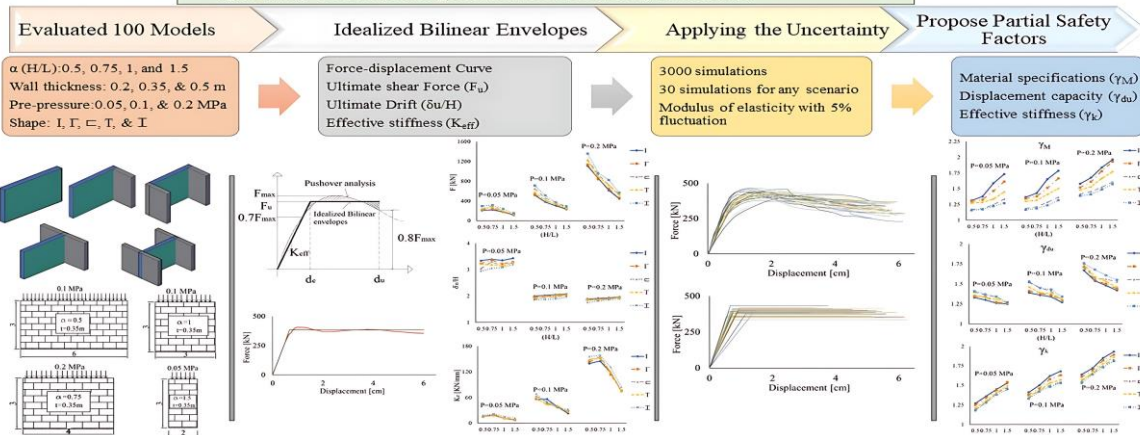
This comprehensive study investigates the nuanced impact of flanges, height-to-length aspect ratios, wall thickness, and pre-compression levels on Persian historical masonry walls under uncertainty conditions. Numerical testing of 100 masonry wall specimens, varying across five lateral constraints (flanges), four height-to-length ratios, three wall thicknesses, and three pre-compression levels, was conducted. The study also examined the influence of uncertainty on the modulus of elasticity. Results demonstrated a substantial dependency of ultimate shear force (F_u), ultimate drift (δ_u/H), and effective stiffness (K_{eff}) on the considered variables. F_u and K_{eff} increased with higher lateral constraints, wall thicknesses, and pre-compression levels, decreasing with reduced aspect ratios. Simultaneously, δ_u/H decreased with higher lateral constraints, wall thicknesses, and pre-compression levels, increasing with reduced aspect ratios. Estimated values for F_u ranged from 292.5 to 1357.4 MPa, δ_u/H spanned from 1.61 to 3.43, and K_{eff} varied from 7.72 to 158.9 kN/mm. Proposed partial coefficients for partial coefficients (γ_M), displacement capacity (γ_{du}), and effective stiffness (γ_k) were introduced through models incorporating uncertainty, revealing that increasing lateral constraints and wall thicknesses, and decreasing aspect ratios, led to heightened values for γ_M and γ_k and reduced values for γ_{du} . With increasing pre-compression levels, all safety factors increased. The safety factors (γ_M : 1.18–1.96, γ_{du} : 1.16–1.76, γ_k : 1.157–1.967) optimize Persian historical masonry structures, providing crucial insights for varied conditions were proposed.

doi: 10.5829/ije.2024.37.06c.10

Graphical Abstract

Flanges' Impact on Persian Historical Masonry Walls: Modeling Safety Factors

- ✓ Investigates Persian masonry, emphasizing the crucial in-plane role of flanges
- ✓ Optimizing the structural performance of masonry structures.



*Corresponding Author Institutional Email: Mehrdad.ghamari@napier.ac.uk (M. Ghamari)

Please cite this article as: Ghamari M, Karimi MS, Lourenço PB, Sousa HS. Flanges' Impact on Persian Historical Masonry Walls: Modeling Safety Factors. International Journal of Engineering, Transactions C: Aspects. 2024;37(06):1136-45.

1. INTRODUCTION

In a changing global landscape, masonry structures face seismic vulnerabilities and climate change impacts, underscoring the urgent need for sustainable and green initiatives in the realm of construction (1). The 2023 Türkiye earthquake highlighted the urgent need for seismic strategies, especially in rural masonry buildings (2, 3). Iran, with over 70% of residential buildings using unreinforced masonry (URM), exemplifies seismic vulnerability (4). The study delves into the intricate behavior of masonry structures, employing sophisticated analytical procedures (5, 6). Recognition of failure modes and determination of lateral strength and displacement capacity are crucial aspects in design equations by FEMA-356 and ASCE-41, providing notable approaches to address seismic challenges in masonry construction (7-9).

The significant challenge lies in the seismic vulnerability of load-bearing walls (10). When subjected to seismic loads, assessing ultimate shear force (F_u), ultimate drift (expressed as δ_u/H , signifying the ultimate deformation capacity relative to the wall height), and effective stiffness (K_{eff}) becomes pivotal for structurally evaluating masonry, an area where limited research exists (11). Various factors, including aspect ratio, thickness, lateral constraints, vertical pre-compression level, and material properties, affect these parameters in masonry shear walls—the primary structural element. Initiating the investigation involves studying force-deformation curves. Recent research using finite element methods has often adopted a homogenized set of units and mortar, overlooking mortar bonds and local failures (12, 13). This led to the proposing of a nonlinear finite element model based on biaxial experiments on brick units (14), capable of considering nonlinear material effects and progressive local failures. Consequently, masonry materials are assessed as a homogeneous model comprising bricks and mortar, known as macro modeling (15, 16).

In this investigation, the approach of macro modeling is employed to simulate masonry materials in constructed finite element models of walls. This method proves effective for comprehensively studying the general behavior of structures. The specimens are modeled by substituting a homogeneous material, with characteristic equations derived from Eurocode-8, for the actual material used in the model (17). Loading on masonry walls involves in-plane shear and out-of-plane bending, and to accurately model seismic behavior, both loadings are simultaneously applied in various aspect ratios on smaller-than-actual-sized specimens (18, 19). Aspect ratios are noted to significantly impact masonry structure behavior. Former studies often focused solely

on in-plane shear loading due to numerical analysis limitations, addressed through appropriate lateral constraints to prevent out-of-plane failure (20, 21). Simplified equations for shear strength under different loading conditions are proposed (22). As research advances, more comprehensive relationships for determining shear strength on a finite element basis are proposed (23). Additionally, a force-deformation curve based on elastic-perfectly plastic behavior of masonry materials is suggested through analytical methods (24).

Standards like Eurocode-8 indicate that the deformation capacity of masonry structures depends on the aspect ratio and modes of failure (17). However, factors such as F_u , δ_u/H , and K_{eff} are primarily influenced by lateral constraints, defining the stiffness and strength of vertical constraints, termed as flange walls. The study highlights the substantial impact of geometry and aspect ratio on wall parameters, investigating the in-plane behavior of various masonry walls with different failure modes and lateral constraints. Outcomes are compared with standards like FEMA 306, and FEMA 356 (25, 26).

The study also examines methods for determining the strength of the materials used for masonry buildings in Iran. In addition, the role of design parameters, especially bearing capacity (R_d), in the evaluation of structures is emphasized. Material specifications, including those on secondary deformation and modulus of elasticity, are evaluated to account for the non-linear and uncertain behavior of masonry materials. The nonlinearity and variability of the material are effectively taken into account by using the partial safety factor, which plays a particularly important role in accurately assessing the load-bearing capacity of pre-existing structures (27, 28).

By comparing F_u , δ_u/H , and K_{eff} between specimens with and without uncertainty effects, this research extracted numerical values for partial coefficients (γ_M), displacement capacity (γ_{du}), and effective stiffness (γ_k) for historical Persian masonry dating back to the 11th and 12th centuries AD (29). In this study, the application of nonlinear analysis in conjunction with probabilistic methods enabled the determination of the partial safety factor to generalize the safety criteria in the design of masonry structures. The research dealt with complicated data sets and examined a variety of scenarios and conditions. Detailed analyzes were conducted for various parameters that provided a nuanced understanding of the behavior of the masonry structure. The results of this research serve as an extensive data set and provide a wealth of detail that could form the basis for the potential inclusion of a refined indicator in building codes and regulations.

2. MATERIALS METHOD AND MODELLING

The investigation focuses on the evaluation of shear strength of masonry wall specimens in five distinct scenarios. These scenarios involve walls with various shapes, including I, Γ , \sqsubset , T, and \sqsupset ; which are formed by interconnected cross walls. The presence of flanges is taken into consideration, as depicted in Figure 1. Furthermore, four different aspect ratios, namely 0.5, 0.75, 1, and 1.5, are considered, along with three thickness values of 0.2, 0.35, and 0.5 meters.

To investigate wall conditions on different floors, specimens are analyzed under corresponding vertical pre-compression levels in one-, two-, and three-story structures. The pre-pressure is determined based on a dead load of 400 kg/m² and a live load of 200 kg/m². Consequently, vertical pre-compression loads of 50 kN/m², 100 kN/m², and 200 kN/m² (0.05 MPa, 0.1 MPa, and 0.2 MPa) are uniformly applied to samples with a 35 cm thickness, representing a prevalent traditional wall in Iran.

Additionally, three different pre-pressure gravity loading levels of 0.05, 0.1, and 0.2 MPa are uniformly applied to all samples. The dimensions of the I wall are specified as a length of 4 meters and a height of 3 meters. The length of the transverse walls adjacent to the main wall remains constant at 3 meters.

To address uncertainties, especially in modulus of elasticity parameters, each model undergoes thirty analyses, resulting in a total of 3000 simulations. The study unveils noteworthy insights into the impact of different parameters on the F_u , δ_u/H , and K_{eff} of Persian historical masonry materials. Table 1 presents the mechanical properties of masonry assemblages (29, 30).

Nonlinear analysis is employed to generate force-displacement (capacity) curves for all specimens subjected to in-plane loading. A gradual horizontal force is applied, and uniform displacement-controlled loading is executed across the entire upper surface area, inducing a 6 cm (2% drift) displacement over 60 steps.

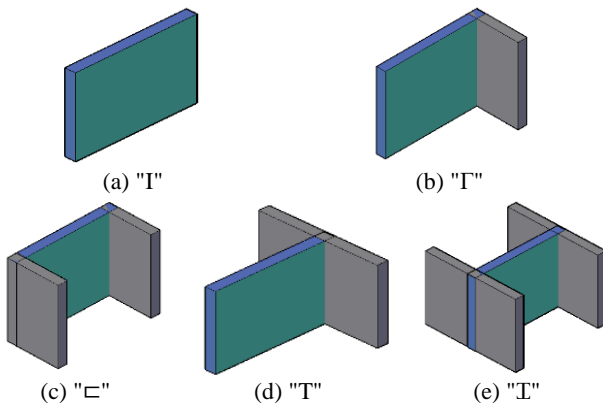


Figure 1. Structured Masonry Wall with Clearly Defined Lateral Constraints

The nonlinear analysis follows stress-strain relationships, employing Newton-Raphson iteration with displacement control and a convergence criterion set at a tolerance level of 10⁻⁴. Transverse direction displacement of the walls is modeled with freedom in specific planes, parallel and perpendicular to the ground surface, while constrained in the direction perpendicular to the load. Elements with surface contact are utilized to model each connection, ensuring structural integrity. For implementing lateral restraints at the base, all nodes of the masonry units are modeled as fully rigid (24). Masonry strength is associated with the modulus of elasticity, with a correlation that varies in tandem with changes in elasticity. The lognormal probability distribution is used to determine the modulus of elasticity, incorporating a coefficient of variation (CoV) of 0.25 (31).

Utilizing Finite element method software, this study employs macro-modeling of masonry walls with the free mesh element to depict their quasi-brittle traits (19). The Willam-Warnke failure criterion, which is frequently employed, takes into account both cracking and crushing. This criterion is utilized in finite element simulations to establish failure by assessing the principal stresses (27, 32). The validation of the numerical model is affirmed through a comparison with experimental outcomes obtained from in-plane stone walls, showcasing a meticulous analysis of masonry materials under various constraints. The investigation, incorporating the modulus of elasticity as a parameter, utilizes straightforward compression experiments conducted on walls constructed with masonry materials. The precision of the numerical model in predicting in-plane behavior is substantiated by closely aligning capacity curves with experimental results from two differently sized wall samples (33, 34).

3. PARAMETRIC STUDY

The investigation focuses on crucial parameters such as shear force, stiffness, and ductility. Employing pushover curves derived from numerical simulations, an equivalent bilinear curve is established following ASCE41-2017 (35) guidelines. The K_{eff} is determined by the convergence of the pushover curve and bilinear

TABLE 1. Mechanical Properties for Masonry Assemblage [29]

Modulus of elasticity	2730 MPa
Poisson's ratio	0.17
Bulk density	1530 kg/m ³
Compressive strength (fc)	2.73 MPa
Tensile strength (ft)	0.273 MPa

curve at 0.7 of the maximum shear force (F_{max}). The normalized F_u is calculated using an energy-equivalent approach to ensure equal areas under both curves. The ultimate displacement (δ_u) at 0.8 F_y post-strength degradations is also identified, as illustrated in Figure 2 outlining the calculation process.

The investigation of F_u , δ_u/H , and K_{eff} for different walls encompassed the manipulation of diverse parameters as reported in Table 2. The parameters discussed in this study were obtained by converting the pushover curves obtained from numerical simulation into an equivalent bilinear curve, as illustrated in Figure 2.

3. 1. Ultimate Shear Force

Figure 3 exhibits the variation of F_u of URM walls about the aspect ratio and wall thickness for a total of 5 distinct models under a pre-compression of 0.1 MPa. The results reveal a noteworthy trend: F_u tends to decrease as the aspect ratio increases. Conversely, an increase in wall thickness corresponds to higher values of F_u for each sample.

The results indicate that I-shape walls exhibit the lowest values in F_u , while T-shape walls demonstrate the highest values. The maximum shear force of an I-shaped wall, which has thicknesses of 0.35 m and 0.50 m and an aspect ratio of 0.5, exceeds the maximum shear force of an I-shaped wall with a thickness of 0.20 m by 15% and 63%, respectively. This emphasizes the impact of both aspect ratio and wall thickness on the

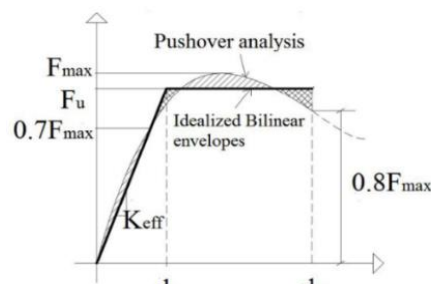


Figure 2. Definition of the parameters of the idealized bilinear envelope (36)

TABLE 2. F_u , δ_u/H and K_e for various walls

Sample	Wall thickness=35 cm			Wall thickness=20 cm			Wall thickness=50 cm			Wall thickness=35 cm			Wall thickness=35 cm		
	Pre-compression= 0.1 MPa			Pre-compression= 0.1 MPa			Pre-compression= 0.1 MPa			Pre-compression= 0.05 MPa			Pre-compression= 0.2 MPa		
H/L	F_u [kN]	δ_u/H	K_{eff} [KN/mm]	F_u [kN]	δ_u/H	K_{eff} [KN/mm]	F_u [kN]	δ_u/H	K_{eff} [KN/mm]	F_u [kN]	δ_u/H	K_{eff} [KN/mm]	F_u [kN]	δ_u/H	K_{eff} [KN/mm]
I	517.9	1.99	56.19	450.6	2.19	31.13	734.6	1.85	90.07	210.7	3.34	15.9	1107.8	1.88	139.47
Γ	532.6	1.96	56.56	446.1	2.17	33.12	793.6	1.8	93.37	220.6	3.23	15.27	1135.7	1.86	143.69
□	643.8	1.87	62.88	491.6	2.12	33.31	830.7	1.7	106.2	236.7	3.04	16.14	1228.6	1.85	148.06
T	572.3	1.91	58.73	488.3	2.12	32.97	810.5	1.73	102.2	233.7	3.21	16.05	1220.3	1.85	147.75
⊥	709.8	1.86	67.91	553.5	2.01	38.01	967.1	1.61	110.0	296.8	2.94	17.69	1357.4	1.75	155.5
I	378.5	2.02	56.15	312.1	2.59	18.65	517.6	1.89	58.97	218.6	3.39	18.79	862.2	1.91	145.09
Γ	407.1	1.98	46.44	330.2	2.48	19.61	512.3	1.85	61.5	243.5	3.36	20.15	841.1	1.88	152.41
□	456.5	1.96	50.11	350.7	2.37	20.26	575.3	1.73	66.84	306.8	3.3	17.9	935.6	1.84	155.66
T	408.5	1.97	43.22	360.4	2.45	19.93	523.4	1.76	65.64	277.1	3.18	17	889.6	1.84	152.85
⊥	510.3	1.87	48.16	401.1	2.24	23.06	645.6	1.75	75.02	315.7	3.05	21.92	965.3	1.81	158.9
I	303.2	2.05	38.31	247.7	2.59	10.15	395.7	1.91	35.29	176.3	3.35	11.35	613.8	1.93	118.17
Γ	331.4	2.03	38.11	271.1	2.48	11.14	397.8	1.89	39.74	180.4	3.22	11.57	645.8	1.91	113.45
□	364.7	1.97	40.14	265.9	2.27	12.51	447.1	1.86	44.29	188.1	3.12	12.59	722.1	1.9	118.64
T	341.5	2	40.99	260.4	2.48	12.02	453.7	1.85	42.63	192.6	3.14	11.29	715.2	1.89	119.04
⊥	370.4	1.89	35.84	303.6	2.24	13.5	493.6	1.8	55	239.7	2.76	15.5	825.9	1.86	130.5
I	233.4	2.07	23.01	176.4	2.63	10.33	331.3	1.96	32.01	114.8	3.43	7.72	448.6	1.96	74.58
Γ	248.6	2.05	27.72	190.4	2.58	10.73	348.7	1.95	33.06	123	3.29	8.22	463.2	1.94	75.96
□	266.7	2.02	27.81	201.6	2.41	11.7	374.6	1.88	34.18	128.1	3.27	9.37	536.5	1.93	74.86
T	241.7	2.04	25.55	197.5	2.49	11.2	370.5	1.91	34.3	133.5	3.26	8.88	514.7	1.94	73.65
⊥	292.5	1.96	32.08	218.5	2.32	12.81	423.1	1.84	37.28	151.7	3.19	11.58	565.8	1.89	84.05

structural strength of URM walls, with practical implications for design and construction considerations.

Figure 4 depicts the variations in F_u under different pre-compression levels and aspect ratios, with a consistent wall thickness of 0.35 m. The results underscore a noteworthy trend: an increase in pre-compression, coupled with the introduction of flanges, corresponds to a notable enhancement in F_u . The impact of increased pre-compression becomes more pronounced, particularly in conjunction with the presence of flanges, leading to a noticeable widening of the gap between each result. This suggests a synergistic effect between pre-compression and flanges, emphasizing their combined influence on boosting F_u . Notably, the effect of the presence of flanges observed in the previous figure is further accentuated in Figure 4, underscoring the importance of these factors in understanding and optimizing the structural performance of URM walls.

3. 2. Ultimate Drift

Figure 5 illustrates the drift values associated with aspect ratio and wall thickness for URM walls across five distinct models, all subjected to 0.1 MPa pre-compression. The results suggest that increasing wall thickness and introducing boundary conditions, such as flanges, lead to a decrease in ultimate deformation and drift. Importantly, the range of drift variations among the samples diminishes with the rise in wall thickness. Furthermore, there is a notable observation that the wall drift value increases in correlation with an increase in aspect ratio. The δ_u/H ratio is observed to range from 1.3% to 2.6% for shear walls built with Persian historical material. This analysis yields a significant understanding of the structural response exhibited by URM walls, highlighting the notable impact of factors such as wall thickness, aspect ratio, and boundary conditions on the overall drift behavior.

Figure 6 presents the variations in δ_u/H under different pre-compression levels and aspect ratios, with a constant wall thickness of 0.35 m.

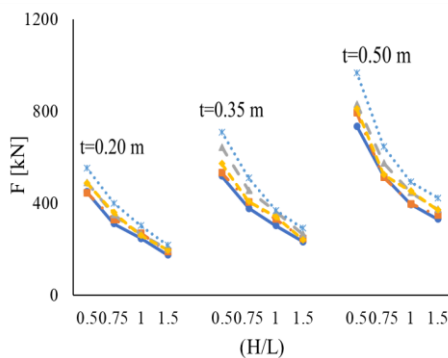


Figure 3. F_u variations in URM under different wall thickness and aspect ratios with a fixed pre-compression of 0.1 MPa

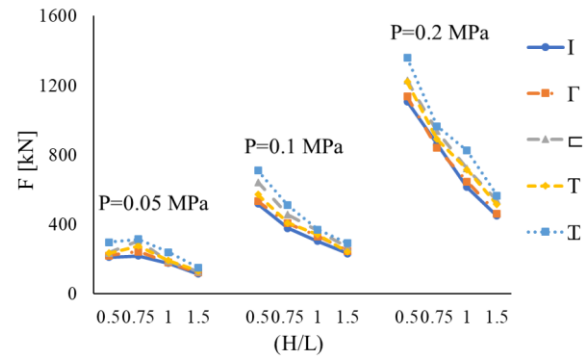


Figure 4. F_u variations in URM under different pre-compression levels and aspect ratios with a fixed wall thickness of 0.35 m

The results reveal a notable pattern wherein the outcomes for the two samples subjected to 0.1 MPa and 0.2 MPa pre-compression closely resemble each other, indicating significant similarity. Furthermore, the data from these samples demonstrate a reduction in scatter when compared to the sample subjected to 0.5 MPa pre-compression. This shows that the results at the upper pre-compression levels (0.1 MPa and 0.2 MPa) are close to each other, indicating a more consistent response within the analyzed parameters. Conversely, at a pre-compression of 0.5 MPa, the sample shows greater variability, indicating increased sensitivity or a stronger influence of the higher pre-compression on the observed results. Understanding these variations in data dispersion is crucial for comprehending the nuanced effects of pre-compression on the results.

It is noteworthy that the impact of aspect ratio in these samples across various pre-pressures can be disregarded, underscoring the predominant influence of pre-compression levels on the observed outcomes.

3. 3. Effective Stiffness

In this section, the influence of wall thickness and aspect ratio on the

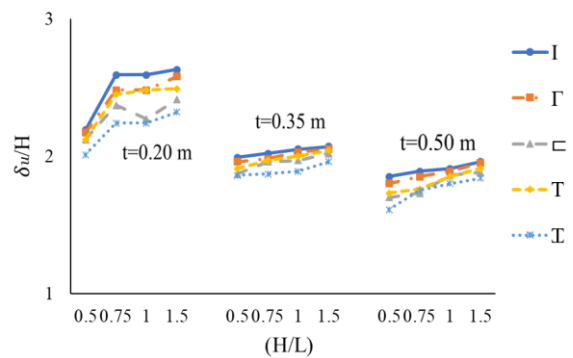


Figure 5. δ_u/H variations in URM under different wall thickness and aspect ratios with a fixed pre-compression of 0.1 MPa

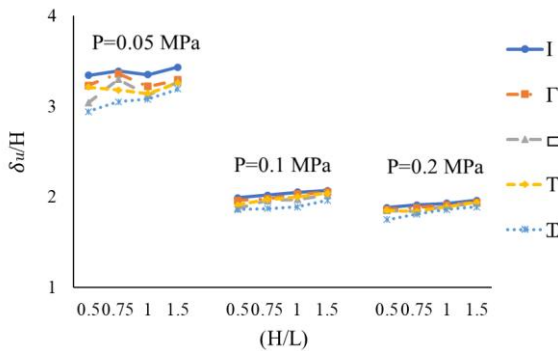


Figure 6. δ_u/H variations in URM under different pre-compression levels and aspect ratios with a fixed wall thickness of 0.35 m

stiffness of masonry walls is analyzed. Figure 7 shows the variations in the comparative K_{eff} of the walls as a function of different aspect ratios and varying wall thickness.

The results disclose a consistent pattern: as the aspect ratio of the walls increases, the comparable rigidity decreases for all wall thicknesses. This aligns with the established comprehension that walls generally exhibit greater rigidity at lower aspect ratios and greater flexibility at higher aspect ratios.

Furthermore, an intriguing observation arises with an increase in thickness—there is a corresponding rise in dispersion. This highlights the substantial impact of wall thickness on stiffness. The results underscore the intricate interplay between aspect ratio, wall thickness, and stiffness in masonry walls, offering valuable insights for structural considerations.

Figure 8 illustrates the variations in K_{eff} of walls concerning different aspect ratios and varying pre-compression levels. Notably, an increase in the placement of flanges corresponds to an elevation in K_{eff} , with ⊥-shape walls consistently exhibiting the highest values across all specimens, except for one model (I-shape with 0.75 aspect ratio and 0.1 MPa pre-compression). Specifically, for the 0.75 aspect ratio, K_{eff} values in some models surpass other aspect ratio values, highlighting the influence of this particular aspect ratio on stiffness. It is interesting to note that the overall trends align with the findings in Figure 7, confirming the interplay between aspect ratio, pre-compression, and stiffness in masonry walls.

4. RESULT ANALYSIS

In the pursuit of understanding uncertainty in F_u , δ_u/H , and K_{eff} within historic Persian masonry, three numerical values corresponding to the partial coefficients γ_M , γ_{du} , and γ_k were determined. The

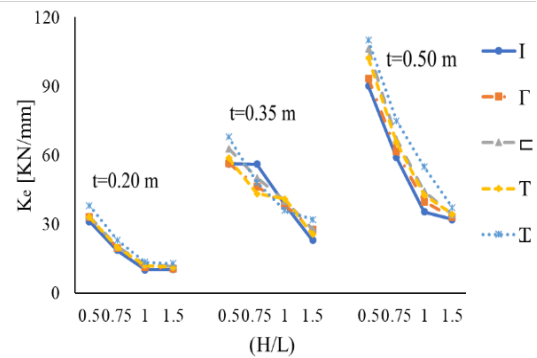


Figure 7. K_{eff} variations in URM under different wall thickness and aspect ratios with a fixed pre-compression of 0.1 MPa

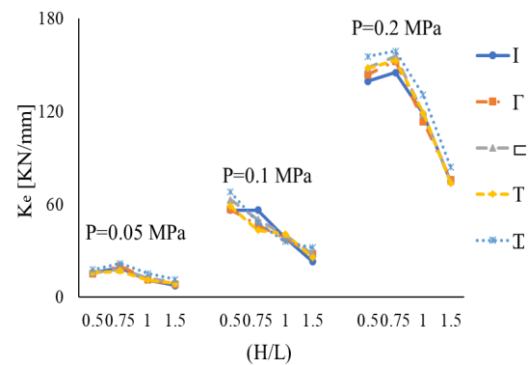


Figure 8. K_{eff} variations in URM under different pre-compression levels and aspect ratios with a fixed wall thickness of 0.35 m

primary goal of this study was to refine and idealize the results, incorporating modified characteristics derived from bilinearization to calculate these partial safety factors. Employing the finite element software, the analysis of uncertainty effects utilized tools that integrated probability distribution functions of variables and their covariance values as input data (24).

To ensure the reliability of the outcomes, thirty simulations were conducted with careful consideration to limit the fluctuation in the average wall response value to a maximum of 5% as the number of simulations increased. Following this, the force-displacement curves derived from the analysis of each of the thirty specimens were utilized as input data for the random variables. The exploration of γ_M , γ_{du} , and γ_k values for various walls involved systematic variations in different parameters, as detailed in Table 3. This comprehensive approach aimed to provide a nuanced understanding of the uncertainties associated with key structural characteristics in Persian historical masonry.

Figure 9 displays the values of γ_M , γ_{du} , and γ_k for URM under various wall thicknesses and aspect ratios, with a constant pre-compression of 0.1 MPa.

Additionally, Figure 10 illustrates the values of γ_M , γ_{du} , and γ_k under different pre-compression levels and aspect ratios, with a consistent wall thickness of 0.35 m. These figures offer a visual representation of the variations in partial coefficients concerning different structural parameters. They provide insights into how wall thickness, aspect ratio, and pre-compression impact γ_M , γ_{du} , and γ_k in URM.

The results depicted in the figure reveal a discernible trend: as the thickness of the samples increases, there is a corresponding decrease in the values of all three coefficients— γ_M , γ_{du} , and γ_k . Additionally, with an increase in the dimensional ratio, both γ_M and γ_k

coefficients exhibit higher values, while the γ_{du} coefficient decreases. Furthermore, the influence of boundary conditions is evident, particularly in samples with additional boundary features such as the T-shaped sample. In these cases, the value of γ_{du} coefficients is notably higher compared to other samples, while the γ_M and γ_k coefficients are observed to be the lowest.

Figure 10 illustrates that increasing pre-compression levels lead to higher safety coefficients across the samples. This observation underscores the impact of pre-compression on γ_M , γ_{du} , and γ_k in the analyzed structural elements.

TABLE 3. γ_M , γ_{du} and γ_k for various walls

Sample	Wall thickness=35 cm			Wall thickness=20 cm			Wall thickness=50 cm			Wall thickness=35 cm			Wall thickness=35 cm		
	Pre-compression= 0.1 MPa			Pre-compression= 0.1 MPa			Pre-compression= 0.1 MPa			Pre-compression= 0.05 MPa			Pre-compression= 0.2 MPa		
H/L	γ_M	γ_{du}	γ_k	γ_M	γ_{du}	γ_k	γ_M	γ_{du}	γ_k	γ_M	γ_{du}	γ_k	γ_M	γ_{du}	γ_k
I	1.41	1.39	1.365	1.66	1.51	1.559	1.3	1.34	1.241	1.27	1.33	1.312	1.64	1.67	1.578
Γ	1.38	1.41	1.342	1.62	1.53	1.539	1.28	1.36	1.234	1.25	1.34	1.298	1.61	1.71	1.52
□	1.34	1.52	1.185	1.56	1.58	1.369	1.24	1.38	1.169	1.19	1.4	1.173	1.56	1.73	1.412
T	1.36	1.46	1.301	1.58	1.53	1.498	1.27	1.36	1.189	1.21	1.36	1.273	1.57	1.75	1.478
⊥	1.33	1.53	1.165	1.55	1.56	1.328	1.23	1.38	1.157	1.18	1.41	1.158	1.53	1.76	1.386
I	1.5	1.36	1.428	1.74	1.48	1.637	1.39	1.31	1.276	1.36	1.3	1.375	1.72	1.54	1.675
Γ	1.46	1.38	1.378	1.71	1.5	1.569	1.37	1.33	1.253	1.34	1.34	1.326	1.69	1.55	1.609
□	1.44	1.45	1.212	1.63	1.53	1.403	1.33	1.36	1.176	1.28	1.36	1.183	1.65	1.57	1.453
T	1.43	1.39	1.315	1.67	1.52	1.513	1.35	1.34	1.207	1.3	1.33	1.283	1.66	1.59	1.529
⊥	1.42	1.45	1.187	1.63	1.51	1.349	1.32	1.36	1.165	1.28	1.37	1.172	1.64	1.68	1.409
I	1.62	1.34	1.653	1.88	1.43	1.839	1.49	1.25	1.453	1.45	1.26	1.586	1.85	1.48	1.836
Γ	1.58	1.36	1.512	1.85	1.45	1.776	1.46	1.25	1.426	1.44	1.27	1.463	1.82	1.5	1.779
□	1.5	1.41	1.286	1.76	1.46	1.459	1.4	1.3	1.318	1.4	1.34	1.245	1.75	1.56	1.524
T	1.53	1.38	1.408	1.77	1.46	1.624	1.42	1.3	1.362	1.41	1.31	1.334	1.78	1.53	1.663
⊥	1.48	1.43	1.236	1.74	1.47	1.423	1.38	1.33	1.286	1.38	1.34	1.221	1.73	1.61	1.486
I	1.68	1.27	1.785	1.96	1.36	1.967	1.58	1.16	1.543	1.53	1.25	1.732	1.93	1.42	1.963
Γ	1.63	1.29	1.663	1.92	1.37	1.869	1.56	1.18	1.517	1.54	1.26	1.613	1.89	1.44	1.932
□	1.54	1.29	1.362	1.78	1.43	1.526	1.49	1.24	1.336	1.47	1.26	1.336	1.83	1.53	1.607
T	1.57	1.31	1.503	1.84	1.41	1.685	1.53	1.21	1.419	1.49	1.26	1.448	1.86	1.46	1.769
⊥	1.53	1.34	1.315	1.76	1.45	1.486	1.47	1.24	1.308	1.45	1.27	1.268	1.81	1.55	1.573

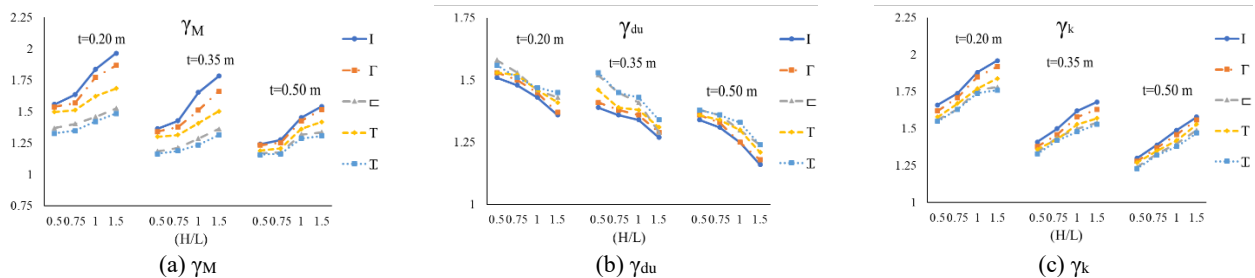


Figure 9. γ_M , γ_{du} , and γ_k in URM under different wall thickness and aspect ratios with a fixed pre-compression of 0.1 MPa

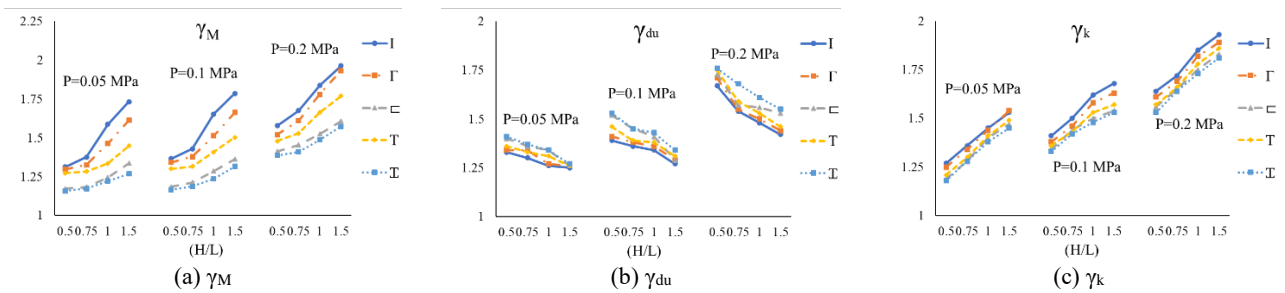


Figure 10. γ_M , γ_{du} , and γ_k in URM under different pre-compression levels and aspect ratios with a fixed wall thickness of 0.35 m

5. SUMMARY AND DISCUSSION

In this comprehensive study, the primary objective was to investigate the nuanced impact of flanges, height-to-length aspect ratios, wall thickness, and pre-compression levels on Persian historical masonry walls, taking into account uncertainty conditions. The examination involved the numerical testing of 100 masonry wall specimens under in-plane loading, varying across five lateral constraints involving transverse walls (flanges with shapes such as I, Γ , \square , T, and \bar{I}), four height-to-length ratios, three wall thicknesses, and three pre-compression levels. Additionally, the study explored the influence of uncertainty on the modulus of elasticity of the specimens.

The results unveiled a substantial dependency of F_u , δ_u/H , and K_{eff} on the considered variables. F_u and K_{eff} demonstrated an increase in higher lateral constraints, wall thicknesses, and pre-compression levels, accompanied by a decrease in reduced aspect ratios. Simultaneously, δ_u/H exhibited a decrease in higher lateral constraints, wall thicknesses, and pre-compression levels, while increasing with reduced aspect ratios. In conclusion, the estimated values for F_u ranged from 292.5 to 1357.4 MPa, δ_u/H spanned from 1.61 to 3.43, and K_{eff} varied from 7.72 to 158.9 kN/mm. Subsequently, three numerical values corresponding to partial coefficients (γ_M , γ_{du} , and γ_k) were proposed, calculated by comparing the deformation capacity of specimens with and without the introduction of an uncertainty parameter.

The outcomes from models incorporating uncertainty elucidated that increasing lateral constraints and wall thicknesses, along with decreasing the height-to-length aspect ratio, resulted in heightened values for γ_M and γ_k and reduced values for γ_{du} . Furthermore, as pre-compression levels increased, all safety factors exhibited an increase. In the final analysis, the proposed partial safety factors for Persian historic brick masonry were determined, ranging from 1.18 to 1.96 for γ_M , 1.16 to 1.76 for γ_{du} , and 1.157 to 1.967 for γ_k . These findings provide crucial insights for optimizing the structural performance of Persian historical masonry structures,

offering a nuanced understanding of their behavior under diverse conditions.

6. REFERENCES

- Kryeziu D, Selmani F, Mujaj A, Kondi I. Recycled concrete aggregates: a promising and sustainable option for the construction industry. *Journal of Human, Earth, and Future*. 2023;4(2):166-80. 10.28991/hef-2023-04-02-03
- Hussain E, Kalaycıoğlu S, Milliner CW, Çakir Z. Preconditioning the 2023 Kahramanmaraş (Türkiye) earthquake disaster. *Nature Reviews Earth & Environment*. 2023;4(5):287-9. 10.1038/s43017-023-00411-2
- Balamuralikrishnan R, Al-Mawaali A, Al-Yaarubi M, Al-Mukhaini B, Kaleem A. Seismic upgradation of RC beams strengthened with externally bonded spent catalyst based ferrocement laminates. *HighTech and Innovation Journal*. 2023;4(1):189-209. 10.28991/hij-2023-04-01-013
- Yazdani A, Kowsari M. Statistical prediction of the sequence of large earthquakes in Iran. *International Journal of Engineering, Transactions B: Applications*. 2011;24(4):325-36. 10.5829/idosi.ije.2011.24.04b.03
- Zamani-Ahari G, Yamaguchi K. Experimental investigation on cyclic in-plane behavior of URM walls retrofitted with AFRP. *Case Studies in Construction Materials*. 2022;17:e01558. 0.1016/j.cscm.2022.e01558
- Sivandi-Pour A, Noroozinejad Farsangi E. Statistical prediction of probable seismic hazard zonation of Iran using self-organized artificial intelligence model. *International Journal of Engineering, Transactions A: Basics*. 2019;32(4):467-73. 10.5829/IJE.2019.32.04A.02
- Engineers ASoc, editor *Seismic evaluation and retrofit of existing buildings*, ASCE/SEI 41-172017: American Society of Civil Engineers. 10.1061/9780784416112
- Asgari M, Tariverdilo S. Investigating the seismic response of structural walls using nonlinear static and incremental dynamic analyses. *International Journal of Engineering, Transactions B: Applications*. 2017;30(11):1691-9. 10.5829/ije.2017.30.11b.09
- Nateghi F. Earthquake evaluation of the non structural elements in a thermal power plant. *International Journal of Engineering, Transactions A: Basics*. 2016;29(1):8-13. 10.5829/idosi.ije.2016.29.01a.02
- Wilding B, Beyer K. Effective stiffness of unreinforced brick masonry walls. *Brick and Block Masonry—Trends, Innovations and Challenges*. 2016. 10.1201/b21889-248
- Salmanpour AH, Mojsilovic N, Schwartz J. Deformation capacity of unreinforced masonry walls subjected to in-plane loading: a state-of-the-art review. *International Journal of Advanced Structural Engineering*. 2013;5:1-12. 10.1186/2008-6695-5-22

12. Parisi F, Acconcia E. Formulation and experimental validation of distributed plasticity macro-element for unreinforced masonry walls. *Brick and Block Masonry-From Historical to Sustainable Masonry*: CRC Press; 2020. p. 152-8.
13. Tariq H, Najafgholipour MA, Sarhosis V, Milani G, editors. In-plane strength of masonry wall panels: A comparison between design codes and high-fidelity models. *Structures*; 2023: Elsevier. 10.1016/j.istruc.2022.11.125
14. Hatif Obaid A, Jaafar A, Noroozinejad Farsangi E. Experimental Investigation of Brick-Slabs: Evaluation of the Performance and Ductility of Various Brick Materials. *International Journal of Engineering, Transactions C: Aspects*. 2023;36(9):1636-44. 10.5829/ije.2023.36.09c.07
15. Lourenco P, Rots J, Blaauwendraad J, editors. Assessment of a Strategy for the Detailed Analysis of Masonry Structures. DIANA Computational Mechanics '94: Proceedings of the First International Diana Conference on Computational Mechanics; 1994: Springer. 10.1007/978-94-011-1046-4_34
16. Wani FM, Kodali R, Reddy VA, Sowmya D, Bondada A, Reddy S, et al. Finite element analysis of unreinforced masonry walls with different bond patterns. *Sustainable Engineering and Innovation*. 2023;5(1):58-72. 10.37868/sei.v5i1.id194
17. Code P. Eurocode 8: Design of structures for earthquake resistance-part 1: general rules, seismic actions and rules for buildings. Brussels: European Committee for Standardization. 2005. 10.3403/03244372u
18. Najafgholipour M, Maheri MR, Lourenço PB. Capacity interaction in brick masonry under simultaneous in-plane and out-of-plane loads. *Construction and building materials*. 2013;38:619-26. 10.1016/j.conbuildmat.2012.08.032
19. Vincent Sam Jebadurai S, Tensing D, Freeda Christy C. Enhancing performance of infill masonry with skin reinforcement subjected to cyclic load. *International Journal of Engineering, Transactions B: Applications*. 2019;32(2):223-8. 10.5829/ije.2019.32.02b.06
20. LI S, Yu T, Jia J. Empirical seismic vulnerability and damage of bottom frame seismic wall masonry structure: A case study in Dujiangyan (China) region. *International Journal of Engineering, Transactions C: Aspects*. 2019;32(9):1260-8. 10.5829/IJE.2019.32.09C.05
21. Siqi L, Tianlai Y, Junfeng J. Investigation and analysis of empirical field seismic damage to bottom frame seismic wall masonry structure. *International Journal of Engineering, Transactions B: Applications*. 2019;32(8):1082-9. 10.5829/IJE.2019.32.08B.04
22. Roca P. Assessment of masonry shear-walls by simple equilibrium models. *Construction and Building Materials*. 2006;20(4):229-38. 10.1016/j.conbuildmat.2005.08.023
23. Giordano A, De Luca A, Mele E, Romano A. A simple formula for predicting the horizontal capacity of masonry portal frames. *Engineering structures*. 2007;29(9):2109-23. 10.1016/j.engstruct.2006.10.011
24. Ghamari M, Karimi M, AmirShahkarami A. Effects of Lateral Constraints and Geometrical Characteristics on Deformation Capacity of the Persian Historic Unreinforced Masonry Shear Walls under Uncertainty Conditions. *International Journal of Engineering, Transactions B: Applications*. 2020;33(11):2127-36. 10.5829/IJE.2020.33.11B.02
25. Manual BP. Evaluation of earthquake damaged concrete and masonry wall buildings. Federal emergency management agency, FEMA. 1999. 10.1007/springerreference_225387
26. FEMA N. NEHRP, Prestandard and commentary for the seismic rehabilitation of buildings. Report; 2000.
27. Ghamari M, Karimi MS, Amirshahkarami A. Determination of Partial Safety Factors (γ_M) for Model Uncertainties for Persian Historical Masonry Materials. *Journal of Structural and Construction Engineering*. 2021;8(5):315-32. 10.22065/JSCE.2020.200249.1943
28. Karimi MS, Ghamari M, Amirshahkarami A. Effects of lateral constraints, geometrical characteristics and pre-compression level on the Drift capacity of Persian historical masonry walls. *Journal of Structural and Construction Engineering*. 2021;8(Special Issue 1):111-31. 10.22065/JSCE.2020.209984.2007
29. Hejazi M, Ghamari M, Beheshti H. Parametric Study of Failure Load of Persian Brick Masonry Domes Stiffened by FRP Strips under Concentrated Monotonic Loads. 2016. 10.22067/CIVIL.V28I1.34028
30. Ramakrishna U, Mohan S. Experiments on coupled technique for adjacent similar buildings. *International Journal of Engineering, Transactions C: Aspects*. 2020;33(9):1703-9. 10.5829/IJE.2020.33.09C.02
31. Vrouwenvelder T. The JCSS probabilistic model code. *Structural Safety*. 1997;19(3):245-51. 10.1016/S0167-4730(97)00008-8
32. El Yassari S, El Ghoulboursi A. Numerical simulation of fiber-reinforced concrete under cyclic loading using extended finite element method and concrete damaged plasticity. *International Journal of Engineering, Transactions A: Basics*. 2023;36(10):1815-26. 10.5829/IJE.2023.36.10A.08
33. Araújo AS, Oliveira DV, Lourenço PB, Magenes G, Penna A. In-plane shear behaviour of stone masonry piers: A numerical study. 2014. 10.4203/ccp.106.114
34. Magenes G, Penna A, Senaldi IE, Rota M, Galasco A. Shaking table test of a strengthened full-scale stone masonry building with flexible diaphragms. *International Journal of Architectural Heritage*. 2014;8(3):349-75. 10.1080/15583058.2013.826299
35. Institute SE, editor ASCE Standard, ASCE/SEI, 41-17: Seismic Evaluation and Retrofit of Existing Buildings 2017: American Society of Civil Engineers. 10.1061/9780784416112
36. Tomazevic M. Earthquake-resistant design of masonry buildings: World Scientific; 1999.

COPYRIGHTS

©2024 The author(s). This is an open access article distributed under the terms of the Creative Commons Attribution (CC BY 4.0), which permits unrestricted use, distribution, and reproduction in any medium, as long as the original authors and source are cited. No permission is required from the authors or the publishers.

**Persian Abstract****چکیده**

مطالعه حاضر به بررسی نقش فلنج‌ها، نسبت‌ابعاد طول به ارتفاع، و ضخامت نمونه‌ها و تأثیرات پیش‌فشرده‌سازی در دیوارهای مصالح بنایی تاریخی ایرانی با در نظر گرفتن شرایط عدم قطعیت می‌پردازد. صد نمونه عددی از دیوارهای مصالح بنایی در پنج حالت شرایط مرزی با حضور دیوارهای متقاطع (فلنج)، چهار نسبت‌ابعادی، سه ضخامت، و سه مقدار پیش‌فشرده‌سازی مختلف مورد مطالعه قرار گرفته است. تأثیر شرایط عدم قطعیت بر پارامتر مدول الاستیسیته مورد بررسی مطالعه گرفته است. نتایج، وابستگی مقادیر نیروی برشی نهایی (F_u)، دررفت نهایی (δ_u/H) و سختی موثر (K_{eff}) را با هر کدام از متغیرهای مورد بررسی نشان داده است. مقادیر F_u و K_{eff} با مقیدتر شدن شرایط مرزی، افزایش ضخامت و سطح پیش‌فشرده‌سازی، افزایش می‌یابد و با افزایش در مقدار نسبت ابعادی، کاهش می‌باشد. مقدار δ_u/H با مقیدتر شدن شرایط مرزی، افزایش ضخامت و سطح پیش‌فشرده‌سازی، کاهش می‌یابد و با افزایش در مقدار نسبت ابعادی، کاهش می‌یابد. محدوده نتایج برای F_u در بازه ۲۹۲.۵-۱۳۵۷.۴ مگاپاسکال، δ_u/H در بازه ۱.۶۱-۳.۴۳ و برای K_{eff} در بازه ۷.۷۲-۱۵۸.۹ کیلونیوتن بر میلی‌متر می‌باشد. سه ضریب ایمنی جزئی برای مصالح (γ_M)، ظرفیت جابجایی (γ_{du}) و سختی موثر (γ_k) با لحاظ نمودن شرایط عدم قطعیت، پیشنهاد شده است. نتایج نشان می‌دهد که با مقیدتر شدن شرایط مرزی و افزایش ضخامت و کاهش نسبت ابعادی، مقادیر γ_M و γ_k افزایش و مقدار γ_{du} کاهش یافته است. با افزایش مقدار پیش‌فشرده‌سازی، هر سه ضریب ایمنی افزایش یافته‌اند. مقادیر پیشنهادی برای این ضرایب برای γ_M در بازه ۱.۱۸-۱.۹۶، γ_{du} در بازه ۱/۱۶-۱/۷۶ و برای γ_k در بازه ۱/۱۵۷-۱/۹۶۷ می‌باشد. این نتایج می‌تواند ملاحظات ارزشمندی را برای بهینه‌سازی عملکرد ساختاری مصالح بنایی تاریخی ایرانی فراهم نماید.



Compressive Mechanical Properties and Water Absorption of Glass fiber-reinforced Plastics Pipes Aged in Caspian SeaWater

H. Rohbani, A. Moazemi Goudarzi*, F. Morshedsolouk

Faculty of Mechanical Engineering, Babol Noshirvani University of Technology, Babol, Iran

PAPER INFO

Paper history:

Received 27 November 2023

Received in revised form 30 December 2023

Accepted 21 January 2024

Keywords:

Water Absorption

Seawater Absorption

Carbon Fiber Reinforced Polymer

Glass Fiber-reinforced plastics Pipe

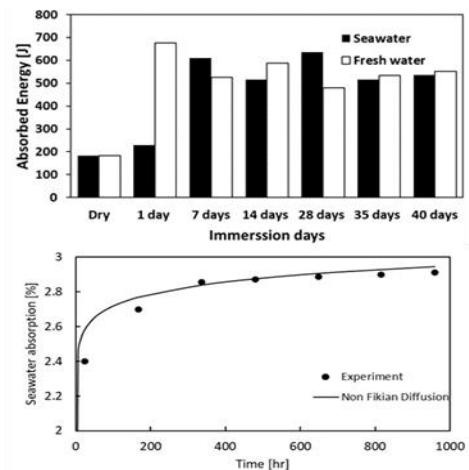
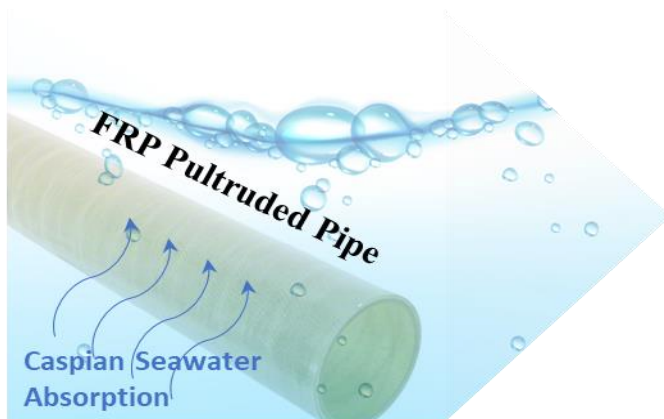
Pultruded Pipe

ABSTRACT

Glass fiber-reinforced plastics (GFRPs) have been widely used in marine structures, recently. In this paper, the water absorption and compressive behaviour of pultruded fiber-reinforced plastic pipes (GFRPs) after immersion in Caspian sea water and distilled water for 1, 7, 14, 21, 28, 35, and 40 days is experimentally investigated. In this respect, the specimens are submerged in Caspian seawater and distilled water and then their water absorption rate, length, and their compressive strength were measured every day. The compressive mechanical properties of the specimens in the as-received and water-aged states are obtained using quasi-static compression tests. The amount of water absorption and length change due to immersion in these two cases have also been investigated. After 40 days, the average relative humidity absorption of the samples in Caspian Sea water and distilled water were 2.88% and 2.89%, respectively. It was observed that after immersion in both Caspian Sea water and distilled water, the final compressive strength and absorbed energy of the pultruded pipes increased.

doi: 10.5829/ije.2024.37.06c.11

Graphical Abstract



NOMENCLATURE

m_t	mass of specimens after immersion	m_0	mass of specimens before immersion
M_i	percentage of moisture absorbed	W_i	weight of the sample in the i th stage
W_b	initial weight of the sample	C	moisture concentration
z	thickness	D_z	diffusion coefficient

*Corresponding author email: goudarzi@nit.ac.ir (A. Moazemi Goudarzi)

Please cite this article as: Rohbani H, Moazemi Goudarzi A, Morshedsolouk F. Compressive Mechanical Properties and Water Absorption of Glass fiber-reinforced Plastics Pipes Aged in Caspian SeaWater. International Journal of Engineering, Transactions C: Aspects. 2024;37(06): 1146-53.

1. INTRODUCTION

Fiber-reinforced plastics (FRPs) have been used in marine structures since the 1940s (1). In a marine environment, the polymer-based matrix will absorb water and its strength might significantly decrease; moreover, the interface strength between the fibers and matrix might adversely decline with respect to time due to aging in water or seawater. Given that the FRP marine structures are designed to withstand various severe load cases, it is of great importance to understand the aging process of marine FRP in different environments. It is also observed that the composite geometrical dimensions changes when they absorb water. This study investigated the changes in weights, compressive mechanical behaviors and geometrical properties of pultruded GFRP pipes after immersion in seawater.

Therefore, many researchers have conducted studies on how water absorption may affect the strength of fiber-reinforced plastics. The first serious discussions and analyses of the problem emerged during the 1970s when Ishai (2) studied the effect of cyclic water exposure on the weight gain, length change, and tensile strength deterioration of unidirectional Glass-Fiber-reinforced Plastics (GFRP). A literature review demonstrates that, after Ishai (2), many researchers have experimentally studied the effect of distilled water absorption on the mechanical properties of the various ranges of fibrous composites, including Carbon fiber reinforced polymer (CFRP), GFRP, and basalt fiber-reinforced polymeric (BFRP). In some experiments, after exposure to distilled water, there was no change in the strength of the specimens. For instance, Selzer and Friedrich (3) observed that the strength of the FRP composite did not change in the direction parallel to the fibers. Similarly, Zulueta et al. (4) concluded that water absorption did not change the strength of the carbon fiber-reinforced epoxy panels. On the contrary, many researchers observed that the mechanical properties of the water-aged composites were decreased due to the matrix and matrix-fiber interface degradation (5, 6).

Having studied the effect of distilled water on FRPs, it is also of great importance to know the seawater effect on composite marine structures. In recent years, there has been an increasing amount of literature on the effect of seawater on the mechanical properties of marine composite structures. Wood and Bradley (7) considered two different seawater exposure conditions, one saturated specimen and a specimen immersed in water 80 days after saturation. They observed that the cracks are more difficult to initiate in the aged specimen rather than in the intact specimen. Jeshti and Nayak (8) proposed a new hybrid CFRP and GFRP laminated composite to increase the durability of the composite's structures exposed to seawater. They succeeded in decreasing the hybrid composite seawater diffusivity by 44%. Li et al. (9)

immersed the CFRP specimens in artificial seawater with different salt concentrations for 7 months. They found that the tensile strength was sensitive to aging duration, while the salinity of the water did not change the tensile strength of the CFRP. Abdallah et al. (10) investigated the shear behaviour of beams reinforced with GFRP bars in seawater. They studied the effect of fiber reinforcement fraction. Gani et al. (11) also studied the water absorption in membrane of chitosan-resveratrol.

In addition to the studies above, there has been an increasing amount of literature on the mechanical properties of composite pipes, profiles, and piles in water and seawater. Shao and Kouadio (12) observed that composite piles immersed in 20°C and 70°C water would gain and lose weight respectively. The weight loss in 70°C water was due to leaching out some of the material. Ellyin and Maser (13) studied the multi-axial strains in FRP pressurized vessels which were immersed in water. Like Shao and Kouadio (12), they saw that the structure's strength loss is proportioned to the water temperature. They also noted that the swollen wet matrix can cause stress in the structures. Yao and Ziegmann (14) and d'Almeida et al. (15) conducted a series of tests to evaluate the strength of FRP pipes immersed in distilled water. They identified that the mechanical properties of the FRP pipes degrade by immersion in the distilled water. Liao et al. (16) conducted the flexural strength test on pultruded GFRP samples immersed in 70°C water, two different salt solutions. They observed that the salt concentration did not have much effect on flexural strength. Akil et al. (17) used distilled water, seawater, and acidic solutions at room temperature for a period of up to 3 weeks. They compared the strength of jute fiber-reinforced unsaturated polyester composite exposed to a different aqueous environment. Hawa et al. (18) studied water-aging at high temperatures and its effect on the impact and bursting strength of E-glass fiber/epoxy composite pipes. They proposed that the hyperbolic tangential method is a better method to model water absorption in pipes. Eslami et al. (19) modeled the transient moisture diffusion of E-glass fiber-reinforced Vinyl Ester composite pipes fabricated by a filament winding machine and investigated the buckling strength of aged specimens. Silva et al. (20) studied the flexural and radial compression of composite pipes aged in various fluids and observed that the compressive strength of the pipes was reduced, while the flexural strength of the pipes increased after 60 days. Mei et al. (21) studied the moisture absorption and compressive strength in the hygrothermal environment for a composite lattice core sandwich panel. They concluded that the failure modes did not change by aging time, while the strength of the sandwich panel decreased with aging time and temperature.

From the literature review, it is clear that various studies have assessed the tensile and flexural strength

reduction due to immersion in aqueous solutions. While there remain several aspects of water immersion effects on compressive strength which relatively little is known about it. Recently, Li et al. (22) and Liu et al. (23) presented a review of the research on the aging and environmental effects on the mechanical performance of composites. They concluded that water and seawater may cause matrix plasticization and –matrix-fiber debonding and decrease the strength of the composites immersed in water. They argued that –matrix-fiber debonding can affect the compressive strength of the composite structures more than the tensile strength. Thus, it is important to study this failure mode, while the study on this subject is rare. However, researchers have not studied compressive strength change due to immersion in water and seawater in much detail. On the other hand, the Caspian Sea is one of the important inland water bodies, and its water's ionic composition is different from that of open seawaters (24), and the standard solutions are not appropriate to model its effect on the structures. Thus, the objective of this study is to investigate the ultimate compressive strength of pultruded FRP pipes in an in-situ condition, in which, the specimens are immersed in Caspian seawater and distilled water for 1, 7, 14, 21, 28, 35, and 40 days and after that, their water absorption, length change, and ultimate compressive strength are measured. In this article, cylindrical samples of GFRP (pultruded) were immersed in distilled Caspian sea water, the edges of the sample were sealed. The purpose of this article is to study the water absorption behavior of composite materials and compare the compressive strength and absorbed energy before and after It was immersion

2. MATERIALS AND METHODS

In this study, the compressive mechanical behaviors of pultruded GFRP pipes, from the Asia Composite Company in Iran, in as-received conditions as well as after immersion in Caspian seawater and distilled water for 1, 7, 14, 21, 28, 35, and 40 days were investigated by conducting quasi-static compression tests. The pipes' diameter and thickness are 50 mm and 5 mm, respectively. The test procedure is conducted in the following steps (Figure 1), and then the results of the experiment were extracted and analyzed:

1. The test specimens are cut from commercial pultruded FRP pipes to 50 mm specimens in length.
2. The specimens are immersed in the Caspian seawater and distilled water at ambient temperature for 1, 7, 14, 21, 28, 35, and 40 days.
3. Before and after the immersion test, the specimens are weighed and their dimensions are measured using a Vernier scale.
4. The quasi-static crushing tests are conducted for as-received, water-aged, and Caspian seawater-aged

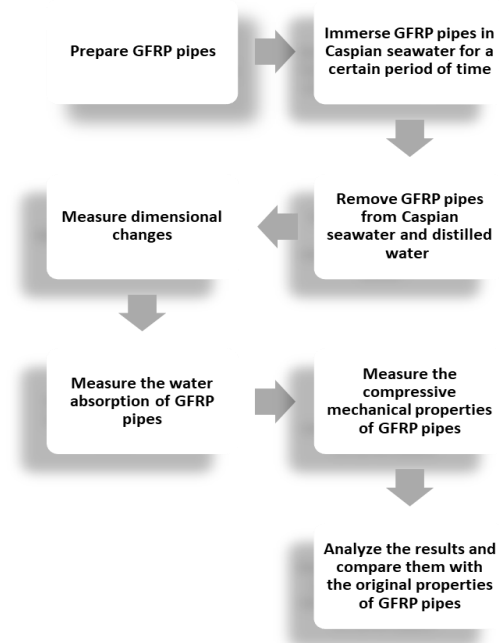


Figure 1. The test procedure

specimens using the SANTAM compression test instrument.

The water absorption for the test specimens at each day is calculated as follows:

$$M_i = \frac{m_t - m_0}{m_0} \times 100 \quad (1)$$

m_0 and m_t are the mass of specimens before and after immersion in (sea)water for t hours.

Moisture penetration inside most composites follows Fick's law Equation 2:

$$\frac{\partial c}{\partial t} = D_z \frac{\partial^2 c}{\partial z^2} \quad (2)$$

where c is the moisture concentration of the sample (g/mm), (t) time (s), (z) the thickness of the sample (mm) and D_z is the diffusion coefficient along the thickness (mm²/s). By solving Fick's second law with the help of boundary conditions, two practical relationships 3 and 4 are obtained to find the weight gain percentage:

$$M(T, t) = M_b + G(T, t)(M_b - M_b) \quad (3)$$

$$G(T, t) = 1 - \exp \left[-7.3 \left(\frac{D_z(T)t}{h^2} \right)^{0.75} \right] \quad (4)$$

With the help of Equation 3, the moisture content of the material is obtained at different temperatures and times, and Equation 4 is the moisture absorption function, where M_b is the initial moisture absorption rate and M_m is the moisture absorption rate in the saturated state. If only one side of the sample is in contact with the environment, instead of using parameter h as thickness, $2h$ is used in equation G. To predict the amount of

penetrant at time t , it is necessary to have the values of D_z and M_m . By calculating the slope, the linear part of the graph of weight gain in terms of the root of immersion time can be used to obtain the value of D with the help of Equation 5, and the horizontal asymptote of the graph also determines the value of M_m (25).

$$D_z = \pi \left(\frac{h}{4M_m} \right)^2 \left(\frac{M_2 - M_1}{\sqrt{t_2} - \sqrt{t_1}} \right)^2 \quad (5)$$

In relation 6, h is the thickness of the sample (mm), M_m is the percentage of equilibrium moisture, M_1 is the percentage of moisture at time t_1 , M_2 is the percentage of moisture at time t_2 , and D_z is the permeability coefficient of the composite. According to Figure 1, an increase in weight percentage is A maximum limit is reached and over time, the rate of moisture absorption increases and decreases, which is the reason for the filling of voids, cracks, and holes in the composite.

The diffusion mechanisms were divided into three: (1) typical behaviour according to Fick's law; when $n = 0.5$; and (2) when $n = 1$. the composites rapidly achieved water balance and maintained it as the immersion duration increased. the n was between 0.5 and 1 for anomalous diffusions. the water absorption diffusion mechanism was determined using the kinetic parameters of the slope (n) and intersection (k), which were obtained from the initial linear portion of the water absorption curve ($\log(M_t/\text{Max})$ vs. $\log(t)$)

$$\log\left(\frac{M_t}{M}\right) = \log(k) + n \log(t) \quad (6)$$

Our samples did not match the Fickian sample, so we used the non-fickian method according to Equation 6.

3. RESULTS AND DISCUSSION

Figures 2 and 3, which show the relative content of water after immersion in distilled water and Caspian sea water, show the relative amount of water after immersion in distilled water and Caspian sea water at equal time intervals. Each data point represents the relative content. water in a certain period of time. Analyzing the general trend of the curve can provide insight into the water absorption behavior of the material. If it is increasing, it indicates that the material absorbs more water over time. The steepness of the curve, it shows water absorption. A steeper curve indicates rapid water absorption, while a gentler curve indicates slower absorption, until the material has reached its maximum water absorption capacity. It indicates that the materials have reached equilibrium with water. This means that further immersion does not significantly affect the relative water content. It can be concluded that the amount of saturated water is the same for both cases (aged in Caspian Sea water and distilled water), while the water absorption process is faster for samples in Caspian Sea water before

saturation. After saturation, the average relative humidity of the samples in Caspian sea water and distilled water is 2.88% and 2.89%, respectively.

The change in length due to water absorption may cause additional stresses or create geometric defects in the structures. Therefore, the length change after immersion is also studied. Figure 4 shows the relative length change after immersion in Caspian Sea water and distilled water.

It shows the relative length change of the samples that were exposed to immersion in Caspian Sea water and distilled water. Each data point represents the relative length change after immersion in Caspian Sea water and distilled water. By comparing the length change The ratio of each substance in Caspian sea water and distilled water, the effect of these two liquids on the dimensional stability of the materials can be evaluated. A higher data point for Caspian Sea water indicates that the material has experienced a greater length change in seawater than in distilled water, and vice versa. The relative length change can be positive or negative, depending on whether the material expands after immersion. or contracted. Positive values indicate an increase in length and negative values indicate a decrease in length. Samples in Caspian Sea

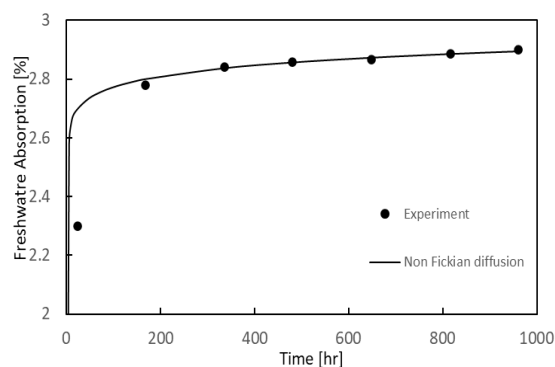


Figure 2. Relative water content after immersion in distilled water

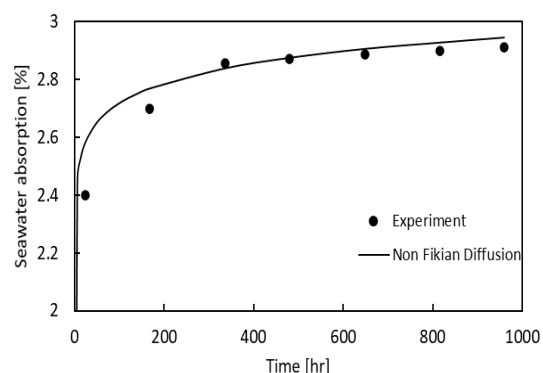


Figure 3. relative water content after immersion in Caspian seawater

water increased to 1% of their length in 14 days, and then their length remained almost unchanged. On the other hand, the length of samples aged in distilled water increases in the first 14 days, and then their length decreases until the final length is 1% shorter than the initial length. The reduction in the length of the pipes is due to the washing of material at both ends of the cut. The color change at both ends of the cut and the significant reduction of their local stiffness at both ends of the cut confirm this assumption.

In this study, a quasi-static compression test is performed using the SANTAM compression test instrument, which applies displacement at a constant rate of 5 mm/min to one end of the specimen and measures the applied load. The displacement load diagram obtained for aged samples in distilled water and Caspian sea water are shown in Figures 5 and 6, respectively. It can be the physical displacement or deformation of a substance or object. It shows the amount of force applied to the object. Each data point represents a specific measurement of force and displacement. The line shows the trend or relationship between force and displacement. By examining the trends of data points or lines, the relationship between force and displacement can be determined. The curved line represents a non-linear relationship.

The diagram can provide insight into the behavior of materials under external forces. Initially, the line or data points may show a linear relationship indicating elastic deformation. When a certain point is reached, the line may begin to curve or the data points may deviate, indicating plastic deformation where the material undergoes permanent deformation. The graph can identify the maximum force and displacement. Help the material before it breaks or becomes permanently deformed. This can be determined by the point at which the line level turns off or the data points do not increase.

The damage modes under the compressive loads for all the specimens aged in seawater and distilled water were the same. At first, at the bottom and top of the specimen small cracks started to grow and with a

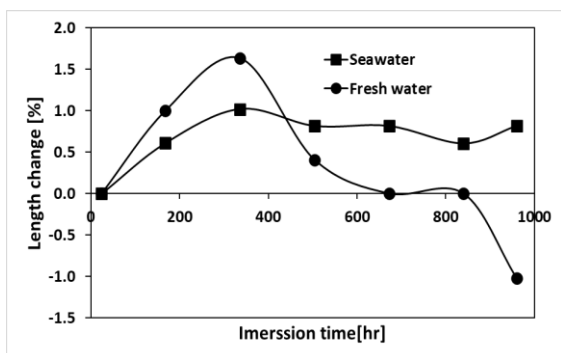


Figure 4. Effects of Distilled Water and Caspian Seawater on the Relative Length of Immersed Materials

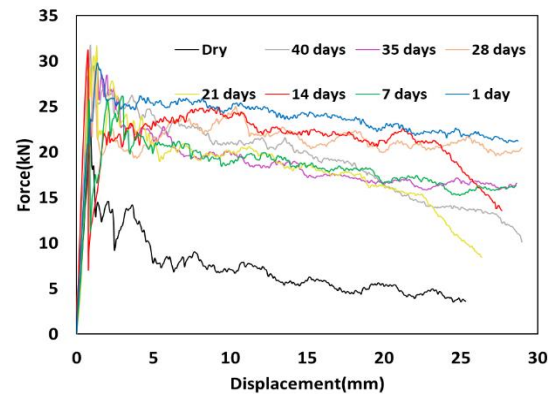


Figure 5. Force-displacement diagrams for specimens after n days in Caspian seawater

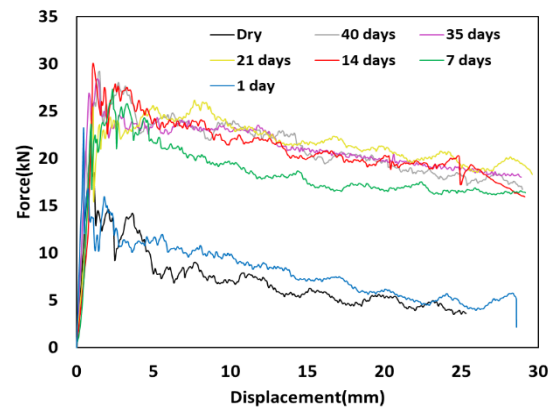


Figure 6. Force-displacement diagrams for specimens after n days in distilled water

cracking sound, the load gets to the ultimate load. Then the load decreased drastically and cracks grew larger and the fiber-matrix debonding occurred. The damage modes for a typical specimen are shown in Figure 7.

The mechanical properties of the aged specimens in seawater and distilled water under compression are obtained by quasi-static axial compression tests.

The ultimate compressive strength (σ_{ult}), and absorbed energy (EA) are calculated from the force-displacement diagrams for each specimen. From the force-displacement diagram, the nominal ultimate compressive strength of the specimens can be calculated and is equal to:

$$\sigma_{ult} = \frac{P_{max}}{A} \tag{7}$$

in which, Pmax and A are the first maximum force in the force-displacement diagram and the cross-section area of the specimen, respectively. The nominal ultimate compressive strength for aged specimens in Caspian seawater and distilled water is shown in Figure 8. The nominal ultimate compressive strength of the aged specimens is increased in both cases after some days in

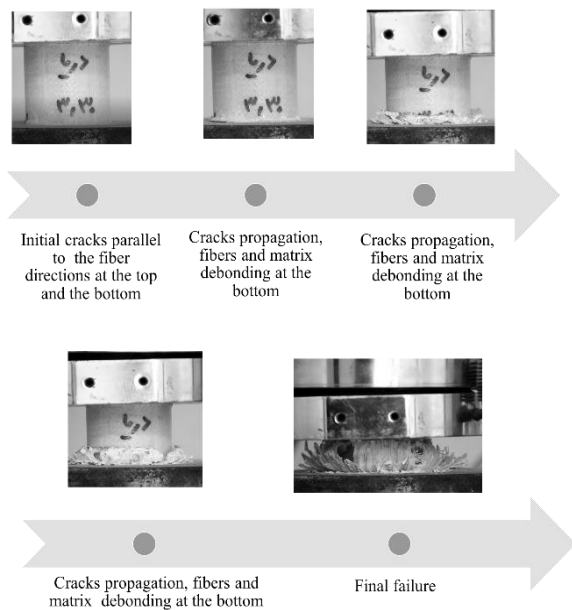


Figure 7. The failure modes and damage propagation in a specimen after one day of submersion in Caspian seawater

the water and after that, it remains almost constant, but it is notable that in distilled water the ultimate compressive strength increases faster. Figure 8, which shows the ultimate compressive strength. It is usually measured in units of pressure such as megapascals(MPa). It represents the maximum compressive stress that a material can withstand before failure. Each data point represents the ultimate compressive strength for a particular sample. By comparing the values of the data points, the relative strength of different materials can be evaluated in terms of compressive strength. The material with the highest ultimate compressive strength has the highest data point.

The other important parameter that can be derived from the force-displacement diagram is absorbed energy and can be calculated as follows:

$$EA = \int P \cdot du \tag{8}$$

in which, P and u are the force and the displacement in the force-displacement diagram. The absorbed energy is increased for aged specimens in both cases in comparison to the as-received specimen. However, the ultimate compressive strength of the aged specimens in distilled water is increased after one day of immersion. The amount of energy absorbed during the crushing test vs the immersion time in distilled water and Caspian seawater is plotted in Figure 9; the amount of absorbed energy is increased in both groups. However, from the force-displacement diagram (Figures 5 and 6), it can be deduced that the elastic modulus of the specimens, remains almost the same. An increase in the absorbed energy is due to the increase in average crushing force for all specimens.

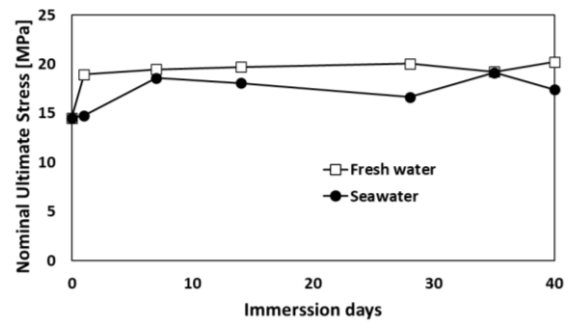


Figure 8. Ultimate compressive strength of pultruded pipes after immersion in Caspian seawater and distilled water

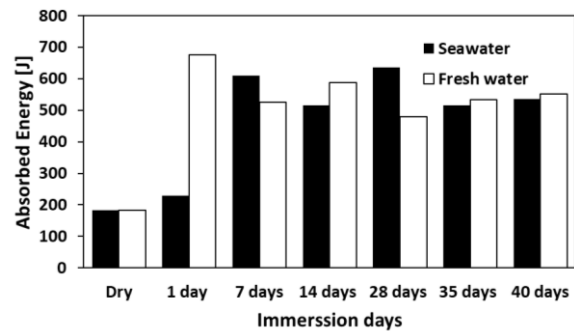


Figure 9. Absorbed energy during compression of pultruded pipes after immersion in Caspian seawater and distilled water

Increasing the nominal ultimate compressive strength and absorbed energy can be explained by Zhou and Lucas' theory [26]. The absorbed water in the polymeric matrix of the GFRP material can create two types of hydrogen bonds within the epoxy structure. These bonds seem to improve the compressive mechanical behavior of the Pultruded FRP pipes. Das et al. [27] in their work, E GFRP samples have used to monitor the moisture absorption behavior. The amount of water absorption is almost the same, but the slope is different. It was observed that after immersion in both Caspian sea water and distilled water, the final compressive strength and absorbed energy of the filled tubes increases.

4. CONCLUSIONS

This paper presents the ultimate compressive strength and energy absorption of pultruded fiber reinforced plastic pipes (GFRPs) after immersion in Caspian sea water and distilled water for 1, 7, 14, 21, 28, 35 and 40 days. It was investigated experimentally by performing quasi-static compression tests with the SANTAM tool. After saturation, the average absorption of relative humidity of the samples in Caspian sea water and distilled water were 2.88% and 2.89%,

respectively. The amount of water absorption, length change and final compressive strength were measured. The samples are immersed in Caspian sea water and distilled water for a certain period of time. By comparing the length change of the ratio of each material in Caspian sea water and distilled water, the effect of these two liquids on the dimensional stability of the materials can be evaluated. The samples in the Caspian sea water increased to 1% of their length in 14 days and then their length remained almost unchanged. On the other hand, the length of samples aged in distilled water increases in the first 14 days and then their length decreases until the final length is 1% shorter than the initial length. The damage modes under compressive loads were the same for all aged specimens in seawater and distilled water. It is noteworthy that the ultimate compressive strength increases faster in distilled water. The ultimate compressive strength of aged samples in distilled water increases after one day of immersion. The amount of absorbed energy increases in both groups. The ultimate compressive strength of all pultruded pipes immersed in Caspian seawater and distilled water is increased after saturation. And after 7 days it stays almost unchanged. The absorbed energy is also increased for both distilled water and Caspian seawater and after saturation, it stays almost constant as well.

5. REFERENCES

- Mouritz A, Gellert E, Burchill P, Challis K. Review of advanced composite structures for naval ships and submarines. *Composite structures*. 2001;53(1):21-42. 10.1016/S0263-8223(00)00175-6
- Ishai O. Environmental effects on deformation, strength, and degradation of unidirectional glass-fiber reinforced plastics. II. Experimental study. *Polymer Engineering & Science*. 1975;15(7):491-9. 10.1002/pen.760150704
- Selzer R, Friedrich K. Mechanical properties and failure behaviour of carbon fibre-reinforced polymer composites under the influence of moisture. *Composites Part A: Applied Science and Manufacturing*. 1997;28(6):595-604. 10.1016/S1359-835X(96)00154-6
- Zulueta K, Burgoa A, Martinez I. Effects of hygrothermal aging on the thermomechanical properties of a carbon fiber reinforced epoxy sheet molding compound: An experimental research. *Journal of Applied Polymer Science*. 2021;138(11):50009. 10.1002/app.50009
- Afshar A, Liao H-T, Chiang F-p, Korach CS. Time-dependent changes in mechanical properties of carbon fiber vinyl ester composites exposed to marine environments. *Composite Structures*. 2016;144:80-5. 10.1016/j.compstruct.2016.02.053
- Tual N, Carrere N, Davies P, Bonnemains T, Lolive E. Characterization of sea water ageing effects on mechanical properties of carbon/epoxy composites for tidal turbine blades. *Composites Part A: Applied Science and Manufacturing*. 2015;78:380-9. 10.1016/j.compositesa.2015.08.035
- Wood CA, Bradley WL. Determination of the effect of seawater on the interfacial strength of an interlayer E-glass/graphite/epoxy composite by in situ observation of transverse cracking in an environmental SEM. *Composites science and Technology*. 1997;57(8):1033-43. 10.1016/S0266-3538(96)00170-4
- Jesthi DK, Nayak RK. Evaluation of mechanical properties and morphology of seawater aged carbon and glass fiber reinforced polymer hybrid composites. *Composites Part B: Engineering*. 2019;174:106980. 10.1016/j.compositesb.2019.106980
- Li H, Zhang K, Fan X, Cheng H, Xu G, Suo H. Effect of seawater ageing with different temperatures and concentrations on static/dynamic mechanical properties of carbon fiber reinforced polymer composites. *Composites Part B: Engineering*. 2019;173:106910. 10.1016/j.compositesb.2019.106910
- Abdallah W, Farrag AM, Deifalla AF, Ibrahim AH, Mohamed HM, Ali AH. Shear Performance of GFRP Reinforced Concrete Beams with Seawater and Chopped Fiber. *Civil Engineering Journal*. 2023;9(4):835-48. 10.28991/cej-2023-09-04-05
- Gani BA, Asmah N, Soraya C, Syafriza D, Rezeki S, Nazar M, et al. Characteristics and antibacterial properties of film membrane of chitosan-resveratrol for wound dressing. *Emerging Science Journal*. 2023;7(3):821-42. <https://doi.org/10.28991/esj-2023-07-03-012>
- Shao Y, Kouadio S. Durability of fiberglass composite sheet piles in water. *Journal of composites for construction*. 2002;6(4):280-7. 10.1061/(ASCE)1090-0268(2002)6:4(280)
- Ellyin F, Maser R. Environmental effects on the mechanical properties of glass-fiber epoxy composite tubular specimens. *Composites Science and Technology*. 2004;64(12):1863-74. 10.1016/j.compscitech.2004.01.017
- Yao J, Ziegmann G. Water absorption behavior and its influence on properties of GRP pipe. *Journal of composite materials*. 2007;41(8):993-1008. 10.1177/0021998306067265
- d'Almeida J, de Almeida R, De Lima W. Effect of water absorption on the mechanical behavior of fiberglass pipes used for offshore service waters. *Composite structures*. 2008;83(2):221-5. 10.1016/j.compstruct.2007.04.020
- Liao K, Schultheisz C, Hunston DL. Effects of environmental aging on the properties of pultruded GFRP. *Composites Part B: Engineering*. 1999;30(5):485-93. 10.1016/S1359-8368(99)00013-X
- Akil HM, Cheng LW, Ishak ZM, Bakar AA, Abd Rahman M. Water absorption study on pultruded jute fibre reinforced unsaturated polyester composites. *Composites Science and Technology*. 2009;69(11-12):1942-8. 10.1016/j.compscitech.2009.04.014
- Hawa A, Majid MA, Afendi M, Marzuki H, Amin N, Mat F, et al. Burst strength and impact behaviour of hydrothermally aged glass fibre/epoxy composite pipes. *Materials & Design*. 2016;89:455-64. 10.1016/j.matdes.2015.09.082
- Eslami S, Honarbakhsh-Raouf A, Eslami S. Effects of moisture absorption on degradation of E-glass fiber reinforced Vinyl Ester composite pipes and modelling of transient moisture diffusion using finite element analysis. *Corrosion Science*. 2015;90:168-75. 10.1016/j.corsci.2014.10.009
- Silva ANd, Mori GS, d'Almeida JRM. Evaluation of the effects of fluids upon the flexural and parallel-plate loading behavior of glass fiber reinforced-vinyl ester resin matrix composite pipes. *Materials Research*. 2015;18:121-6. 10.1590/1516-1439.285614
- Mei J, Tan P, Liu J, He Z, Huang W. Moisture absorption characteristics and mechanical degradation of composite lattice truss core sandwich panel in a hygrothermal environment. *Composites Part A: Applied Science and Manufacturing*. 2019;127:105647. 10.1016/j.compositesa.2019.105647
- Li S, Guo S, Yao Y, Jin Z, Shi C, Zhu D. The effects of aging in seawater and SWSSC and strain rate on the tensile performance of GFRP/BFRP composites: A critical review. *Construction and Building Materials*. 2021;282:122534. 10.1016/j.conbuildmat.2021.122534

23. Liu T, Liu X, Feng P. A comprehensive review on mechanical properties of pultruded FRP composites subjected to long-term environmental effects. *Composites Part B: Engineering*. 2020;191:107958. 10.1016/j.compositesb.2020.107958
24. Zaker NH, Ghaffari P, Jamshidi S. Physical study of the southern coastal waters of the Caspian Sea, off Babolsar, Mazandaran in Iran. *Journal of Coastal Research*. 2007:564-9.
25. Zhou J, Lucas JP. Hygrothermal effects of epoxy resin. Part I: the nature of water in epoxy. *Polymer*. 1999;40(20):5505-12. 10.1016/S0032-3861(98)00790-3

COPYRIGHTS

©2024 The author(s). This is an open access article distributed under the terms of the Creative Commons Attribution (CC BY 4.0), which permits unrestricted use, distribution, and reproduction in any medium, as long as the original authors and source are cited. No permission is required from the authors or the publishers.



Persian Abstract

چکیده

اخیراً پلاستیک های تقویت شده با الیاف شیشه (GFRPs) به طور گسترده در سازه های دریایی مورد استفاده قرار گرفته است. این مقاله، مقاومت فشاری نهایی لوله های پلاستیکی تقویت شده با الیاف pultruded (GFRPs) پس از غوطه وری در آب دریای خزر و آب مقطر به مدت ۱، ۷، ۱۴، ۲۱، ارائه شده است. ۲۸، ۳۵ و ۴۰ روز با انجام تست های فشرده سازی شبه استاتیکی با ابزار SANTAM به صورت تجربی بررسی می شود. خواص مکانیکی فشاری نمونه ها در حالت های دریافتی و پیری آب با حل قانون دوم فیک با کمک شرایط مرزی به دست می آید. میزان جذب آب و تغییر طول ناشی از غوطه وری در این دو مورد نیز بررسی شده است. پس از اشیاع، میانگین جذب رطوبت نسبی نمونه ها در آب دریای خزر و آب مقطر به ترتیب ۲ / ۸۸ درصد و ۲ / ۸۹ درصد است. پس از آن، خواص فشاری نمونه های غوطه ور در دو مایع اندازه گیری و مقایسه می شود. یک آزمایش فشاری شبه استاتیکی انجام شده و مقاومت فشاری نهایی و جذب انرژی مورد ارزیابی قرار می گیرد. مشاهده شد که پس از غوطه ور شدن در هر دو آب دریای خزر و آب مقطر، مقاومت فشاری نهایی و انرژی جذب شده لوله های پر شده افزایش می یابد.



Improvement of Surface Evaporation by Reducing Heat Transfer to Fluid Bulk and Increasing Heat Absorption

A. Anjomrouz*

Department of Mechanical Engineering, Sharif University of Technology, Tehran, Iran

PAPER INFO

Paper history:

Received 23 December 2023

Received in revised form 14 January 2024

Accepted 22 January 2024

Keywords:

Surface Evaporation

Plant Structures

Expanded Polystyrene Foam

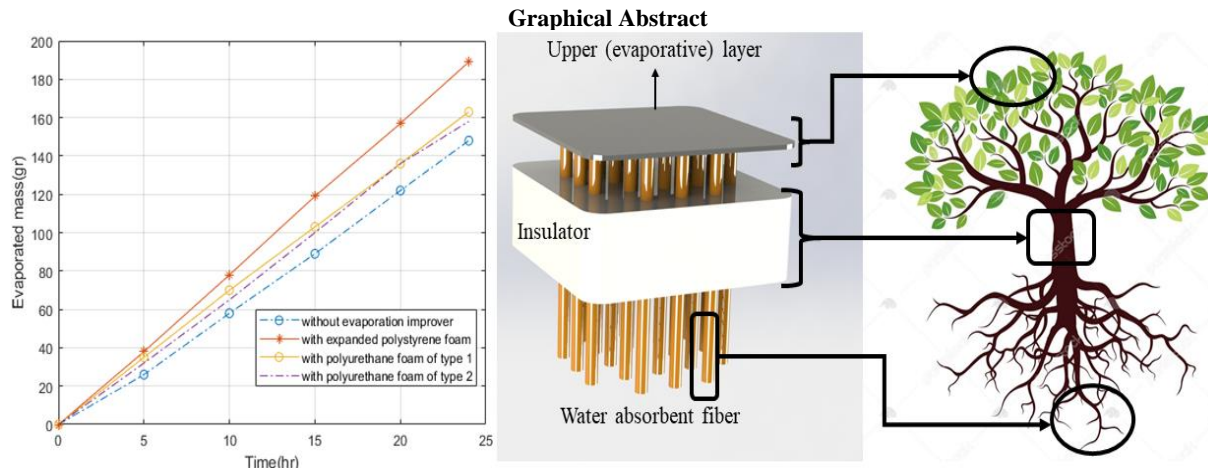
Cotton Fibers

Economic Efficiency

ABSTRACT

Surface evaporation is important in many natural phenomena and industrial applications; Therefore, improving this phenomenon is very useful. In this research, the water evaporation rate is increased by designing an innovative structure by inspiring from plant structures. This structure has two main effects, firstly, it reduces the amount of heat transferred to the fluid bulk through the surface and secondly, it increases the amount of heat absorption on the surface. This structure consists of three parts: an evaporation layer, insulation, and water-absorbing fibers. After many investigations on different materials to choose the best materials for these three parts, expanded polystyrene foam and cotton fibers showed the best performance. The structure after construction and testing was able to increase the mass of evaporated water during 24 hours by 28%. It also increased the temperature of the water surface in the evaporation process during 24 hours by 16%; This caused the water to evaporate at a high temperature. In addition, the mentioned structure increased the thermal efficiency up to 85% in the radiant flux of 0.6 kW/m^2 . The proposed structure is scalable for any size and cost-effective.

doi: 10.5829/ije.2024.37.06c.12



NOMENCLATURE

A Area

h_{fg} Enthalpy of vaporization

\dot{m} Mass flow rate

q'' Heat flux

Greek Symbols

η_{th} Thermal efficiency

*Corresponding Author Email: amin.anjomrouz@mech.sharif.edu (A. Anjomrouz)

Please cite this article as: Anjomrouz A. Improvement of Surface Evaporation by Reducing Heat Transfer to Fluid Bulk and Increasing Heat Absorption. International Journal of Engineering, Transactions C: Aspects. 2024;37(06):1154-63.

1. INTRODUCTION

Today, the process of fluid evaporation plays an important role in different industries and human life. From cooling towers in power plants to water desalination industries and even cooling a glass of hot tea, all of them are among the applications of the evaporation phenomenon. Given this widespread use of evaporation, the improvement of this process is also of particular importance. For example, one of the applications of this research is the evaporation of water by solar heat in water desalination which is important in many parts of the world. The main focus of the present study is on improving surface evaporation by reducing heat transfer to the fluid bulk and increasing heat absorption. This method of improving surface evaporation can improve the evaporation rate and efficiency of solar water purification.

According to the latest research, Ghasemi et al. (1) were able to achieve a thermal efficiency of more than 95% at a radiation intensity of 10 kW/m^2 by designing an innovative structure. This structure consists of two main parts: the upper part of the structure is an absorbent hydrophilic layer, and the lower part of it, is an insulating hydrophilic layer. Chen et al. (2), stated that in some applications such as solar water heaters, solar thermoelectric generators, etc.; there is a need for a type of solar absorber with high absorption and low radiation coefficients. They designed several colored absorber layers, on the TiN_xO_y base, which had an absorption coefficient of more than 95% and a radiation coefficient of less than 5%. Ni et al. (3) developed a floating absorber that was able to produce $100 \text{ }^\circ\text{C}$ vapor in ambient conditions under sunlight without the use of optical focusing methods. The idea used in this research was to use heat centralization and reduce the conduction and radiation heat transfer losses. Another feature of this structure is the low cost of construction and the ability to build on different scales. Li et al. (4) developed a graphene oxide-based evaporation-improving structure for desalination applications. This structure increased the thermal efficiency of the evaporation process by up to 80% and increased the desalination process's efficiency by four times. Zhu et al. (5) used black titania to create a nanocage structure to trap the light, increasing the rate of water evaporation to achieve a thermal efficiency of 70.9% at a flux of 1 kW/m^2 . Zhou et al. (6) developed an evaporation-improving structure using aluminum nanoparticles embedded in a three-dimensional porous layer. This layer floats on the surface of the water, absorbs more than 96% of the sun's radiation, and concentrates it on the water's surface. With this structure, they were able to complete the water desalination process with 90% efficiency. Ouar et al. (7) examined the effect of three different coatings (bitumen, charcoal, and ink) to improve heat absorption and increase evaporation in a

solar desalination plant and found that bitumen, charcoal, and ink coverages were approximately 25%, 18%, and 6% increase the efficiency of the desalination system respectively. Liu et al. (8) were able to improve the efficiency of a solar desalination plant by adding a suitable structure with a high absorption rate so that under one sun, the evaporation efficiency is 79% per day. To make this structure, they used active plasma filter paper as a photothermal material with a pleasant light absorption range of up to 92%. Huang et al. (9) used polypropylene coating on a polypropylene membrane to increase the efficiency of solar water vapor production by up to 72%. The reason for using polypropylene coating has a broad absorption spectrum that is almost consistent with the radiation spectrum of the sun, high efficiency in converting radiation into heat, and high stability of this material. Xu et al. (10) used a mushroom as a living organism that can improve the evaporation rate. They found that due to the structural properties of some mushrooms, they could be used as an evaporation-improving structure. In this study, they were able to achieve a thermal efficiency of 62% and 78% at a radiation intensity of 1 kW/m^2 , using a natural mushroom and a carbonized mushroom, respectively. Ni et al. (11) were able to build a floating solar desalination plant that improved the rate of water evaporation and desalination efficiency by adding a floating structure on the water. Important features of this innovative structure were removing salt from the structure, increasing the absorption coefficient of solar energy, cost-effectiveness, etc. Li et al. (12) while stating that in general the rate of water evaporation is limited by radiant heat from the sun, designed a structure that, assumes a 100% efficiency of solar energy transfer for water evaporation. To make this structure, they used a linen core and several rods made of multilayer plant cellulose, which were deeply coated with ethyl alcohol-soluble carbon nanoparticles. The core was then placed on an insulating layer of polystyrene foam. Zhao et al. (13) developed a surface evaporation enhancer using a nanostructured gel based on polyvinyl alcohol and polypyrrole. Using this structure, they were able to achieve an evaporation rate of 2.3 kg/h/m^2 at a radiation intensity of 1 kW/m^2 . They also increased the thermal efficiency of the evaporation process by 94%. Hu et al. (14) improved the surface evaporation rate in a desalination plant by designing a multilayer structure. This structure is composed of several materials including silicon oxide, cellulose nanofiber, and carbon nanotube. The bottom layer of this structure is hydrophilic to absorb and pump the water, and at the upper part where the evaporation process takes place, a hydrophobic layer is considered. Also, the special design and porosity of this structure prevent the separated salt from depositing on the upper layer of the structure and moving toward the lower part of the structure. Miao et al. (15) designed an innovative structure to increase heat transfer efficiency

by 84.6%. In this structure, a layer of carbon nanotube was used as a solar absorber, a piece of aerogel as heat insulation, and a layer of filter paper to transfer water. In a review article, Wang et al. (16) investigated the methods and challenges of desalination of water with solar energy. A lot of research has been done in the field of improving evaporation efficiency. In this article, they reviewed the basic principles of optimal design of a solar desalination system which includes the development of suitable materials for this application and system development. Guo et al. (17) developed an evaporation-improving structure made of hydrophilic hydrogels with island-like fragments of hydrophobic material. This structure was able to increase the evaporation rate to about 4 kg/h/m^2 with an efficiency of 93% (at a radiant heat flux of 1 kW/m^2). They also examined the fabricated structure and the rate of water evaporation at the molecular level using molecular dynamics simulations, and a logical output consistent with the experimental results was obtained.

In lots of previous research, studied the evaporation efficiency specifically for the application of solar desalination and pure water generation. They proposed method improved evaporation in appropriate manor for this application (18-20); However, in this study, the surface evaporation has been improved for a general case and the proposed solution is not limited to a specific application.

In previous research, increasing the evaporation efficiency has been studied by methods such as using micro and nanostructures (21-23), using strong adsorbents (2, 7, 8), using hydrogel materials (24-26), etc. Many previous methods of evaporation improvement are so complex and expensive to use by everyone, but in the present study, the main emphasis is on improving the evaporation rate with a high thermal efficiency by using an innovative, economical, simple, and scalable structure inspired by the structure of plants is proposed for this purpose.

The idea of this study is to improve the evaporation rate, by reducing the heat transfer from the fluid surface to the fluid bulk and concentrating the heat in a thin layer of fluid on the fluid surface.

As can be seen in Figure 1 fluid heating occurs in three modes: bottom heating, bulk heating, and interfacial heating. In this research, the heating of the fluid volume should be prevented and the heat radiated to the fluid (for example, from the sun) should be concentrated on the surface. In this way, surface evaporation should be improved.

2. MATERIAL AND METHODS

In this section, the test device and measuring instruments used in this research are described and at the end, how the experiments are performed is explained.

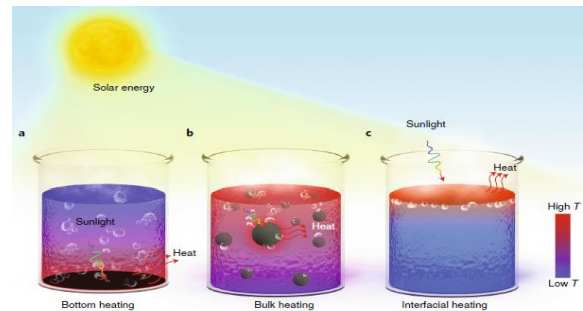


Figure 1. Three types of fluid heating (27)

2. 1. Setup Preparation

In this study, since the purpose is to investigate surface evaporation, the heat transferred to the fluid must also be from the fluid surface, such as fluid evaporation using heat from sunlight. To keep the heating conditions constant during the test, a heat source with an output power of approximately 0.6 kW/m^2 is used. Also, a container with dimensions of $10*10*20 \text{ cm}^3$ is used to store the fluid. The main part of the test apparatus in this study (by which the test goal i.e., improving surface evaporation is achieved) is an innovative structure that improves evaporation. This structure consists of several parts. Figure 2 shows the test bed details.

2. 2. Materials

The first part of the innovative structure is an insulator that aims to prevent heat transfer to the fluid volume; Which must be on the surface of the fluid and therefore need to have a lower density than the fluid. In this research, three types of foam with a thickness of 3.5 cm have been used as insulating material.

The second part of the structure is the fiber, which at this structure has the same function as plant vessels; The purpose of these fibers is fluid suction and according to this purpose, cotton has been selected as the material for these fibers. How to connect these two parts of the desired structure should be such that the water under the insulation layer is sucked by the fibers to the top of the structure.

The third part of the structure designed in this research is a type of hydrophilic layer that in addition to high wettability, must also have a high heat absorption coefficient. In this research, this layer is known as the evaporative layer. Many factors affect the high thermal absorption coefficient of this layer, which are the material, color of the layer, etc. The first feature considered in this study for the evaporative layer is that the effective surface of this layer is high relative to the geometric dimensions. This feature increases the rate at which fluid evaporates from the surface. To create this condition, a layer of cloth with regular villi in millimeter dimensions was used. The second feature of the evaporative layer used in this research is its color. Since black color has the highest heat absorption coefficient, it has been used as a suitable color for the evaporative layer.

The third feature of this layer is its material. The material of the evaporative layer should be selected from a hydrophilic material that has a good water absorption rate. For this purpose, cotton is used as the evaporative layer material.

As mentioned above, this structure has the same function as what happened in the plants and there is an analogy between them. More details on how plants work are explained by Bohr et al. (28). Figure 3 shows this analogy. According to this figure, the water-absorbing fibers are equivalent to the root and the vessels connected to it (which have the task of transferring water to different parts), the insulation part is equivalent to the stem (which is the place where the vessels pass), and the evaporation surface is equivalent to the leaf in a plant.

In this research, one type of expanded polystyrene foam and two types of polyurethane foam were used as insulation on the evaporation-improving structure. The expanded polystyrene foam is impermeable (closed cell) but polyurethane foams are permeable (open cell). The characteristics of these three types of foam are presented in Table 1.

2.3. Measuring Instruments A digital scale and a digital thermometer are mainly used. The scale has a measurement resolution of 1 gram with a measurement error of ± 1 gram. Also, the thermometer has a measurement resolution of $0.1\text{ }^{\circ}\text{C}$ with an accuracy of $0.1\text{ }^{\circ}\text{C}$.

The characteristics of foams are measured. The density is obtained by measuring the mass and volume of a sample of each foam. The water absorption is measured by subtraction of the maximum mass of a wet foam and a dry one for each experimented foam. Contact angle measurement was performed according to ASTM D-7334-08 (29) with Jikan (30)CAG-20 SE device.

2.4. Test Procedure The experiments performed in the present study are divided into two categories. To reduce the effect of errors in the experiment, in each category, if necessary, the experiments are repeated and averaging is used.

In the first group of experiments, the effect of reducing the fluid mass on the evaporation rate is investigated. In this section, no evaporation-improving structure is used and by reducing the mass of the initial water in the container from 1900 to 1700, 1500, and 1300 grams, its effect on the amount of water evaporation is checked.

In the second group, four experiments are done. This group aims to find the effect of the evaporation-improving structure. The mass of water in this group is 1900 grams. In the first experiment, there is no evaporation improver. In the second experiment, an evaporation improver with expanded polystyrene foam is used, in the third experiment evaporation improver with polyurethane foam of type 1 is used and in the fourth experiment evaporation improver with polyurethane foam of type 2 is used.

In this research, the tests were performed within 24 hours, and data collection was done at 0, 5, 10, 15, 20, and 24 hours after the start of the test. Data recorded in each experiment includes fluid mass and fluid surface temperature. In Table 2. the number of each experiment can be seen along with its specifications.

3. RESULTS AND DISCUSSION

For the first group of experiments, in Figures 4 and 5 the mass of evaporated water and Fluid surface temperature are presented in terms of the initial mass of water, respectively.

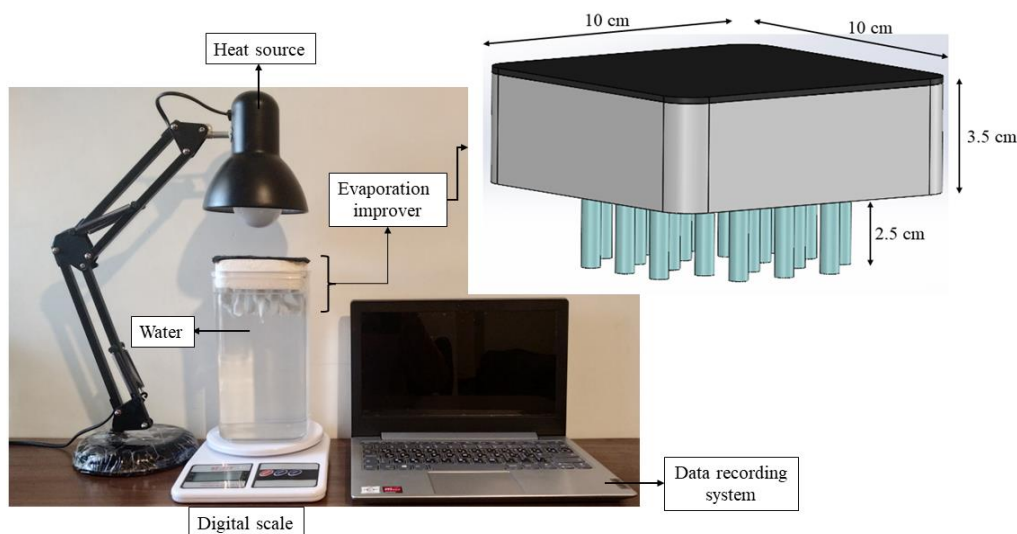


Figure 2. Test bed details

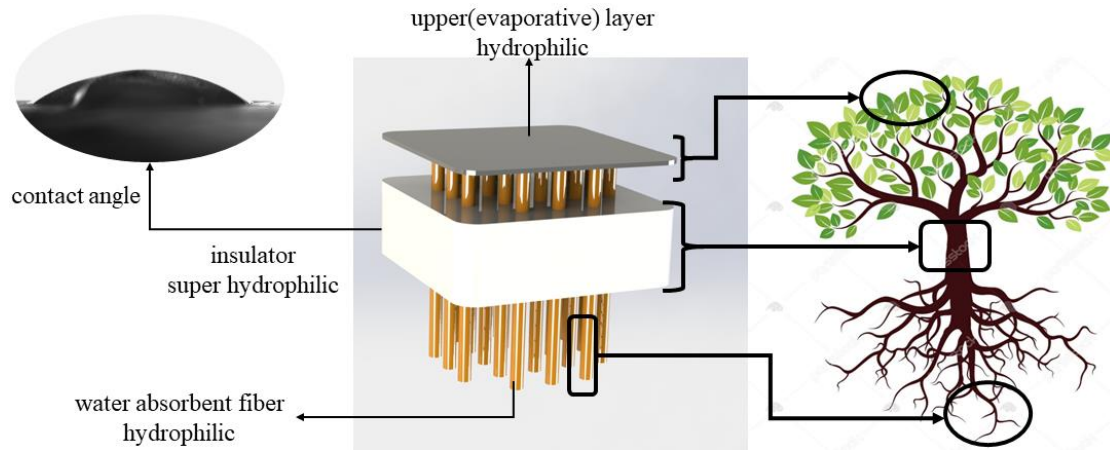


Figure 3. Details of the evaporation-improving structure and the analogy with the plants

TABLE 1. Characteristics of three types of foam used in this research

	Density ($\frac{kg}{m^3}$)	Water absorption (g)	Average contact angle (°)
Expanded polystyrene foam	27.5	0	under 10
Polyurethane foam of type 1	38.6	27	71.4
Polyurethane foam of type 2	13.6	70	78.3

TABLE 2. Specifications of experiments

Number of experiment	Specification
1st group	1 Without evaporation improver, initial water mass is 1900 gr.
	2 Without evaporation improver, initial water mass is 1700 gr.
	3 Without evaporation improver, initial water mass is 1500 gr.
	4 Without evaporation improver, initial water mass is 1300 gr.
2nd group	1 Without evaporation improver, initial water mass is 1900 gr.
	2 With evaporation improver by expanded polystyrene foam, initial water mass is 1900 gr.
	3 With evaporation improver by polyurethane foam of type 1, initial water mass is 1900 gr.
	4 With evaporation improver by polyurethane foam of type 2, initial water mass is 1900 gr.

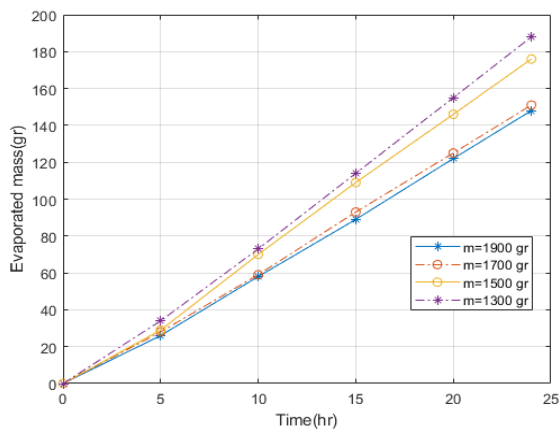


Figure 4. The mass of evaporated water in terms of initial water mass (without evaporation improver structure)

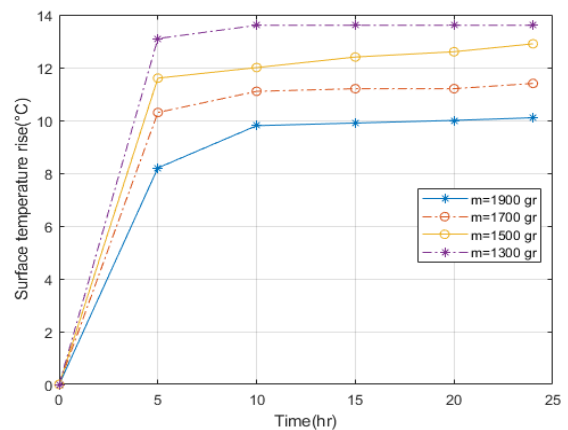


Figure 5. Fluid surface temperature rise in terms of initial water mass (without evaporation improver structure)

According to Figure 4 the amount of water evaporation increases with a decrease in the mass of the fluid bulk. Although this increase in evaporation is not the same for all experiments, on average, with each reduction of 200 grams of fluid mass, the amount of water evaporation increases by about 8%. To compare the temperature changes similarly, according to Figure 5 with the reduction of the fluid bulk mass, the changes in the water surface temperature increase. Although this increase is not the same for all experiments, on average, the water surface temperature gradient increases by about 8% with each 200g reduction of the fluid mass. According to the results of the first group of experiments, if the mass of the fluid bulk continues to decrease, it will lead to a thin film of fluid that is against the heat in the

limiting case; In this case, the rate of evaporation will be higher than all the previous cases (with more fluid mass). With this idea, in the second group of experiments, a thin fluid film is tried to be exposed to heat.

For the second group of experiments, in Figure 6 the change in the fluid mass and temperature of the fluid surface in 24 hours for experiments 1 to 4 are presented, respectively. The initial surface temperature is about 27 °C in these experiments.

For a more detailed analysis, in Figure 7 a comparison between the mass of evaporated water in experiments 1 to 4 has been made. According to this figure, the evaporation-improving structure with expanded polystyrene foam, the evaporation-improving structure with polyurethane foam of type 1, and the

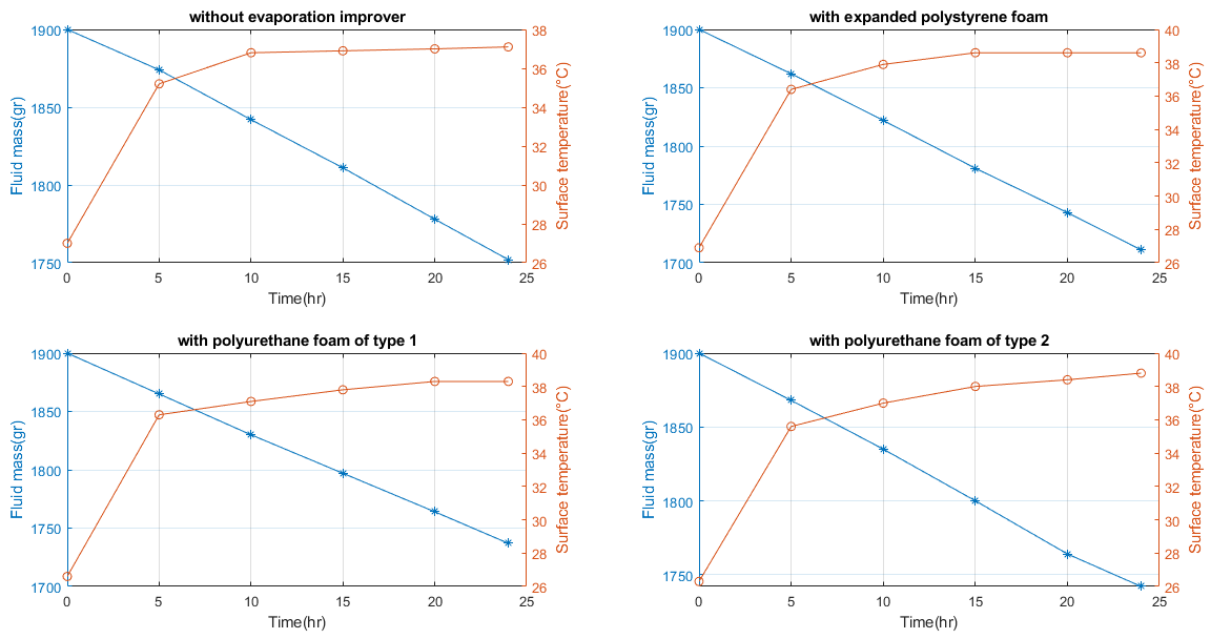


Figure 6. Fluid mass and temperature of the fluid surface with different evaporation improver structures

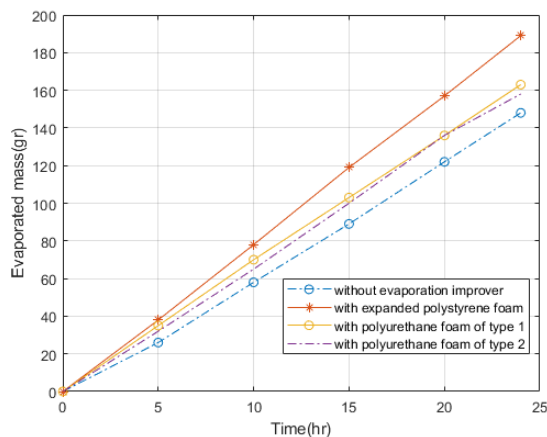


Figure 7. Comparison between the mass of evaporated water with different evaporation improver structures

evaporation-improving structure with polyurethane foam of type 2 respectively improved about 28, 10, and 7% in the amount of water evaporation in 24 hours.

In Figure 8, a comparison has been made between the temperature of the fluid surface in these four tests. According to this figure, the evaporation-improving structure with expanded polystyrene foam, the evaporation-improving structure with polyurethane foam of type 1, and the evaporation-improving structure with polyurethane foam of type 2 cause an increase of about 16, 13 and 20% in the temperature of the fluid surface, respectively. In this way, it is understood that the use of an evaporation-improving structure increases the steady-state surface temperature of water by about 2 degrees, which is an effective factor in the rate of water evaporation.

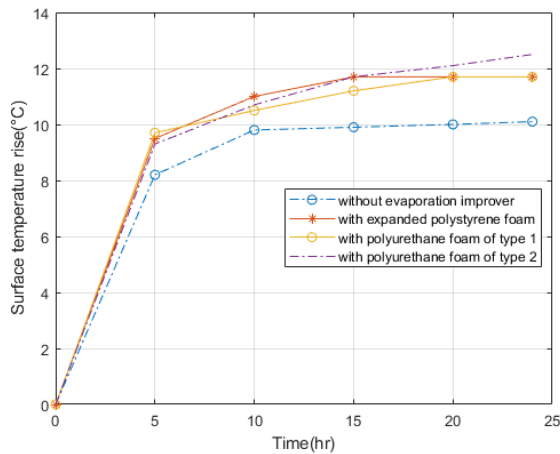


Figure 8. Comparison between fluid surface temperature rise with different evaporation improver structures

TABLE 3. Summary of the results for the second group of experiments

Specification	Increase in mass of evaporated water (%)	Increase in water surface temperature (%)
Evaporation improver with expanded polystyrene foam	28	16
Evaporation improver with polyurethane foam of type 1	10	13
Evaporation improver with polyurethane foam of type 2	7	20

In the continuation of this section, the physical justification related to the cause of the difference between the results of the proposed structures in this research is discussed. It was observed above that in general the results of the structure made of expanded polystyrene foam are better than the results of the structure made of polyurethane foam of type 1. Also, the results of the structure made of polyurethane foam of type 1 are better than the results of the structure made of polyurethane foam of type 2. The reason for this issue can be attributed to the main difference between the two types of expanded polystyrene foam and polyurethane foam, which is water permeability. Expandable polystyrene foam does not allow water to pass through itself, and therefore all the insulation capacity is used to prevent heat transfer to the fluid volume. However, polyurethane foam passes water and gets wet after a while, and this makes the thermal conductivity of the wet foam to be higher than the thermal conductivity of the dry foam, and the performance of the insulation is problematic. This issue is also true for the two types of polyurethane foam used because one of the differences between the first and second type polyurethane foam is that the second type foam has a higher permeability than the first type foam,

and as a result, after wetting will make the insulation weaker.

The main heat transfer mechanisms and energy balance between them are shown in Figure 9. According to Zhang et al. (31) and Zhuang et al. (32), thermal efficiency can be defined as Equation 1, where \dot{m} is the evaporated mass flow rate, $h_{f,g}$ is the total enthalpy of liquid to vapor phase change, A is the cross-sectional area exposed to heat, and q'' is the heat flux radiated to the surface.

$$\eta_{th} = \frac{\dot{m}h_{f,g}}{q''A} \quad (1)$$

By using the above relationship, the thermal efficiency related to the evaporation process with the improving structure with expanded polystyrene foam is obtained at approximately 85% at a heat flux of 0.6 kW/m^2 . In Table 4 a comparison of heat flux, efficiency and evaporation rate for some similar research is done.

One of the advantages of the method presented in this research is its economic efficiency. The majority of the cost spent on the construction of the evaporation-improving structure is related to the insulation and cotton fibers. Roughly, the cost spent for the construction of

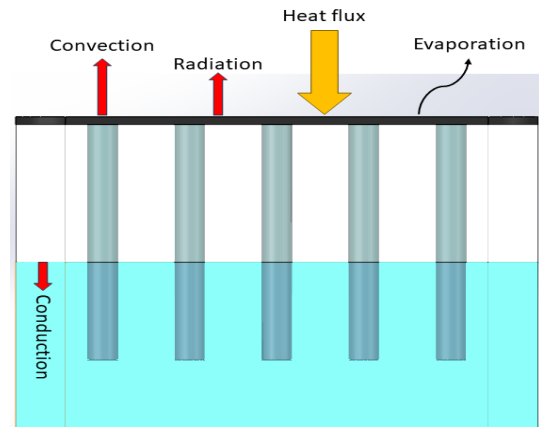


Figure 9. Energy balance and heat transfer diagram

TABLE 4. Comparison of heat flux, efficiency and evaporation rate for some similar research

Research	Heat flux (kW/m^2)	Efficiency (%)	Evaporation rate (kg/h/m^2)
Liu et al. (8)	0.9	79	0.97
Miao et al. (15)	1	84.6	1.31
Guo et al. (17)	1	93	4.0
Wang et al. (33)	1	54.6	0.87
Li et al. (34)	1	84	1.3
Lu et al. (35)	1	80	2.4
Present Study	0.6	85	0.79

each square meter of this structure is estimated at \$15. Also, according to the scalability of the designed structure and the linear growth of costs, the cost of building this structure can be calculated by the proportional method.

4. CONCLUSION

In summary, the cost-effective, innovative, simple, and scalable structure inspired by plant structure is proposed to improve the evaporation rate with a high efficiency.

In the present study, two groups of experiments are conducted. The first group of tests is performed to check the effect of fluid mass reduction on the rate of evaporation. The results of this group of experiments showed the upward trend of improving the evaporation rate with the reduction of the fluid mass so that with each reduction of 200 grams of the fluid mass, the fluid evaporation rate increased by about 8%; Also, the increase in water surface temperature also increased by about 8%. The results of this group of experiments inspired the fact that by gradually reducing the fluid mass until a thin film is reached, the evaporation rate can be continuously increased, which became the basis of the second group of experiments.

In the following, by designing and building an innovative structure and placing it on water, the rate of evaporation of water due to the heat radiating to its surface was increased. The main reason for this improvement in evaporation is two main things: the first reason is that the designed structure prevents the heat transfer from the surface to the depth of the water, and the heat radiated to the fluid is concentrated in a thin film; the second reason is that an increase in the heat absorption coefficient by the improving structure. The second group of experiments conducted in this research is dedicated to investigating the effects of the evaporation-improving structure on the rate of water evaporation.

The evaporation-improving structure designed in this research in the best case (use of expanded polystyrene foam) was able to increase the amount of water evaporation during 24 hours by 28%. This improving structure also increased the surface temperature of water in the evaporation process by 16%. It was also able to increase the thermal efficiency of the evaporation process to about 85% at a heat flux of 0.6 kW/m^2 , which is at an optimal level compared to previous research.

To enhance future investigations, it is recommended to explore alternative absorbent materials for the top layer of the structure and conduct further experiments with varying heat fluxes to improve the efficiency and evaporation rate. Additionally, it would be beneficial to seek out a numerical simulation approach to eliminate the need for further experimentation.

5. ACKNOWLEDGEMENTS

The author would like to acknowledge Dr. Ali Nouri-Borujerdi for giving the first idea of this research and helpful comments.

6. REFERENCES

- Ghasemi H, Ni G, Marconnet AM, Loomis J, Yerci S, Miljkovic N, et al. Solar steam generation by heat localization. *Nature Communications*. 2014;5(1):4449. <https://doi.org/10.1038/ncomms5449>
- Chen F, Wang S-W, Liu X, Ji R, Yu L, Chen X, et al. High performance colored selective absorbers for architecturally integrated solar applications. *Journal of Materials Chemistry A*. 2015;3(14):7353-60. <https://doi.org/10.1039/C5TA00694E>
- Ni G, Li G, Boriskina SV, Li H, Yang W, Zhang T, et al. Steam generation under one sun enabled by a floating structure with thermal concentration. *Nature Energy*. 2016;1(9):1-7. <https://doi.org/10.1038/nenergy.2016.126>
- Li X, Xu W, Tang M, Zhou L, Zhu B, Zhu S, et al. Graphene oxide-based efficient and scalable solar desalination under one sun with a confined 2D water path. *Proceedings of the National Academy of Sciences*. 2016;113(49):13953-8. <https://doi.org/10.1073/pnas.1613031113>
- Zhu G, Xu J, Zhao W, Huang F. Constructing black titania with unique nanocage structure for solar desalination. *ACS Applied Materials & Interfaces*. 2016;8(46):31716-21. <https://doi.org/10.1021/acsami.6b11466>
- Zhou L, Tan Y, Wang J, Xu W, Yuan Y, Cai W, et al. 3D self-assembly of aluminium nanoparticles for plasmon-enhanced solar desalination. *Nature Photonics*. 2016;10(6):393-8. <https://doi.org/10.1038/nphoton.2016.75>
- Ouar MA, Sellami M, Meddour S, Touahir R, Guemari S, Loudiyi K. Experimental yield analysis of groundwater solar desalination system using absorbent materials. *Groundwater for Sustainable Development*. 2017;5:261-7. <https://doi.org/10.1016/j.gsd.2017.08.001>
- Liu Z, Yang Z, Huang X, Xuan C, Xie J, Fu H, et al. High-absorption recyclable photothermal membranes used in a bionic system for high-efficiency solar desalination via enhanced localized heating. *Journal of Materials Chemistry A*. 2017;5(37):20044-52. <https://doi.org/10.1039/C7TA06384A>
- Huang X, Yu Y-H, de Llergo OL, Marquez SM, Cheng Z. Facile polypyrrole thin film coating on polypropylene membrane for efficient solar-driven interfacial water evaporation. *RSC Advances*. 2017;7(16):9495-9. <https://doi.org/10.1039/C6RA26286D>
- Xu N, Hu X, Xu W, Li X, Zhou L, Zhu S, et al. Mushrooms as efficient solar steam-generation devices. *Advanced Materials*. 2017;29(28):1606762. <https://doi.org/10.1002/adma.201606762>
- Ni G, Zandavi SH, Javid SM, Boriskina SV, Cooper TA, Chen G. A salt-rejecting floating solar still for low-cost desalination. *Energy & Environmental Science*. 2018;11(6):1510-9. <https://doi.org/10.1039/C8EE00220G>
- Li X, Li J, Lu J, Xu N, Chen C, Min X, et al. Enhancement of interfacial solar vapor generation by environmental energy. *Joule*. 2018;2(7):1331-8. <https://doi.org/10.1016/j.joule.2018.04.004>
- Zhao F, Zhou X, Shi Y, Qian X, Alexander M, Zhao X, et al. Highly efficient solar vapour generation via hierarchically nanostructured gels. *Nature Nanotechnology*. 2018;13(6):489-95. <https://doi.org/10.1038/s41565-018-0097-z>

14. Hu R, Zhang J, Kuang Y, Wang K, Cai X, Fang Z, et al. A Janus evaporator with low tortuosity for long-term solar desalination. *Journal of Materials Chemistry A*. 2019;7(25):15333-40. <https://doi.org/10.1039/C9TA01576K>
15. Miao E-D, Ye M-Q, Guo C-L, Liang L, Liu Q, Rao Z-H. Enhanced solar steam generation using carbon nanotube membrane distillation device with heat localization. *Applied Thermal Engineering*. 2019;149:1255-64. <https://doi.org/10.1016/j.applthermaleng.2018.12.123>
16. Wang Z, Horseman T, Straub AP, Yip NY, Li D, Elimelech M, et al. Pathways and challenges for efficient solar-thermal desalination. *Science Advances*. 2019;5(7):eaax0763. <https://doi.org/10.1126/sciadv.aax0763>
17. Guo Y, Zhao X, Zhao F, Jiao Z, Zhou X, Yu G. Tailoring surface wetting states for ultrafast solar-driven water evaporation. *Energy & Environmental Science*. 2020;13(7):2087-95. <https://doi.org/10.1039/D0EE00399A>
18. Wang Z, Wu X, He F, Peng S, Li Y. Confinement capillarity of thin coating for boosting solar-driven water evaporation. *Advanced Functional Materials*. 2021;31(22):2011114. <https://doi.org/10.1002/adfm.202011114>
19. Wang Z, Wu X, Dong J, Yang X, He F, Peng S, et al. Porifera-inspired cost-effective and scalable "porous hydrogel sponge" for durable and highly efficient solar-driven desalination. *Chemical Engineering Journal*. 2022;427:130905. <https://doi.org/10.1016/j.cej.2021.130905>
20. Munasir N, Lutfiana S, Nuhaab F, Evia S, Lydiaa R, Ezaac S, et al. Graphene Based Membrane Modified Silica Nanoparticles for Seawater Desalination and Wastewater Treatment: Salt Rejection and Dyes. *International Journal of Engineering, Transactions A: Basics*, 2023;36(4):698-708. <https://doi.org/10.5829/ije.2023.36.04a.09>
21. Chen J, Li B, Hu G, Aleisa R, Lei S, Yang F, et al. Integrated evaporator for efficient solar-driven interfacial steam generation. *Nano Letters*. 2020;20(8):6051-8. <https://doi.org/10.1021/acs.nanolett.0c01999>
22. Lu Q, Shi W, Yang H, Wang X. Nanoconfined water-molecule channels for high-yield solar vapor generation under weaker sunlight. *Advanced Materials*. 2020;32(42):2001544. <https://doi.org/10.1002/adma.202001544>
23. Liu H, Ye HG, Gao M, Li Q, Liu Z, Xie AQ, et al. Conformal Microfluidic-Blow-Spun 3D Photothermal Catalytic Spherical Evaporator for Omnidirectional Enhanced Solar Steam Generation and CO₂ Reduction. *Advanced Science*. 2021;8(19):2101232. <https://doi.org/10.1002/advs.202101232>
24. Guo Y, Bae J, Fang Z, Li P, Zhao F, Yu G. Hydrogels and hydrogel-derived materials for energy and water sustainability. *Chemical Reviews*. 2020;120(15):7642-707. <https://doi.org/10.1021/acs.chemrev.0c00345>
25. Zhou X, Guo Y, Zhao F, Shi W, Yu G. Topology-controlled hydration of polymer network in hydrogels for solar-driven wastewater treatment. *Advanced Materials*. 2020;32(52):2007012. <https://doi.org/10.1002/adma.202007012>
26. Guo Y, Yu G. Engineering hydrogels for efficient solar desalination and water purification. *Accounts of Materials Research*. 2021;2(5):374-84. <https://doi.org/10.1021/accountsmr.1c00057>
27. Tao P, Ni G, Song C, Shang W, Wu J, Zhu J, et al. Solar-driven interfacial evaporation. *Nature Energy*. 2018;3(12):1031-41. <https://doi.org/10.1038/s41560-018-0260-7>
28. Bohr T, Rademaker H, Schulz A. Water Motion and Sugar Translocation in Leaves. *Plant Biomechanics: From Structure to Function at Multiple Scales*. 2018:351-74. https://doi.org/10.1007/978-3-319-79099-2_16
29. ASTM D. 7334-08; Standard Practice for Surface Wettability of Coatings, Substrates and Pigments by Advancing Contact Angle Measurement. ASTM International: West Conshohocken, PA, USA. 2008.
30. Jikan company 2023 [Available from: <https://www.jikangroup.com/wp-content/uploads/2018/10/CAG-20-PE-Catalogue.pdf>].
31. Zhang L, Tang B, Wu J, Li R, Wang P. Hydrophobic light-to-heat conversion membranes with self-healing ability for interfacial solar heating. *Advanced Materials*. 2015;27(33):4889-94. <https://doi.org/10.1002/adma.201502362>
32. Zhuang S, Zhou L, Xu W, Xu N, Hu X, Li X, et al. Tuning transpiration by interfacial solar absorber-leaf engineering. *Advanced Science*. 2018;5(2):1700497. <https://doi.org/10.1002/advs.201700497>
33. Wang X, He Y, Liu X, Zhu J. Enhanced direct steam generation via a bio-inspired solar heating method using carbon nanotube films. *Powder Technology*. 2017;321:276-85. <https://doi.org/10.1016/j.powtec.2017.08.027>
34. Li R, Zhang L, Shi L, Wang P. MXene Ti₃C₂: an effective 2D light-to-heat conversion material. *ACS Nano*. 2017;11(4):3752-9. <https://doi.org/10.1021/acs.nano.6b08415>
35. Lu H, Shi W, Zhao F, Zhang W, Zhang P, Zhao C, et al. High-yield and low-cost solar water purification via hydrogel-based membrane distillation. *Advanced Functional Materials*. 2021;31(19):2101036. <https://doi.org/10.1002/adfm.202101036>

COPYRIGHTS

©2024 The author(s). This is an open access article distributed under the terms of the Creative Commons Attribution (CC BY 4.0), which permits unrestricted use, distribution, and reproduction in any medium, as long as the original authors and source are cited. No permission is required from the authors or the publishers.

**Persian Abstract****چکیده**

تبخیر سطحی در بسیاری از پدیده‌های طبیعی و کاربردهای صنعتی مهم است؛ بنابراین بهبود این پدیده بسیار مفید است. در این پژوهش، نرخ تبخیر آب با طراحی یک ساختار ابتکاری الهام گرفته شده از ساختار گیاهان بهبود یافته است. این ساختار دو اثر اصلی دارد: اولاً گرمای انتقال یافته به حجم سیال از طریق سطح را کاهش داده و ثانیاً جذب سطحی حرارت را افزایش می‌دهد. این ساختار از سه بخش تشکیل شده است: لایه تبخیری، عایق و الیاف جاذب آب. پس از بررسی فراوان بر روی مواد مختلف برای انتخاب بهترین ماده برای این سه بخش، فوم پلی استایرن انبساطی و الیاف کتانی بهترین عملکرد را از خود نشان دادند. این ساختار پس از ساخت و آزمایش توانست جرم آب تبخیر شده در مدت ۲۴ ساعت را به اندازه ۲۸ درصد افزایش دهد؛ همچنین دمای سطح آب در فرآیند تبخیر در طول ۲۴ ساعت به اندازه ۱۶ درصد افزایش یافت که باعث تبخیر آب در دمای بالاتر گردید. این ساختار همچنین بازده حرارتی را تا ۸۵ درصد در شار حرارتی ۰.۶ کیلووات بر متر مربع افزایش داد. سطح پیشنهاد شده دارای قابلیت مقیاس پذیری برای هر ابعادی و مقرون به صرفه است.



Proposing New Artificial Intelligence Models to Estimate Shear Wave Velocity of Fine-grained Soils: A Case Study

M. Khanmohammadi*^a, S. Razavi^b

^a Department of Civil Engineering, Isfahan University of Technology, Isfahan, Iran

^b Department of Mining Engineering, Islamic Azad University, Science & Research Branch, Tehran, Iran

PAPER INFO

Paper history:

Received 09 December 2023

Received in revised form 18 January 2024

Accepted 09 February 2024

Keywords:

Fine-grained Soil

Shear Wave Velocity

Down-hole Test

Geophysics

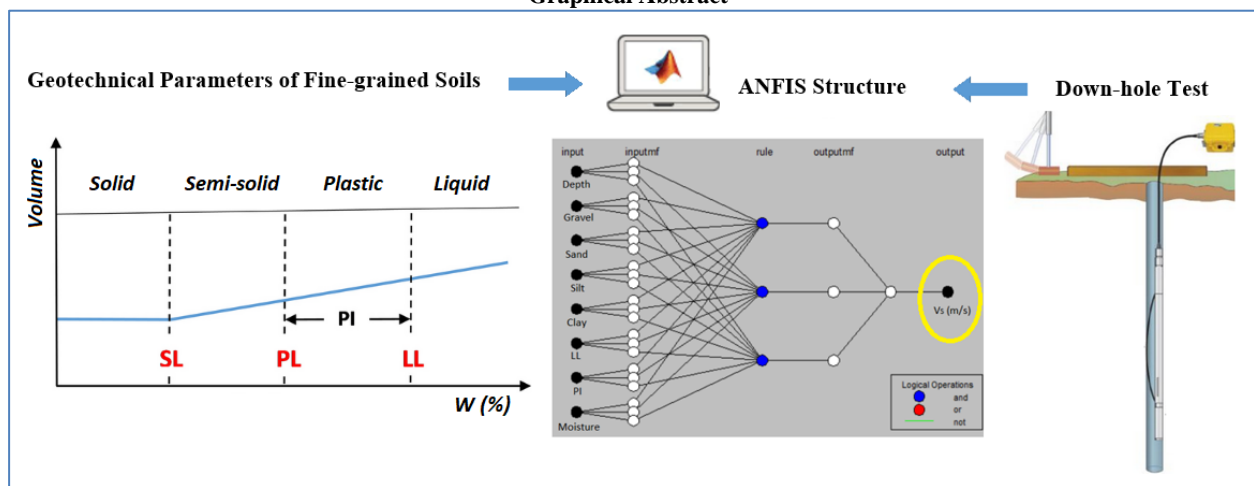
Adaptive Neuro-fuzzy Inference System

ABSTRACT

Dynamic parameters are the most important geotechnical data used to understand the behavior of soil media under dynamic loads and to recognize the seismic response of the soil. Several in-situ and laboratory geophysical tests, such as the down-hole test, are used to determine these parameters. Since this experiment is costly and time-consuming and the preparation of appropriate boreholes is not easy, it is preferable to estimate the results of this test with the help of empirical correlations or experimental models. The main output of the down-hole test is the shear wave velocity (V_s) of soils, which can be used to obtain the dynamic shear modulus (G_d) indirectly. The relationship between physical properties and mechanical specifications of soils is a well-known principle of geotechnical engineering. Utilizing the results of 19 down-hole experiments and available geotechnical data in the southern regions of Tehran, as well as the inputs of an adaptive neuro-fuzzy inference system (ANFIS). This study attempts to provide practical models to predict shear wave velocity of fine-grained soils in Tehran. Two new models have been proposed as a result of preprocessing and smart modeling. The independent variables of the first suggested model included the moisture content, plasticity index (PI), liquid limit (LL), depth of test, and grain size distribution of soils. In the second model, the number of standard penetration test (N_{SPT}) is also used in addition to the mentioned independent variables. The proposed models had coefficients of determination (R^2) of 0.74 and 0.8 for the total training and validation data, respectively.

doi: 10.5829/ije.2024.37.06c.13

Graphical Abstract



*Corresponding Author Email: mkhanmohammadi@iut.ac.ir (M. Khanmohammadi)

1. INTRODUCTION

Dynamic modulus (shear and Young's modulus) as a significant parameter in geotechnical analysis and especially seismic design of structures can be obtained by determining the shear wave velocity of soils. Down-hole test (1) is one of the most well-known geophysical tests used to determine the shear wave velocity of soils. This test is costly and time-consuming. Preparing appropriate boreholes is another challenge in performing this test. Also, some variables may influence the results. Due to the mentioned limitations, it is helpful to predict the results of this test by using empirical correlations or models.

Typically, using new artificial intelligence (AI) methods to solve complex multivariate problems leads to better outcomes compared to conventional regression methods. In recent years, researchers have utilized various AI methods to predict the results of geotechnical (2-9) and geophysical (10-12) tests.

In this regard, Table 1 summarizes the most important AI models available to predict the shear wave velocity obtained from in-situ tests. This table shows that despite numerous studies in this field, a comprehensive and acceptable model has not been yet proposed. Therefore, it seems that there is still a necessity for new models or relationships for different regions to predict the shear wave velocity of soils.

Due to the access to geotechnical data of several projects in which both conventional geotechnical tests and down-hole tests were performed, it was possible to prepare a considerable amount of data that can be cited for this research. Then, it was attempted to apply the ANFIS method to introduce new practical models to predict the shear wave velocity of fine-grained soils in Tehran. It should be noted that the models developed in this research are different from the models of other researchers in terms of input variables, modeling method and applied data.

2. METHODOLOGY

In AI techniques for nonlinear multiple analysis, data sets are divided into two different sets of training and testing. The training data set is used to find the potential relationship between independent and dependent

variables, and the reliability of this relationship is verified with the testing data set (13). Artificial Neural Network (ANN), Fuzzy, and Neuro-fuzzy are some examples of the widely used methods.

The ANN method can find the relationship between the input and output variables of a complicated problem with the help of self-learning ability. The performance of artificial neural networks is directly related to the given amount of training data (14). When the number of data is low, neural networks and fuzzy logic combinations (neuro-fuzzy) can improve the performance of the neural network system (15). A fuzzy system can simulate the qualitative aspects of human knowledge and reasoning processes, whereas it does not have any self-training abilities. Nevertheless, ANNs can do learning using data sets (16, 17). Then, ANFIS has the advantages of both neural networks and fuzzy systems (18). The main purpose of the ANFIS approach is to automate fuzzy modeling using real data. In the fuzzy Takagi-Sugeno method, the following If-Then rules apply:

$$\text{If } x=A_1 \text{ and } y=B_1 \text{ then } f_1(x,y)=p_1x+q_1y+k_1 \quad (1)$$

$$\text{If } x=A_2 \text{ and } y=B_2 \text{ then } f_2(x,y)=p_2x+q_2y+k_2 \quad (2)$$

where x and y are the inputs, A_i and B_i are labels of the fuzzy set (small, large, etc.) defined as suitable membership functions, and p_i , q_i , and k_i are output parameters resulting from the training. The process of ANFIS performance contains five steps (layers). The schematic structure of this method is displayed in Figure 1.

2. 1. ANFIS-FCM The ANFIS model developed in the present study is based on the fuzzy clustering method (FCM). Fuzzy C-Means is an approach of data clustering in which a given dataset is grouped into some clusters according to the principles of the fuzzy C-partition. The introduction of this algorithm is generalized by Ming-Chuan and Don-Lin (19). In this algorithm, each data can belong to one or more clusters (groups) in soft fuzzy clustering, and the data closer to the center of a cluster has a higher degree of membership (20).

The coefficient of determination (R^2), Mean Absolute Error (MAE), and Root Mean Squared Error (RMSE), which are shown in Equations 3 to 5, are selected to assess the model.

TABLE 1. Summary of the some suggested AI models to predict V_s

Case study	Model	Ranges of V_s (m/s)	Method	Reference
A database from 10 different countries	$V_s = f(N_{60}, \sigma')$	66-169.66	PNN	(21)
Urmia City, Iran	$V_s = f(N_{60}, \sigma', FC, PI, d_{50})$	82-566	GRNN	(22)
Mashhad City, Iran	$V_s = f(D, N_{SPT}, FC)$	202-850	ANN-BP	(23)

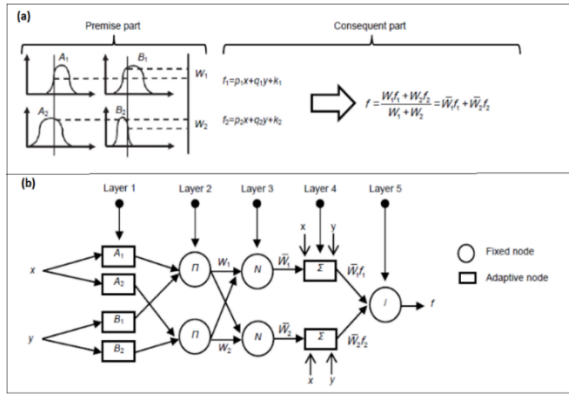


Figure 1. The process of ANFIS performance; (a) the first-order fuzzy model (b) schematic structure of ANFIS (16, 24, 25)

$$R^2 = \left(\frac{\sum_{i=1}^n (p_i - \bar{p})(a_i - \bar{a})}{\sqrt{\sum_{i=1}^n (p_i - \bar{p})^2 \sum_{i=1}^n (a_i - \bar{a})^2}} \right)^2 \quad (3)$$

$$MAE = \frac{1}{n} \sum_{i=1}^n |a_i - p_i| \quad (4)$$

$$RMSE = \sqrt{\frac{1}{n} \sum_{i=1}^n (a_i - p_i)^2} \quad (5)$$

In these equations, a_i is the real values (targets) of the V_s , p is the predicted V_s , \bar{a} is the average of the actual V_s , \bar{p} is the average of the predicted V_s , and n is the number of data sets.

2. 2. Sensitivity Analysis Method In the current study, a sensitivity analysis method of single variable training was used to identify the relative importance of inputs on the outputs of ANFIS-FCM models. The optimum ANFIS model is trained separately for each variable and then tested again in this technique. It should be noted that the optimal parameters obtained in the final model (including the type of membership function, the number of rules, the method of optimization, and the number of iterations) are also maintained in this step. Finally, any model which predicted outputs closer to the actual values (target) or, in other words, had the highest coefficient of determination, was introduced as the most effective variable [25, 26].

Figure 2 illustrates an overall strategy and main steps performed to achieve the purpose of the current study. It should be noted that in primary analyses of this study, ANFIS had a better performance in comparison with ANN method, therefore, only the results of ANFIS models are mentioned in the following.

3. DATA COLLECTION

In Tehran, geologically, from north to south of the city, the percentage of coarse aggregates is almost reduced,

and the southern regions are mainly composed of fine-grained clayey soils. This study used the findings of 19 study projects in different regions of southern Tehran. The fine-grained soils include CL, ML, CH and CL-ML.

It should be noted that in all these projects, the same equipment and technicians were employed, as well as the method presented in ASTM-D7400 (1). As previously described, shear wave velocity is the most important direct output of down-hole test, which can determine the dynamic moduli of soils. In all boreholes in which down-hole test was performed, disturbed and undisturbed high-quality samples were taken and all conventional geotechnical laboratory tests were performed on the samples. Besides, the standard penetration test (SPT) was performed by ASTM-D1586 (26) in almost all depths where the shear wave was recorded.

3. 1. Effective Parameters on the Down-hole Test

To accurately determine particle size, the percentage of different soils has been obtained through ASTM-D422 standard (27). By expressing the percentage of different soils, it is possible to make a good judgment of the type and initial characteristics of the materials. The desired properties of soils also included moisture content (w), liquid limit (LL), and plasticity index (PI) that have been determined through ASTM-D2216 (28) and ASTM-D4318 (29) standards, respectively.

Regarding the compaction condition of the tested soils, two indices of depth and number of standard penetration tests (N_{SPT}) were considered. In general, the density of soils increases with increasing depth. Standard Penetration Test (SPT) is one of the most common, inexpensive, and simplest geotechnical in situ experiments that can be utilized to determine soil compaction. In principle, this test is utilized to determine the relative compaction of soils. Therefore, considering that the depth of the test section and N_{SPT} can be easily determined, these two parameters were selected as the basic parameters to ascertain the compaction of soils.

3. 2. Preprocess of Independent and Dependent Variables

Several different models were developed to investigate the relationships between independent variables and shear wave velocity in this section. To this end, several different data sets of fine-grained soils were evaluated. The two final models (relationships) were considered according to Table 2. It should be noted that these models are selected after several statistical analyses and data processing.

Independent variables related to the first data set (No. 1) included the percentage of soil particles (clay, silt, sand, and gravel), depth of test, liquid limit, plasticity index, and moisture content. The range of variation of these data were summarized in Table 3. The best simple regression between shear wave velocity and the independent variables is also displayed in Figure 3.

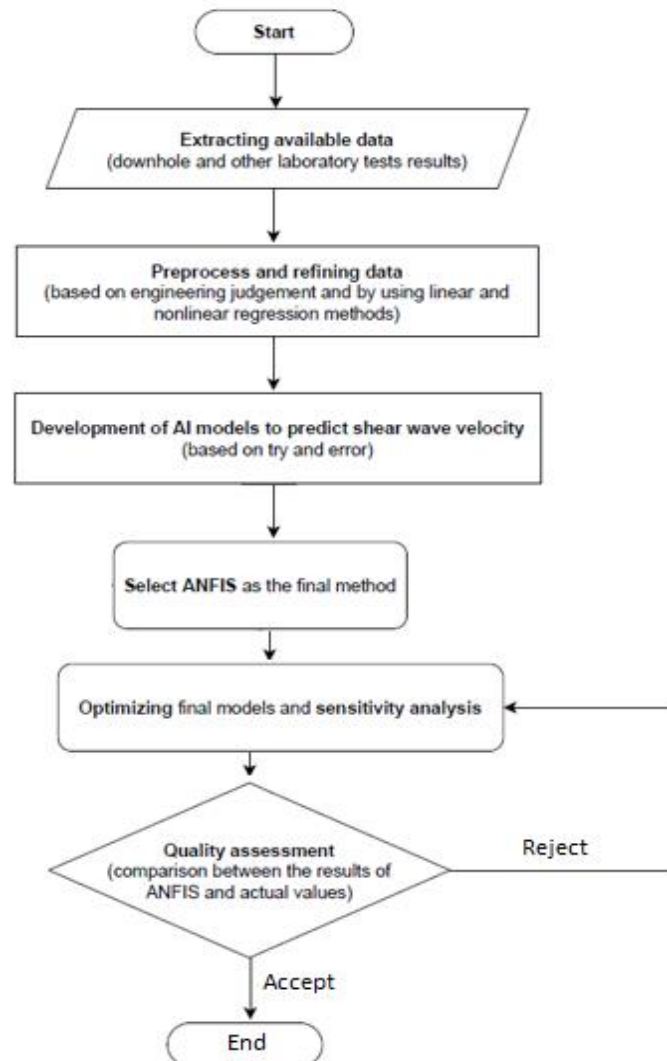


Figure 2. Overall strategy and main steps of the current study

TABLE 2. Proposed models obtained from preprocessing of data

No.	Equation/model	Number of data sets
1	$V_S = f(D, G, S, M, C, PI, LL, w)$	275
2	$V_S = f(D, G, S, M, C, PI, LL, w, N_{SPT})$	126

Parameters:

V_S (m/s): Shear wave velocity

D (m): Depth of test

G (%): Gravel-grained content

S (%): Sand-grained content

M (%): Silt-grained content

C (%): Clay-grained content

PI (%): Plastic Index

LL (%): Liquid limit

w (%): Moisture content

N_{SPT} : Uncorrected SPT blow counts

TABLE 3. Ranges of soil parameters for the first data set

Parameter	Depth (m)	Gravel (%)	Sand (%)	Silt (%)	Clay (%)	Liquid limit (%)	Plastic index (%)	Moisture content (%)	Shear wave velocity (m/s)
Min	2	0	0.10	18.40	16.90	21	2	5.40	130
Max	38	34.30	49.40	60.10	69.20	72	41	34.90	598
Mean	15.93	3.28	13.60	41.85	41.25	38.40	17.02	20.68	382.25
Standard deviation	8.43	4.97	11.43	8.02	10.56	9.84	7.08	5.19	104.78

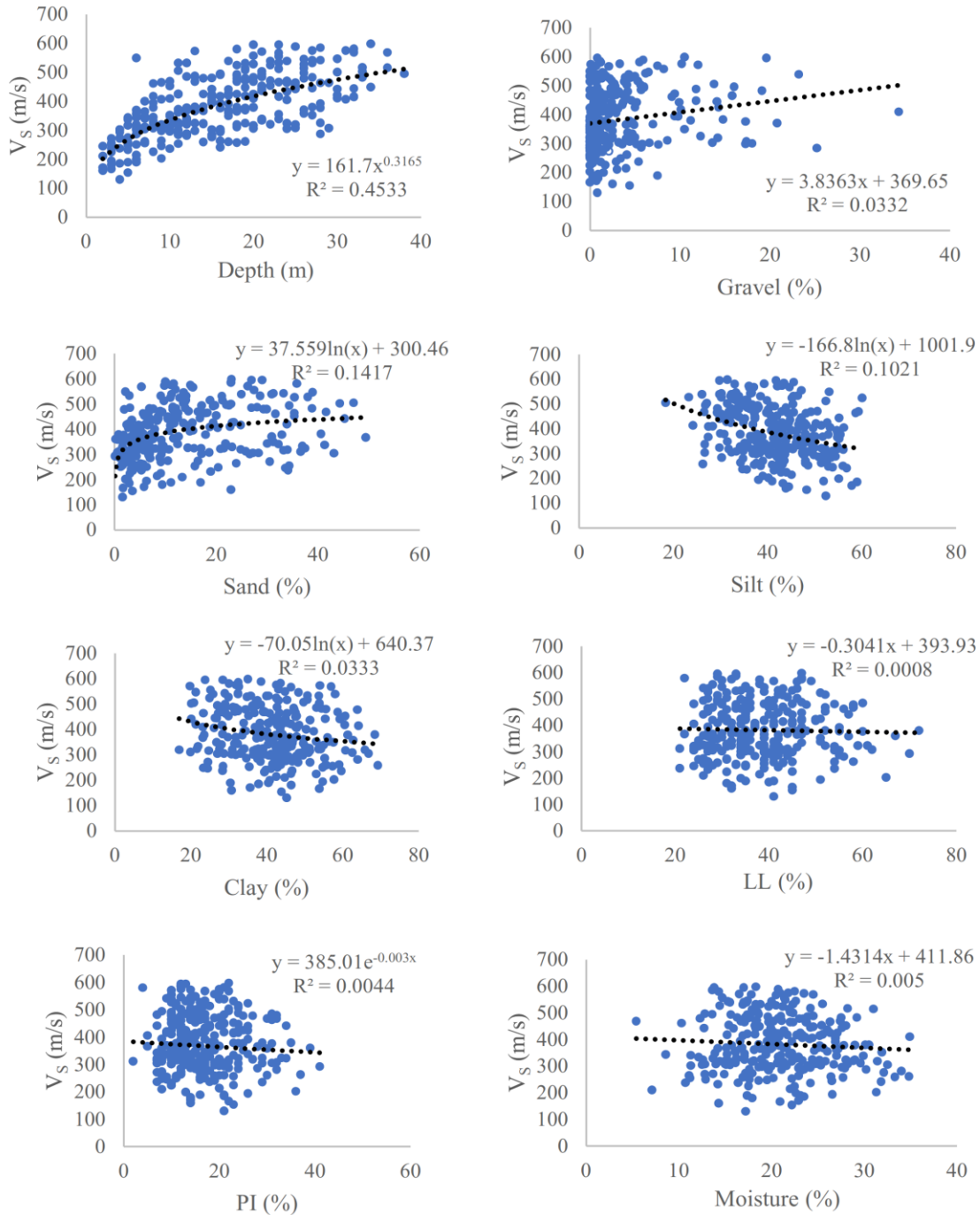


Figure 3. The best simple regression between dependent and the independent variables for the first data set

Independent variables related to the second data set (No. 2) includes the percentage of soil particles (clay, silt, sand, and gravel), depth of test, liquid limit, plasticity index, moisture content, and N_{SPT} . The range of variations of these data are presented in Table 4. Existing

values of N_{SPT} indicate that the relative density of soils ranged from soft to hard. The optimum simple regression between V_S and the mentioned independent parameters is also illustrated in Figure 4.

TABLE 4. Ranges of soil parameters for the second data set

Parameter	Depth (m)	Gravel (%)	Sand (%)	Silt (%)	Clay (%)	Liquid limit (%)	Plastic index (%)	Moisture content (%)	N_{SPT}	Shear wave velocity (m/s)
Min	3	0	0.90	18.40	16.90	21	2	8.60	7	130
Max	36	20.80	47	58.70	65.80	65.80	36	3480	65	688
Mean	10	6.62	5.45	48.40	39.52	39.52	15.50	20.45	34.75	318.25
Standard deviation	3.05	5.14	3.01	3.34	3.97	3.97	4.04	1.58	5.51	27.42

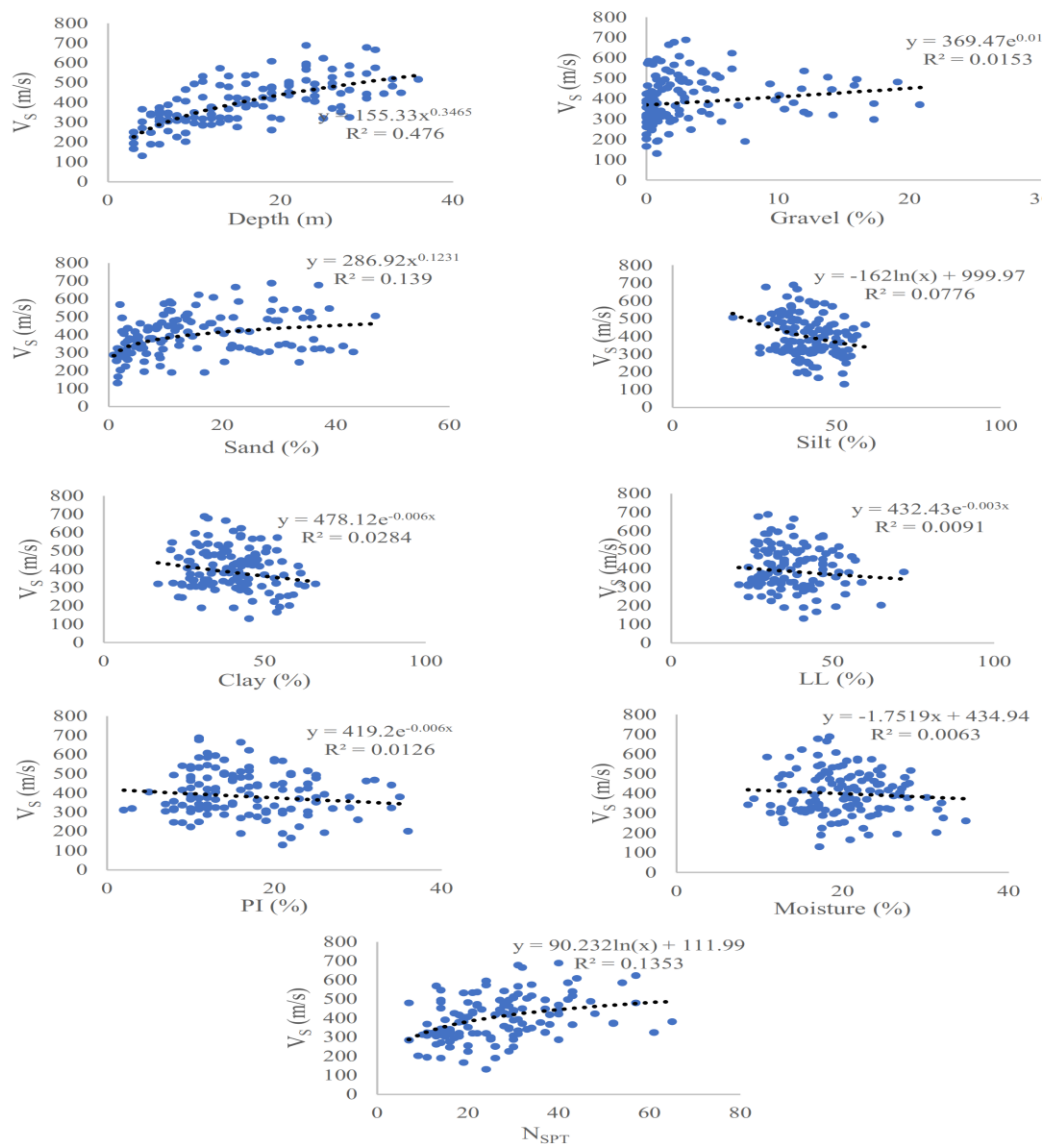


Figure 4. The best simple regression between dependent and the independent variables for the second data set

4. MODEL DEVELOPMENT TO PREDICT SHEAR WAVE VELOCITY

4. 1. The Optimum Model for the First Data Series

The settings relevant to the best structure of the ANFIS-FCM model, which includes the number and type of membership functions (MFs), the training algorithm, and the number of iterations, are obtained based on the trial and error approach. The available data sets were randomly divided into training data (220 data sets) and test data (55 data sets). After completing the learning phase, the final model was validated. The specifications of the most appropriately designed ANFIS model are given in Table 5. The constructed structure consists of five layers and three if-then rules that are connected by the "and" operator (Figure 5). The results and the suggested model determination coefficient graph for the two training and testing stages are indicated in Table 6 and Figure 6, respectively.

Then, with the mentioned sensitivity analysis method, the effect of each independent variable was investigated separately for the performance of the designed ANFIS model. As shown in Figure 7, the depth of test and the percent of sand-grained content were the most effective, and the variables of liquid limit and plasticity index had the least impact on the performance of the optimum model.

TABLE 5. Main parameters for the optimal ANFIS-FCM model

Parameter	Type/value
Number of MFs	3

Input MF	Gaussian
Output MF	Linear
Optimization method	Hybrid
Number of rules	3
Epoch	100

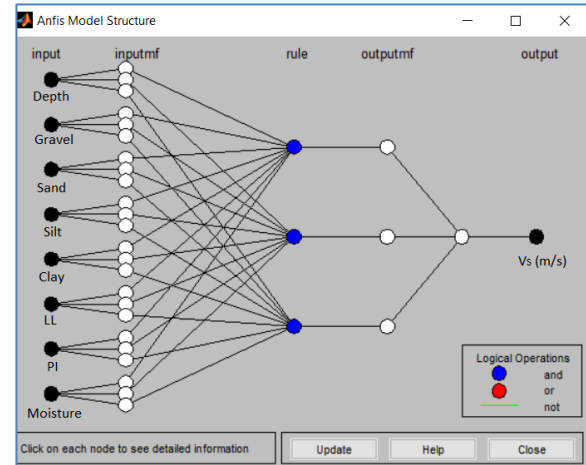


Figure 5. Optimal ANFIS-FCM structure for the first model

TABLE 6. Results and error values of ANFIS-FCM model for training, testing, and all data sets

Data	R ²	MAE	RMSE
Train	0.75	40.09	52.69
Test	0.73	48.04	59.61
All	0.74	42.34	54.19

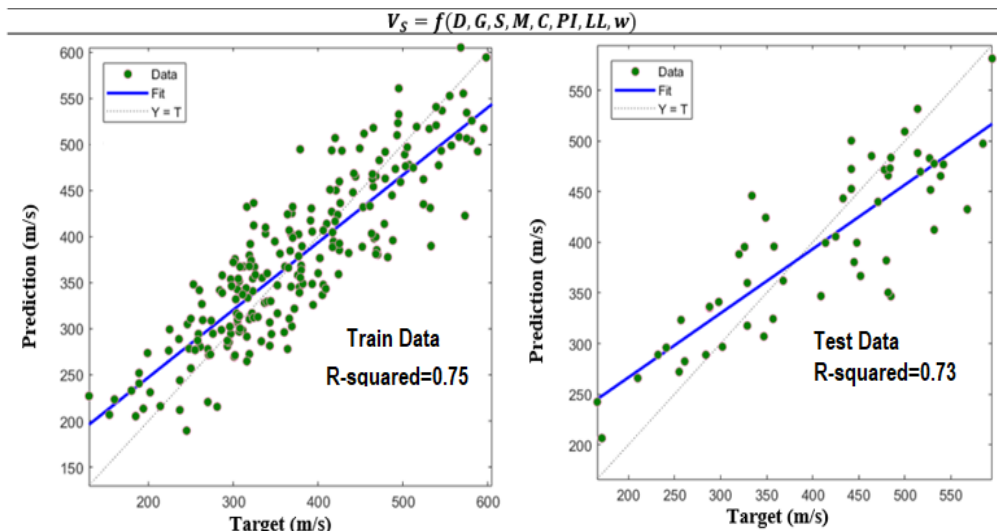


Figure 6. The obtained determination coefficients from the first model

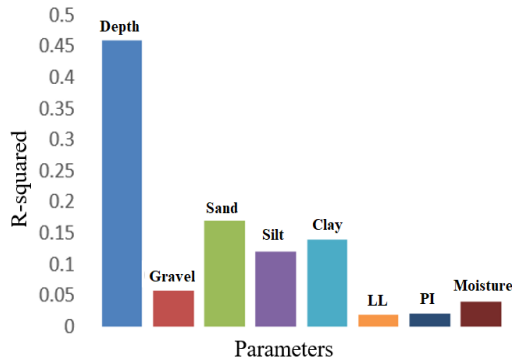


Figure 7. The results of sensitivity analysis on independent variables

4. 2. The Optimum Model for the Second Data Series

The same as previous step, the settings relevant to the optimum structure of the ANFIS-FCM model, which contains the number and type of membership functions (MF_s), the training algorithm, and the number of iterations, are determined. The available data sets were randomly divided into training data (101 data sets) and test data (25 data sets). The specifications of the developed model are given in Table 7. The structure of the optimum model is illustrated in Figure 8. The results and the proposed model determination coefficient graph for all stages are indicated in Table 8 and Figure 9, respectively.

Using the mentioned sensitivity analysis method, the effect of each independent variable was investigated separately to evaluate the performance of the designed ANFIS model. As shown in Figure 10, the depth of test and the percentage of sand-grained content have the most effect, and the variables of liquid limit and moisture content have the least impact on the performance of the optimum model.

TABLE 7. Main parameters for the optimal ANFIS-FCM model

Parameter	Type/value
Number of MF _s	2
Input MF	Gaussian
Output MF	Linear
Optimization method	Hybrid
Number of rules	2
Epoch	100

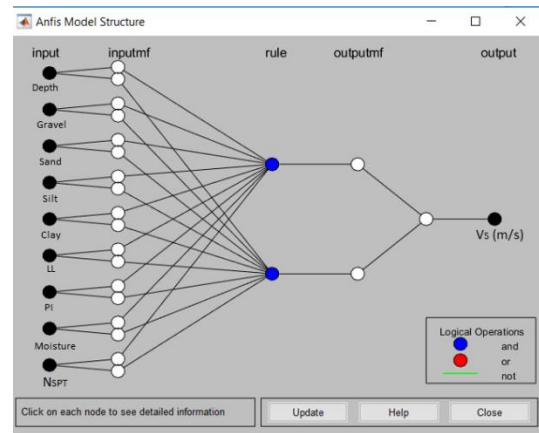


Figure 8. Optimal ANFIS-FCM structure for the second model

TABLE 8. Results and error values of ANFIS-FCM model for training, testing, and all data sets

Data	R ²	MAE	RMSE
Train	0.79	41.95	55.94
Test	0.82	37.91	51.57
All	0.8	40.91	54.95

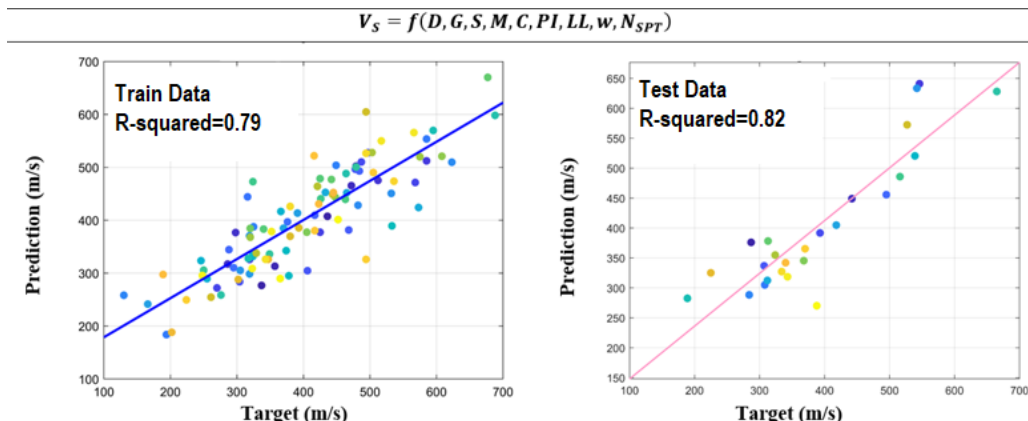


Figure 9. The obtained determination coefficients from the second model

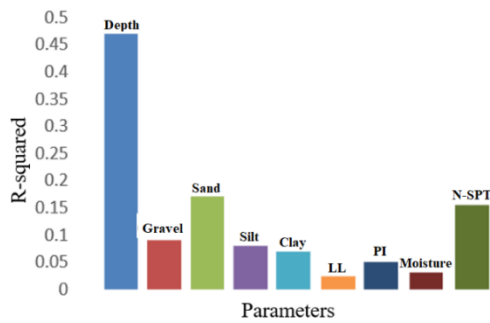


Figure 10. The results of sensitivity analysis on independent variables

5. RESULTS AND DISCUSSIONS

The obtained results from the two final ANFIS models are presented in Table 9. In general, both models can be roughly similar in terms of correlation and error values. For the whole first data series, the coefficients of determination and the mean absolute error are 0.74 and 42.34, respectively. Also, For the whole second data series, they are 0.8 and 40.91, respectively. It is worth mentioning that this study is the first attempt to use neuro-fuzzy to predict V_s ; therefore, there are some limitations to compare the results of the current study and other studies using the same database. Moreover, the proposed models have two advantages compared to previous studies. The first one is that more independent variables in this research make the final performance of the models less affected by one or more data. In other words, the possible error in the values of one of the data will not affect the output of the model. Typically, smart models that have this feature are also called robust models. Another advantage of this research (related to the first data) is that SPT results are not required to estimate the shear wave velocity of soils. It should be noted that according to the obtained results, the model presented for the second series data was superior model of this study.

TABLE 9. Comparison between the results of the first and second proposed models

Model	No. 1			No. 2		
	Train	Test	All	Train	Test	All
Data						
R²	0.75	0.73	0.74	0.79	0.82	0.8
MAE	40.09	48.04	42.34	41.95	37.91	40.91

6. CONCLUSIONS

In this study, two series of data, with different numbers and variables were employed to develop new smart models to predict the shear wave velocity of the fine-

grained soils. The most important results of this study are as follows:

- Considering the diversity of the studied soils, the results and suggested models can be evaluated as acceptable for most fine-grained soils in Tehran while considering the range of data changes. It is evident that the scope of application of the smart models proposed in current research is only relevant to the data used; therefore, these models need to be evaluated and validated again for new data.
- The performance of the proposed model for the second data (No. 2) has been slightly superior to the data model in terms of the coefficient of determination and error values. Determination coefficients obtained from ANFIS-FCM models for the whole data set numbers 1 and 2 were 0.74 and 0.8, respectively. Also, the choice of the FCM clustering method for making ANFIS models has simplified fuzzy rules and model structure.
- According to the preprocessing and sensitivity analysis performed on the optimal ANFIS models, the depth at which the test has been implemented, the percentage of sand-grained content, and N_{SPT} had the most influence on the shear wave velocity values.
- Due to the problems of the down-hole test (high cost, being time-consuming, and the requirement for a specialized operator) as well as the accuracy of proposed models, they can be used for the initial estimation of V_s and consequently, to determine the dynamic moduli of fine-grained soils. Obtaining the input variables considered for these models is simply possible in all geotechnical studies.

7. REFERENCES

1. Standard A. D7400-08, 2008," Standard Test Methods for Downhole Seismic Testing," ASTM International, West Conshohocken, PA, 2008, DOI: 10.1520/D7400-08.
2. Razavi S, Goshtasbi K, Noorzad A, Ahangari K. Proposing new relationships to estimate the pressuremeter modulus of cohesive and cohesionless media. *Innovative Infrastructure Solutions*. 2018;3(1):1-9. <https://doi.org/10.1007/s41062-018-0172-1>
3. Mohammadzadeh S D, Kazemi S-F, Mosavi A, Nasseralshariati E, Tah JH. Prediction of compression index of fine-grained soils using a gene expression programming model. *Infrastructures*. 2019;4(2):26. <https://doi.org/10.3390/infrastructures4020026>
4. Kordnaej A, Kalantary F, Kordtabar B, Mola-Abasi H. Prediction of recompression index using GMDH-type neural network based on geotechnical soil properties. *Soils and Foundations*. 2015;55(6):1335-45. <https://doi.org/10.1016/j.sandf.2015.10.001>
5. Moayed RZ, Kordnaej A, Mola-Abasi H. Pressuremeter modulus and limit pressure of clayey soils using GMDH-type neural network and genetic algorithms. *Geotechnical and Geological Engineering*. 2018;36(1):165-78. <https://doi.org/10.1007/s10706-017-0314-9>
6. Bardhan A, Singh RK, Ghani S, Konstantakatos G, Asteris PG. Modelling soil compaction parameters using an enhanced hybrid

- intelligence paradigm of ANFIS and improved grey wolf optimiser. *Mathematics*. 2023;11(14):3064. <https://doi.org/10.3390/math11143064>
7. Khanmohammadi M, Armaghani DJ, Sabri Sabri MM. Prediction and optimization of pile bearing capacity considering effects of time. *Mathematics*. 2022;10(19):3563. <https://doi.org/10.3390/math10193563>
 8. Banaei Moghadam S, Khanmohammadi M. Prediction of time-dependent bearing capacity of pile driven in cohesive soil using group method of data handling. *Sharif Journal of Civil Engineering*. 2021;37(3.2):27-35. <https://doi.org/10.24200/j30.2021.56892.2865>
 9. Banaei Moghadam S, Khanmohammadi M. Proposing new models to predict pile set-up in cohesive soils. *Geomechanics and Engineering*. 2023;33(3):231. <https://doi.org/10.12989/gae.2023.33.3.231>
 10. Yadav A, Yadav K, Sircar A. Feedforward neural network for joint inversion of geophysical data to identify geothermal sweet spots in Gandhar, Gujarat, India. *Energy Geoscience*. 2021;2(3):189-200. <https://doi.org/10.1016/j.engeos.2021.01.001>
 11. Calderón-Macias C, Sen MK, Stoffa PL. Artificial neural networks for parameter estimation in geophysics [Link]. *Geophysical prospecting*. 2000;48(1):21-47. <https://doi.org/10.1046/j.1365-2478.2000.00171.x>
 12. Kim J, Kang J-D, Kim B. Machine-learning models to predict P- and S-wave velocity profiles for Japan as an example. *Frontiers in Earth Science*. 2023;11:1267386. <https://doi.org/10.3389/feart.2023.1267386>
 13. Aladag C, Kayabasi A, Gokceoglu C. Estimation of pressuremeter modulus and limit pressure of clayey soils by various artificial neural network models. *Neural Computing and Applications*. 2013;23(2):333-9.
 14. Kosko B. *Neural networks and fuzzy systems: a dynamical systems approach to machine intelligence*: Prentice hall; 1992.
 15. Rajabi M, Bohloli B, Ahangar EG. Intelligent approaches for prediction of compressional, shear and Stoneley wave velocities from conventional well log data: A case study from the Sarvak carbonate reservoir in the Abadan Plain (Southwestern Iran). *Computers & Geosciences*. 2010;36(5):647-64.
 16. Behnia D, Ahangari K, Noorzad A, Moeinossadat SR. Predicting crest settlement in concrete face rockfill dams using adaptive neuro-fuzzy inference system and gene expression programming intelligent methods. *Journal of Zhejiang University SCIENCE A*. 2013;14(8):589-602. <https://doi.org/10.1631/jzus.A1200301>
 17. Kartalopoulos SV, Kartakopoulos SV. *Understanding neural networks and fuzzy logic: basic concepts and applications*: Wiley-IEEE Press; 1997.
 18. Jang J-S, Sun C-T. Neuro-fuzzy modeling and control. *Proceedings of the IEEE*. 1995;83(3):378-406.
 19. Hung M-C, Yang D-L, editors. *An efficient fuzzy c-means clustering algorithm*. Proceedings 2001 IEEE international conference on data mining; 2001: IEEE.
 20. Baziar M, Nabizadeh R, Mahvi AH, Alimohammadi M, Naddafi K, Mesdaghinia A. Application of adaptive neural fuzzy inference system and fuzzy C-means algorithm in simulating the 4-chlorophenol elimination from aqueous solutions by persulfate/nano zero valent iron process. *Eurasian Journal of Analytical Chemistry*. 2018;13(1). <https://doi.org/10.12973/ejac/80612>
 21. Ghorbani A, Jafarian Y, Maghsoudi MS. Estimating shear wave velocity of soil deposits using polynomial neural networks: Application to liquefaction. *Computers & Geosciences*. 2012;44:86-94. <https://doi.org/10.1016/j.cageo.2012.03.002>
 22. Bahadori H, Momeni M. ANN for correlation between shear wave velocity of soil and some geotechnical parameters. 2016.
 23. Ataee O, Hafezi Moghaddas N, Lashkari Pour GR, Abbari Nooghabi MJ. Predicting shear wave velocity of soil using multiple linear regression analysis and artificial neural networks. *Scientia Iranica*. 2018;25(4):1943-55. <https://doi.org/10.24200/sci.2017.4263>
 24. Kayadelen C. Soil liquefaction modeling by genetic expression programming and neuro-fuzzy. *Expert Systems with Applications*. 2011;38(4):4080-7. <https://doi.org/10.1016/j.eswa.2010.09.071>
 25. Jalalifar H, Mojedifar S, Sahebi A, Nezamabadi-Pour H. Application of the adaptive neuro-fuzzy inference system for prediction of a rock engineering classification system. *Computers and Geotechnics*. 2011;38(6):783-90. <https://doi.org/10.1016/j.compgeo.2011.04.005>
 26. Soil ACD-o, Sampling RSDo, Investigations RFTfS, editors. *Standard test method for penetration test and split-barrel sampling of soils 1999*: American Society for Testing and Materials.
 27. Testing ASf, Materials. *Standard test method for particle-size analysis of soils*. Subcommittee D18. 03 of the American Society for Testing and Materials; 1998.
 28. Standard A. D2216-10: *Standard Test Methods for Laboratory Determination of Water (Moisture) Content of Soil and Rock by Mass*. ASTM International, West Conshohocken, PA. 2010.
 29. Soil ACD-o, Rock. *Standard test methods for liquid limit, plastic limit, and plasticity index of soils*: ASTM International; 2010.

COPYRIGHTS

©2024 The author(s). This is an open access article distributed under the terms of the Creative Commons Attribution (CC BY 4.0), which permits unrestricted use, distribution, and reproduction in any medium, as long as the original authors and source are cited. No permission is required from the authors or the publishers.

**Persian Abstract****چکیده**

پارامترهای دینامیکی مهمترین داده‌های ژئوتکنیکی برای درک رفتار محیط خاکی تحت بارهای دینامیکی و شناسایی پاسخ لرزه‌ای خاک می‌باشند. برای تعیین این پارامترها از چندین آزمایش ژئوفیزیکی آزمایشگاهی و برجا مانند آزمایش لرزه‌ای درون گمانه‌ای استفاده می‌شود. از آنجایی که این آزمایش پرهزینه و زمان بر است و آماده سازی گمانه‌های مناسب آسان نیست، نیاز است نتایج این آزمایش با کمک مدل‌ها و روابط تجربی تخمین زده شود. خروجی اصلی آزمایش لرزه‌ای درون گمانه‌ای سرعت موج برشی (V_s) خاک است که می‌توان از آن به صورت غیر مستقیم برای بدست آوردن مدول برشی دینامیکی خاک (G_s) استفاده کرد. رابطه بین خصوصیات فیزیکی و پارامترهای مکانیکی خاک از اصول شناخته شده مهندسی ژئوتکنیک است. در این مطالعه از نتایج ۱۹ آزمایش لرزه‌ای درون گمانه‌ای و داده‌های ژئوتکنیکی موجود در مناطق جنوبی شهر تهران به عنوان داده‌های ورودی یک سیستم استنتاج عصبی فازی تطبیقی (ANFIS) برای توسعه مدل‌هایی کاربردی به منظور پیش‌بینی سرعت موج برشی خاک‌های ریزدانه در تهران استفاده شده است؛ در نتیجه پیش پردازش و مدل سازی هوشمند صورت گرفته دو مدل جدید برای این مهم پیشنهاد شده است. متغیرهای مستقل اولین مدل پیشنهادی شامل درصد رطوبت، شاخص خمیری (PI)، حد روانی (LL)، عمق انجام آزمایش و توزیع اندازه ذرات خاک‌ها بوده است. در مدل دوم علاوه بر ورودی‌های ذکر شده از عدد آزمایش نفوذ استاندارد (\dot{N}_{SPT}) نیز به عنوان متغیر مستقل استفاده شده است. ضرایب تعیین (R^2) مدل‌های پیشنهادی به ترتیب ۰/۷۴ و ۰/۸ برای کل داده‌های آموزش و آزمایش بوده است.



A Mathematical Model for Resource Sharing with Bilateral Contracts in a Supply Chain with Government Intervention under a Game Theory Approach

G. R. Einy-Sarkalleh^a, R. Tavakkoli-Moghaddam^{*b,c}, A. Hafezalkotob^d, S. E. Najafi^a

^a Department of Industrial Engineering, Science and Research Branch, Islamic Azad University, Tehran, Iran

^b School of Industrial Engineering, College of Engineering, University of Tehran, Tehran, Iran

^c Research Center of Performance and Productivity Analysis, Istinye University, Istanbul, Turkey

^d School of Industrial Engineering, South Tehran Branch, Islamic Azad University, Tehran, Iran

PAPER INFO

Paper history:

Received: 18 January 2024

Received in a revised form: 09 February 2024

Accepted: 16 February 2024

Keywords:

Supply Chain Management

Bilateral Contract

Alliance

Coordination

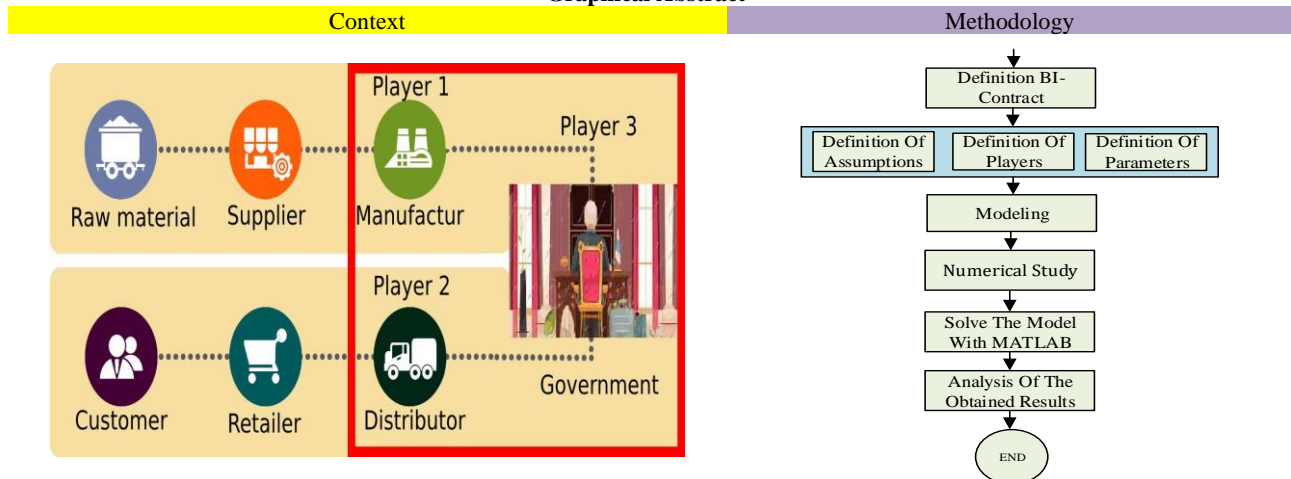
Game Theory

ABSTRACT

Contracts have been used for coordination in many supply chain alliances among businesses. Because bilateral contracts are significantly more successful and profitable than uni-contracts, In this article, the issues of implementing bilateral contracts are investigated with the approach of game theory and government intervention to increase bilateral interaction between members of co-production and co-distribution in the supply chain. By adopting the game theory model between these two members of the chain and intervention government, this research seeks to increase production and distribution by making maximum use of the excess capacity of production and distribution in the chain. In this way, the producer uses his surplus capacity in two ways: one is produced directly by the producer and enters the market by the distributor, and the other is an order that the distributor gives to the producer, which is different from the product that the producer produces. It is produced directly and given by the distributor. The purpose of this research is to investigate and analyze the amounts and profits resulting from the participation of production and distribution with government intervention in the supply chain. According to this research, governments should provide an environment for supply chain members to have more cooperation with each other because, in the case of cooperation among supply chain members, the profits of the chain and the members will increase.

doi: 10.5829/ije.2024.37.06c.14

Graphical Abstract



* Corresponding Author. Email: tavakoli@ut.ac.ir (R. Tavakkoli-Moghaddam)

Please cite this article as: Einy-Sarkalleh GR, Tavakkoli-Moghaddam R, Hafezalkotob A, Najafi SE. A Mathematical Model for Resource Sharing with Bilateral Contracts in a Supply Chain with Government Intervention under a Game Theory Approach. International Journal of Engineering, Transactions C: Aspects. 2024;37(06):1175-82.

1. INTRODUCTION

In today's world, many companies, to maintain their growth in the consumer goods market, try to develop their product share on the one hand and reduce their operational costs on the other; however unfortunately, nowadays, issues (e.g., increasing customer tastes, competitiveness, and a variety of products in business markets) that increase the operating costs of companies have become a common concern of all manufacturing companies to reduce this operating cost in the supply chain (SC) (1). In this regard, companies have turned to coordination in the SC to integrate and coordinate the SC to increase profits, reduce costs and shortages, and share the amount of risk among the players and partners of the SC (2).

Coordination in the SC is done through mechanisms in the chain. One of these mechanisms is a contract. SC contracts are useful tools for multiple SC members to behave in a coordinated manner in a non-integrated chain (3). A contract is a set of terms and conditions that provide appropriate information and incentive mechanisms such as risk sharing among chain members as well as rewards that ensure all parts of the SC coordinate and share the optimal amount of profit. Due to their positive impact on the chain, coordination contracts have significantly been considered by researchers and executives over the last few decades (4). There are different contracts in the SC, which are called uni-contracts. However, this article deals with a type of contract, called a bilateral contract.

In bilateral contracts, one company shares a part of its surplus capacity, for example, its production capacity, with another company, and the other company shares a part of its surplus capacity, such as its distribution capacity, with this company (5). It should be noted that in such cases, each of the companies is both a producer and a distributor; the only issue is the excess capacity of these companies.

As an example, Nestlé and Spray Ocean in America have developed a long-term strategic operation contract to increase production and efficiency in the chain. Under this contract, Spray Ocean is responsible for charging bottles for two companies "for fruit juice drinks," while Nestlé is in charge of the supply and distribution process of Ocean Spray Company (6). An example of these contracts can be mentioned regarding Fiat and Tata Company in India regarding engine manufacturing. In this cooperation, Fiat produces its engines, and Tata Company shares its agencies and marketing management networks for Fiat in India. This type of contract can also refer to the contract for both the distribution and production of Bosch and Panasonic companies (7).

In this research, bilateral contracts in the SC have been investigated and modeled so that each member of the chain provides production-distribution of its surplus

capacity to the other. In this research, there are three players: the producer, the distributor, and the government. The producer gives two types of products to the distributor for distribution in the market: one is his production, and the other is the production that he gives to the producer on the order of the distributor. In the same way, distributors distribute two types of products: one is produced by the manufacturer, and the other is ordered by themselves. The types of these two products are not similar. In this research, mathematical modeling is first carried out for each member of the supply chain, and then their profit values are calculated based on random numbers for each player. Finally, charts are drawn by changing the parameters. Also, the government's goal as the third player in this model is to increase cooperation among members, cooperation, social welfare, price reduction, maximum use of companies' capacity

2. LITERATURE REVIEW

In general, there are two types of structures in the SC: centralized and decentralized SCs. In a centralized SC, decisions are made centrally for the entire chain, and the profit of the entire chain is considered (8). However, in a decentralized SC, every one of the members decides in a decentralized manner, independently from other members, and based on his knowledge. The coordination mechanism in the SC is one of the most important issues in the decentralized SC (9). In the research literature, the issue of contracts and the SC coordination with the intervention of the government has been investigated with the approach of game theory.

About emission of carbon reduction in an SC focused on retailers in which consumer awareness of such issues as environment and tax, Revenue-sharing against cost-sharing is studied in the context. They design some incentive schemes and show their effectiveness and perfect consistency for both retailers and manufacturers (10).

Asghari et al. (11) discussed developing an improved Particle Swarm Optimization (PSO) algorithm using crowd-learning theory to solve complex optimization problems involving pricing and advertising decisions in closed-loop supply chain networks. The proposed algorithm is validated through testing and shown to perform better than existing algorithms in terms of computational time and solution quality. Heydari et al. (12) studied reverse and closed-loop SC coordination with government roles. They showed that government-sponsored incentives for the manufacturer are preferred by the retailer. In an SC, the final product is distributed in multiple channels. Zheng et al. (13) studied the effects of government subsidies for green products. They show that the social welfare under the high replacement subsidy is not always superior to the low subsidy. Cao et

al. (14) considered an optimization problem, in which two important decision variables are regarded: 1. Production level, 2. Carbon level enhancement. They also consider cap-and-trade and low-carbon subsidy policies in their analysis. They show that a low-carbon subsidy policy is more beneficial to society when the environmental damage coefficient is less than a threshold; however, otherwise, cap-and-trade policy is more beneficial. Xu et al. (15) investigated joint production and pricing decisions for multiple products with cap-and-trade and carbon tax regulations. They demonstrate that the social welfare under carbon tax regulation is not less than that under cap-and-trade regulation. Despite this, no one regulation always generates more profit and has advantages in curbing carbon emissions than the other one.

Fathollahi-Fard et al. (16) proposed a bi-level programming model for home healthcare supply chain (HHSC) planning considering demand outsourcing. The paper develops mathematical formulations for the bi-level model and proposes several meta-heuristic algorithms to solve it. A hybrid heuristic-exact method is also presented to validate the meta-heuristics on small instances. Hafezalkotob et al. (17) adopted a multi-level game theory approach to study government financial intervention in regular and green SCs. They stress the impact of budgetary limitations of the government on efficiency decisions for the decrease of pollution of the products. Hafezalkotob (18) studied competition to improve sustainability stressed and emphasized by the government. They consider two players: 1. Internal suppliers, 2. External suppliers. The study concludes that limitations imposed by the government are effective on stability, competitiveness, or monopoly of the market. Mahmoudi and Rasti-Barzoki (19) adopted an evolutionary game theoretic approach to study sustainable SCs under government intervention. They find that government policy impacts producers' activity, competitive markets, and emissions.

Fathalikhani et al. (20) studied the impact of government intervention on cooperation, competition, and cooperation of humanitarian SCs and found that the cooperation of donors increases the donors' utility. Javadi et al. (21) studied a setting with the distribution of products in multiple channels in which the policy of the SC is determined directly by two factors: 1. Return regulations that focus on flexibility, and 2. Regulation that intensifies saving of energy. They discovered that the revenue-seeking policy does not necessarily lead to a higher energy-saving level and better social welfare unless the government's budget is increased. Hadi et al. (22) investigated an optimization problem that assumes production is hybrid and the intervention of government is allowed. They also assumed the policies of SC support the protection of the environment and revenue goals. The study leads to the finding that players of SC and the government experience improved the profit performance

when they decide together. Hafezalkotob (23) modeled intervention policies of the government in the price-energy-saving competition of green SCs. They find that when the government intervenes, the utility of society improves in all cases. Yet, the environment, SCs with green strategy, and consumers must not be ignored in designing the policies of the SC.

Liu et al. (24) used a three-level game theory model with government intervention. The outputs showed that excess costs play a key role in reducing carbon in the chain, and the government also plays a very important role in this regard. The outputs through numerical values were also confirmed. This article examines a comprehensive approach to determining the quantity of coordination in the SC to effectively evaluate the performance of the SC in the 4th industrial age. It was observed that senior management focuses more on organizational issues (e.g., lean structure, organizational culture, and accountability factors) for improving coordination in the SC than on technology in the Industry 4.0. Ghozatfar et al. (25) focused on waste management, with waste being converted into energy and compost, using a game theory approach with the government intervening in municipal management. The government intervenes by determining the level of subsidy for the purchase of recyclable waste and imposing penalties for the emission of greenhouse gases and effluents, within a set of policy choices between income generation, environmental efforts, and social welfare.

3. PROBLEM STATEMENT

As mentioned, in this case, it is assumed that the goods produced by the manufacturer in two ways (i.e., direct production by the manufacturer and custom production given to the manufacturer by the distributor) are not the same. In this case, the assumption is that the price of the goods imported into the market, where the value of A and A' is the base price of these two products, and according to the famous economist Smith's rule, by producing as much as possible by the manufacturer, whether in the mode of sending by the distributor or in the mode of ordering production from the distributor, this base amount will be reduced. The production and distribution model with the game theory approach and government intervention is shown in Figure 1.

3.1. Definition of Parameters

The model parameters are as follows:

A : The basic price of the product that the manufacturer produces directly and distributes to the distributor.

A' : The base price of the custom product that the distributor orders from the manufacturer and is distributed by the distributor.

α : The base price of the product ordered by the distributor for the manufacturer.

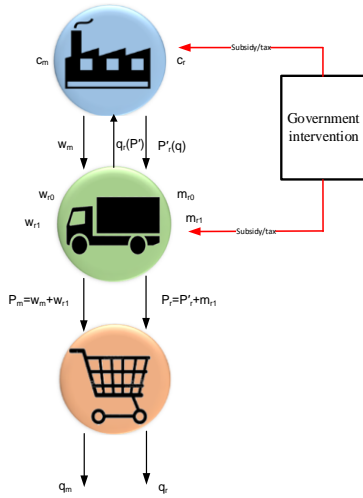


Figure 1. Game theory model with the government intervention in the supply chain

γ : The coefficient that is deducted from the base price of the product by the distributor to the manufacturer for each order unit

β : The coefficient that is deducted by the manufacturer from the price of the base product for each unit of product production

$\hat{\beta}$: The coefficient that is deducted by the distributor from the price of the base product for each custom product production unit.

c_m : The cost of each unit of product production by the manufacturer

c_r : The cost per unit of production of the product ordered by the distributor and produced by the manufacturer.

w_{r0} : Cost per unit of handling by the distributor from each unit of product produced by the manufacturer

w_{r1} : The amount received by each distribution unit from the manufacturer's products by the distributor

w_m : The amount that the manufacturer receives from the distributor for each product.

m_{r0} : Cost per unit of handling by the distributor of each unit of product ordered by the distributor

m_{r1} : The amount received by the distributor for each unit of ordered product per distribution unit

LS: It is a proportion of the subsidy that the government allocates for greater use of the power and capacity of both production and distribution companies.

P_m : The price that is offered to the market by the distributor for each unit of product production

P_r : The price that is offered to the market by the distributor for each unit of production of the customized product.

3. 2. Definition of Decision Variables Modelling variations are as follows:

q_m : The amount of production that the producer produces from her excess capacity and is distributed by the distributor

q_r : The order quantity is distributed to the manufacturer by the distributor, which is distributed by the distributor
 s : It is the amount that is deducted by the government for each production unit from the production and added to the producer for each unit of order for production.

3. 3. Definition of Auxiliary Variables Modelling auxiliary variables are as follows:

$\hat{p}_r(q)$: The price per unit of the product produced by the manufacturer that is ordered by the distributor.

π_m : Producer's profit function

π_r : Distributor profit function

π_G : Subject to the government's goal

Note: the price distribution function $\hat{p}_r(q)$ can be considered as follows:

$$\hat{p}_R(q) = \alpha - \gamma q_r \tag{1}$$

3. 4. Manufacture The goal of the manufacturer is to make the most of the surplus capacity that they produce from this capacity for themselves as well as for customized products ordered by the distributor. The manufacturer's model is as follows:

$$\max_{q_m} \pi_m = (A - \beta q_m - w_{r1} - 2c_m)q_m + (\alpha - \gamma q_r - c_r)q_r - (q_m - q_r)s(1 - ls) \tag{2}$$

s.t.

$$q_m + q_r \leq CAP_m \tag{3}$$

$$q_r \leq \frac{(\alpha - c_r)}{\gamma} \tag{4}$$

$$A - \beta q_m - w_{r1} - c_m \geq 0 \tag{5}$$

$$A - \beta q_m \leq ld \tag{6}$$

$$\hat{A} - \hat{\beta} q_r \leq \hat{ld} \tag{7}$$

$$q_m s(1 - ls) - q_r s(ls) \geq \lambda \tag{8}$$

$$q_m \geq 0 ; q_r \geq 0 \tag{9}$$

3. 5. Distributor The distributor earns profits in two ways: one by selling the products it gives and distributes to the producer, and the other by distributing the products of the manufacturer. The distributor model is as follows:

$$\max_{q_r} \pi_R = (\hat{A} - \hat{\beta} q_r)q_r - (\alpha - \gamma q_r)q_r - m_r q_r + (q_m(w_{r1} - w_{r0})) + q_r s(ls) \tag{10}$$

s.t.

$$q_m + q_r \leq CAP_m \tag{11}$$

$$q_r \leq \frac{(\alpha - c_r)}{\gamma} \tag{12}$$

$$\hat{A} - \hat{\beta}q_r - (\alpha - \gamma q_r) - m_r \geq 0 \tag{13}$$

$$A - \beta q_m \leq ld \tag{14}$$

$$\hat{A} - \hat{\beta}q_r \leq \hat{ld} \tag{15}$$

$$-q_m s(1 - ls) + q_r s(ls) \geq \lambda \tag{16}$$

$$q_m \geq 0 \tag{17}$$

$$q_r \geq 0 \tag{18}$$

3. 6. Government The goal of the government is to maximize the use of capacities and increase the amount of production:

$$\max \pi_G = q_m + q_r \tag{19}$$

s.t.
$$q_m + q_r \leq CAP_m \tag{20}$$

$$A - \beta q_m \leq ld \tag{21}$$

$$\hat{A} - \hat{\beta}q_r \leq \hat{ld} \tag{22}$$

$$-q_m s(1 - ls) + q_r s(ls) \geq \lambda \tag{23}$$

$$q_m \geq 0 \tag{24}$$

$$q_r \geq 0 \tag{25}$$

4. NUMERICAL STUDY

In this section, by providing a numerical example of the parameters of the model for the three players (i.e., producer, distributor, and government), it is shown that the product produced by the producer and the distributor is it, and the government in this model, by providing subsidies and taxation, encourages two actors to cooperate more and produce more. In this part, the effect of parameter changes on the performance of the chain and decision variables, i.e., production values by two actors, as well as the profit of the actors in this model, will be analyzed along with the presentation of the diagram. In this regard, numerical values have been assigned to the parameters of the model. It should be noted that these values must be reasonable for the model to be solvable; otherwise, the model will not be solvable.

The parameters of the model in this problem are as follows:

$capm=3500$	$gama=0.01$	$alpha=1500$	$wr0=100$
$A=3400$	$beta=0.08$	$AP=2250$	$betap=0.08$
$ld=3500$	$ldp=2300$	$wr1=150$	$cm=1000$
$mr0=150$	$ls=0.4$	$cr=280$	$landa=100$

According to the given data, the decision variables or the Nash equilibrium, which are the same production values as well as the profit function for the producer (π_m), distributor (π_r) and government profit in the SC are shown in Table 1. After solving this model by MATLAB software, the results are listed in Table 1.

5. SENSITIVITY ANALYSIS

As shown in Table 1, with the given parameters, the amount of production by the manufacturer with the production of 1813 units reaches a profit of 3,998,241, and also the distributor’s orders of 1687 units of the product, which is a profit of 1,217,394 units. Finally, the government also gets a profit of 191,648 units with the amount of 464 units of tax and subsidy. The changes of variables based on some parameters are depicted in Figure 2. As shown in this figure, with an increase in the base price by the producer, the amount ordered by the distributor decreases, and the producer uses her/his excess capacity to produce her/his product.

As shown in Figure 3, with the increase in the price of the producer’s product in the market, the amount of production by the producer will increase, and her desire to produce a customized product by the distributor will decrease.

As shown in Figure 4, with an increase in the price of the manufacturer’s customized product in the market, the amount of production by the manufacturer will decrease and the desire to produce the customized product by the distributor will increase.

TABLE 1. Values of the decision variables and functions of profiteers

q_m	q_r	s	Profit/ Manufacture (π_m)	Profit/ distributor (π_r)	Profit/ Government (π_G)
1813	1687	464	3,998,241	1,217,394	191,648

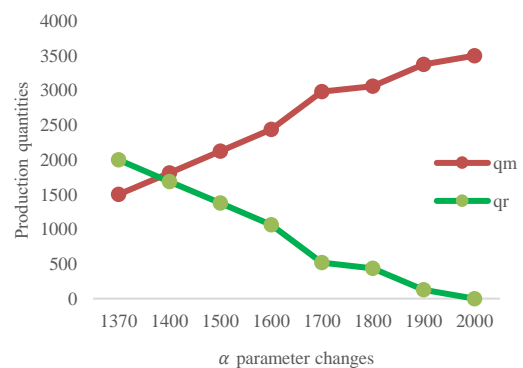


Figure 2. Changes in alpha value on decision variables

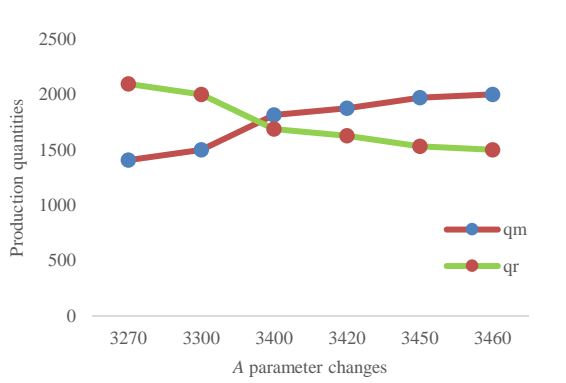


Figure 3. Changes in producer's product price value on decision variables

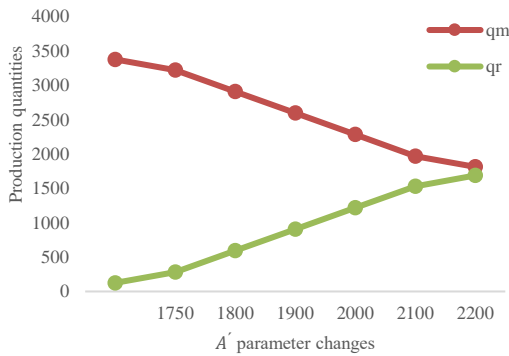


Figure 4. Changes in the ordered product price value on decision variables

In Figure 4, when the manufacturer produces the distributor's customized product, the profit of both members of the chain increases as depicted in Figure 5. It means that when the members of the supply chain cooperate with each other, the profit of the entire chain and, as a result, the profit of all members will increase.

6. RESEARCH GAP

Similarly, an extensive research has been conducted on types of coordination as well as types of contracts in the SC, along with the presentation of mathematical models. Unfortunately, it should be noted that on bilateral contracts in general, not much research has been done in this area of research attempting to examine the subject of bilateral agreements with view of theory of the game as well as the government as a player in the game that is known as government intervention. Bilateral contracts are the sharing of resources and excess capacity of each other, while uni-contracts are a kind of delivery (i.e., part of their work is transferred to another); however, in bilateral agreements, this is not the case; the action of each of the parties affects the other. In this study, the

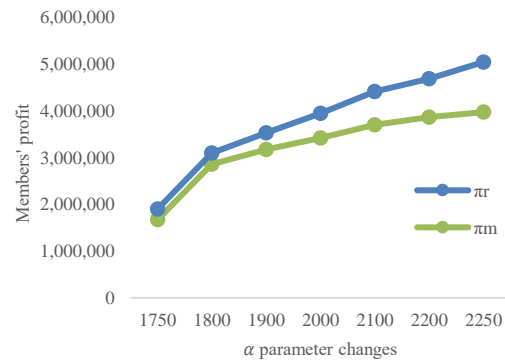


Figure 5. Changes in alpha value on decision variables

subject of bilateral contracts is analyzed and examined with theory of the game approach and government intervention.

7. MANAGERIAL INSIGHTS

In this model, all three players in the SC (i.e., producer, distributor, and government) seek to reach an equilibrium point based on the parameters that are assigned, and with each change in the parameter, a new Nash equilibrium point is obtained. For example, based on the existing parameters, by changing the price of the producer's product in the market, the producer has more incentive to produce, even though he has to pay taxes to the government. In this model, the government, in addition to trying to increase the amount of production and cooperation between the producer and distributor by giving subsidies and charging taxes. In the real world, in addition to subsidies and taxes, the government tries to create information infrastructure, laws, and regulations, provide facilities, etc., so that players in the SC can, buy sharing excess capacity in the direction of social welfare, reduce prices, etc., make maximum use of resources. In general, it can be said that the basis of the government's intervention is that incentives such as increasing social welfare, reducing prices, maximizing the use of companies' capacity, and finally making money in the SC can increase motivation and encouragement for members in different SCs to use the maximum amount of excess capacity.

The government should encourage the supply chain members to collaborate and cooperate more for the general well-being of society, reduce prices, distribute profits justly, and share risk among members by creating appropriate infrastructures.

8. CONCLUSION AND FUTURE STUDIES

The modeling in this research is in a three-level SC, producer, and distributor, with the intervention of the

government, where all three members of this chain try to reach the Nash equilibrium point in this game based on the parameters that have been defined. These parameters apply within the limitations of the model.

As it has been observed with changes in parameters, players' strategies change because each of the players seeks to maximize their profits. As seen in the model, by changing the parameters, the decision variables are also changed, and the new Nash equilibrium point is reached.

It is important to state this point that in defining the parameters it must be done very carefully that the model must have an optimal response.

This paper may be extended in several directions; for example, using the Nash equilibrium with the bargaining power approach, without complete information, using advanced optimization algorithms (e.g., hybrid heuristics and meta-heuristics), relaxing some assumptions of the model and re-formulating the model again. Modeling in probabilistic mode with a game theory approach, increasing the number of SC levels; for example, a multi-level SC, using the Stackelberg approach or another method, different functions to use the changes in the amount of the production order that the distributor gives to the manufacturer.

9. REFERENCES

- Mazinani M, Tavakkoli-Moghaddam R, Bozorgi-Amiri A. A Multi-objective Cash-in-transit Pollution-location-routing Problem Based on Urban Traffic Conditions. *International Journal of Engineering, Transactions B: Applications*. 2023;36(2):299-310. 10.5829/IJE.2023.36.02B.10
- Al-Saadi M. Coordination of Load and Generation Sides to Reduce Peak Load and Improve Arbitrage of Smart Distribution Grid. *International Journal of Engineering, Transactions B: Applications*. 2023;36(2):226-35. 10.5829/IJE.2023.36.02B.04
- Mostofi A. Select issues in designing license contracts of strategic alliances in the pharmaceutical supply chain: Open Access Te Herenga Waka-Victoria University of Wellington; 2022.
- Kanda A, Deshmukh S. Supply chain coordination: perspectives, empirical studies and research directions. *International journal of production Economics*. 2008;115(2):316-35. 10.1016/j.ijpe.2008.05.011
- Hoey L. Reclaiming the authority to plan: how the legacy of structural adjustment affected Bolivia's effort to recentralize nutrition planning. *World Development*. 2017;91:100-12. 10.1016/j.worlddev.2016.10.016
- Einy-Sarkalleh G, Tavakkoli-Moghaddam R, Hafezalkotob A, Najafi S. Developing a Fuzzy Measurement of Alternatives and Ranking Compromise Solution Method for Determining Essential Barriers in Iranian Car Industry. *International Journal of Engineering, Transactions A: Basics*. 2023;36(1):90-7. 10.5829/IJE.2023.36.01A.11
- Roels G, Tang CS. Win-win capacity allocation contracts in coproduction and codistribution alliances. *Management science*. 2017;63(3):861-81. 10.1287/mnsc.2015.2358
- Rached M, Bahroun Z, Campagne J-P. Decentralised decision-making with information sharing vs. centralised decision-making in supply chains. *International Journal of Production Research*. 2016;54(24):7274-95. 10.1080/00207543.2016.1173255
- Lee S, Kumara S. Decentralized supply chain coordination through auction markets: Dynamic lot-sizing in distribution networks. *International Journal of Production Research*. 2007;45(20):4715-33. 10.1080/00207540600844050
- Yang H, Chen W. Retailer-driven carbon emission abatement with consumer environmental awareness and carbon tax: Revenue-sharing versus cost-sharing. *Omega*. 2018;78:179-91. 10.1016/j.omega.2017.06.012
- Asghari M, Afshari H, Mirzapour Al-e-hashem S, Fathollahi-Fard AM, Dulebenets MA. Pricing and advertising decisions in a direct-sales closed-loop supply chain. *Computers & Industrial Engineering*. 2022;171:108439. 10.1016/j.cie.2022.108439
- Heydari J, Govindan K, Jafari A. Reverse and closed loop supply chain coordination by considering government role. *Transportation Research Part D: Transport and Environment*. 2017;52:379-98. 10.1016/j.trd.2017.03.008
- Zheng X, Lin H, Liu Z, Li D, Llopis-Albert C, Zeng S. Manufacturing decisions and government subsidies for electric vehicles in China: a maximal social welfare perspective. *Sustainability*. 2018;10(3):672. 10.3390/su10030672
- Cao K, Xu X, Wu Q, Zhang Q. Optimal production and carbon emission reduction level under cap-and-trade and low carbon subsidy policies. *Journal of cleaner production*. 2017;167:505-13. 10.1016/j.jclepro.2017.07.251
- Xu X, Xu X, He P. Joint production and pricing decisions for multiple products with cap-and-trade and carbon tax regulations. *Journal of Cleaner Production*. 2016;112:4093-106. 10.1016/j.jclepro.2015.08.081
- Fathollahi-Fard AM, Hajiaghahi-Keshteli M, Tavakkoli-Moghaddam R, Smith NR. Bi-level programming for home health care supply chain considering outsourcing. *Journal of Industrial Information Integration*. 2022;25:100246. 10.1016/j.jii.2021.100246
- Hafezalkotob A, Alavi A, Makui A. Government financial intervention in green and regular supply chains: Multi-level game theory approach. *International Journal of Management Science and Engineering Management*. 2016;11(3):167-77. 10.1080/17509653.2015.1004202
- Hafezalkotob A. Competition of domestic manufacturer and foreign supplier under sustainable development objectives of government. *Applied Mathematics and Computation*. 2017;292:294-308. 10.1016/j.amc.2016.07.007
- Mahmoudi R, Rasti-Barzoki M. Sustainable supply chains under government intervention with a real-world case study: An evolutionary game theoretic approach. *Computers & Industrial Engineering*. 2018;116:130-43. 10.1016/j.cie.2017.12.028
- Fathalikhani S, Hafezalkotob A, Soltani R. Government intervention on cooperation, competition, and competition of humanitarian supply chains. *Socio-Economic Planning Sciences*. 2020;69:100715. 10.1016/j.seps.2019.05.006
- Javadi T, Alizadeh-Basban N, Asian S, Hafezalkotob A. Pricing policies in a dual-channel supply chain considering flexible return and energy-saving regulations. *Computers & Industrial Engineering*. 2019;135:655-74. 10.1016/j.cie.2019.06.014
- Hadi T, Chaharsooghi SK, Sheikhmohammady M, Hafezalkotob A. Pricing strategy for a green supply chain with hybrid production modes under government intervention. *Journal of Cleaner Production*. 2020;268:121945. 10.1016/j.jclepro.2020.121945
- Hafezalkotob A. Modelling intervention policies of government in price-energy saving competition of green supply chains. *Computers & Industrial Engineering*. 2018;119:247-61. 10.1016/j.cie.2018.03.031
- Liu Z, Qian Q, Hu B, Shang W-L, Li L, Zhao Y, et al. Government regulation to promote coordinated emission reduction among enterprises in the green supply chain based on evolutionary game

analysis. Resources, Conservation and Recycling. 2022;182:106290. doi.org/10.1016/j.resconrec.2022.106290

Journal of Engineering. 2023;36(2):299-310. 10.1016/j.psep.2023.03.057

25. Mazinani M, Tavakkoli-Moghaddam R, Bozorgi-Amiri A. A Multi-objective Cash-in-transit Pollution-location-routing Problem Based on Urban Traffic Conditions. International

COPYRIGHTS

©2024 The author(s). This is an open access article distributed under the terms of the Creative Commons Attribution (CC BY 4.0), which permits unrestricted use, distribution, and reproduction in any medium, as long as the original authors and source are cited. No permission is required from the authors or the publishers.



Persian Abstract

چکیده

امروزه در بسیاری از ائتلاف‌ها، شرکت‌ها در زنجیره تامین هماهنگی‌های خود را از طریق قراردادهای انجام می‌دهند. از آنجائیکه موفقیت و عایدی قراردادهای دو طرفه نسبت به قراردادهای یک طرفه بسیار زیاد می‌باشد. در این مقاله مسائل پیاده‌سازی قراردادهای دو طرفه را با رویکرد تئوری بازی‌ها و مداخله دولت جهت افزایش تعامل دو سویه بین اعضای هم تولید و هم توزیع در زنجیره تامین مورد بررسی قرار گرفته است. در این تحقیق با اتخاذ مدل تئوری بازی‌ها بین این دو عضو زنجیره، با مداخله دولت به دنبال افزایش تولید و توزیع با استفاده حداکثری از ظرفیت مازاد تولید و توزیع در زنجیره است. بدین صورت تولید کننده به دو صورت از ظرفیت مازاد خود استفاده می‌نماید یکی بصورت مستقیم توسط تولید کننده، تولید و توسط توزیع کننده وارد بازار می‌شود. و دیگری سفارشی است که از طرف توزیع کننده به تولید کننده داده می‌شود که متفاوت با کالایی است که تولید کننده بطور مستقیم تولید می‌کند. هدف این تحقیق بررسی و تحلیل مقادیر و سود حاصله از مشارکت تولید و توزیع با مداخله دولت در زنجیره تامین می‌باشد. بر اساس این تحقیق، دولت‌ها باید محیطی را فراهم کنند تا اعضای زنجیره تامین همکاری بیشتری با یکدیگر داشته باشند. زیرا در صورت همکاری بین اعضای زنجیره تامین، سود کل زنجیره و در نتیجه سود اعضا افزایش می‌یابد.



Using Reluctance Torque Theory in Spoke Type Permanent Magnet Vernier Motors to Increase Average Torque

A. Imanifar, H. Yaghoobi*

Faculty of Electrical and Computer Engineering, Semnan University, Semnan, Iran

PAPER INFO

Paper history:

Received 21 December 2023

Received in revised form 03 January 2024

Accepted 20 January 2024

Keywords:

Average Torque

Finite-element-method

Spoke type Vernier Permanent-magnet Motor

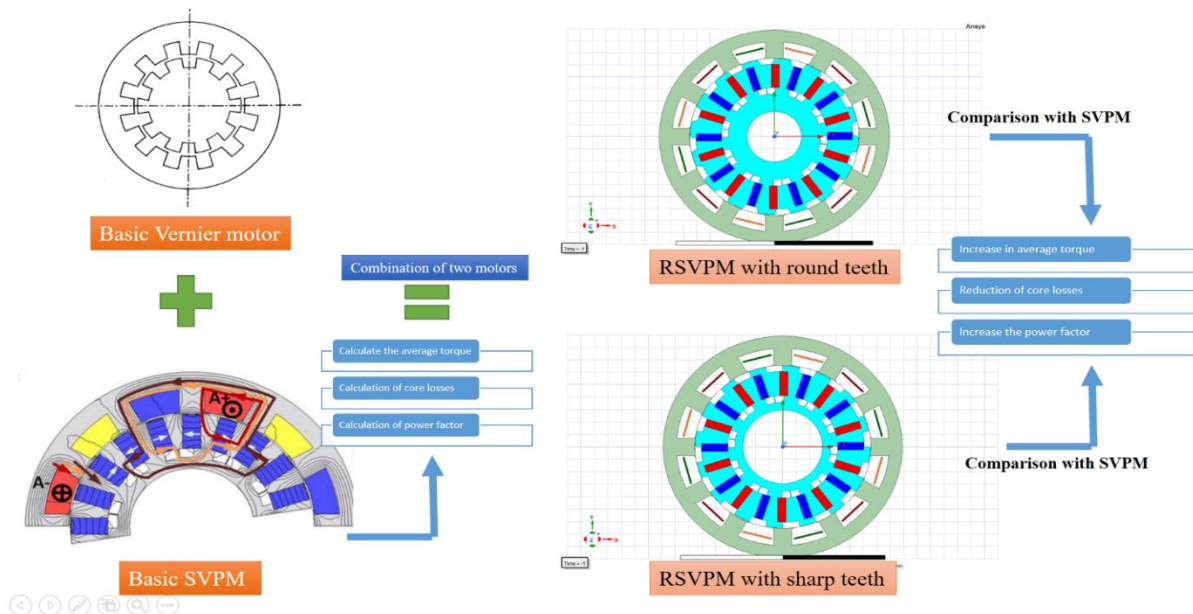
Reluctance Permanent Magnet Vernier Motor

ABSTRACT

Conventional energy sources like fossil fuels are no longer viable due to their limitations and environmental impact. The demand for cleaner, more efficient energy solutions has led to the development of electric machines with smaller volumes and higher output. The family of permanent magnet Vernier motors have high torque output at very low speeds while being very small in volume. In conventional SVPM, the core losses are high, which leads to heating and reducing the efficiency of the motor, and the power factor of the motor is also low, and the torque can increase in relation to the motor volume. The reluctance torque theory, along with the normal output torque of the motor, increases the final torque of the motor. In addition, the toothing of the rotor reduces the cross-sectional area and weight of the rotor. With the reduction of the cross-sectional area, the eddy currents in the core are reduced, the power factor increases and the efficiency of the motor improves. Therefore, in this paper, a spoke-type permanent magnet Vernier motor with a rotor similar to the reluctance rotor has been designed, which has higher torque, lower losses, and higher power factor compared to conventional spoke-type permanent magnet Vernier motors.

doi: 10.5829/ije.2024.37.06c.15

Graphical Abstract



*Corresponding Author: Email: yaghoobi@semnan.ac.ir (H. Yaghoobi)

1. INTRODUCTION

Permanent magnet motors are used in various industries such as electric traction, material forming, and electric vehicle industry (1). These motors are used in turbine systems due to their high efficiency and low maintenance costs (2). Economic reasons, cost competitiveness and availability of rare earth magnets are among the reasons that have made permanent magnet Vernier motors as well as permanent magnet motors important and widely used (3).

Rare earth magnets ultimately reduce the volume of the machine due to increased flux density compared to other magnets (4). Two kinds of interior PM (IPM) and surface mounted PM (SPM) machines are becoming candidates in high speed applications and Vernier machines are used in low speed applications (5). The shape of the placement of magnets in these motors has caused them to have various applications in the industry, of which the Halbach and spoke arrangement is one of the newest types (6). In other permanent magnet motors, in addition to the type of placement of magnets, the reluctance torque theory is used, which operates based on two different paths for the flux produced by the armature coil in the air gap (7).

The design of machine controlled with flux by high speed, as well as the design of the machine with low speed and high production torque, are very important and have many applications (8). The idea of the Vernier machine was first expressed in 1963 when it was proposed as a synchronous motor that has a reluctance model (9). The principle of operation of reluctance motors is the existence of non-uniform areas with low and high magnetic permeability between the stationary and moving parts of a motor. In the reluctance Vernier motor, the shape of the rotor and stator are made of teeth, and the number of teeth is not equal and slightly different. In these motors, in the areas where the stator teeth are aligned with the rotor teeth, the magnetic permeance is higher, and in the areas where the stator teeth are opposite to the rotor teeth, the magnetic permeance is lower (10). In 1995, a design was given that optimized Vernier motors, and in this design, a permanent magnet was used to increase the output torque density at the low speed (11). This design was named permanent magnet Vernier motors (PMVM).

Torque density has always been an important issue regarding Vernier machines (VM), which has been addressed over time by presenting different structures. These structures include the double rotor structures and the double excitation structure, which increase the torque density by increasing the area of the air gap (12-14).

High power factor is important in permanent magnet Vernier motors (PMVM) (15). A model for increasing the power factor is proposed by Li et al. (16). In this design, the magnets are placed in such a way that

compared to the conventional permanent magnet Vernier motors, it has less air gap. In these motors, magnetic flux is used in such a way that it has a higher torque density than conventional models (17, 18).

The magnets used on the surface of the rotor of this motor are of the rare earth type, which is very expensive. Manufacturers can use cheaper magnets to reduce costs as reviewed by Du and Lipo (18). The permanent magnet Vernier motor that has been reviewed by Liu and Lipo (19) uses flux barriers, which causes high torque density to be produced.

In this paper, the permanent magnet Vernier motor will be discussed with the reluctance design on its rotor, which ultimately has a higher density and average torque than conventional permanent magnet Vernier motors. In this study, a permanent magnet Vernier machine with a flux barrier behind the magnet is designed and a reluctance scheme is implemented on it. In this design, the air gap between the rotor and the stator is non-uniform and the rotor is toothed. In this type of motor, in addition to the main torque that is produced, the reluctance torque caused by the rotor teeth will be created and will be added to the main torque of the machine.

2. OPERATION PRINCIPLE OF VERNIER MACHINE

The operation of the permanent magnet Vernier motor is similar to a gearbox. In gearboxes, the torque of the outer rotor is different from the torque of the inner rotor. In these motors, the frequency caused by the torque of the rotor is different from the frequency caused by rotation, and this property is similar to the operation of a gearbox (20), so to better understand how to produce torque in permanent magnet Vernier motors (PMVMs), studies on torque production in gearboxes carried out.

The family of Vernier machines is very diverse. The performance of each of them is different from each other and they have different applications in the industry. Figure 1 illustrates the geometry of a simple Vernier motor. This motor has a toothed stator and a toothed rotor. The geometry of this motor is similar to synchronous reluctance motors and its torque increases as the rotor speed decreases. The stator of this type of motor has open slots with uniform winding distribution similar to an induction motor.

The reluctance Vernier motor (RVM) that can be seen in Figure 2 has a toothed rotor and a toothed stator [10], and in some areas the magnetic permeability between the rotor and stator is maximum and in some areas, the magnetic permeability is minimum because the air gap between the rotor and stator is uniform. In these motors, sometimes the pitch of the stator slot is larger than the pitch of the rotor slot, and sometimes the pitch of the rotor slot is larger than the pitch of the stator slot. The torque production in RVM depends on the teeth, gaps,

and magnetomotive force waveform. The rotor speed of RVM is a fixed fraction of the rotation speed of the magnetomotive force waveform, which is constant and synchronous.

The permanent magnet Vernier motor shown in Figure 3 is another type of Vernier motor family that has a magnet placed on its rotor. The air gap between the rotor and the stator of these types of motors is uniform. In these motors, due to the presence of magnets on the rotor, the rotor torque density is higher and as a result, the output torque is higher. This motor has the same structure as the surface permanent magnet Vernier motor, and their difference is in the number of rotor poles and the winding, which has more rotor poles. This motor has similar teeth on the surface of the stator towards the air gap (12).

2. 1. Flux Barrier Design In permanent magnet Vernier machines, there is a virtual gearbox, which is suitable for low-speed, high-torque direct drive applications. Usually, the gear ratio of this virtual gearbox is $\frac{p_r}{p_s}$; where p_r is the number of rotor poles

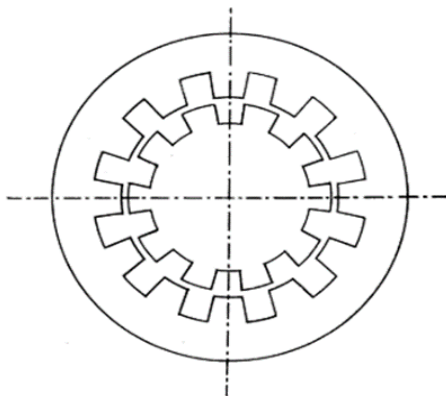


Figure 1. A simple Vernier motor (9)

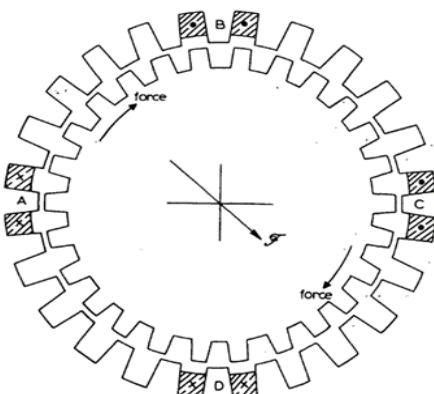


Figure 2. Reluctance Vernier motor (RVM) (10)

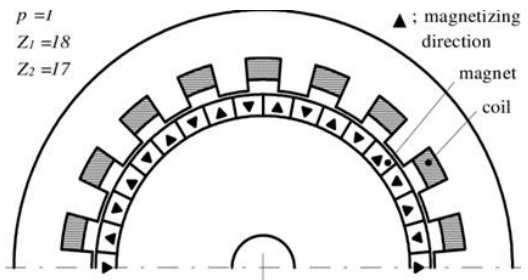


Figure 3. A simple permanent magnet Vernier machine (13)

and p_s is the number of stator poles. Figure 4 shows the design of a piecemeal flux barrier on the rotor of a permanent magnet Vernier machine, abbreviated as SVPM (17), is introduced. This type of flux barrier can maintain the power factor of the motor and simplify the production process of this type of motor for use in the industry.

Figure 5 shows unlike the previous case, the flux barriers are placed continuously. The number of these flux barriers under each pole is half of the case where the flux barriers are placed in pieces under each pole.

Flux barriers cause the magnetic flux to be locked in a specific path between the rotor and the stator. In the case where continuous flux barriers are used because the iron of the rotor is used less, the iron loss of the rotor is reduced, and this causes the heat of the rotor core to decrease during operation. Figure 6 shows the comparison result between the two cases mentioned above.

3. DESIGN RELATION OF PERMANENT MAGNET VERNIER MACHINE

In this section, the equations governing permanent magnet Vernier machines were discussed. These equations include torque theory in conventional

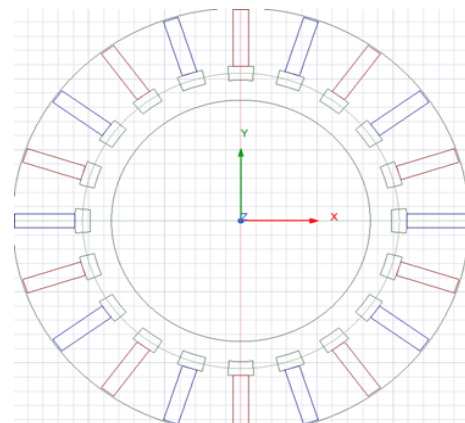


Figure 4. Topology of patchy flux barrier

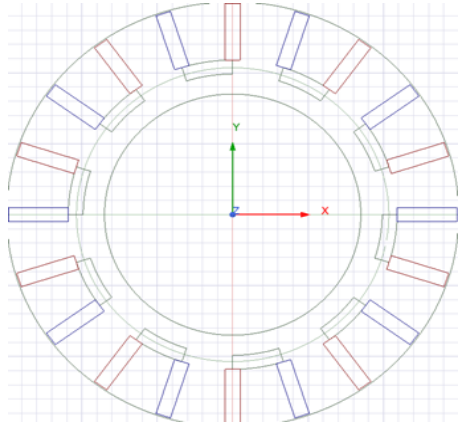


Figure 5. Topology of continuous flux barrier

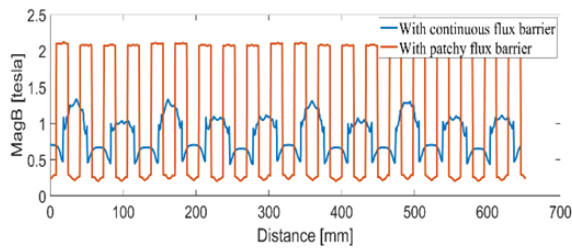


Figure 6. Comparison of the rotor magnetic flux density between the two states of continuous flux barrier and patchy flux barrier, which indicates the heat of the rotor

permanent magnet Vernier machines. The torque caused by the magnetic driving force is expressed, and then the torque caused by the magnetic flux is given, and after that, the theory of torque in permanent magnet Vernier machines is discussed.

3. 1. Design Equation

In a permanent magnet Vernier machine, the number of slots on the stator is obtained as follows (11):

$$z_1 = 6pq \quad (1)$$

where p shows the number of stator poles and q shows the number of stator slots per phase. For as much as (11):

$$z_2 = z_1 + p \quad (2)$$

By inserting Equation 2 into Equation 1, the following equation is obtained (4).

$$z_2 = (1 + 6q)p \quad (3)$$

where the number of rotor slots is obtained. The three-phase current of the start winding is obtained according to Equation 4 (11).

$$i_{1h} = \sqrt{2}i_1 \cos(\omega t - (h-1)\frac{2\pi}{3}) \quad (4)$$

where the value h depends on the phase. This value is 1

for the first phase, 2 for the second phase, and 3 for the third phase. The magnetomotive force resulting from per phase is obtained from Equation 5 (11).

$$F_1 = \sum (-1)^q \frac{3N_1 i_1 k_w (1+6l)}{\sqrt{2}p\pi(1+6l)} \times \cos((1+6l)p\theta_1 - \omega t) \quad (5)$$

Respectively, N_1 , i_1 , $k_w (1+6l)$, θ_1 , ω are the number of conductors connected in series in the stator winding, the effective value of the stator current, the winding factor, spatial angle, and the frequency angle of the stator current.

Specific loading in permanent magnet machines is obtained as follows (11):

$$ac = \frac{3k_w N_1 i_1}{\pi D} \quad (6)$$

where D is the inner diameter of the stator core. The polar pitch in permanent magnet Vernier machines is obtained from Equation 7 (11).

$$\tau = \frac{\pi D}{2p} \quad (7)$$

3. 2. The Torque Caused by The Magnetic Driving Force

The magnetic driving force and the flux density are used to obtain the output torque, which is given in Equation 8 (11).

$$T = z_2 \times \frac{3\tau l_a N_1 i_1}{\sqrt{2}\pi} \times \left\{ k_{w1} B_{m1} + (-1)^q \frac{k_w (1+6q)}{1+6q} B_m (1+6q) \right\} \times \sin\{(\omega - z_2 \omega_m)t + z_2 \xi \phi_2\} \quad (8)$$

where l_a the length of the core and other parameters are introduced in the previous equations. Figure 7 shows the geometry of the $\xi \phi_2$.

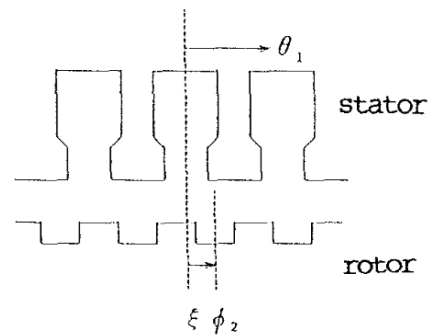


Figure 7. Geometric view of θ_1 and $\xi \phi_2$ on rotor and stator geometry of permanent magnet Vernier machine (11)

If the rotor moves at a constant speed, its angular is as follows (11).

$$\omega_m = \frac{\omega}{z_2} \quad (9)$$

The torque equation obtained in Equation 8 is written as Equation 9 (11).

$$T = z_2 \times \frac{3\tau l_a N_1 i_1}{\sqrt{2\pi}} \times \left\{ k_{w1} B_{m1} + (-1)^q \frac{k_w (1+6q)}{1+6q} B_m (1+6q) \right\} \times \sin \{ z_2 \xi \phi_2 \} \quad (10)$$

There is a sinusoidal expression in Equation 10. So the maximum and minimum torque values can be calculated. The maximum and minimum values are respectively at $\xi \phi_2 = \pm \pi/2$ because the sinusoidal expression is placed between its minimum and maximum values at these points.

3.3. Torque Due to Magnetic Flux The magnetic flux caused by the magnet on the rotor produces torque. The maximum torque produced due to this flux is obtained from Equation 11 (11).

$$T_{vm1} = z_2 \times \frac{3\tau l_a N_1 i_1}{\sqrt{2\pi}} k_{w1} B_{m1} \quad (11)$$

3.4. Torque Theory in SPVM In SPVM, magnets on the surface of the rotor use flux barriers, which are called flux barriers because of the use of these flux barriers. In these machines, the magnetic flux closes its path in such a way that it can perform better in torque production and ultimately produce better torque compared to conventional permanent magnet Vernier machines.

The magnets on the rotor may be placed on the surface of the rotor or buried in the rotor, depending on the type of application in the industry. Figure 8 shows a view of the SPVM, with a piecemeal flux barrier placed on the rotor and behind the magnets.

The spatial angle of the rotor magnets in the SPVM is as follows (18).

$$\theta_r = \theta_s - \theta_m \quad (12)$$

where the spatial angle of the MMF stator θ_r and spatial angle of the rotor magnet θ_s and mechanical rotor rotation angle θ_m . In the air gap of SPVM, the flux density is calculated through Equation 13 (18).

$$B_{rg} = \hat{P}(\theta) B_g(\theta_s) \quad (13)$$

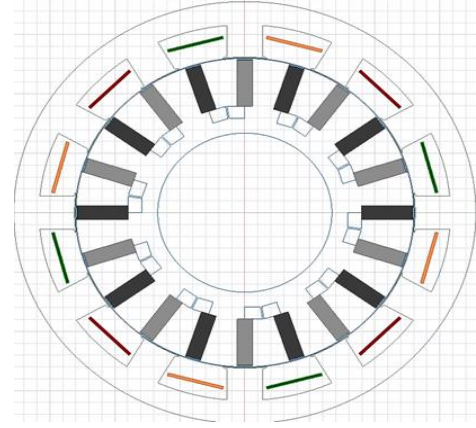


Figure 1. A view of the SPVM with flux barrier

where the magnetic permeability $\hat{P}(\theta)$ and the air gap flux density $B_g(\theta_s)$ modulated by the stator teeth. Finally, the torque in SVPM is obtained from Equation 14 (11).

$$T = \frac{d_{is} l_i}{2} \int_0^{2\pi} \left(\frac{\partial}{\partial \theta_m} B_{rg} \right) F_{sg} d\theta_s \quad (14)$$

where the magnetic driving force F_{sg} by the permanent magnets on the rotor.

4. THE PROPOSED RELUCTANCE SPOKE TYPE PERMANENT MAGNET VERNIER MACHINE

Nowadays, motors with low heat losses, low noise, low weight, and low iron losses are highly regarded (21). Conventional SVPMs have a simple circular rotor. In this research, the idea of a reluctance motor is taken. The basis of reluctance motors is the theory of reluctance torque, which is made by a non-uniform and toothed rotor. In this paper, a non-uniform and toothed rotor is designed for conventional spoke-type permanent magnet motors, the resulting reluctance torque comes with the help of the main torque of the motor and increases the average torque produced from its conventional state. Du and Lipo (18) simulated a conventional spoke-type permanent magnet Vernier motor. The stator of this motor has 4 poles and its rotor has 20 poles, and the motor excitation frequency is 66.67 Hz. The average torque produced by this motor is around 605 Nm. The idea of this paper is implemented on this motor, and it is designed in a non-uniform and toothed way so that the reluctance torque increases the average torque produced by this motor. In other words, the motor designed in this paper is a new type of SVPM in which reluctance torque is used, which is an RSVPM (Reluctance Spoke Type Permanent Magnet Vernier motor). Equation 15

generally obtained the method of calculating the core losses in an electric machine.

$$P_{core} = KB^2 f n_f s f_{loss} \quad (15)$$

In Equation 15, with decreasing cross-section (s), the losses decrease. Therefore, toothing the rotor reduces core losses. On the other hand, the core leakage factor (f_{loss}) also decreases significantly because with toothing the rotor, the magnetic field around the rotor is cut off and fewer eddy currents flow in the core. Therefore, by reducing the weight and core leakage factor, core losses are greatly reduced and the efficiency of the motor is increased.

4. 1. Equation of Number of Rotor Teeth

According to Equation 2, the number of rotor teeth can be calculated. To calculate the number of rotor teeth, the number of stator slots must be calculated first. In an SVPM, the number of stator slots is calculated from Equation 16 (18):

$$S_s = 3Pq \quad (16)$$

where P is the number of poles of the rotating magnetic field and q is a quantity related to the winding factor, which is 1 for the type of winding. Therefore, by substituting Equation 16 into Equation 2, the following equation is calculated, which shows the number of rotor teeth:

$$Z_2 = (3Pq) + P = P(3q + 1) \quad (17)$$

The number of stator poles is 4. According to Equation 16, the number of stator teeth is 12 and According to Equation 17, the number of rotor teeth is 16.

4. 2. Finite Element Method Analysis In this section, computer simulation in Ansys Electronics software is presented in two dimensions. Maxwell software can analyze the target motor in transient mode (22, 23). In Figure 9 the rotor teeth are designed as sharp teeth.

In Figure 10 the rotor is designed as a toothed rotor with round teeth.

For RSVPM, the simulation is done for two types of rotors designed separately and the torque results are reported. The motor design parameters are listed in Table 1.

The parameters shown in the SVPM in Figure 11 are similar to the RSVPM, and only its rotor is toothed. The geometry model of the first simulation of RSVPM is shown in Figure 12 and the rotor teeth are sharp in this simulation.

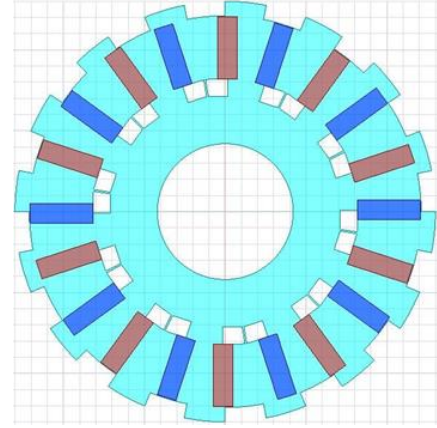


Figure 9. A view of the rotor with sharp teeth in the RSVPM

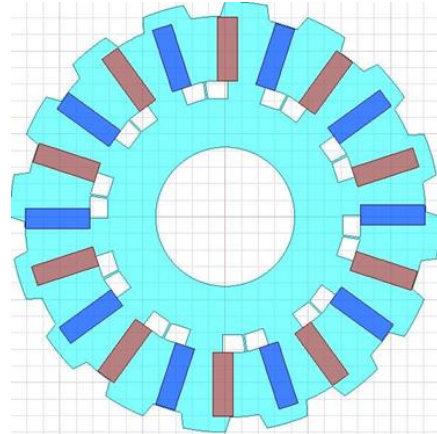


Figure 10. A view of the rotor with round teeth in the RSVPM

TABLE 1. Design Key Dimensions

Parameters	Conventional SVPM [19]	Proposed RSVPM
Stator OD/ID [mm]	355.6/261.7	360/262
Rotor OD/ID [mm]	259.7/133	260/84
D_{cs} [mm]	19.8	19.8
D_{cr} [mm]	13.5	13.5
τ_s [°]	30	30
τ_{pr} [°]	18	18
d_{pm}/w_{pm} [mm]	20.8/38.9	20.8/38.9
d_{bg1}/d_{bg2} [mm]	0.5/0.8	0.5/0.8
d_b/w_b [mm]	14.6/10.4	14.6/10.4
Number of rotor teeth	-	16

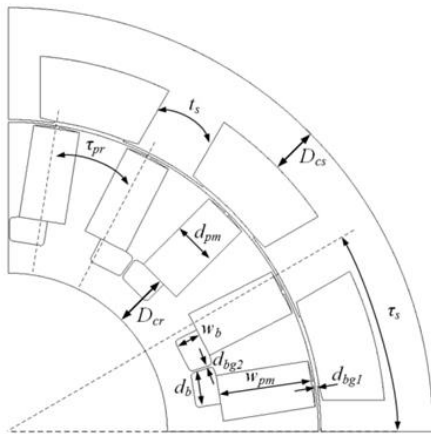


Figure 11. The parameters used in the geometry of the SVPM (19)

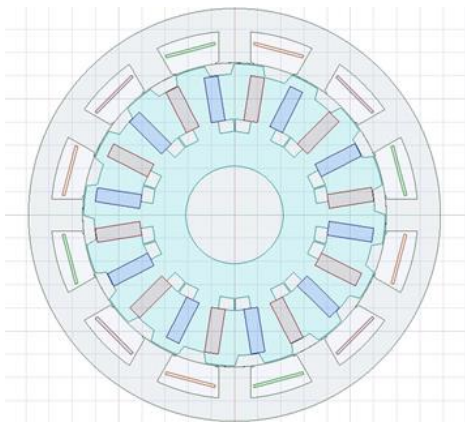


Figure 12. A view of the RSVPM with round teeth

The simulation done by the finite element analysis method is for the round tooth RSVPM. The average motor torque is shown in Figure 13.

The average torque of this motor is 931.8 Nm. Core losses are also shown in Figure 14.

The average loss of the rotor core is 128.31 W. Core losses are higher in conventional SVPM. By analyzing

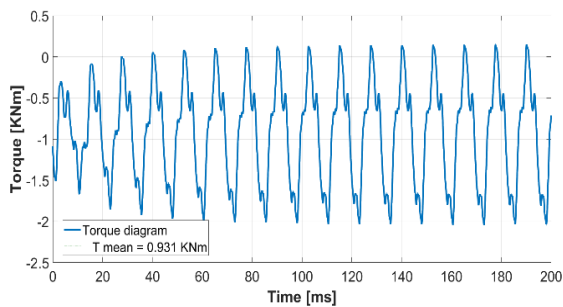


Figure 13. RSVPM torque diagram and the average value of the produced torque with a round-toothed rotor

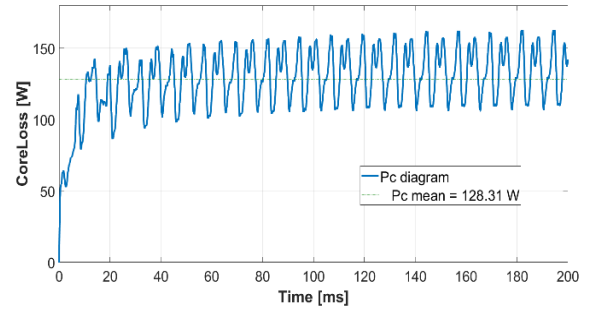


Figure 14. RSVPM core loss diagram with a round-toothed rotor

the simulation and drawing the core loss diagram in Figure 15, the average value of core loss in SVPM is obtained.

The back EMF diagram for three phases of the proposed RSVPM is shown in Figure 16.

The maximum voltage value in phase A is 283.4 V, in phase B is 281.9 V, and in phase c is 282.2 V. The direction of movement of magnetic flux lines and distribution of flux density is shown in Figure 17.

Now the second design is done for RSVPM with sharp teeth. The result of the finite element method for this motor is reported. The average torque produced by this motor is given in Figure 18.

The diagram of core losses in the RSVPM with sharp teeth is shown in Figure 19. It can be seen that the core

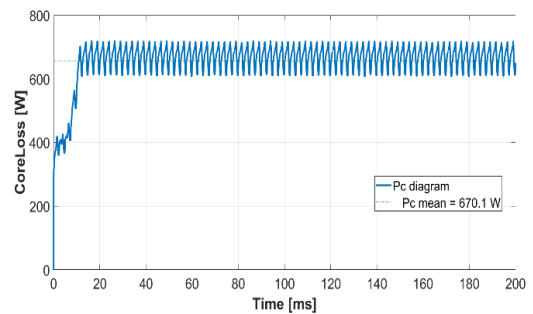


Figure 15. Core losses in conventional SVPM [18]

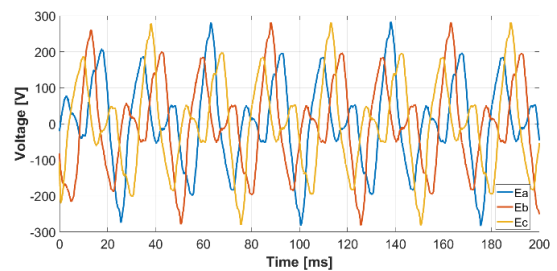
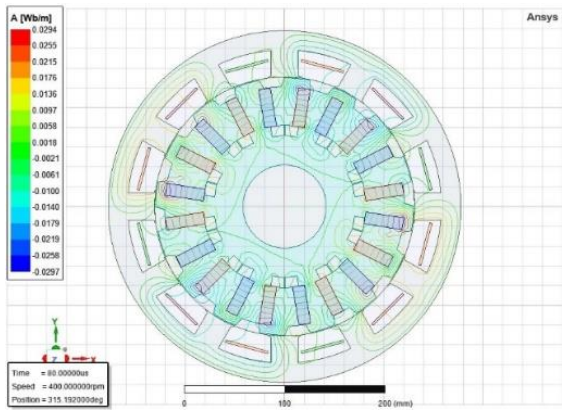
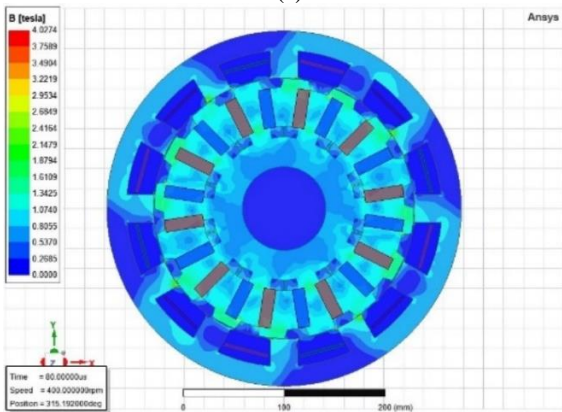


Figure 16. RSVPM back EMF diagram with a round-toothed rotor



(a)



(b)

Figure 17. The RSVPM with round teeth. (a) The path of the flux lines. (b) Distribution of flux density

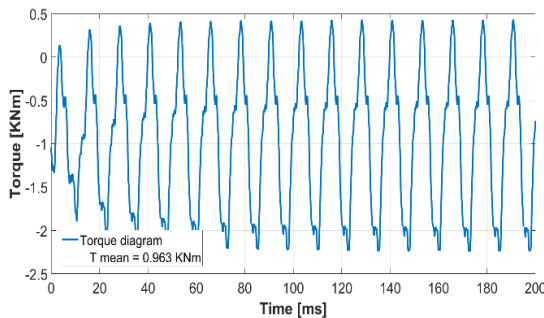


Figure 18. Torque diagram of an RSVPM with sharp teeth

loss in this motor is less than that of conventional SVPM and it is almost the same compared to RSVPM with round teeth. The large difference in core losses between the RSVPM and the conventional SVPM is seen in Figure 20, which are compared to each other.

The path of flux lines in RSVPM with sharp teeth is shown in Figure 21. In Figure 22, the distribution of the magnetic flux density of the motor is also done, which shows that the motor does not reach saturation at any point.

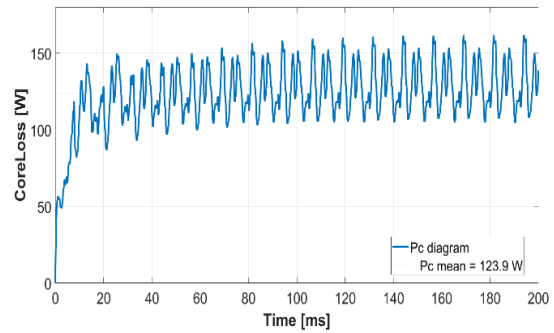


Figure 19. Core losses in RSPVM with sharp teeth

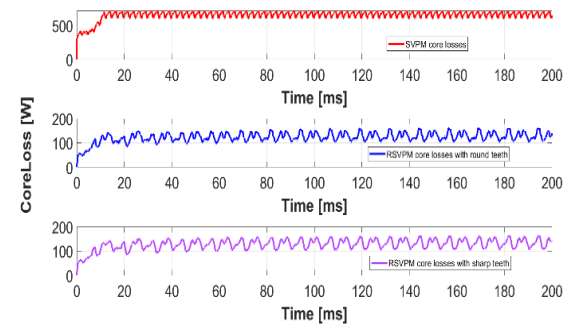


Figure 20. Comparison of core losses of RSVPM and SVPM

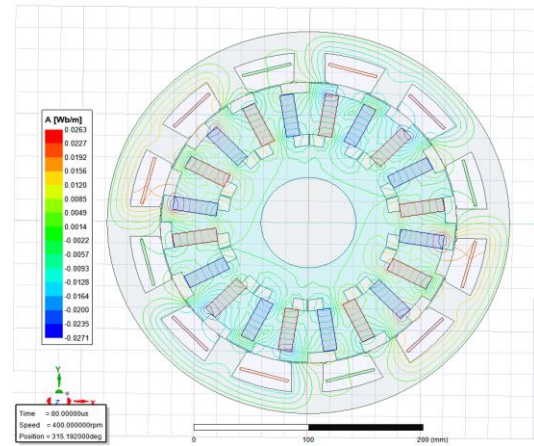


Figure 21. The path of flux lines in RSVPM with sharp teeth

To calculate the power factor, the voltage and current diagrams of the motor are drawn in a coordinate plane (24). The horizontal axis of time is common to both graphs in the coordinate plane. Then, in the selected cycle, the times when the voltage and current become zero are extracted and multiplied by the motor excitation frequency. The angle between voltage and current is calculated using this technique. Then, through the cosine between the angle of voltage and current in that cycle, the power factor of the motor can be calculated. The power

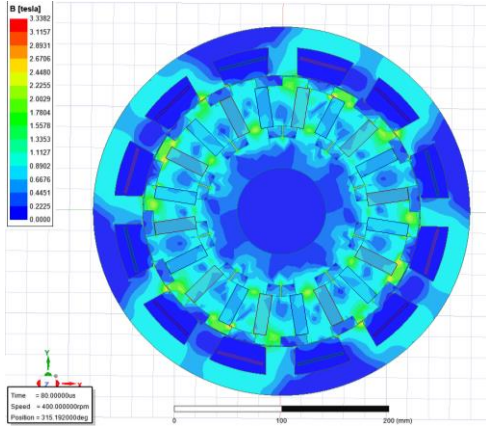


Figure 22. Distribution of flux density in the RSVPM with sharp teeth

factor in conventional SVPM is 0.62. According to Figure 23, which is obtained from the software simulation, it can calculate the value of the power factor for the RSVPM with sharp teeth.

$$\phi_{RSVPM}^{sharp} = \frac{m_1 - m_2}{\frac{1}{f_{ex}}} = \frac{4.9997 - 6.9328}{\frac{1}{66.67}} = -132.1799^\circ$$

$$PF_{RSVPM}^{sharp} = \cos(\phi) = \cos(-132.1799) = -0.6715$$

According to Figure 24, which is obtained from the software simulation, it can calculate the value of the power factor for the RSVPM with round teeth.

$$\phi_{RSVPM}^{round} = \frac{m_1 - m_2}{\frac{1}{f_{ex}}} = \frac{4.9998 - 7.2914}{\frac{1}{66.67}} = -152.7810^\circ$$

$$PF_{RSVPM}^{round} = \cos(\phi) = \cos(-152.7810) = -0.8893$$

To calculate the efficiency, the output power must be calculated. With the help of Equations 18 and 19, the efficiency can be calculated.

$$P_{out} = \frac{T_m \cdot N_m}{9.5488} \quad (18)$$

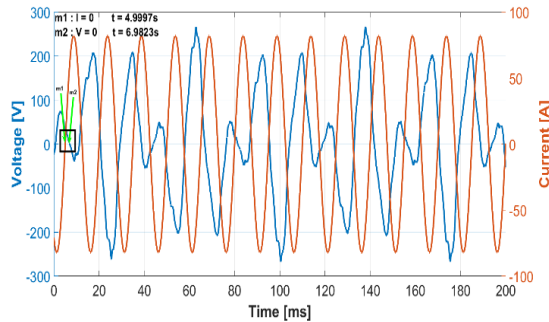


Figure 23. Voltage and current diagram with the common time axis in the RSVPM with sharp teeth

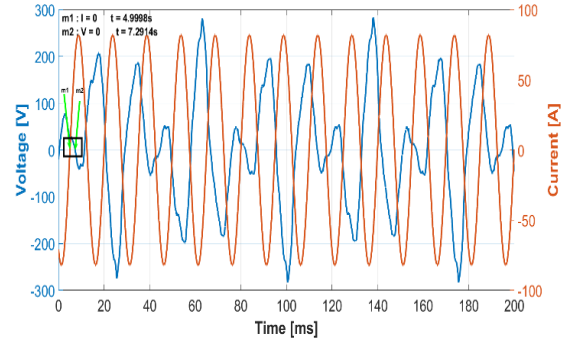


Figure 24. Voltage and current diagram with the common time axis in the RSVPM with round teeth

$$\eta = \frac{P_{out}}{P_{out} + P_{fe} + P_{cu}} \quad (19)$$

where the average torque T_m , the rotor speed N_m , the output power P_{out} , core loss P_{fe} , copper loss P_{cu} and efficiency η . According to the excitation frequency and the number of rotor poles, the rotor speed is 400 rpm. Through the simulations, the values of core loss, copper loss, and average torque have been calculated for sharp tooth and round tooth rotors. Therefore, the amount of return can be calculated for each.

$$P_{out}^{RSVPM_sharp} = \frac{963N.m \times 400rpm}{9.5488} = 40340.147W$$

$$\eta_{RSVPM}^{sharp} = \frac{40340.147}{40340.147 + 123.9 + 979.16} = 0.9734$$

$$P_{out}^{RSVPM_round} = \frac{931N.m \times 400rpm}{9.5488} = 38999.664W$$

$$\eta_{RSVPM}^{round} = \frac{38999.664}{38999.664 + 128.3 + 979.16} = 0.9724$$

According to the calculations, the efficiency in the case of the rotor with round teeth is 97.24%, and in the case of the rotor with sharp teeth 97.34%.

Table 2 shows a comparison between the RSVPM with sharp teeth the RSVPM with round teeth and the conventional SVPM.

TABLE 2. Parameters and Performance Comparison

	Proposed RSVPM with round teeth	Conventional SVPM [18]	Proposed RSVPM with sharp teeth
Machine type	VPM	VPM	VPM
Magnet type	NdFeB/1.2	NdFeB/1.2	NdFeB/1.2

SSP	1	1	1
Stator/rotor pole number	4/20	4/20	4/20
Stator OD [mm]	355.5	360	355.5
Stack length [mm]	311	311	311
Excitation frequency [Hz]	66.67	66.67	66.67
Power factor	0.88	0.62	0.67
Torque [Nm]	931	605	963
Core loss [W]	128.3	671.3	123.9

5. CONCLUSIONS

In this paper, permanent magnet motors were investigated. First, the conventional spoke-type permanent magnet Vernier motor (SVPM) was checked and from the simulation, it was concluded that the average torque produced by this motor is 605 Nm and the core loss of the rotor is 671 watts. Then two types of rotors are designed using the reluctance torque theory, in the first case, the rotor with sharp teeth, and it was observed that in this case, the average torque produced is about 963 Nm, which has improved by about 59% and the core loss of rotor is about 124 watts, which has improved by about 81% compared to the conventional SVPM, and this makes the rotor core cooler while working. This issue can be seen in the monitoring of the magnetic flux density distribution of the motor, In the second case, the rotor with round teeth, it was observed that in this case, the average torque produced is 931 Nm, which is about 53% better compared to the conventional SVPM, and of course compared to the sharp tooth type it has a lower average torque, but the advantage of a round tooth over a sharp tooth is that it has a lower torque ripple. Also, in the round tooth type, the core loss of the rotor is almost 128 watts, which is 81% better compared to the conventional SVPM and it is almost no difference compared to the sharp tooth type. Regarding the power factor, the power factor has increased by 8.06% in RSVPM with sharp-toothed rotors, and the power factor has increased by 41.94% in RSVPM with round-toothed rotors.

6. REFERENCES

- Gherabi Z, Toumi D, Benouzza N, Bendiabdellah A. A proposed approach for separation between short circuit fault, magnetic saturation phenomenon and supply unbalance in permanent magnet synchronous motor. *International Journal of Engineering, Transactions A: Basics.* 2020;33(10):1968-77. [10.5829/IJE.2020.33.10A.15](https://doi.org/10.5829/IJE.2020.33.10A.15)
- Karimpour S, Besmi M, Mirimani S. Multi-objective optimization design and Verification of Interior PMSG Based on Finite Element Analysis and Taguchi method. *International Journal of Engineering, Transactions C: Aspects.* 2021;34(9):2097-106. <https://doi.org/10.5829/IJE.2021.34.09C.07>
- Parivar H, Seyyedbarzegar S, Darabi A. An improvement on slot configuration structure of a low-speed surface-mounted permanent magnet synchronous generator with a wound cable winding. *International Journal of Engineering, Transactions C: Aspects.* 2021;34(9):2045-52. [10.5829/ije.2021.34.09c.01](https://doi.org/10.5829/ije.2021.34.09c.01)
- Patel A, Suthar B. Cogging torque reduction of sandwiched stator axial flux permanent magnet brushless dc motor using magnet notching technique. *International Journal of Engineering, Transactions A: Basics.* 2019;32(7):940-6. [10.5829/ije.2019.32.07a.06](https://doi.org/10.5829/ije.2019.32.07a.06)
- Parivar H, Darabi A. Design and Modeling of a High-Speed Permanent Magnet Synchronous Generator with a Retention Sleeve of Rotor. *International Journal of Engineering, Transactions B: Applications.* 2021;34(11):2433-41. [10.5829/IJE.2021.34.11B.07](https://doi.org/10.5829/IJE.2021.34.11B.07)
- Song N, Zhu M, Zhou G, Guo L, Mu Y, Gao J, et al. Design and optimization of halfbach permanent magnet array with rectangle section and trapezoid section. *International Journal of Engineering, Transactions B: Applications.* 2021;34(11):2379-86. [10.5829/IJE.2021.34.11B.01](https://doi.org/10.5829/IJE.2021.34.11B.01)
- Aghazadeh H, Afjei E, Siadatan A. Comprehensive design procedure and manufacturing of permanent magnet assisted synchronous reluctance motor. *International Journal of Engineering, Transactions C: Aspects.* 2019;32(9):1299-305. <https://doi.org/10.5829/ije.2019.32.09c.10>
- Liu C, Zhong J, Chau K. A novel flux-controllable vernier permanent-magnet machine. *IEEE Transactions on Magnetics.* 2011;47(10):4238-41. <https://doi.org/10.1109/TMAG.2011.2152374>
- Lee C. Vernier motor and its design. *IEEE Transactions on Power Apparatus and Systems.* 1963;82(66):343-9. <https://doi.org/10.1109/TPAS.1963.291362>
- Mukherji K, Tustin A, editors. Vernier reluctance motor. *Proceedings of the Institution of Electrical Engineers;* 1974: IET.
- Ishizaki A, Tanaka T, Takasaki K, Nishikata S, editors. Theory and optimum design of PM Vernier motor. *1995 Seventh International Conference on Electrical Machines and Drives (Conf Publ No 412);* 1995: IET.
- Toba A, Lipo TA, editors. Novel dual-excitation permanent magnet vernier machine. *Conference Record of the 1999 IEEE Industry Applications Conference Thirty-Forth IAS Annual Meeting (Cat No 99CH36370);* 1999: IEEE.
- Toba A, Lipo TA. Generic torque-maximizing design methodology of surface permanent-magnet vernier machine. *IEEE transactions on industry applications.* 2000;36(6):1539-46. <https://doi.org/10.1109/28.887204>
- S. Niu, Ho SL, Fu WN, Wang LL. Quantitative Comparison of Novel Vernier Permanent Magnet Machines. *IEEE Transactions on Magnetics.* 2010;46:2032-5. <https://doi.org/10.1109/28.887204>
- Arish N, Teymoori V. Development of linear vernier hybrid permanent magnet machine for wave energy converter. *International Journal of Engineering, Transactions B: Applications.* 2020;33(5):805-13. <https://doi.org/10.5829/ije.2020.33.05b.12>
- Li D, Qu R, Lipo TA. High-power-factor vernier permanent-magnet machines. *IEEE transactions on industry applications.* 2014;50(6):3664-74. <https://doi.org/10.1109/TIA.2014.2315443>

17. Kim B, Lipo TA. Analysis of a PM vernier motor with spoke structure. *IEEE Transactions on Industry Applications*. 2015;52(1):217-25. <https://doi.org/10.1109/TIA.2015.2477798>
18. Du ZS, Lipo TA, editors. High torque density ferrite permanent magnet vernier motor analysis and design with demagnetization consideration. 2015 IEEE Energy Conversion Congress and Exposition (ECCE); 2015: IEEE.
19. Liu W, Lipo TA, editors. A family of vernier permanent magnet machines utilizing an alternating rotor leakage flux blocking design. 2017 IEEE energy conversion congress and exposition (ECCE); 2017: IEEE.
20. Liu W, Lipo TA, editors. Alternating flux barrier design of vernier ferrite magnet machine having high torque density. 2017 IEEE electric ship technologies symposium (ESTS); 2017: IEEE.
21. Siadatan A, Ghasemi S, Shamsabad Farahani S. Design and Construction of a Sensorless Circuit for Brushless DC Motor using Third Harmonic back Electromotive Force. *International Journal of Engineering, Transactions A: Basics*. 2017;30(4):500-6. 10.5829/idosi.ije.2017.30.04a.07
22. Arish N, Yaghoobi H. Analysis of a New Linear Dual Stator Consequent Pole Halbach Array Flux Reversal Machine. *International Journal of Engineering, Transactions B: Applications*. 2021;34(8):2002-9. 10.5829/ije.2021.34.08b.21
23. Ardestani M, Arish N, Yaghoobi H. A new HTS dual stator linear permanent magnet Vernier machine with Halbach array for wave energy conversion. *Physica C: Superconductivity and its Applications*. 2020;569:1353593. 10.1016/j.physc.2019.1353593
24. Xu L, Zhao W, Liu G, Song C. Design optimization of a spoke-type permanent-magnet vernier machine for torque density and power factor improvement. *IEEE Transactions on Vehicular Technology*. 2019;68(4):3446-56. <https://doi.org/10.1109/TVT.2019.2902729>

COPYRIGHTS

©2024 The author(s). This is an open access article distributed under the terms of the Creative Commons Attribution (CC BY 4.0), which permits unrestricted use, distribution, and reproduction in any medium, as long as the original authors and source are cited. No permission is required from the authors or the publishers.

**Persian Abstract****چکیده**

منابع انرژی متعارف مانند سوخت های فسیلی به دلیل محدودیت ها و اثرات زیست محیطی دیگر قابل دوام نیستند. تقاضا برای راه حل های انرژی پاک تر و کارآمدتر منجر به توسعه ماشین های الکتریکی با حجم کمتر و خروجی بیشتر شده است. خانواده موتورهای ورنیه آهنربای دائمی دارای گشتاور خروجی بالا در سرعت های بسیار کم هستند در حالی که حجم بسیار کمی دارند. تنوری گشتاور رلوکتانسی همراه با گشتاور خروجی معمولی موتور، گشتاور نهایی موتور را افزایش می دهد. علاوه بر این، دندانه دار شدن روتور باعث کاهش سطح مقطع و وزن روتور می شود. با کاهش سطح مقطع، جریان های گردابی در هسته کاهش می یابد، ضریب قدرت افزایش می یابد و راندمان موتور بهبود می یابد. از این رو در این مقاله موتور ورنیه آهنربای دائم اسپوک با روتوری مشابه روتور رلوکتانسی طراحی شده است که در مقایسه با موتورهای ورنیه آهنربای دائمی معمولی دارای گشتاور بیشتر، تلفات کمتر و ضریب توان بالاتر است.



Framework of Electric Vehicle Fault Diagnosis System Based on Diagnostic Communication

X. Yang*

Automobile & Rail Transportation School, Tianjin Sino-German University of Applied Sciences, Tianjin, China

PAPER INFO

Paper history:

Received 02 Novembr 2023
 Received in revised 06 December 2023
 Accepted 24 December 2023

Keywords:

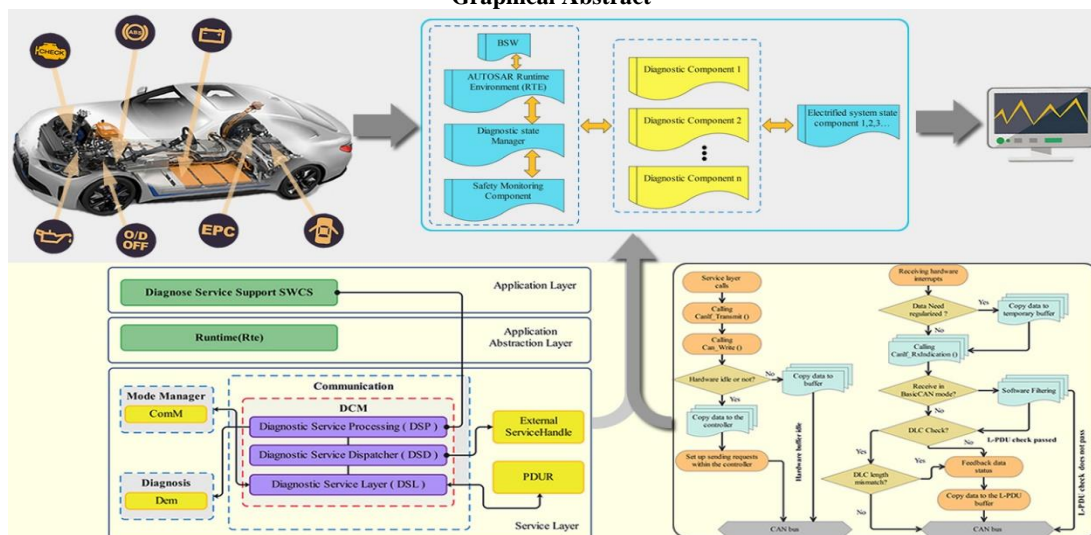
Electric Vehicle
 AUTOSAR
 Fault Diagnosis
 Fusion

A B S T R A C T

With the escalating integration of Electronic Control Units (ECUs) in contemporary vehicles, the intricacy of vehicle networks is incessantly advancing. Diagnostic communication, as a pivotal facet within these networks, grapples with protracted development cycles and heightened intricacies. In a bid to augment software reusability and portability, this study meticulously scrutinized pertinent research and proffered an electric vehicle fault diagnosis system predicated on the Controller Area Network (CAN) bus, leveraging the diagnostic communication architecture advocated by the AUTOSAR standard. The integration of AUTOSAR seeks to pioneer an innovative software development paradigm for automotive fault diagnosis systems, thereby remedying extant limitations. The communication and diagnostic module of this study were instantiated using AUTOSAR, thereby obviating the necessity for developers to immerse themselves in hardware intricacies and communication implementations. This allows developers to focalize their efforts on crafting software features for fault diagnosis. Empirical results illustrate that the single-core CPU utilization rate of the proposed method in this article stands at 40.68%, with a fault detection time of 0.0217. The success rate of fault detection is 98.70%, indicating an increase of 12.97% and 8.98% when compared to the CAN bus and structural analysis methods, respectively. Testing indicators are significantly mitigated, yielding more precise fault detection outcomes. The exploration of this avant-garde software development methodology in automotive electronic products markedly amplifies the efficiency of automotive troubleshooting system software, underscoring its potential for academic contribution and application in real-world scenarios.

doi: 10.5829/ije.2024.37.06c.16

Graphical Abstract



*Corresponding Author Email: yangxiaogang@tsguas.edu.cn (X. Yang)

1. INTRODUCTION

Approximately 70% of the time spent in the maintenance process of traditional cars is devoted to fault identification, with the remaining 30% allocated to troubleshooting. In comparison to conventional vehicles, the electrical system of pure electric vehicles is more intricate and electronic in nature. It encompasses several subsystems, such as the vehicle, drive motor, battery management, high-voltage electrical safety, instrument panel control, auxiliary power system, air conditioning, power steering, and electronic brakes. Each subsystem carries out its functions through its dedicated Electronic Control Unit (ECU), and communication between ECUs is facilitated through the Controller Area Network (CAN) bus network, ensuring the coordinated operation of the entire vehicle (1-3).

Gholami and Sanjari (4) designed a real-time fault diagnosis system for pure electric vehicles. This system can promptly identify potential faults and implement appropriate strategies to ensure the safe and reliable operation of vehicles. Bhosale and Mastud (5) developed a fault diagnosis system for pure electric vehicles based on the CAN bus. They completed the design of a fault diagnosis instrument for pure electric vehicles and tested the fault diagnosis system with CANoe software. Ahmadigorji and Mehrasa (6) used the structural analysis method to establish a fault diagnosis system for the power system of pure electric vehicles. Jian et al. (7) established diagnosis rules and constructed the corresponding fault tree based on the study of fault diagnosis technology for pure electric vehicles. Subsequently, a set of expert fault diagnosis system models was designed using WPF software language to enhance fault diagnosis efficiency and compensate for the lack of technical expertise among after-sales personnel. Ochando et al. (8) developed a pure electric vehicle status monitoring and fault diagnosis system based on the onboard CAN network. They utilized LabVIEW and Kvaser USBcan communication card to achieve real-time monitoring of the status and fault information of pure electric vehicles during operation. Faults were analyzed based on monitored status and specific fault phenomena when encountered, leading to effective solutions. Wang (9) studied the fault diagnosis of the distributed control system of electric vehicles based on the CAN bus. This involved discussions on fault diagnosis modes, fault monitoring and diagnosis methods, and the coding method of fault codes (DTC) and fault information for electric vehicles, representing a valuable exploration into the in-depth study of electric vehicle fault diagnosis based on the CAN bus.

As the integration of Electronic Control Units (ECUs) with modern vehicles continues to rise, the complexity of the entire vehicle network is increasing. As a critical function within the onboard network, the development

cycle and difficulty of diagnostic communication are escalating. To enhance software reuse and portability, this paper develops an electric vehicle fault diagnosis system based on the CAN bus, incorporating the diagnostic communication architecture recommended by the AUTOSAR standard through an analysis of relevant research.

2. INTRODUCTION TO RELATED THEORIES

2. 1. AUTOSAR Architecture Haur (10) endeavored to implement crucial functions within an automotive electronic software system, with the objective of standardizing functional interfaces. This standardization facilitates the seamless integration and effective reuse of software modules, thereby enhancing the efficiency of software updates and development processes. To achieve this, the software architecture is structured into three layers: the application layer, the run-time environment layer, and the base software layer. This hierarchical and modular approach aligns with contemporary software development and design philosophy (11), as illustrated in Figure 1.

2. 1. 1. Application Layer The application architecture of AUTOSAR comprises interconnected software components (SWCs) linked through a virtual function bus. Each SWC incorporates one or more ports, and these SWCs establish connections through these ports. Within the SWCs, running entities (REs) represent the smallest code fragments, eventually mapped to specific operating system (OS) tasks and scheduled by the OS to execute corresponding functions (12).

To facilitate system integration, AUTOSAR introduces the Virtual Function Bus (VFB) (13). The VFB enables the design of application software without direct dependence on the underlying hardware and communication mechanisms. SWCs communicate through ports, interacting with hardware resources via the VFB. This design choice renders the application layer software implementation independent of the specific hardware, thereby significantly enhancing the portability of the application software.

2. 1. 2. RTE Layer At the core of the AUTOSAR architecture lies the Run-time Environment (RTE), serving as a tangible realization of the Virtual Function Bus (VFB). The RTE plays a pivotal role by mapping Running Entities (REs) within all Software Components (SWCs) on the local Electronic Control Unit (ECU) to tasks in the operating system (OS). It is responsible for establishing communication among these REs. In cases where REs are mapped to different ECUs, the RTE takes on the responsibility of facilitating communication between them.

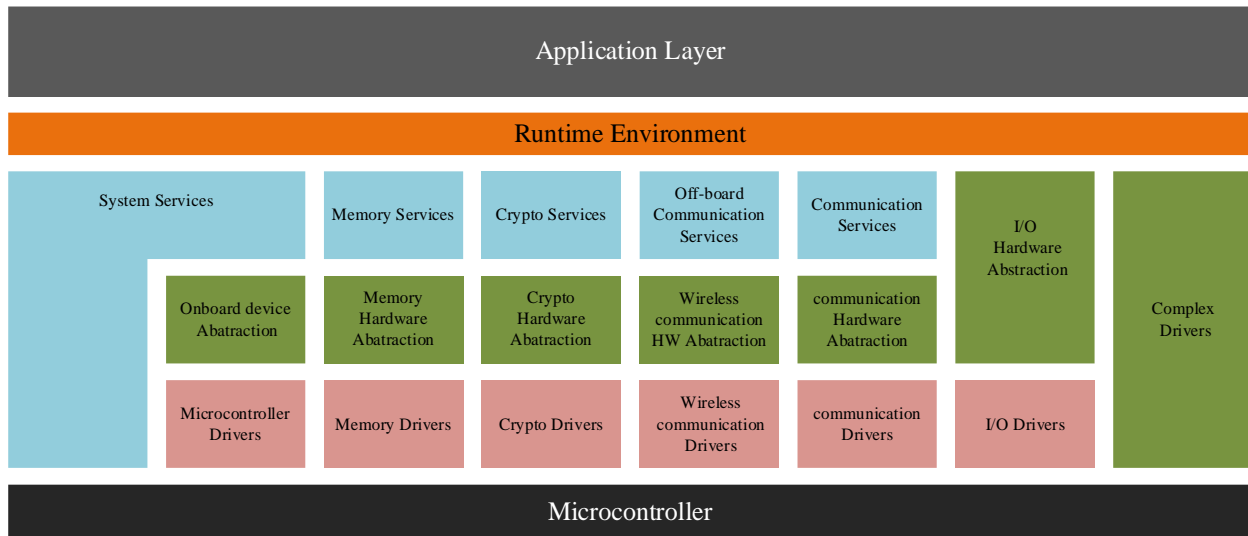


Figure 1. AUTOSAR architecture

Furthermore, the RTE is instrumental in implementing the segregation between application and base software. It provides communication services between SWCs in the application layer and acts as a conduit for communication within single ECU systems or across multi-ECU systems (14). The RTE defines interfaces for data communication between application layer SWCs and the underlying software modules. This includes standardizing interfaces for input/output (I/O), storage, and other fundamental accesses, thus ensuring the application's independence from underlying hardware characteristics.

2. 1. 3. Base Software Layer The base software layer serves as a crucial foundation, delivering essential services to the application layer's software components. These services encompass a spectrum of functionalities, including underlying hardware drivers, bus and network communication, real-time task scheduling, vehicle troubleshooting, and other foundational services. Comprising approximately 80 base software modules, this layer is organized into the microcontroller abstraction layer, ECU abstraction layer, service layer, and complex driver layer, following a bottom-up hierarchy.

The microcontroller abstraction layer, ECU abstraction layer, service layer, and complex driver layer collectively enable applications to access microcontroller hardware resources directly. This access is facilitated through the complex driver layer, allowing the implementation of intricate sensor and controller operations, such as fuel injection, ignition control, and other specific and complex functions. The complex driver layer is particularly valuable for implementing hardware resources not supported by AUTOSAR or not

standardized, while ensuring compliance with real-time requirements for specific operations (15).

2. 2. AUTOSAR Diagnostic Functions The diagnostic-related modules within the AUTOSAR automotive electronics software architecture are depicted in Figure 2.

The Function Inhibition Manager (FIM) module plays a pivotal role in enabling or disabling functional entities within the software component based on event statuses reported by the Diagnostic Event Manager (DEM). The Diagnostic Communication Manager (DCM) and DEM serve as core modules responsible for implementing the diagnostic functions inherent in AUTOSAR. As of the current version, AUTOSAR version 3.1 diagnostics encompass a comprehensive suite of 9 On-Board Diagnostics (OBD) services.

2. 3. Multi-sensor Information Fusion

2. 3. 1. Multi-sensor Information Fusion Concept Multi-sensor fusion, commonly known as data fusion, involves amalgamating pertinent information gathered by various environmental sensing sensors installed on an innovative electric vehicle. The synthesis of information detected by multiple sensors, when combined and complemented, addresses the limitations of individual sensors under external influences. This collaborative approach mitigates the risk of decision errors and enhances overall recognition capabilities (16–19).

The integration of information data and the location of fusion delineate three distinct levels from low to high abstraction: the data layer (sensor-level data fusion), feature layer (central-level data fusion), and decision layer (hybrid data fusion).

(1) Data Layer Fusion

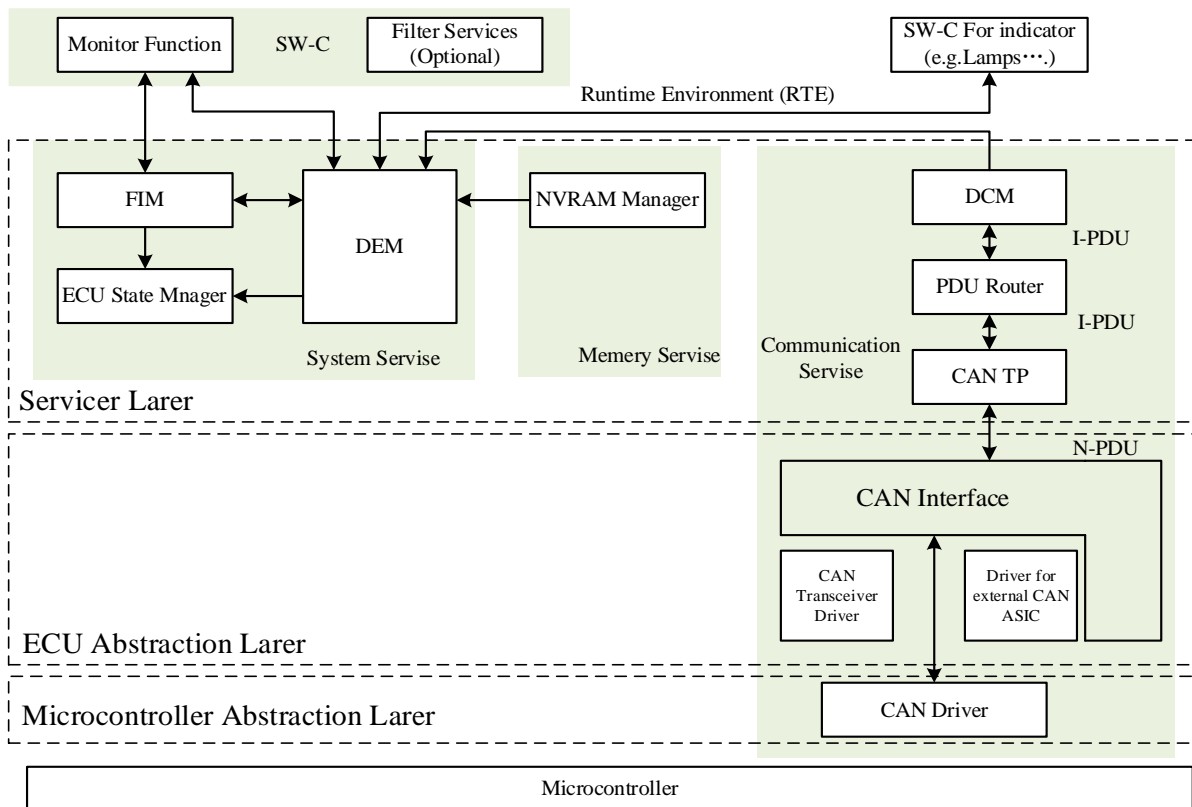


Figure 2. AUTOSAR Diagnostic functions

At the lowest fusion level, known as data layer fusion, raw data is directly transmitted to the fusion center without undergoing any preliminary processing or analysis. The process of data layer fusion is illustrated in Figure 3.

This fusion level, while minimizing original data loss, is characterized by extensive redundant data processing, resulting in compromised real-time robustness and interference resistance.

(2) Feature Layer Fusion

Feature layer fusion involves extracting target features, such as boundary, distance, velocity, size, orientation, and angle, through simple filtering. Subsequently, the collected data undergoes classification and analysis to eliminate invalid information before the actual data fusion process. The feature layer fusion process is depicted in Figure 4.

This fusion level necessitates preliminary data processing, involving the compression of raw data information to ensure effective real-time processing. However, this approach may introduce the potential loss of critical raw data, leading to biases in the fusion results (20).

(3) Decision-Level Integration

Decision-level fusion entails the amalgamation of local decisions made by sensors through a mid-level

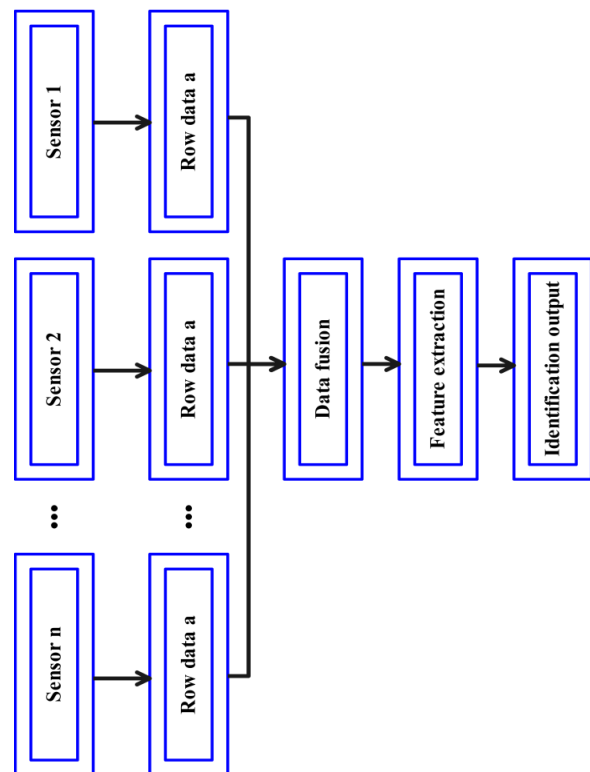


Figure 3. Data layer fusion process

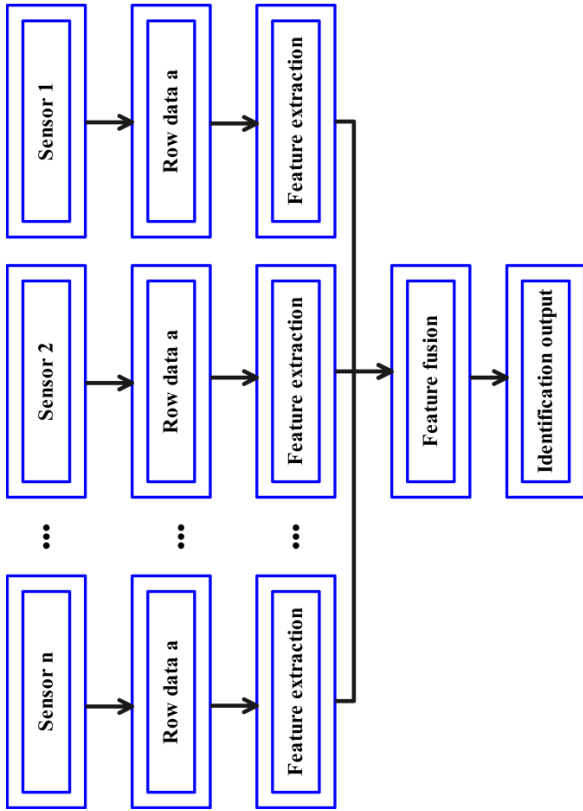


Figure 4. Feature layer fusion process

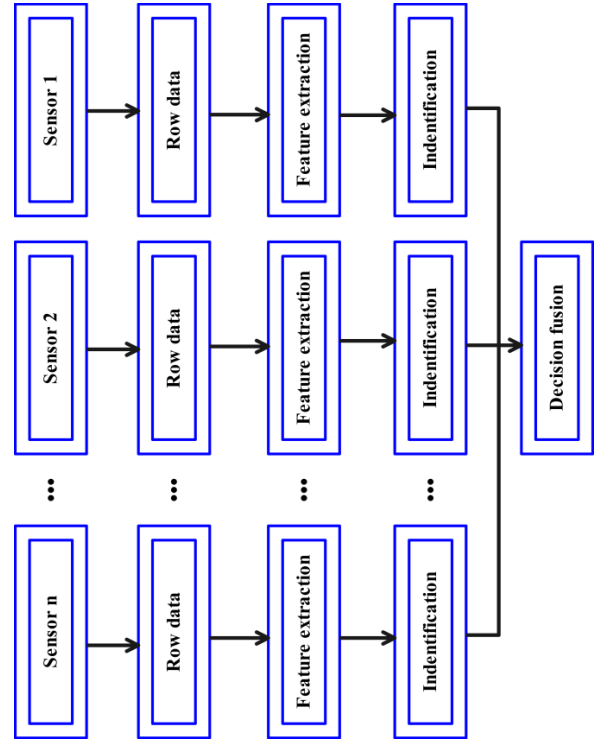


Figure 5. Decision-level integration process

fusion processor. This occurs subsequent to the pre-processing of collected data for tasks such as classification, identification, and decision-making. The decision layer fusion process is illustrated in Figure 5. Since the fusion process is not directly involved in system decision-making, it guarantees flexibility in fusion and robust anti-interference capabilities. Even if certain sensor functions experience failure, it does not result in significant errors in the fusion results. However, the trade-off is that the pre-processing of data becomes more intricate, thereby increasing the processing difficulty.

2. 3. 2. Methods for Multi-sensor Information Fusion

The algorithm for information fusion in electric vehicles, leveraging multiple sensors, incorporates a range of techniques, including weighted average, Kalman filter, Bayesian estimation, D-S evidence theory, fuzzy logic inference, and artificial neural network (21-23). In this paper, the approach employed is the weighted average method.

Let the target data acquired by multiple sensors be denoted as a_1, a_2, \dots, a_n , with variances $\sigma_1^2, \sigma_2^2, \dots, \sigma_n^2$, t and the corresponding weights of each sensor as l_1, l_2, \dots, l_n . After fusion, the resulting state data is:

$$\tilde{x} = l_1 a_1 + l_2 a_2 + \dots + l_n a_n = \sum_{i=1}^{i=n} l_i a_i \tag{1}$$

The weighting conditions are defined as follows:

$$\sum_{i=1}^{i=n} l_i = 1 \tag{2}$$

If each sensor weight is equally distributed, with equal weights denoted as $l = \frac{1}{n}$, then the fused data can be expressed as:

$$\tilde{x} = \sum_{i=1}^{i=n} l_i a_i = \frac{1}{n} \sum_{i=1}^{i=n} a_i \tag{3}$$

The total variance after fusion is given by:

$$\sigma^2 = E[(a - \tilde{x})^2] = E\left[\sum_{i=1}^{i=n} l_i (a - a_i)\right]^2 \tag{4}$$

$$E[(a - a_i)(a - a_j)] = 0(i, j = 1, 2, 3, \dots, n, i \neq j) \tag{5}$$

The total variance of the weighted average fusion algorithm is calculated as follows:

$$\sigma^2 = \frac{\sum_{i=1}^{i=n} \sigma_i^2}{n^2} \tag{6}$$

3. DESIGN AND IMPLEMENTATION OF COMMUNICATION DIAGNOSIS MODULE

3. 1. Design for Information Fusion Information fusion technology integrates processed multi-sensor

information to delineate specific characteristics of the external environment or the object under observation. In modern society, sensors play a fundamental role, serving as essential tools for monitoring the surrounding environment. They provide a tangible representation of the world to human perception and contribute significantly to technological progress. As depicted in Figure 6, the information fusion process in this paper unfolds in four distinct steps:

(1) Acquisition of Experimental Data: Data is collected in various scenarios, and the raw sensor data obtained is segmented into samples and labeled. These data serve as the foundation for the information fusion process.

(2) Extraction of Features: Feature extraction is conducted separately on the data, yielding features that constitute the feature layer for information fusion.

(3) Training the Respective Recognition Models: The features from the feature layer undergo training using various machine learning algorithms, resulting in the creation of recognition models and their respective decision results.

(4) Decision Layer Fusion: The decision results obtained in the third step are amalgamated using a designed fusion method, ultimately yielding the final recognition result.

3. 2. Design of AUTOSAR Communication Module

The design and implementation flow of the AUTOSAR communication module is depicted in Figure 7.

Firstly, through a comprehensive study of the AUTOSAR communication module standard, the entire file structure of the communication module is designed to capture the overarching design process from a macro perspective.

Secondly, the module undergoes configuration based on the AUTOSAR methodology. The configuration set is acquired by visually representing the module configuration using the self-developed ECU configuration tool, ReDe (24, 25).

Next, the data structure and standard function interfaces of the communication driver and interface layers are implemented in accordance with the specification.

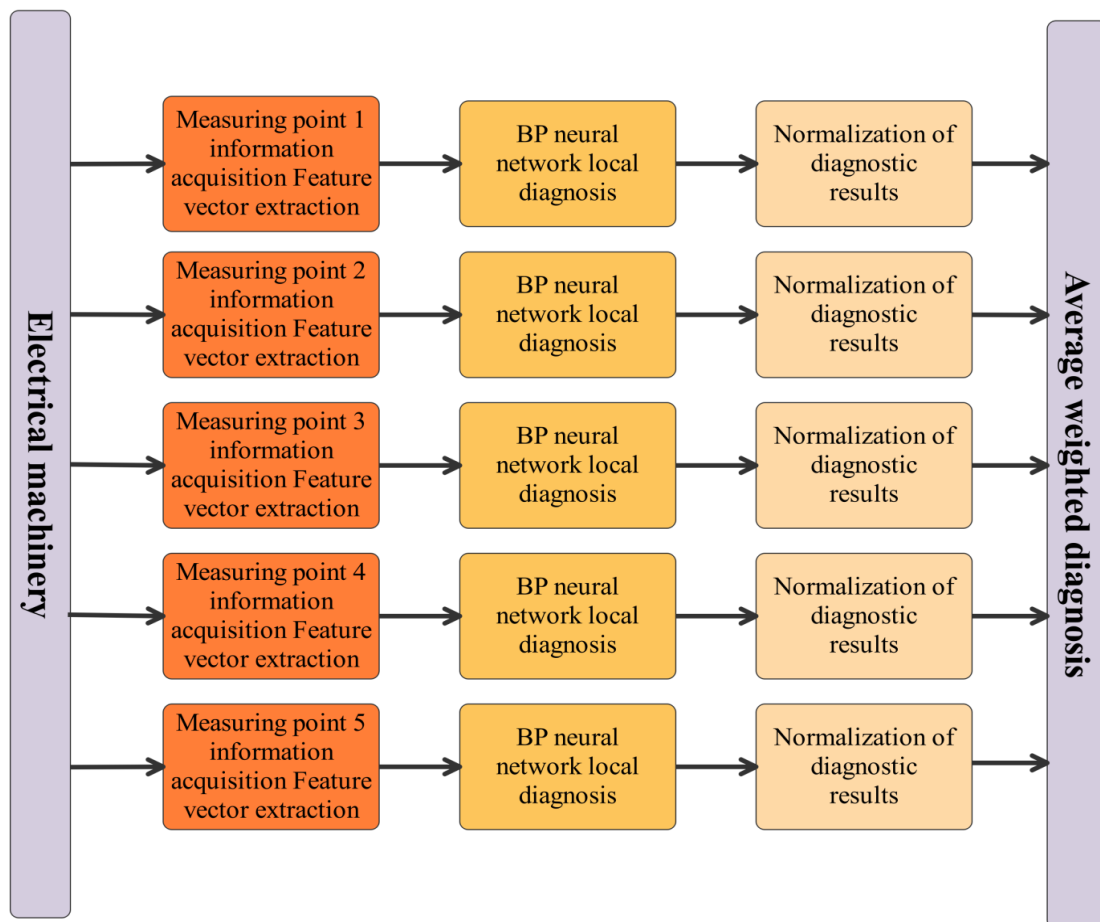


Figure 6. Information Fusion

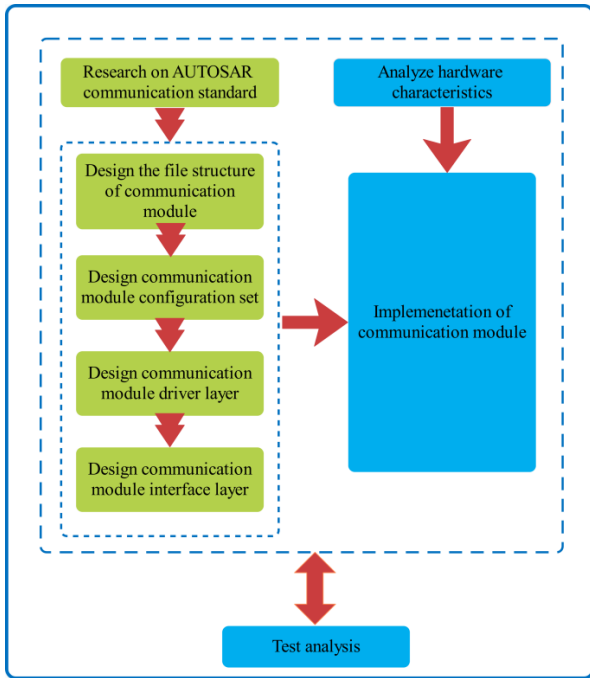


Figure 7. Design of AUTOSAR communication module

Finally, the complete AUTOSAR communication module is implemented in conjunction with the hardware ECU characteristics. To ensure the reliability and reusability of the module, thorough testing and analysis are conducted post-implementation to identify and rectify any errors that may have occurred throughout the entire design and implementation process.

3. 2. 1. AUTOSAR Communication Module File Structure

Given the extensive and intricate nature of the AUTOSAR software architecture, we illustrate the communication system using the CAN bus as an exemplary case. The CAN bus stands out as a highly prevalent Fieldbus in the automotive domain and is widely adopted in current vehicle communication systems. Notably, it serves as the primary Fieldbus for European and American models, which constitute a substantial portion of the vehicle fleet in China. As a result, the CAN bus is ubiquitously employed in virtually all bus technology-equipped models in China (26, 27). In Figure 8, the file structure is presented, meticulously designed in accordance with the AUTOSAR communication specification.

3. 2. 2. Communication Module File Structure

The communication driver layer provides a 'Can.h' header file encompassing the definitions of the CAN module API, incorporating variables, global data, and types meant exclusively for internal use by the CAN driver. Simultaneously, the CAN layer furnishes 'Can_Cfg.h' to house configuration parameter information necessary during the pre-compilation phase. The specific services are then implemented in 'Can.c' (28).

Concurrently, the communication interface layer contributes the 'CanIf.h' header file, featuring external variables, global parameters, and services outlined in the specification. These elements are declared in 'CanIf.c' and are restricted to internal usage within the CanIf layer. 'Can_GeneralTypes.h' defines the general data structures

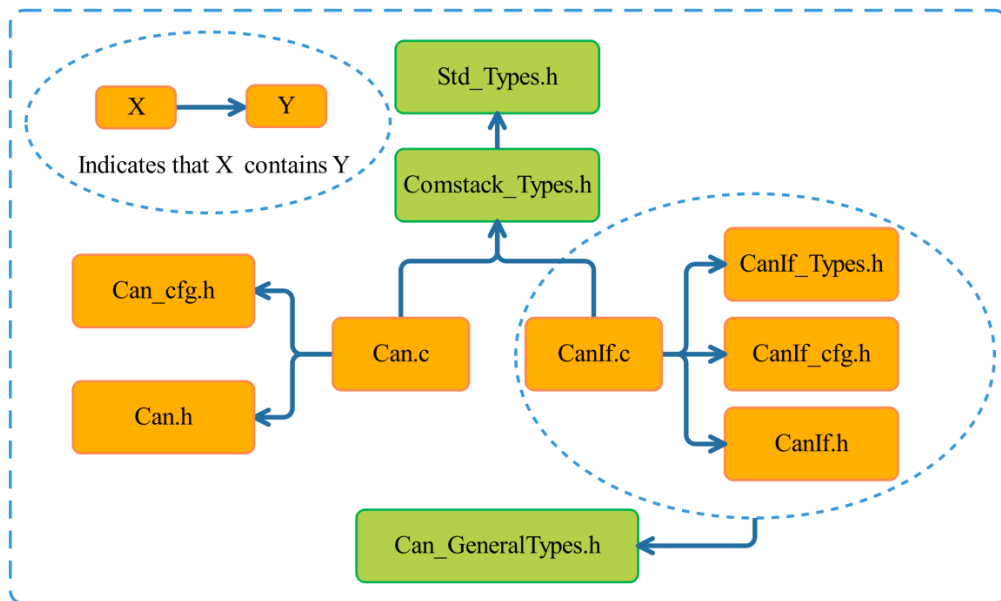


Figure 8. File structure designed for AUTOSAR communication specifications

of the Can driver layer, utilized by the CanIf layer (29, 30). Additionally, 'ComStack_Types.h' encapsulates the definitions of communication-related types, while 'std_Types.h' contains standard type definitions for AUTOSAR.

Upon the incorporation of a communication service module, the headers of each service are added to both the driver and interface layers. The file structure of the communication module is visually represented in Figure 9.

The data sending and receiving process is illustrated in Figure 10. During the transmission, the interface layer assumes the responsibility of assembling data from the upper layers into CAN protocol layer data units, adhering to the CAN specification format. It then invokes 'CanIf_Transmit()' and transfers this data frame to the driver layer. Subsequently, the driver layer employs 'Can_Write()' to initiate the transfer request from the controller. In cases where no hardware object is available, the request is buffered and transmitted once the hardware becomes available. Upon successful transmission, a transmission success confirmation is dispatched to the upper layer module as a callback function, signifying a successful transmission action when received by the sender.

On the reception end, the driver layer reads data from the bus through polling or interrupt mechanisms. Following data regularization, it invokes 'CanIf_RxIndication()' to signal the arrival of the data to the interface layer. The interface layer, upon receiving the CAN data frame from the driver layer, validates and filters the Data Length Code (DLC). After extracting pertinent information, the interface layer communicates the reception event to the corresponding module in the

upper communication service layer via 'user_RxIndication()'. If an error is detected during reception, the corresponding processing function is invoked. Additionally, the indication of the data arrival to the upper layer is halted.

3. 3. Design of AUTOSAR diagnostic module The Diagnostic Event Manager (DEM) module, in collaboration with the Software Component (SWC), undertakes the diagnosis of an event within the AUTOSAR system. Upon a change in the event status, the DEM is responsible for notifying the relevant SWC indicator module and various software modules. This notification allows for the display or handling of the detected fault. Additionally, the DEM enables other modules to query and modify the event's status at any given time.

Within the DEM, a counter records the judgment result, with a minimum value of -128 and a maximum value of 127. Upon receiving a message marked as 'PREPASSED,' the counter is decremented by one step. When the counter reaches a predefined threshold value, the event is deemed to be a fault. Following the diagnosis of a fault, the DEM generates a Diagnostic Trouble Code (DTC) based on the collected information and relevant criteria. This DTC provides valuable information about the detected fault.

The AUTOSAR diagnostic process is visually represented in Figure 11.

After diagnosing a fault, the Diagnostic Event Manager (DEM) calls the relevant Non-Volatile Random Access Memory (NVRAM) interface to store data. Events may involve storing various data types, broadly categorized as FreezeFrame and Extended Data Record.

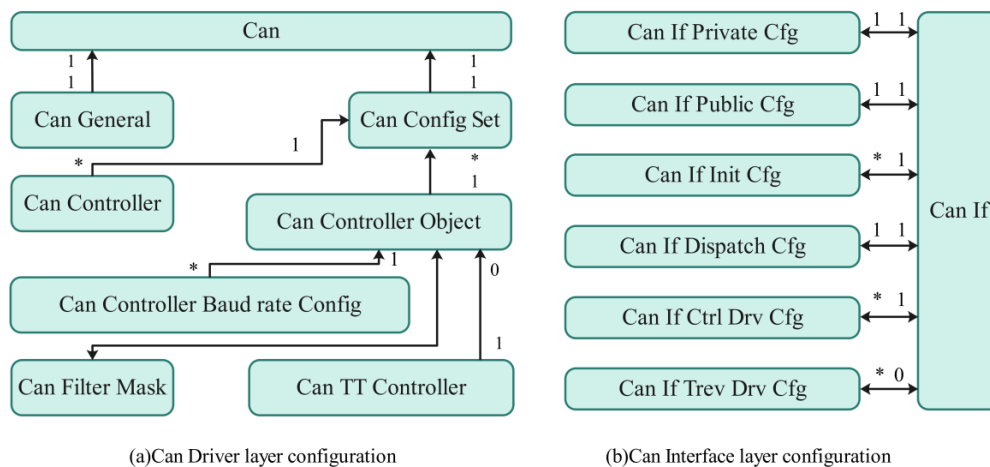


Figure 9. Can driver and interface layer configuration

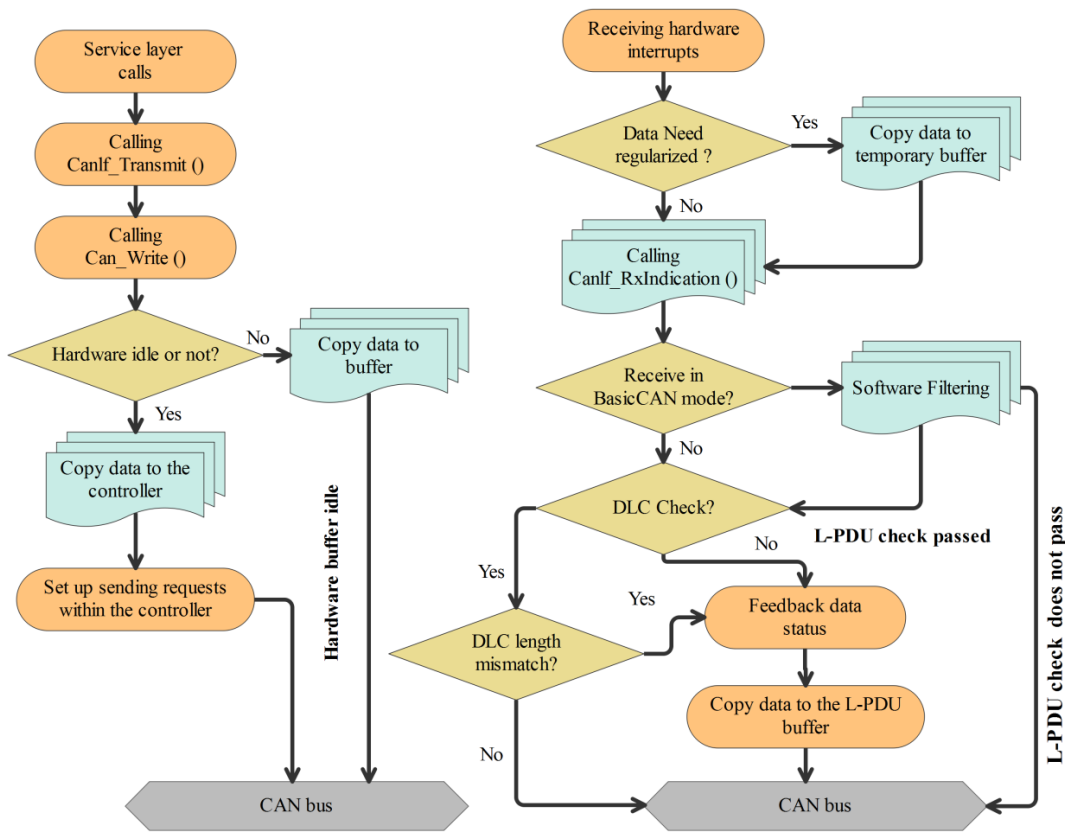


Figure 10. Flow chart for sending and receiving data

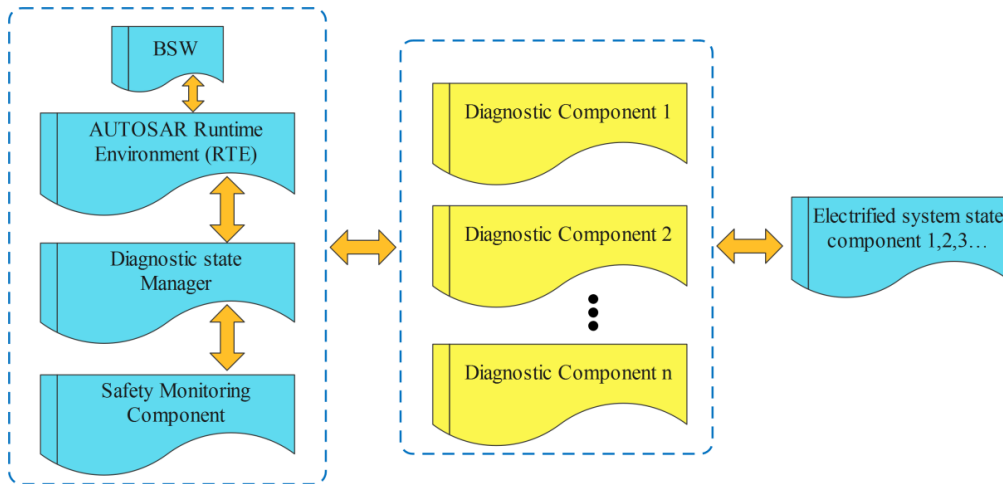


Figure 11. ASW for Electric Vehicle Diagnostic System

FreezeFrame captures information about the environment and data at the time of the fault, while Extended Data Record includes information from software modules, such as frequency clock data. Due to the possibility of multiple data collection instances, there can be more than one FreezeFrame for a single event. The continuity of time-related data may be influenced by different sources and storage times.

In the diagnostic service processing, the Diagnostic Communication Manager (DCM) module follows a defined flow illustrated in Figure 12. Three sub-modules, namely DSL, DSD, and DSP, are developed within the DCM module to meet specific requirements. DSL interacts directly with the Protocol Data Unit Router (PduR), facilitating the reception and transmission of service response messages to fulfill service requests.

Upon receiving a DiagnosticSessionControl (0x10) service, DSL switches the diagnostic session mode, providing timing parameters such as the time interval for the requesting party to receive the service response message (P2CAN_Client). This interval sets the timeout mechanism of the application layer in the current session mode. When receiving a SecurityAccess (0x27) service, DSL returns the seed, verifies the received key, and decides whether to grant security access. DSL resets the session timeout timer, maintaining the current session mode without forwarding the service to the Diagnostic Service Dispatcher (DSD) for further processing.

DSD, the second module, verifies the validity of the service request message, checking supported services, session modes, security rights, and ECU status. If the message is valid, DSD routes the request to the Diagnostic Service Processor (DSP) module for execution. DSP, the third module, executes the precise service request operation. For tasks like reading or clearing fault information, DSP accesses the DEM

module. For data upload/download or reading data streams, DSP accesses the memory stack. For input and output control requests, DSP uses DCM_Send/ReceiveSignal() to interact with the Runtime Environment (RTE) and access the Software Component (SWC).

4. TROUBLESHOOTING TESTS

To validate the accuracy of the fault determination in the diagnostic system and assess the system's configurability, this paper conducts tests on several commonly used services, as outlined in Table 1.

The Diagnostic Trouble Code (DTC) serves as an identification code presented when a fault occurs or is detected in an Electronic Control Unit (ECU). The fault information corresponding to the DTC can be retrieved by referencing a lookup table. A DTC comprises two parts: DTC Category and Failure Type. The DTC

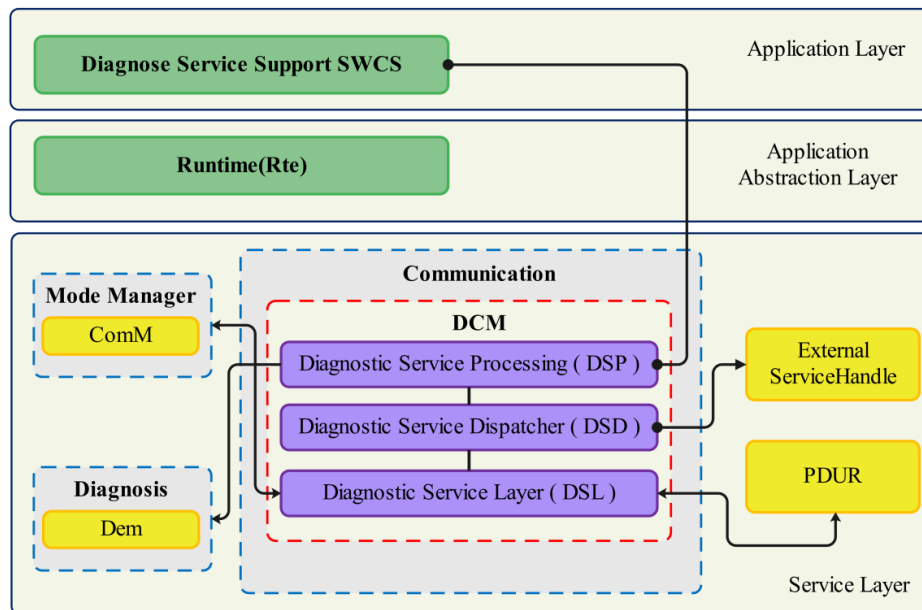


Figure 12. DCM flow chart

TABLE 1. Diagnostic Services

Service ID	Service name
0X10	Diagnostic session control
0x27	Secure access control
0x22	Read data according to the data identifier
0x2E	Write data according to the data identifier
0x19	Read DTC according to the status mask
0x14	Clear DTC

Category can be further categorized into four subsystems: Powertrain, Body, Chassis, and Network.

For our testing purposes, two DTCs, 0x00599A and 0x00599C, are configured with DID 0x2345, parameters P2 set to 50 ms, and P2* set to 5 s. CAN messages are transmitted and parsed following the ISO15765-2 and ISO11898-1 protocol specifications.

We conduct tests on the three sub-services of the 0x10 service using the diagnostic control tool in CANoe, and the results of these tests are summarized in Table 2.

TABLE 2. Diagnostic session-related service tests

Service ID	S/R	Data	Result
10 01	Send	02 10 01 00 00 00 00 00	Default session switching through
	Receive	06 50 01 00 32 01 F4 00	
10 02	Send	02 10 02 00 00 00 00 00	Refresh session switch passed
	Receive	06 50 02 00 32 01 F4 00	
10 03	Send	02 10 03 00 00 00 00 00	Extended session switching through
	Receive	06 50 0300 32 01 F4 00	

Based on the preceding test results, all three sub-service switches of the Diagnostic Session Control 0x10 service were successfully executed, with the corresponding parameters returned. Subsequently, service tests related to diagnostic fault codes (DTC) are detailed in Table 3.

From the aforementioned tests, the Read DTC (0x19 02) and Clear DTC (0x14) tests were successfully executed based on the status mask, while the Report DTC Number (0x19 01) test, also based on the status mask, did not pass. The configuration for the 0x19 01 service was not in place during the setup, and it appropriately returned a Negative Response Code (NRC) of 0x12, indicating that the sub-service is not supported—a correct result.

Service tests related to reading and writing data based on Data Identifiers (DID) are elaborated in Table 4.

Building on the preceding test outcomes, the Read and Write Data by Data Identifier (0x22 and 0x2E)

TABLE 3. DTC-related service testing

Service ID	S/R	Data	Result
19 02	Send	03 19 02 2F 00 00 00 00	Read the DTC according to the status mask and pass the test
	Receive	10 0B 59 02 FF 00 59 9A	
	Send	30 00 14 00 00 00 00 00	
	Receive	21 2F 00 59 9C 2F 00 00	
14	Send	04 14 FF FF FF 00 00 00	Clear DTC, service test passed
	Receive	01 54 00 00 00 00 00 00	
19 01	Send	03 19 01 7F 00 00 00 00	Service failed
	Receive	03 7F 19 12 00 00 00 00	

TABLE 4. DID-related service testing

Service ID	S/R	Data	Result
22	Send	03 22 23 45 00 00 00 00	Read DID value successfully
	Receive	04 62 23 45 55 00 00 00	
2E	Send	04 2E 23 45 EB 00 00 00	The value of DID was modified successfully
	Receive	03 6E 23 45 00 00 00 00	
22	Send	03 22 23 45 00 00 00 00	Successfully read and re-write the DID value
	Receive	04 62 23 45 EB 00 00 00	
22	Send	03 22 23 44 00 00 00 00	Failure to read a value that does not support DID
	Receive	03 7F 22 31 00 00 00 00	

service passed successfully. However, when attempting to read an unassigned Data Identifier (DID), the service appropriately returned a Negative Response Code (NRC) of 0x31.

To enhance security, the Vehicle Security Bridge (VSB) was reconfigured to establish the security access level and session for the DTC reading service. This adjustment ensures correct reading and clearing of DTCs if the security access level and session credentials are successfully authenticated.

TABLE 5. Security access-related testing

Service ID	S/R	Data	Result
10 03	Send	02 10 03 00 00 00 00 00	Extended Session Switching
	Receive	50 03 00 32 01 F4 00 00	
27 01	Send	02 27 01 00 00 00 00 00	Request seeds and return them successfully
	Receive	67 01 12 34 00 00 00 00	
27 02	Send	04 27 02 12 39 00 00 00	Successfully send the key and successfully match the key
	Receive	07 02 00 00 00 00 00 00	
19 02	Send	03 19 02 2F 00 00 00 00	Read DTC according to the status mask; the test passes
	Receive	10 0B 59 02 FF 59 9A	
	Send	30 00 14 00 00 00 00 00	
	Receive	21 2F 00 59 9C 2F 00 00	

14	Send	04 14 FF FF FF 00 00 00	Clear DTC, the test passes
	Receive	01 54 00 00 00 00 00 00	
10 01	Send	02 10 01 00 00 00 00 00	Default session switching is done
	Receive	06 50 01 00 32 01 F4 00	
19 02	Send	03 19 02 2F 00 00 00 00	Security level not passed, cannot read DTC
	Receive	30 7F 19 33 00 00 00 00	

The results presented in Table 5 demonstrate the successful reading of Diagnostic Trouble Codes (DTC) when the session and security levels are validated. Conversely, in cases of session and security level failure, the service appropriately returned a Negative Response Code (NRC) of 0x33, indicating failed security verification.

To further substantiate the superiority of the proposed method, a comparative analysis of fault detection time and fault detection rates was conducted among three different methods. The experimental comparison results are detailed in Table 6.

The results depicted in Table 6 unequivocally showcase the superiority of our proposed method over the other two methods (5, 6), particularly in terms of fault detection rate and detection time.

TABLE 6. Comparison of Fault Detection Rate

Solution	Single core CPU occupancy rate	Fault detection success rate	Fault detection time
CAN bus [5]	74.94%	85.73%	0.0319
Structural analysis method [6]	68.53%	89.72%	0.0247
Our	40.68%	98.70%	0.0217

5. CONCLUSION

Building upon the existing electric vehicle fault diagnosis system, this paper delineates the design and implementation of an electric vehicle fault detection system adhering to the AutoSAR standard. The design encompasses diagnostic communication and function modules based on the diagnostic protocol, and comprehensive testing has been conducted. The proposed method showcases remarkable attributes, boasting a single-core CPU utilization rate of merely 40.68%, a fault detection time as low as 0.0217 seconds, and an

impressive fault detection success rate of 98.70%. In direct comparison with the CAN bus and structural analysis methods, our proposed method outperforms, exhibiting a 12.97% and 8.98% improvement in fault detection success rates, respectively. Notably, this achievement is accompanied by more efficient test indices, resulting in heightened accuracy in fault detection results.

6. DATA AVAILABILITY STATEMENT

The labeled dataset used to support the findings of this study is available from the corresponding author upon request.

7. FUNDING STATEMENT

This study was supported by Self-made teaching instruments and equipment project of Tianjin Sino German University of applied technology. (No. ZDZY2020-02A)

8. AUTHORSHIP CONTRIBUTION STATEMENT

Xiaogang YANG: Writing-Original draft preparation
Conceptualization, Supervision, Project administration.

9. REFERENCES

1. Abedinia O, Shorki A, Nurmanova V, Bagheri M. Synergizing Efficient Optimal Energy Hub Design for Multiple Smart Energy System Players and Electric Vehicles. *IEEE Access*. 2023;11:116650-116664. 10.1109/ACCESS.2023.3323201.
2. Lu M, Abedinia O, Bagheri M, Ghadimi N, Shafie-khah M, Catalão JPS. Smart load scheduling strategy utilising optimal charging of electric vehicles in power grids based on an optimisation algorithm. *IET Smart Grid*. Wiley Online Library; 2020;3(6):914–23. 10.1049/iet-stg.2019.0334
3. Abedinia O, Lu M, Bagheri M. An improved multicriteria optimization method for solving the electric vehicles planning issue in smart grids via green energy sources. *IEEE Access*. 2019;8:3465–81. 10.1109/ACCESS.2019.2960557
4. Gholami M, Sanjari MJ. Optimal Operation of Multi-Microgrid System Considering Uncertainty of Electric Vehicles. *International Journal of Engineering, Materials and Energy Research Center*; 2023;36(8):1398-1408 10.5829/ije.2023.36.08b.01
5. Bhosale AP, Mastud SA. Comparative Environmental Impact Assessment of Battery Electric Vehicles and Conventional Vehicles: A Case Study of India. *International Journal of Engineering, Materials and Energy Research Center*; 2023;36(5):965–78. 10.5829/ije.2023.36.05b.13
6. Ahmadijorji M, Mehrasa M. A robust renewable energy source-oriented strategy for smart charging of plug-in electric vehicles considering diverse uncertainty resources. *International Journal*

- of Engineering, Transactions A: Basics. 2023;36(4):709–19. 10.5829/ije.2023.36.04a.01
7. Jian Y, Qing X, Zhao Y, He L, Qi X. Application of model-based deep learning algorithm in fault diagnosis of coal mills. *Mathematical Problems in Engineering* Hindawi Limited; 2020;2020:1–14. 10.1155/2020/3753274
 8. Ochando FJ, Cantero A, Guerrero JI, León C. Data Acquisition for Condition Monitoring in Tactical Vehicles: On-Board Computer Development. *Sensors*. MDPI; 2023;23(12):5645. 10.3390/s23125645
 9. Wang Y. Design of Electric Drive System of Electric Vehicle Based on CAN Bus. In: *Journal of Physics: Conference Series*. IOP Publishing; 2021;1982(1): 012131. 10.1088/1742-6596/1982/1/012131
 10. Haur I. AUTOSAR compliant multi-core RTOS formal modeling and verification (Doctoral dissertation, École centrale de Nantes). 2022. <https://theses.hal.science/tel-04025811/>
 11. Staron M, Staron M. AUTOSAR (AUTomotive Open System ARchitecture). *Automotive Software Architectures: An Introduction*. Springer; 2021;97–136. 10.1007/978-3-030-65939-4_5
 12. AUTOSAR GbR. AUTOSAR Methodology V1.2.1. 2008;
 13. AUTOSAR GbR. Specification of the Virtual Functional Bus V1.0.1. 2008;
 14. AUTOSAR GbR. Specification of Run-Time Environment V2.0.1 R3.0 Rev001. 2008;
 15. Khenfri F, Chaaban K, Chetto M. Efficient mapping of runnables to tasks for embedded AUTOSAR applications. *Journal of Systems Architecture*. Elsevier; 2020;110:101800. 10.1016/j.sysarc.2020.101800
 16. Amato F, Coppolino L, Mercaldo F, Moscato F, Nardone R, Santone A. CAN-bus attack detection with deep learning. *IEEE Transactions on Intelligent Transportation Systems*. IEEE; 2021;22(8):5081–90. 10.1109/TITS.2020.3046974
 17. AUTOSAR GbR. Specification of CAN Interface [EB/OL]. . 2009;
 18. Chen W, Wang Y, Zhang Z, Qian Z. Syzgen: Automated generation of syscall specification of closed-source macos drivers. 2021 ACM SIGSAC Conference on Computer and Communications Security. 2021:ACM.749–63. 10.1145/3460120.3484564
 19. Zhang K, Liu Y, Zhang J, Zhang G, Jin J, Li Y, et al. TDCA: improved optimization algorithm with degree distribution and communication traffic for the deployment of software components based on AUTOSAR architecture. *Soft comput*. Springer; 2023;27(12):7999–8012.10.1007/s00500-023-07989-1
 20. Sandhya Devi RS, Sivakumar P, Balaji R. AUTOSAR architecture based kernel development for automotive application. *International Conference on Intelligent Data Communication Technologies and Internet of Things (ICICI)* 2018. 2019:Springer.10.1007/978-3-030-03146-6_104
 21. Ran Z, Yan H, Zhang H, Li Y. Approximate optimal AUTOSAR software components deploying approach for automotive E/E system. *International Journal of Automotive Technology*.2017;18:1109-1119. 10.1007/s12239-017-0108-3
 22. Lv J, Qu C, Du S, Zhao X, Yin P, Zhao N, et al. Research on obstacle avoidance algorithm for unmanned ground vehicle based on multi-sensor information fusion. *Mathematical Biosciences and Engineering*.2021;18(2):1022–39. 10.3934/mbe.2021055
 23. Duan M, Darvishan A, Mohammaditab R, Wakil K, Abedinia O. A novel hybrid prediction model for aggregated loads of buildings by considering the electric vehicles. *Sustain Cities Soc*. 2018;41:205–19. 10.1016/j.scs.2018.05.009
 24. Kuspan B, Bagheri M, Abedinia O, Naderi MS, Jamshidpour E. The influence of electric vehicle penetration on distribution transformer ageing rate and performance. 2018 7th International Conference on Renewable Energy Research and Applications (ICRERA). 2018: IEEE. 10.1109/ICRERA.2018.8566966
 25. Nurmanova V, Sultanbek A, Bagheri M, Ahangar RA, Abedinia O, Phung T, et al. Distribution Transformer Frequency Response Analysis: Behavior of Different Statistical Indices During Inter-disk Fault. 2019 IEEE International Conference on Environment and Electrical Engineering and 2019 IEEE Industrial and Commercial Power Systems Europe (EEEIC/I&CPS Europe). 2019:IEEE. 10.1109/EEEIC.2019.8783252
 26. Devi RSS, Kumar BV, Sivakumar P, Lakshmi AN, Tripathy R. Bootloader design for advanced driver assistance system. *Software Engineering for Automotive Systems*. Boca Raton:CRC Press;2022. p. 31-44
 27. Devi RSS, Sivakumar P, Lakshmi AN, Tripathy R. 3 Design Bootloader Advanced Driver Assistance System. *Software Engineering for Automotive Systems: Principles and Applications*. Boca Raton: CRC Press; 2022. p.31-44
 28. Xiao D, Wang N, Shen X, Landulfo E, Zhong T, Liu D. Development of ZJU high-spectral-resolution LiDAR for aerosol and cloud: Extinction retrieval. *Remote Sensing*. 2020;12(18):3047. 10.3390/rs12183047
 29. Wang N, Shen X, Xiao D, Veselovskii I, Zhao C, Chen F, et al. Development of ZJU high-spectral-resolution lidar for aerosol and cloud: Feature detection and classification. *Journal of Quantitative Spectroscopy and Radiative Transfer*. 2021;261:107513. 10.1016/j.jqsrt.2021.107513
 30. Liu D, Yang Y, Cheng Z, Huang H, Zhang B, Shen Y. Development of the ZJU polarized near-infrared high spectral resolution lidar. *International Symposium on Photoelectronic Detection and Imaging 2013: Laser Sensing and Imaging and Applications*. 2013: SPIE. 10.1117/12.2035435

COPYRIGHTS

©2024 The author(s). This is an open access article distributed under the terms of the Creative Commons Attribution (CC BY 4.0), which permits unrestricted use, distribution, and reproduction in any medium, as long as the original authors and source are cited. No permission is required from the authors or the publishers.

**Persian Abstract****چکیده**

با افزایش ادغام ECU در وسایل نقلیه مدرن، پیچیدگی شبکه های وسایل نقلیه نیز به طور مداوم در حال افزایش است. ارتباطات تشخیصی، به عنوان یک عملکرد کلیدی در شبکه های وسایل نقلیه، با چرخه های توسعه طولانی تر و دشواری های بالاتری مواجه است. به منظور بهبود قابلیت استفاده مجدد و قابل حمل بودن نرم افزار، این مطالعه تحقیقات مربوطه را تجزیه و تحلیل کرد و یک سیستم تشخیص عیب خودروی الکتریکی را بر اساس گذرگاه CAN با استفاده از معماری ارتباط تشخیصی توصیه شده توسط استاندارد AUTOSAR پیشنهاد کرد. با اتخاذ AUTOSAR، هدف ما بررسی یک روش توسعه نرم افزار جدید برای سیستم های تشخیص عیب خودرو برای رفع این محدودیت بود. ماژول ارتباطی و تشخیصی این مطالعه با استفاده از AUTOSAR پیاده سازی شد و نیازی به توسعه دهندگان برای بررسی پیچیدگی سخت افزار و پیاده سازی ارتباطات را از بین برد. توسعه دهندگان اکنون می توانند روی طراحی ویژگی های نرم افزار برای تشخیص عیب تمرکز کنند. نتایج تجربی نشان می دهد که نرخ استفاده از CPU تک هسته ای روش پیشنهادی در مقاله تنها ۴۰.۶۸٪ است. زمان تشخیص خطا ۰.۰۲۱۷ است. میزان موفقیت تشخیص عیب ۹۸.۷۰ درصد است که به ترتیب ۱۲.۹۷ درصد و ۸.۹۸ درصد بیشتر از روش تحلیل سازه و گذرگاه CAN است. شاخص های تست به طور موثر کاهش می یابد، و نتایج تشخیص خطا دقیق تر است. بررسی این روش جدید توسعه نرم افزار در محصولات الکترونیکی خودرو، کارایی نرم افزار سیستم عیب یابی خودرو را تا حد زیادی بهبود می بخشد.

AIMS AND SCOPE

The objective of the International Journal of Engineering is to provide a forum for communication of information among the world's scientific and technological community and Iranian scientists and engineers. This journal intends to be of interest and utility to researchers and practitioners in the academic, industrial and governmental sectors. All original research contributions of significant value focused on basics, applications and aspects areas of engineering discipline are welcome.

This journal is published in three quarterly transactions: Transactions A (Basics) deal with the engineering fundamentals, Transactions B (Applications) are concerned with the application of the engineering knowledge in the daily life of the human being and Transactions C (Aspects) - starting from January 2012 - emphasize on the main engineering aspects whose elaboration can yield knowledge and expertise that can equally serve all branches of engineering discipline.

This journal will publish authoritative papers on theoretical and experimental researches and advanced applications embodying the results of extensive field, plant, laboratory or theoretical investigation or new interpretations of existing problems. It may also feature - when appropriate - research notes, technical notes, state-of-the-art survey type papers, short communications, letters to the editor, meeting schedules and conference announcements. The language of publication is English. Each paper should contain an abstract both in English and in Persian. However, for the authors who are not familiar with Persian, the publisher will prepare the latter. The abstracts should not exceed 250 words.

All manuscripts will be peer-reviewed by qualified reviewers. The material should be presented clearly and concisely:

- *Full papers* must be based on completed original works of significant novelty. The papers are not strictly limited in length. However, lengthy contributions may be delayed due to limited space. It is advised to keep papers limited to 7500 words.
- *Research notes* are considered as short items that include theoretical or experimental results of immediate current interest.
- *Technical notes* are also considered as short items of enough technical acceptability with more rapid publication appeal. The length of a research or technical note is recommended not to exceed 2500 words or 4 journal pages (including figures and tables).

Review papers are only considered from highly qualified well-known authors generally assigned by the editorial board or editor in chief. Short communications and letters to the editor should contain a text of about 1000 words and whatever figures and tables that may be required to support the text. They include discussion of full papers and short items and should contribute to the original article by providing confirmation or additional interpretation. Discussion of papers will be referred to author(s) for reply and will concurrently be published with reply of author(s).

INSTRUCTIONS FOR AUTHORS

Submission of a manuscript represents that it has neither been published nor submitted for publication elsewhere and is result of research carried out by author(s). Presentation in a conference and appearance in a symposium proceeding is not considered prior publication.

Authors are required to include a list describing all the symbols and abbreviations in the paper. Use of the international system of measurement units is mandatory.

- On-line submission of manuscripts results in faster publication process and is recommended. Instructions are given in the IJE web sites: www.ije.ir-www.ijeir.info
- Hardcopy submissions must include MS Word and jpg files.
- Manuscripts should be typewritten on one side of A4 paper, double-spaced, with adequate margins.
- References should be numbered in brackets and appear in sequence through the text. List of references should be given at the end of the paper.
- Figure captions are to be indicated under the illustrations. They should sufficiently explain the figures.
- Illustrations should appear in their appropriate places in the text.
- Tables and diagrams should be submitted in a form suitable for reproduction.
- Photographs should be of high quality saved as jpg files.
- Tables, Illustrations, Figures and Diagrams will be normally printed in single column width (8cm). Exceptionally large ones may be printed across two columns (17cm).

PAGE CHARGES AND REPRINTS

The papers are strictly limited in length, maximum 8 journal pages (including figures and tables). For the additional to 8 journal pages, there will be page charges. It is advised to keep papers limited to 3500 words.

Page Charges for Papers More Than 8 Pages (Including Abstract)

For International Author ***	\$55 / per page
For Local Author	100,000 Toman / per page

AUTHOR CHECKLIST

- Author(s), bio-data including affiliation(s) and mail and e-mail addresses).
- Manuscript including abstracts, key words, illustrations, tables, figures with figure captions and list of references.
- MS Word files of the paper.



THOMSON REUTERS
WEB OF SCIENCE



Scopus®

